Title

CHEMICAL MODIFICATION OF SURFACES: THE EFFECT OF POTASSIUM ON THE CHEMISORPTION OF MOLECULES ON TRANSITION METAL CRYSTAL SURFACES

Author

Crowell, J.E.

Publication Date

1984

Lawrence Berkeley Laboratory
UNIVERSITY OF CALIFORNIA

Materials & Molecular Research Division

CHEMICAL MODIFICATION OF SURFACES: THE EFFECT OF POTASSIUM ON THE CHEMISORPTION OF MOLECULES ON TRANSITION METAL CRYSTAL SURFACES

J.E. Crowell
(Ph.D. Thesis)

January 1984

Prepared for the U.S. Department of Energy under Contract DE-AC03-76SF00098

DISCLAIMER

LBL-17223

CHEMICAL MODIFICATION OF SURFACES: THE EFFECT OF POTASSIUM ON THE CHEMISORPTION OF MOLECULES ON TRANSITION METAL CRYSTAL SURFACES

John Edmund Crowell
(Ph.D. Thesis)

Lawrence Berkeley Laboratory
University of California
Berkeley, California 94720

January 1984

This work was supported by the Director, Office of Energy Research, Office of Basic Energy Sciences, Material Sciences Division of the U.S. Department of Energy under Contract Number DE-AC03-76SF00098 and from a University of California Fellowship.

Dedicated

to my parents

CHEMICAL MODIFICATION OF SURFACES: THE EFFECT OF POTASSIUM ON THE CHEMISORPTION OF MOLECULES ON TRANSITION METAL CRYSTAL SURFACES

John Edmund Crowell

Materials and Molecular Research Division
Lawrence Berkeley Laboratory and
Department of Chemistry
University of California
Berkeley, CA 94720

ABSTRACT

The role of alkali metals in modifying the chemistry at metal surfaces has been explored under ultrahigh vacuum (UHV) conditions. The structure and bonding of pure alkali monolayers and that of coadsorbed molecules has been determined using a variety of surface sensitive spectroscopies. Surface vibrational spectroscopy using high resolution electron energy losses has been utilized and has revealed the nature of the interaction of alkalis with molecular adsorbates. The implications of the chemisorption changes induced by alkalis and their role in industrial catalytic reactions is discussed.

The physical and chemical properties of pure potassium monolayers and its effect on the adsorption of oxygen, carbon monoxide and benzene on the (111) faces of platinum and rhodium single crystals are described. Potassium adsorption on both surfaces is quite similar.

Potassium forms hexagonally close packed structures that are incommensurate with the substrate. The heat of desorption of potassium on these surfaces decreases with increasing potassium coverage. The surface free electron density increases and the work function decreases substantially with alkali adsorption, indicating charge transfer occurs from potassium to the substrate.

Oxygen adsorption increases the potassium binding energy, and forms a surface complex at high potassium coverages. Oxygen adsorption is dissociative on both clean and potassium dosed Rh(111). The metal-oxygen stretching vibration increases in the presence of potassium indicating stronger adsorption.

Carbon monoxide adsorption on both metal surfaces is strongly affected. With increasing potassium coverage, the heat of desorption increases while the C-O stretching frequencies decrease. Also, substantial population shifts from the atop to the bridged site occur. Dissociation of CO is induced on Rh(111) by the presence of potassium.

Benzene is found to be π bonded oriented with the ring plane parallel to the surface with $C_{3v}(\sigma_d)$ symmetry on both the clean and potassium dosed Rh(111) surfaces. Potassium reduces the heat of desorption of molecular benzene and induces a lower temperature pathway to decomposition.

The major influence of potassium is to increase the surface electron density, which, for molecular adsorbates with low lying vacant orbitals of the correct symmetry, can lead to substantial changes in their bonding with the surface.

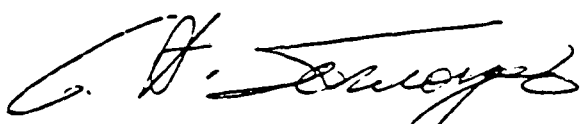

TABLE OF CONTENTS

CHAPTER 1

INTRODUCTION AND OVERVIEW

1.1 Introduction

The chemical modification of surfaces by alkalis plays an important role in heterogeneous and homogeneous catalysis, as well as in the design of electronic devices. In catalysis, alkali promoters (i.e., alkali oxides, hydroxides, and carbonates) are used primarily to alter the selectivity for a particular chemical reaction [1]. Examples of reactions modified by alkalis in an industrial process include the hydrogenation of CO, the ammonia synthesis, hydrocarbon reforming reactions, ethylene oxidation, coal gasification and hydroformylation reactions. In electronic devices such as thermionic energy converters, alkali and alkali oxides alter the electron and ion emission properties, permitting more efficient conversion of thermal power to electrical power [2]. An understanding of catalysts or electronic devices then requires an understanding of the fundamental nature of the surface processes involved. The goal of the surface science investigation described here is to explore the fundamental nature of the influence of alkalis, particularly potassium, in modifying the chemical properties of metal surfaces.

The role alkali adatoms play in altering the chemical bonding at surfaces can best be explored by a combination of surface sensitive spectroscopies. Those employed here include: high resolution electron energy loss spectroscopy (HREELS) for surface vibrational analysis; temperature programmed desorption (TPD) for determining kinetic order,

surface concentration and desorption energies; low energy electron diffraction (LEED) for atomic geometry and structure determination; Auger electron spectroscopy (AES) for qualitative and quantitative determination of surface composition, and second harmonic generation (SHG) for qualitative changes in the free-electron density at the surface. Surface vibrational spectroscopy was emphasized in this investigation due to its ability to investigate the chemical, structural and symmetry properties of these pure and coadsorbed alkali adsorption systems. All five techniques are used in conjunction to provide a detailed description of the chemisorption system under investigation.

1.2 Objectives

The main objective of this dissertation is to determine the role alkalis play in modifying the chemistry at metal surfaces. It is thought that alkalis promote certain reactions because they alter the electronic properties of the metal surface. Alkalis modify the surface electronic structure by transferring electronic charge to the substrate. This is readily achieved due to the low ionization potential of alkali metals. The characteristic dramatic decrease in the work function of a metal surface upon alkali adsorption is evidence that this transfer occurs. As a consequence of the increased electron density at the surface, the chemisorptive properties of these surfaces are altered, resulting in changes in catalyst activity and product distribution. The purpose of the model studies presented here is to

address how alkalis influence chemisorption and quantify the magnitude of the effect. The key questions addressed in this investigation are:

i) How does the chemisorption properties of molecules change upon preadsorption of alkalis?

ii) Do alkalis influence surface structure or site geometry?

iii) Does the nature or magnitude of the interaction vary from metal to metal?

iv) What is the mechanism of the interaction (i.e., does it occur through the substrate or through space)?

v) Is the interaction local or nonlocal, i.e., what is the range of the interaction?

vi) Does coadsorbed potassium affect the dissociation probability or decomposition pathway of molecular adsorbates?

These questions are addressed for a number of adsorption systems by comparing adsorption on the clean surface to that on the potassium predosed surface.

1.3 Overview

In this thesis, the chemisorption changes induced by potassium on the adsorption of oxygen, carbon monoxide, and benzene on the Pt(111) and Rh(111) crystal surfaces are described. The adsorption of these species on the clean Pt(111) and Rh(111) surfaces was also measured to characterize what changes were induced by the preadsorption of the alkali metal. The adsorption and desorption properties of the pure potassium overlayer was also measured, and the changes induced in the alkali layer by coadsorption of the molecular adsorbates was followed.

This thesis is organized as follows. In Chapter 1, the importance of alkali layers is discussed, as are the goals and objectives of this dissertation. A brief summary is also given. A detailed description of the technique used most in this thesis, high resolution electron energy loss spectroscopy, is given in Chapter 2. The basic principles behind all of the surface sensitive techniques used as well as the methodology in which they were employed is detailed in Chapter 3. The experimental configuration of the apparatuses used is also given here. The experimental results obtained are discussed in Chapters 4 through 6. In Chapter 4, the chemisorptive properties of pure alkali layers on both Pt(111) and Rh(111) are presented. Furthermore, the interaction of oxygen with the potassium dosed Rh(111) surface is discussed here. In Chapter 5, the results for the chemisorption of CO on the clean and potassium dosed Pt(111) and Rh(111) surfaces are described. The findings for the two surfaces are discussed separately, with general comparison of the two surfaces appearing in the conclusion portion of this chapter. A structure and bonding determination of benzene on Rh(111) is presented in Chapter 6. The thermal decomposition of this layer is also examined here. Finally, the effect potassium has on the adsorption and thermal decomposition of a benzene layer is given in the latter portion of this chapter.

The physical and chemical properties of alkali overlayers were quite similar on Pt(111) and Rh(111). One characteristic of these potassium adsorption systems is that the substrate is completely covered by the larger potassium atoms at a coverage of $\theta_K = 0.36$, i.e. 0.36 potassium adatoms per surface substrate atoms. At this

coverage, characteristic low energy electron diffracton patterns are seen indicating that potassium exists in a close packed hexagonal array which is incommensurate with the substrate. At slightly lower coverages, orientational reordering of the overlayer occurs, indicating the insensitivity of the alkali to the substrate potential variations. Second harmonic generation indicates that the surface free electron density increases as potassium is adsorbed. Similarly, the work function decreases with alkali adsorption by up to 4 eV, indicating substantial charge transfer.

On both surfaces, the changes seen in the TPD desorption maxima as a function of K coverage correspond to a change in the heat of desorption from 65 kcal/mole at low K coverages to 20 kcal/mole at saturation of the first layer. This variation is common for alkali adsorption and is attributed to depolarization affects at high coverages.

Oxygen adsorption onto a potassium overlayer increases the potassium binding energy by up to 30 kcal/mole at high alkali coverages ($\theta_K > 0.35$). At $\theta_K > 0.2$ the desorption of oxygen begins to occur at the same temperature as that for potassium indicating a surface complex is formed. Oxygen adsorption onto the potassium covered surface is dissociative, similar to that observed for the clean surface. Increases in the temperature where maximum oxygen desorption occurs coupled with the increase in the M-O stretching vibration observed as a function of increasing potassium coverage indicates that atomic oxygen is bonded stronger when potassium is coadsorbed.

Similarly, the presence of preadsorbed potassium strongly increases the adsorption energy of CO on both Pt(111) and Rh(111). The heat of adsorption increases continuously with increasing potassium coverage up to 11 kcal/mole. The CO stretching vibrations decrease continuously with either increasing potassium coverage or decreasing CO coverage. Substantial population and adsorption sequence shifts in site occupancy from the atop to the bridge site occur as a function of increasing potassium coverage. The results indicate both strengthening of the M-C bond and weakening of the C-O bond in the presence of potassium, due presumably to increased electron occupancy of the $2\pi^*$-orbital of CO. Broadening and asymmetry of the vibrational peaks suggest the proximity of the CO molecules to the potassium adatoms influences the chemisorption behavior, although nonlocal interactions are also indicated. C-O vibrational frequencies as low as 1400 cm^{-1} are observed, indicative of a weakened CO molecule of bond order 1.5. Dissociation does not occur on either surface at low pressures without coadsorbed potassium, but does occur for Rh(111) when $\theta_K > 0.10$.

On both clean and potassium dosed Rh(111) the vibrational spectra indicate that benzene adsorbs molecularly at 300K and is π-bonded to the surface with the ring plane parallel to the surface plane.

For the clean Rh(111) surface, recent dynamic LEED calculations [3] together with the angle-dependent HREELS studies reported here establish a $C_{3v}(\sigma_d)$ bonding symmetry for the $c(2\sqrt{3} \times 4)$rect-C_6H_6 structure. Several other ordered benzene overlayers can be formed between 300-400K depending on the benzene coverage. No large

changes occur in the chemisorption bonding mode or geometry coincident with the two-dimensional ordering phase transitions in this temperature range. The TPD and HREELS data on Rh(111) and other single crystal surfaces show correlations between the metal-benzene bond strength, the work function of the clean surface, and the frequency shifts of some of the molecular benzene vibrational modes.

On both the clean and potassium dosed Rh(111) surfaces the vibrational spectra show that two molecular adsorption sites can be populated. On both surfaces benzene adsorption is only partially reversible; less than twenty percent of the adsorbed benzene desorbs molecularly upon heating. The remaining benzene irreversibly decomposes, evolving hydrogen and leaving a carbon-covered surface. The heat of desorption for molecular benzene decreases when potassium is preadsorbed, and a lower temperature pathway to decomposition becomes preferred.

The results show that the chemical properties of a transition metal surface can be modified by potassium. The major influence of alkalis is to increase the electron density at the surface, which, for molecular adsorbates with low lying vacant orbitals of the correct symmetry, can lead to substantial changes in their bonding with the surface.

REFERENCES

1. R. B. Anderson, in Catalysis, Vol. 4 P. H. Emmett, Ed., Reinhold, New York, 1956.

2. G. N. Hatsopoulos and E. P. Gyftopoules, Thermionic Energy Conversion, Vol. 1, Processes and Devices; Vol. 2, Theory, Technology and Application, MIT Press, Cambridge, 1974 and 1979.

3. M. A. Van Hove, R. F. Lin and G. A. Somorjai, Phys. Rev. Lett. 51, 778 (1983).

CHAPTER 2

FUNDAMENTALS OF HIGH RESOLUTION ELECTRON ENERGY LOSS SPECTROSCOPY

2.1 Introduction

Surface vibrational spectroscopy can be used to characterize adsorbed atoms and molecules on solid surfaces. The characteristic vibrational frequencies of each bond permits the structure and bonding of adsorbed species to be determined. In particular, vibrational spectroscopy can provide significant information on the identity of the surface species, its geometric orientation, the adsorption site, the adsorption symmetry, the nature of the bonding ivolved, and in some cases, bond lengths, bond angles, and bond energies.

Several experimental methods have been developed to study the vibrational modes of adsorbed molecules [1,2]. Several optical techniques have been used successfully, including infrared reflection absorption spectroscopy (IRAS) infrared transmission absorption spectroscopy (ITAS) [2,3], and Raman spectroscopy, especially surface enhanced Raman spectroscopy (SERS) [2,4]. Recently, infrared emission spectroscopy [5] has been applied to study surfaces. Electron spectroscopies commonly used include both high resolution electron energy loss spectroscopy (HREELS) [2,6] and inelastic electron tunneling spectroscopy (IETS) [2,7]. Both atom and neutron inelastic scattering (AIS and NIS, respectively) have also found application in surface vibrational studies [2,8], as has photoacoustic spectroscopy (PAS) [9]. Of these, three seem to be used more extensively: HREELS,

IRAS, and SERS [10]. Each of these three techniques has distinct advantages which make it particularly well suited for certain applications, but all have disadvantages limiting their universal use. For instance, HREELS is characterized by high sensitivity, and wide spectral range, but suffers from low resolution (>20 cm^{-1}) and limited ambient pressure conditions. On the other hand, IRAS permits high sensitivity at high resolution, but the accessible spectra range is limited. The capability of detection at pressures from ultrahigh vacuum to an atmosphere is a distinct advantage over HREELS, although single crystal studies have been limited principally to CO adsorption due to difficulties in signal detection (i.e., species with large dynamic dipole moments such as CO are more easily detected than molecules with much weaker signals, such as hydrocarbons). Raman spectroscopy, particularly SERS, have found wide application since it permits high resolution, a wide spectral range, and investigation at high pressures, even at the solid-liquid interface. However, the sensitivity of Raman spectroscopy is rather poor. Under favorable conditions, enhanced scattering intensities are possible, but uncertainty and lack of control in achieving these enhancements, as well as limitations on the substrates showing enhancement, prevent its wide applicability. The other surface vibrational spectroscopies not discussed are in general less applicable and sometimes more difficult experimentally and hence are not used as often as HREELS, IRAS, and SERS. For studying chemisorption on small area samples in high vacuum, HREELS is the most applicable; the remaining portions of this chapter

will focus on the characteristics, instrumentation and practice of this technique. More detailed comparisons of the capabilities of the other surface vibrational spectroscopies can be found elsewhere [6,11].

In HREELS, a collimated monochromatic electron beam of energy 1-15 eV is scattered from a crystal surface. The reflected electrons are then analyzed in energy and angular distribution. The incident electrons, monochromatized typically between 3 and 12 meV (~25-100 cm^{-1}, 1 meV = 8.065 cm^{-1}) and with energy E_i, can lose energy $\hbar\omega_o$ upon exciting a quantizied vibrational mode. These backscattered electrons of energy $E_s - \omega_o$, provide information on the surface layer due to the low penetration depth of these low energy electrons. (As electron spectroscopies are used repeated in this thesis, Chapter 3 contains a more detailed description of this inherent surface sensitivity).

The sensitivity of HREELS in detecting submonolayer quantities of adsorbates on the sample depends on the particular parameters of the spectrometer, the sample, and the adsorbate [6]. However, typical sensitivity is quite high due in part to the high inelastic electron cross section. A detection limit of ~10^{-4} monolayers can be achieved for a strong dipole scatterer when measured at low temperatures [6]. In addition, unlike many other surface spectroscopies, HREELS is also capable of detecting adsorbed hydrogen, although at a lower sensitivity (typically 10^{-1}-10^{-2} monolayers [6]).

The typical electron beam current at the sample in HREELS is 10^{-9}-10^{-11} Amperes. Hence due to the low incident beam currents

and beam energies used, HREELS is non-destructive, and can be used to explore the vibrational modes of weakly adsorbed species and those susceptible to beam damage, such as many hydrocarbon overlayers.

The spectral range accessible with HREELS is quite large. Typical experiments examine between 200 and 4000 cm^{-1}, but much larger regions can be analyzed. Recent experiments by Demuth et al., have examined vibrational modes as far out as 16,000 cm^{-1} [12]. Hence, besides fundamentals, energy losses due to overtones, combination bands, and multiple losses are distinguishable. An example of such losses is given in Chapter 5 for CO adsorbed on Rh(111).

A distinct advantage of HREELS is that electrons can excite the vibrational modes of the surface by three different mechanisms: dipole scattering, impact scattering, and resonance scattering. By analyzing the angular dependence of the inelastically scattered electrons, at least two of these can be explored. Such analysis allows a complete symmetry assignment of the surface-adsorbate complex to be made. This will be discussed further in sections 2.3 and 2.4.

The restrictions on the adsorption system are minimal: ordered or disordered overlayers can be examined, as can either well-structured single crystal samples or optically rough surfaces. Hence, chemisorption on evaporated films can be studied [13], as can the nature of metal overlayer-semiconductor interactions [14]. In addition, coadsorbed atoms and molecules can be studied without

difficulty as shown throughout this thesis. Of course, since electron-gas collisions become significant at pressures between 1-5 x 10^{-5} torr, HREELS is restricted to UHV analysis, preventing direct studies of gas-solid or liquid-solid interfaces at conditions important both catalytically and electrolytically. However, since these experiments require UHV, additional surface science techniques can be utilized to comprehensively explore the adsorption system. The multi--technique approach has been used throughout the research described here.

The major disadvantage of HREELS, especially compared to optical techniques, is the relatively poor instrumental resolution. As mentioned above, resolution can vary between 3-12 meV (25-100 cm^{-1}), although the typical resolution used is 50-80 cm^{-1}. The majority of the spectra presented here were taken at 40 cm^{-1}. The spectral resolution hinders assignment of vibrations to individual modes, although peak assignments can be made to at least within 10 cm^{-1}. However, most of the losses observed are due to a single vibrational mode. Furthermore, if the layer is stable, one can increase the resolution up to 20 cm^{-1}, in this case, and average over a longer time to obtain good signal-to-noise ratio. (The intensity of the elastic and inelastic electrons depends critically on the resolution, as we will see in the next section). Two closely occurring modes were separated for benzene adsorbed on Rh(111) using this procedure, as discussed in Chapter 6. The high sensitivity of HREELS coupled with the advantages discussed above has encouraged rapid development and use of this technique [15], despite resolution limitations.

2.2 Instrumentation

A number of different energy dispersion devices using electrostatic deflection have been successfully employed to monochromate and analyze electrons with high resolution. In particular, 127° cylindrical deflector analyzers [6,16], cylindrical mirror analyzers [17], and 180° spherical analyzers [18] are all currently in use to measure electron energy losses of a few millielectron volts. In the work presented here, spectrometers with 127° cylindrical deflector analyzers were used exclusively. A schematic of one of these is shown in Figure 2.1. Electrons emitted by a filament are focused onto the entrance slit of the monochromator by an Einsel lens (three asymmetric electrostatic lenses). The center of the filmanet is positioned at the focus of a parabolic repeller to collimate the ejected electron beam. The monochromator, consisting of a 127° cylindrical deflector with entrance and exit slits, reduces the energy width of the beam by selecting out electrons of well-defined energy. The electrons are then accelerated and focused onto the sample. The backscattered electrons are then decelerated and energy analyzed with a second electrostatic deflection system, and detected with a channeltron electron multiplier. The electrons are energy analyzed by sweeping the analyzer assembly voltages through the desired energy range. Vibrational energies are measured as the difference $\hbar\omega$ between the elastic and inelastic electron kinetic energies (E_i-E_s).

The power supplies used to create, monochromatize, analyze and detect these low energy electrons is shown schematically in Fig. 2.2.

A low noise, ultra stable power supply is used to provide the voltages for the spectrometer lens and sector elements, and is capable of fast response to permit rapid voltage scanning. The design and fabrication of this HREELS power supply is given in Appendix A. This power supply controls the output of a filament supply used to power the electron filament. A ramp generator is used to sweep the analyzer assembly voltages. Alternatively, a stairstep voltage ramp provided by a digital-to-analog converter of a microcomputer can be used. A triangular wave generator is also used to repetitively scan small energy regions of the spectrum rapidly. A high voltage supply provides the necessary voltage to power the electron multiplier, which is distributed by a resistor and zener diode assembly. The electron pulses detected by the electron multiplier are decoupled from the high voltage bias, amplified, discriminated, shaped, and then counted in analog fashion with a ratemeter. The output of the ratemeter versus the analyzer voltage is plotted on an X-Y recorder. Scattering intensities are typically 10^4-10^6 counts per second (cps) for specular reflection and 1-10^4 cps for inelastic scattering.

As shown in Fig. 2.1, the scattering geometry of the spectrometer is fixed at a total scattering angle of 120°. For specular reflection then the angle of incidence equals the angle of reflection at 60°. To perform off specular measurements to discern between the three possible inelastic scattering mechanisms, the sample can be rotated such that the angle of incidence does not equal the angle of reflection. One spectrometer used was capable of rotation of the monochromator assembly

as well, hence allowing the angle of incidence to remain constant for these such measurements. A schematic diagram of this spectrometer is shown in Fig. A.1.

The technical and physical requirements needed to achieve high resolution are unique in HREELS. Ibach and Mills have addressed the many parameters important in spectrometer design [6]. Briefly, the major requirements are to achieve high resolution and independently control the electron energy. The electrons both excite and detect the vibrational modes of the surface layer. As a consequence, the broad energy distribution of the thermionic or field emission electron source must be filtered to monochromatize the beam to a few millielectron volts. The resolution desired is that of the natural linewidth of adsorbed species, namely 5-10 cm^{-1} [6]. Hence, to achieve high resolution, the energy filtering devices must operate at low pass energies. At these low energies, the work function (or contact potential) of the spectrometer elements (or any given material) is nonuniform. Different crystallographic planes of the same material differ markedly in their work function, as does the same surface when any adsorbate is adsorbed. Furthermore, even in ultrahigh vacuum, unknown carbonaceous overlayers may cause charging of the material. The most important consequence [6] of these uncontrollable work function variations is that as the pass energy of the monochromator is lowered to achieve high resolution, the energy width of the monochromatized electrons approaches a minimum value. Figure 2.3 shows that as

the pass energy is lowered for our spectrometer, the energy width (measured as the full width at half maximum of the elastically scattered beam, and labelled $\Delta E_{1/2}$) reaches a minimum at 20 cm^{-1} (2.5 meV). This then is the work function variation that the electrons feel in their path through the spectrometer. The solid line gives the expected dependence of the resolution on pass energy for our particular spectrometer. The pass energy (E_{pass}) is a linear function of the deflecting potential ΔV (i.e. the voltage difference between the inner and outer sectors of the monochromator or analyzer):

$$E_{pass} = e\Delta V/2[\ln (R_{outer}/R_{inner})] = 1.81\ \Delta V$$

where R_{outer} and R_{inner} are the radii of the outer and inner sectors of the 127° cylindrical deflectors, and are equal to 41.40 and 31.39 mm, respectively. The pass energy is given in electron volts when the deflecting potential is given in volts. The energy resolution of these 127° cylindrical deflectors is approximately given [19] by the equation

$$\frac{\Delta E_{1/2}}{E_{pass}} \approx \frac{\Delta S}{R_{mean}} + \frac{1}{3}\alpha^2 + \frac{1}{4}\beta^2$$

where ΔS is the slit width, R_{mean} is the mean radius of the 127° cylindrical deflectors, and α and β are the angular apertures in the plane and perpendicular to the plane of deflection, respectively. We can estimate the expected performance of our spectrometer. Using $\alpha = \beta = 0$, $\Delta S = 0.2$ mm (0.008 inches), and $R_{mean} = 35.00$ mm, we

estimate that $\Delta E_{1/2}/E_{pass} = 0.006$. As seen in Fig. 2.3, the experimental points fall quite close to this expected dependence.

Besides the leveling off of the energy width to 20 cm^{-1} ($\Delta E_{1/2}$), we also find that elastically scattered electrons are practically undetectable at pass energies less than ~0.15 eV. The reason for this is the severe trade-off between energy resolution and the available signal. It is expected that the monochromatic current at the sample varies with approximately the square of the energy width due to space charge effects [6]. In Fig. 2.4, the elastic scattering intensity detected at the electron multiplier is plotted as a function of the energy resolution $\Delta E_{1/2}$ (FWHM). The data points are shown with two least squares fit to the experimental curves assuming that the intensity measured at the detector is proportional to some power of the resolution $\Delta E_{1/2}$. Additionally assuming that the intensity goes to zero when the resolution goes to zero gives a very poor fit to the data with $I \alpha \Delta E_{1/2}^{3.8}$. Experimentally it is found that the intensity drops to zero at low pass energies. In Fig. 2.3 the resolution levels off near 2 meV (16 cm^{-1}). Assuming that the elastically scattered electron intensity detected at the electron multiplier falls to zero at a resolution of 2 meV, the left curve in Fig. 2.4 is obtained. The fit to the experimental points is quite good (solid line) and the dependence is calculated to be proportional to $(\Delta E_{1/2} - 2)^{1.85}$. Although the origin is readjusted, the measured intensity is very nearly proportional to the square of the resolution, as predicted.

The acceptance angle of the HREELS spectrometer also affects the intensity. Due to space charge effects, the angular resolution should be relatively low in order to accept as much signal as possible. However, due to physical constraints this is not always achievable experimentally [6]. The measured acceptance angle for the spectrometer used here is ~4° (FWHM), as determined from Fig. 2.5 where the measured elastic scattering itensity is plotted versus the difference in the incident and scattered beam angles.

The measured intensity can also vary with the electron beam energy. Consequently most spectrometers are capable of varying the beam energy between 1-10 eV in order to maximize the intensity by choosing regions of high reflectivity for a particular adsorption system. Figure 2.6 depicts the variation in intensity of the elastically scattered beam from benzene adsorbed on Rh(111) as a function of beam energy. Beam energies of ~4 eV were chosen to maximize the scattered intensity, as described in Chapter 6.

Of course, the background present is also important since losses as small as 10^{-6} of the elastic beam intensity are possible. Hence, performance of the spectrometer not only depends on the resolution and intensity, but also the shape and tailing of the energy distribution function [6]. Such tailing originates from electrons passing through the analyzer with a large angular spread. Occasionally, reducing the resolution also decreases such tailing.

The most important aspect of spectrometer performance is the reliability and ease of use in measuring electron energy losses. Figure 2.7 demonstrates typical spectrometer performance for measuring the vibrational modes of species with large dynamic dipoles. The vibrational spectra of species with much weaker cross sections can be measured as readily with only slight resolution degradation (~40–50 cm^{-1}). Examples of both are presented throughout this dissertation.

FIGURE CAPTIONS

Fig. 2.1. Schematic of the HREEL spectrometer used for all vibrational spectra recorded on Rh(111). The individual elements are labelled; the description given in parentheses refers to the applied voltage, as described in Appendix A.

Fig. 2.2. Schematic of the power supplies used in HREELS.

Fig. 2.3. A plot of the measured resolution (points) as a function of pass energy. The solid line gives the predicted linear dependence for this plot.

Fig. 2.4. The intensity of the elastically scattered electrons measured at the electron multiplier plotted as a function of resolution. The dots are experimental points, the solid curves are the result of a least squares analysis assuming an exponential dependence. The best fit occurs when the intensity is assumed to go to zero at 2 meV resolution.

Fig. 2.5. Absolute intensity of the elastically reflected beam as a function of $\theta_s - \theta_i$. The angular FWHM of the detected elastic peak is ~4° at a beam energy of 4 eV.

Fig. 2.6. Variation of the elastic beam intensity as a function of the beam energy.

Fig. 2.7. A vibrational spectrum recorded at 30 cm^{-1} for CO adsorbed on Rh(111) demonstrating the obtainable resolution and background for this HREEL spectrometer.

HREELS SPECTROMETER

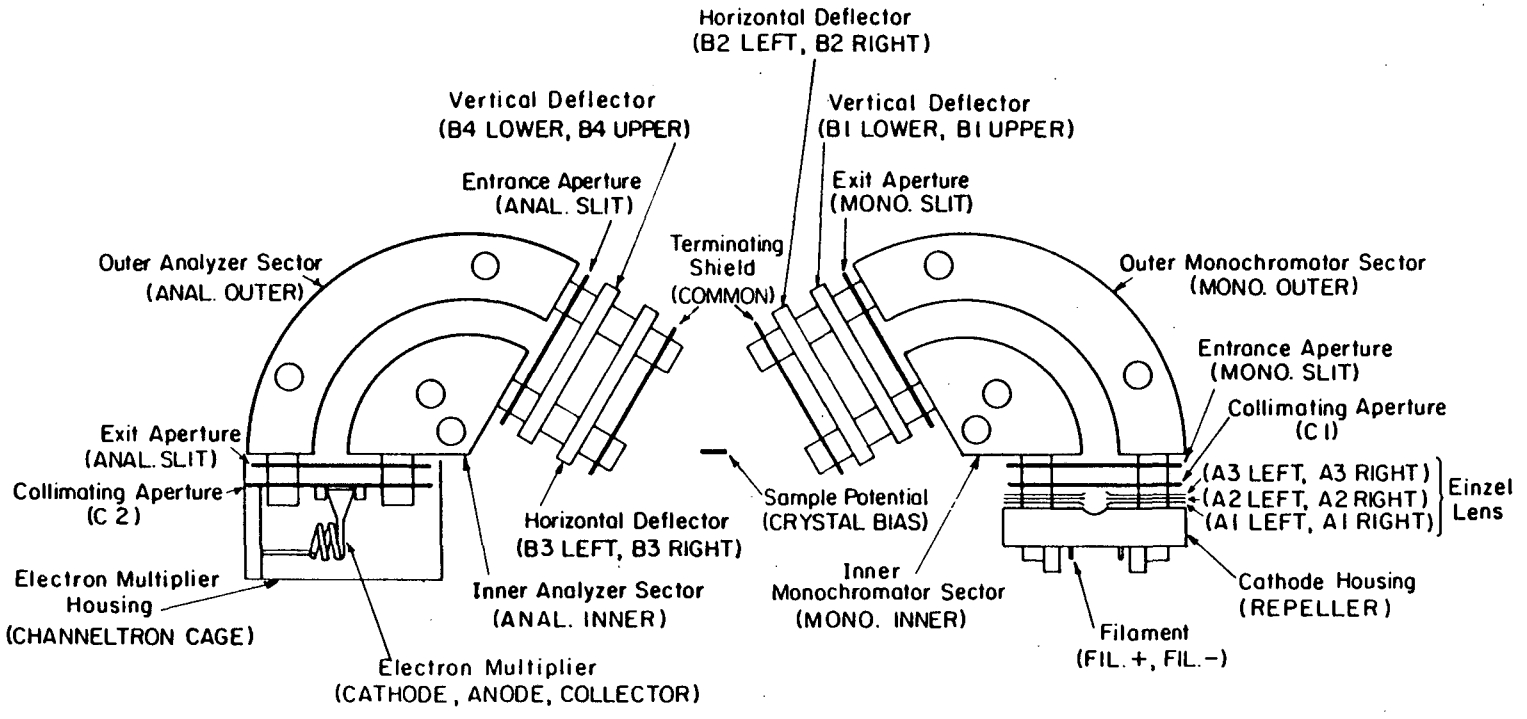

XBL 839-6319

Figure 2.1

HREELS ELECTRONICS

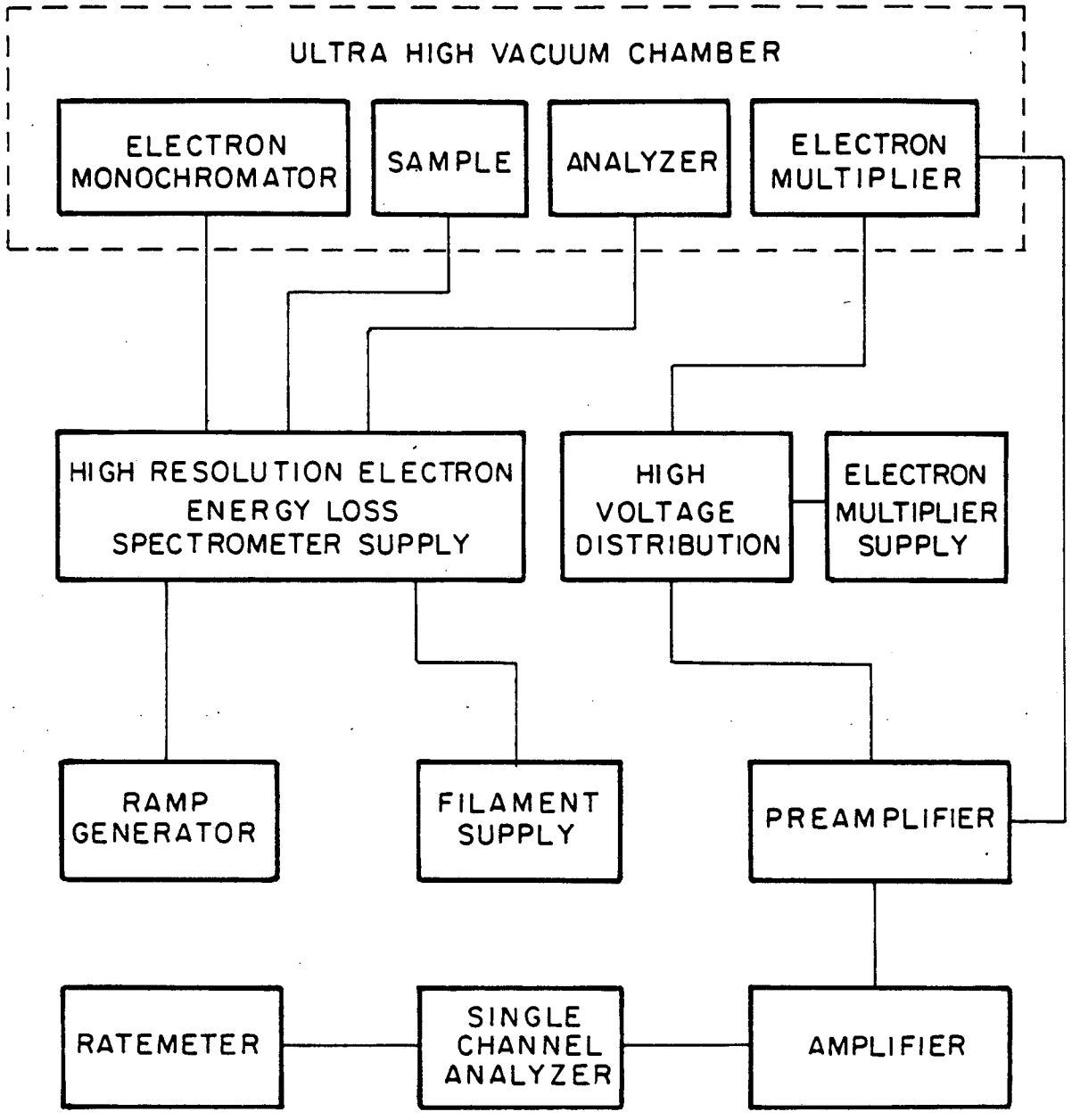

XBL8312-6685

Figure 2.2

RESOLUTION OF ELASTICALLY SCATTERED ELECTRONS
AS A FUNCTION OF PASS ENERGY

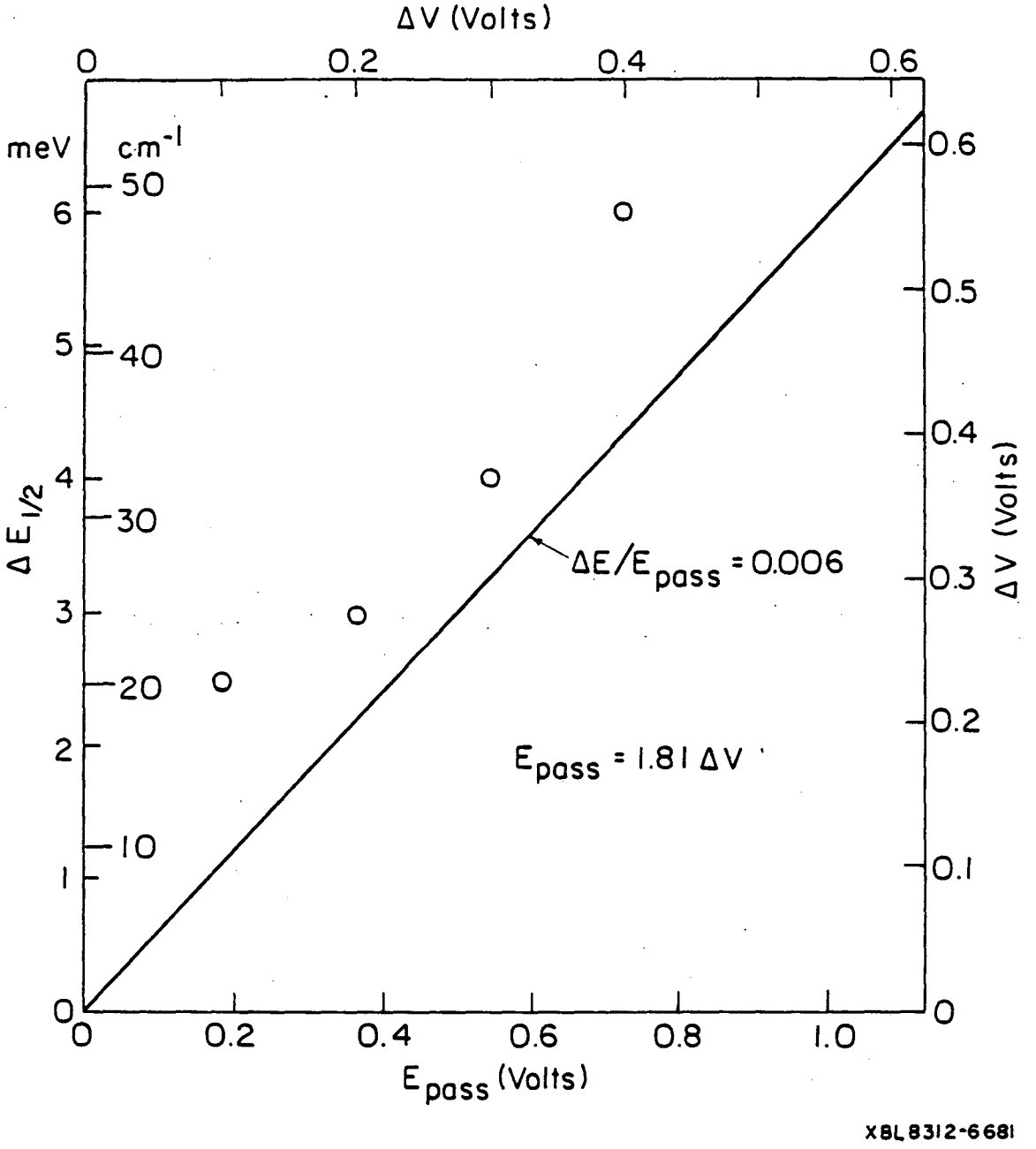

XBL8312-6681

Figure 2.3

ELECTRON ELASTIC SCATTERING INTENSITY AS A FUNCTION OF RESOLUTION

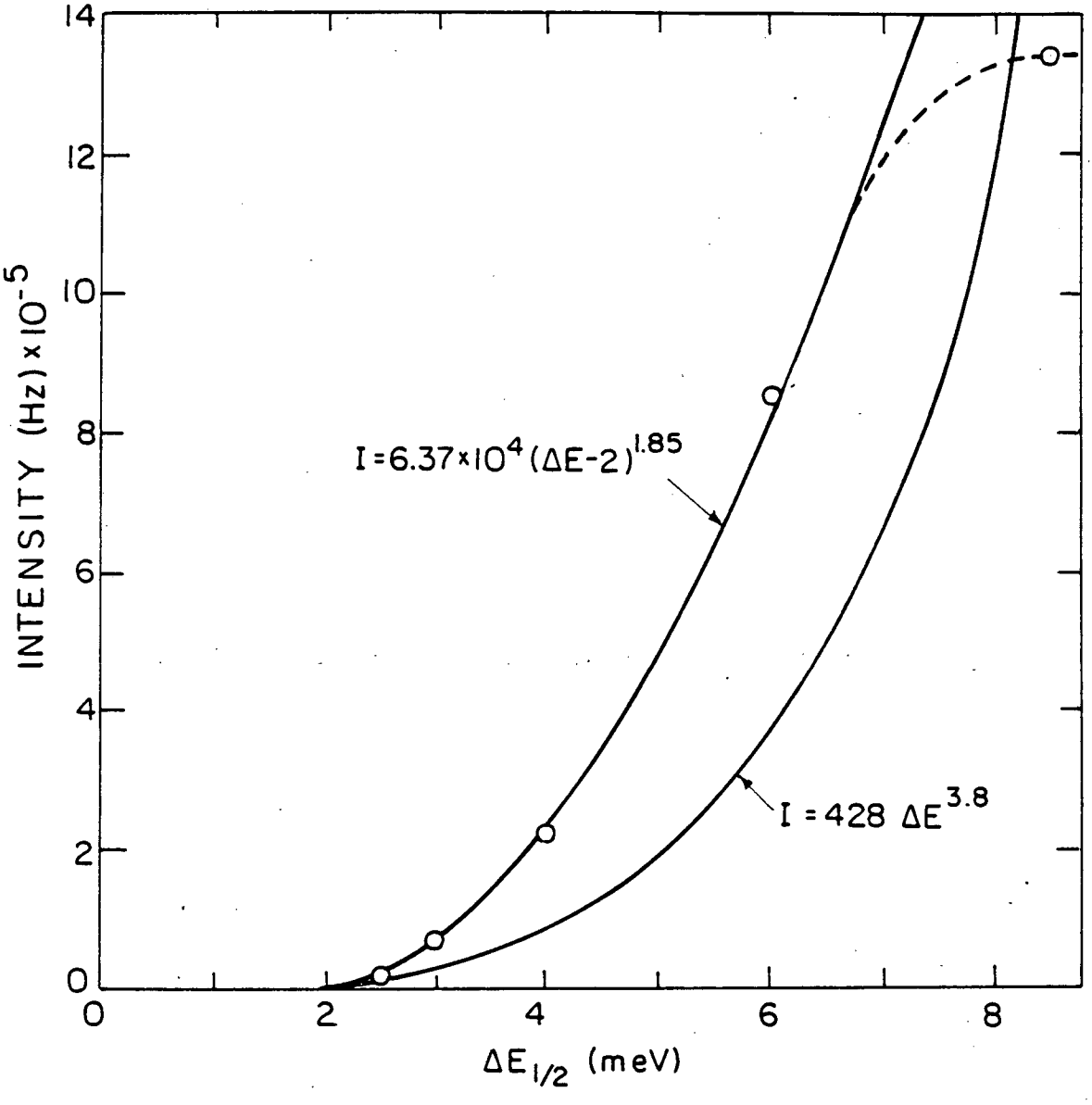

XBL 8312-6680

Figure 2.4

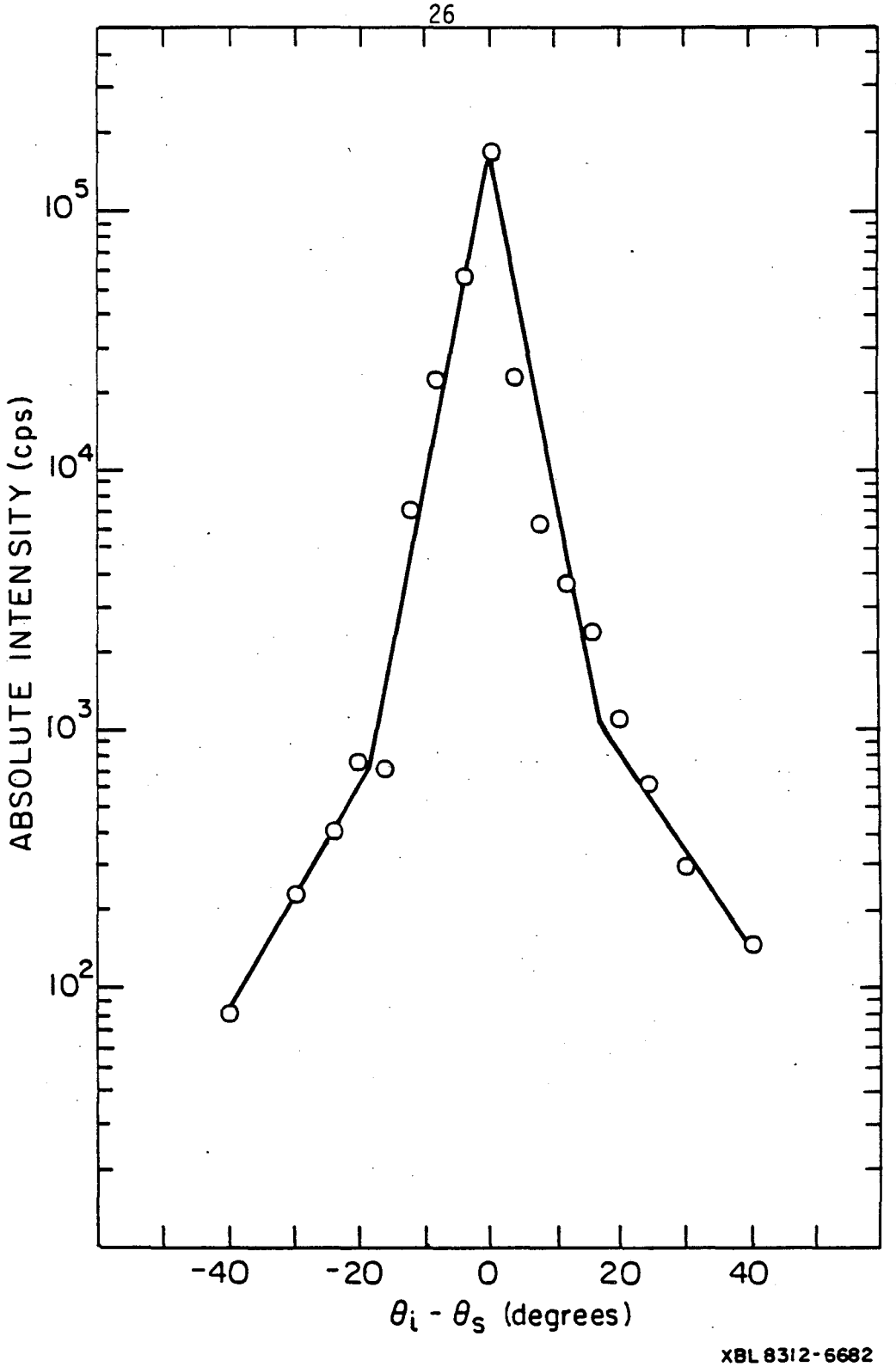
ABSOLUTE INTENSITY (cps)
10^5
10^4
10^3
10^2
-40
-20
0
20
40
$\theta_i - \theta_s$ (degrees)
XBL 8312-6682

Figure 2.5

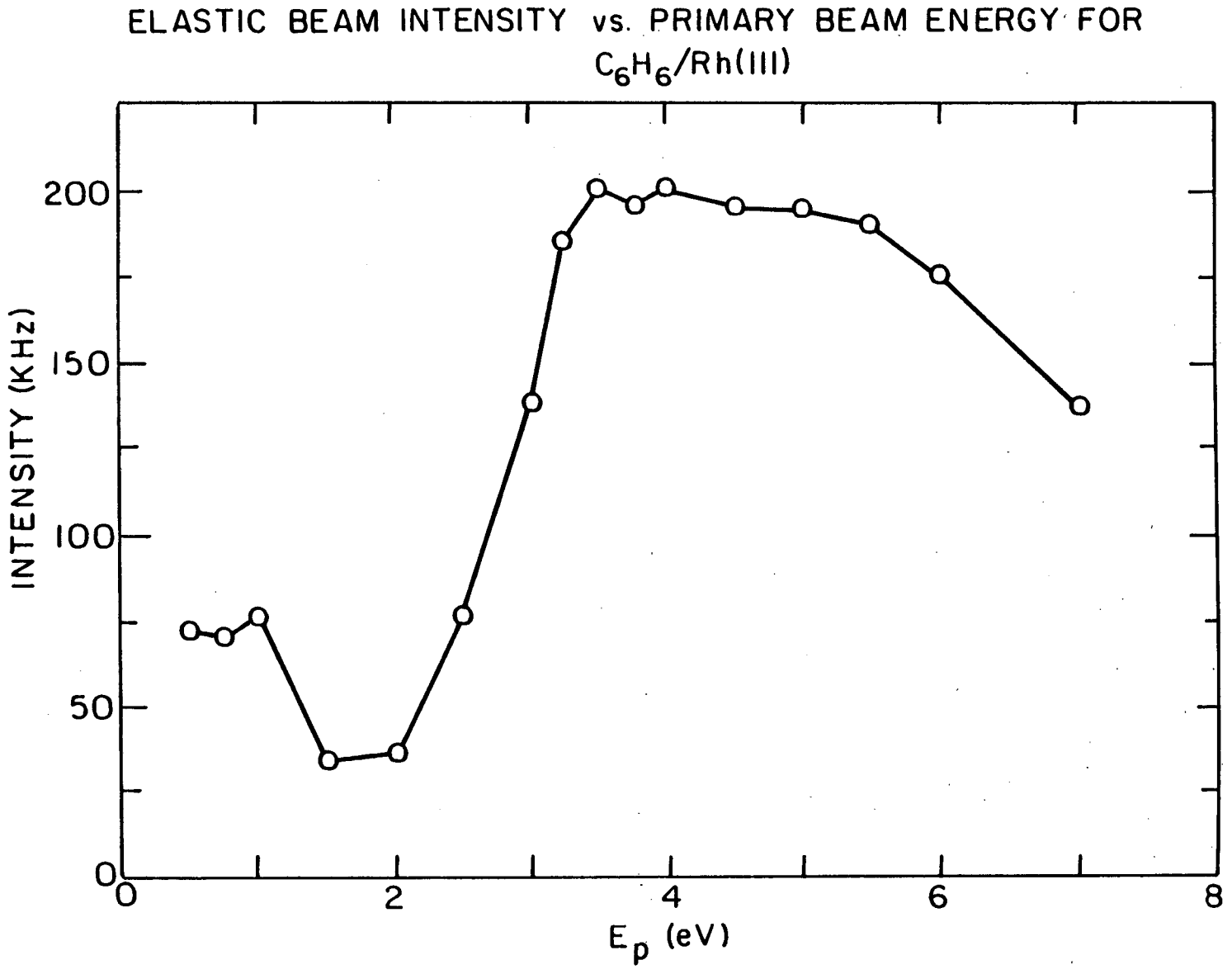

Figure 2.6

XBL8312-6683

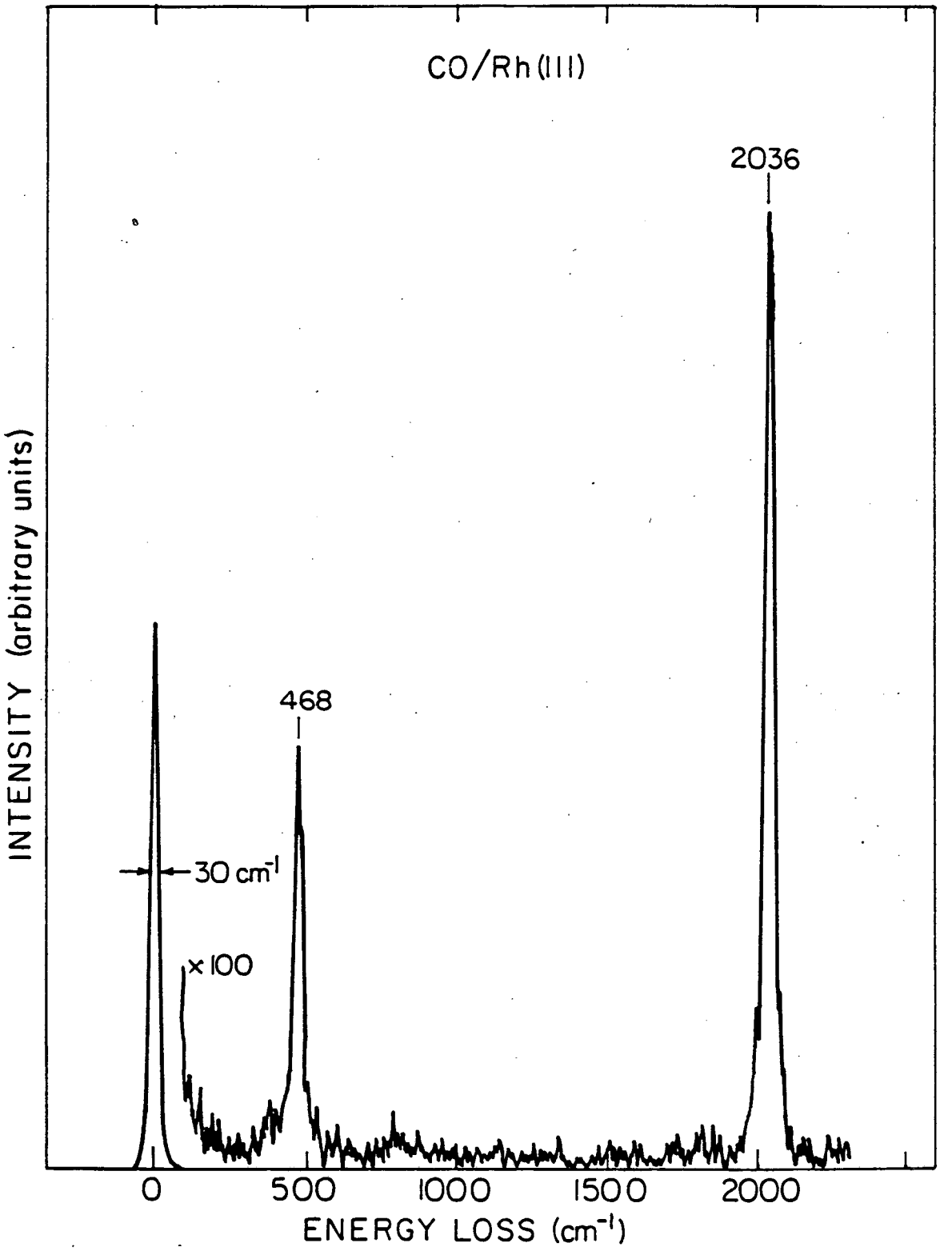
CO/Rh(111)
2036
468
30 cm⁻¹
×100
INTENSITY (arbitrary units)
0
500
1000
1500
2000
ENERGY LOSS (cm⁻¹)
XBL 8312-6684

Figure 2.7

2.3 Scattering Mechanisms

Vibrational modes are measurable in HREELS because some of the electrons inelastically scatter from the surface. These electrons interact strongly with the vibrating surface atoms. This interaction can somewhat artificially be divided into two types: long range and short range inelastic scattering. Long range scattering involves the interaction between the time dependent electric dipole moment of a vibrating atom or molecule and the electrostatic potential of the incoming electron. This is referred to as dipole scattering. Short range scattering involves interaction of the electron with the charge density of the adsorbate through polarization or electron capture in the immediate vicinity of the adsorbate, or through higher order or multipole interaction [20]. These are commonly separated into two categories: impact scattering and resonance scattering.

Dipole scattering produces scatterings at small deflection angles (small angle scattering) resulting in a narrow lobe of inelastically scattered electrons peaked about the specular direction. Dipole scattering leads to the so called dipole selection rule in which only vibrations which produce a net change of the dipole moment perpendicular to the surface are observable. In other words, only vibration which belong to totally symmetric representations (A_1, A' and A) are observable as fundamentals in dipole scattering [6]. This comes about because the dipolar cross section is nonvanishing only when the matrix element $\langle \phi_i | \mu_z | \phi_f \rangle$ is totally symmetric under all

symmetry operations of a point group, where ϕ_i amd ϕ_f are the initial and final vibrational states, respectively, and μ_z is the z component of the dipole moment operator.

Impact scattering and resonance scattering involve large angle scattering because of either multiple excitation or substantial momentum transfer to the surface atom or molecule. Impact scattering induces polarization of the charge density of the adsorbate-substrate system while resonance scattering involves temporary trapping of the electron within the molecule.

Selection rules for impact scattering are based on time-reversal symmetry. Specifically, the cross section for excitation should vanish for vibrations which belong to the same irreducible representation as a two component vector parallel to the surface [6]. As discussed in Chapter 6, impact scattering and dipole scattering can have comparable cross sections for weak transition dipoles and vibrational modes of higher frequency. Dipole scattering is commonly a hundred fold more intense than impact scattering for strong dipole active modes. However, at higher energies, the cross section from impact scattering increases. Most important is that several modes that are not visible in dipole scattering become observable, including those involving parallel dipole moment changes.

Resonance scattering is common in the gas phase and is consequently understood much better than impact scattering [20,21]. The incident electron can become trapped at a particular energy to form a negative ion state or shape resonance. They are characterized by strong energy

dependent variations in the inelastic cross section corresponding to excitation of negative ion states. Again, selection rules exist and permit molecular symmetry and orientation to be determined.

It is clear that simply by recording vibrational spectra as a function of scattering angle (i.e., angular profile), at least two of the three scattering processes can be examined to determine the adsorption symmetry (since different selection rules apply). The narrow, often more intense dipolar lobe can be easily separated from the broad impact or resonance scattering regions.

2.4 Mode Assignments

As discussed earlier, vibrational spectroscopy permits chemical, structural and symmetry analysis of the adsorbed species. Vibrational assignments are made by comparing the observed frequencies to gas and liquid phase frequencies, to tabulated group frequencies, and to frequencies of organometallic analogue compounds. Isotopic labelling is also helpful, as are angular profile studies which take advantage of the different scattering mechanisms possible. These will be discussed briefly below.

First of all, the chemical nature of an unknown adsorbate can be characterized by comparing the observed vibrations with characteristic frequencies of free molecules and molecular subgroups. These can be used not only to assign frequencies to particular subgroups, but also to individual bonds, such as single, double or triple C-C bonds. If the identity of the originally adsorbed species is known, the liquid

and gas phase frequencies can be compared. As substantial shifts in frequency are common as the bonding often changes upon adsorption, it is important to compare to organometallic compounds or matrix isolation species, as vibrational frequency shifts of similar magnitude are often observed. Of course, isotopic labelling quickly permits assignment of the modes which shift upon substitution.

The surface geometry and site symmetry of an adsorbed molecule can be determined through use of the principles of group theory in conjunction with the metal surface selection rules operable in HREELS. The symmetry assignment is made by comparing the number, frequency, and intensity of the dipole active modes observed with the correlation table of the point group for the gas phase molecule. A correlation table makes use of the relationships between the representations of the gas phase point group and its subgroups to allow us to predict which vibrational modes would be observed to be dipole active in HREELS upon reduction of the gas phase symmetry.

Frequency shifts are common for adsorption on surfaces as dramatic bonding changes occur. Chapter 4 demonstrates this for CO chemisorption in the presence of potassium. Changes in bond order occur when the character of the intramolecular bond changes as a result of the bonding to the surface. Frequency shifts due to isotopic substitution have already been mentioned. Frequency shifts due to mechanical coupling and dipole-dipole coupling are also common. Dipole coupling can be identified and eliminated using isotopic dilution experiments. This interaction is one of several lateral interactions

possible. These can be indirect interactions occurring through the substrate or direct chemical interaction. Lateral interactions can be distinguished experimentally from other shifts by following the variation in frequency as a function of coverage.

REFERENCES

1. G. T. Haller, Catal. Rev. Sci. Eng. 23, 477 (1981).
2. For a collection of recent articles on surface vibrational spectroscopy, please see Vibrations at Surfaces, C. R. Brundle and H. Morawitz, Eds., Elsevier, Amsterdam, 1983.
3. M. L. Hair, Infrared Spectroscopy in Surface Chemistry, Dekker, New York, 1967.
4. R. K. Chang and T. E. Furtak, Ed., Surface Enhanced Raman Scattering, Plenum, New York, 1981.
5. P. L. Richards, S. Chiang, and R. G. Tobin, Proceedings of the AVS 30th National Symposium, J. Vac. Sci. Technol., in press.
6. H. Ibach and D. L. Mills, Electron Energy Loss Spectroscopy and Surface Vibrations, Academic Press, New York, 1982.
7. T. Wolfram, Ed., Inelastic Electron Tunneling Spectroscopy, Springer Series in Solid State Sciences, Vol. 4, Springer-Verlag, Berlin, 1978.
8. R. F. Willis, Ed., Vibrational Spectroscopy of Adsorbates, Springer Series in Chemical Physics, Vol. 17, Springer-Verlag, Berlin, 1980.
9. M. J. D. Low and G. A. Parodi, Applied Spectrosc. 34, 76 (1980).
10. F. M. Hoffmann, Surface Science Reports, in press.
11. H. Ibach, J. Electron Spectrosc. Relat. Phenom. 30, 237 (1983).
12. J. E. Demuth, Ph. Avouris, and D. Schmeisser, J. Electron Spectrosc. Relat. Phenom. 29, 163 (1983).

13. L. H. Dubois, P. K. Hansma, and G. A. Somorjai, Appl. Surface Sci. 6, 173 (1983).

14. L. H. Dubois and G. P. Schwartz, Proceedings of the AVS 30th National Symposium, J. Vac. Sci. Technol., in press.

15. P. A Thirty, J. Electron Spectrosc. Relat, Phenom. 30, 261 (1983).

16. H. Froitzheim, H. Ibach, and S. Lehwald, Rev. Sci. Instrum. 46, 1325 (1975).

17. J. Andersson, Surface Sci. 79, 385 (1979).

18. G. E. Thomas and W. H. Weinberg, Rev. Sci. Instrum. 50, 497 (1979).

19. D. Roy and J. D. Carette, in Electron Spectroscopy for Surface Analysis, Topics in Current Physics Vol. 4, H. Ibach, Ed., Springer-Verlag, Berlin, 1977.

20. J. E. Demuth, Ph. Avouris, and D. Schmeisser, J. Electron Spectrosc. Relat. Phenom. 29, 163 (1983).

21. G. J. Schulz, Rev. Mod. Phys. 45, 423 (1973).

CHAPTER 3.

EXPERIMENTAL METHODS

3.1 Apparatuses

The research described in this thesis was performed in stainless steel ultrahigh vacuum (UHV) chambers designed to characterize the physical and chemical properties of clean and adsorbate covered surfaces using several surface sensitive probes. The ultra high vacuum chambers have typical pressures $\leq 1 \times 10^{-10}$ torr and allow the surface of small area samples to be prepared in a reproducible and well characterized manner.

The spectroscopies used to explore the outermost atomic layers of the crystal sample and the atoms and molecules adsorbed on them involve the production and detection of several entities: electrons, ions, atoms, and photons. These surface spectroscopies together allow the bonding, chemical composition, and geometric and electronic structure of adsorbates on surfaces to be explored.

Two very similar ultrahigh vacuum chambers were used to carry out nearly all of the research described in this thesis. Both chambers contain two main levels of analysis: an upper level equipped with a four grid electron optics-energy analyzer (Varian) for low energy electron diffraction (LEED) and Auger electron spectroscopy (AES), a glancing incidence electron gun (Varian or Cliftronics) for Auger excitation, a quadrupole mass spectrometer (UTI 100C) for temperature programmed desorption (TPD) studies and residual gas analysis, an ion sputter gun (PHI) for sample cleaning, a nude ion gauge (Varian) for

pressure measurement, two variable leak valves (Varian) for low pressure gas exposure, and an alkali getter source (SAES) for controlled alkali dosing; the lower level contained a high resolution electron energy loss spectrometer for vibrational analysis. Schematics of these two apparatuses are shown in Figures 3.1 and 3.2.

Each apparatus is equipped with a long travel (25 cm) precision manipulator for accurate reproducible positioning of the crystal sample. In both chambers the HREEL spectrometer is enclosed in μmetal shielding to reduce magnetic fields inside the spectrometer. Both apparatuses are pumped by ion pumps which are enclosed in iron sheet metal and positioned sufficiently far from the spectrometer to eliminate their magnetic field inside the μmetal shielding.

The chamber schematically shown in Fig. 3.1 was employed to obtain all of the experimental data on Pt(111) excluding the CO and potassium TPD spectra. Furthermore, both the CO isotopic scrambling experiments and the second harmonic generation (SHG) experiments obtained on Rh(111) were performed in this chamber. As shown in the schematic, two (Varian) ion pumps (400 and 110 l/sec) and a water-cooled titanium sublimation pump were used to achieve routine base pressures in the 10^{-11} torr range after a 48 hour bake-out at ~500K. The HREEL spectrometer, as configured in this chamber, is shown in Fig. 3.3. A more detailed schematic of the lens elements and analyzer assembly is given in Appendix A (Fig. A.1). This spectrometer is quite similar in design and dimensions to that given by Froitzheim et al. [2] and is described in detail elsewhere [3]. A comparison with the HREEL

spectrometer found in the other apparatus (i.e., Fig. 3.2) appears in Section 2.2 of this thesis. Although rotatable, the spectrometer was used in the fixed position with a total scattering angle of 144° and an angle of incidence of 72° from the surface normal. The crystal sample is mounted on axis on a high precision manipulator (Varian) extensively modified for extended z travel (25 cm) between the two levels.

The second HREELS apparatus, shown schematically in Fig. 3.2, was used for all of the experiments performed on Rh(111) except the CO isotopic scrambling experiments and the SHG experiments (Chapter 5). The actual apparatus is pictured in Fig. 3.4. This chamber is pumped by a 400 l/sec ion pump (Varian), a high speed oil diffusion pump (Varian VHS-6) with liquid nitrogen cooled cryotrap and extended cold cap (Varian), and a water cooled titanium sublimation pump (Varian Ti-ball). Unlike the other HREELS apparatus, all pumps are separated from the chamber by viton O-ring seal gate valves. Routine operating pressures of 1×10^{-10} torr were obtained by baking the chamber at 450K for 48 hours [4]. The HREEL spectrometer in this apparatus is described in section 2.2. As shown schematically in Fig. 2.1, this HREEL spectrometer is fixed at a total scattering angle of 120°. The sample is mounted on-axis on an extremely stable manipulator, as shown in Fig. 3.5. The manipulator is designed for accurate and reproducible positioning of the sample between the two levels (~15 cm). Travel dials are used to record the X-Y position to eliminate error due to back lash. The manipulator is made of aluminum (the surface is

anodized) and requires water cooling during bakeout to prevent seizing. The chamber also contains an environmental cell that can enclose the sample and permit high pressure (up to several atmospheres) exposure of the crystal sample. Because of the bulky manipulator design required to disperse the force needed to seal the environmental cell, the LEED/AES analyzer is mounted on retractable bellows (see Fig. 3.2). This is described in more detail elsewhere [5]. The combination of the environmental cell with the UHV surface analysis chamber permits high pressure reaction monitoring and surface characterization to be carried out in the same apparatus. However, only the UHV surface characterization capabilities of the apparatus were employed in the studies described here.

The TPD studies involving the coadsorption of CO and K on Pt(111) were performed in a commercial (PHI) apparatus containing a cylindrical mirror analyzer (CMA) for AES, a four grid LEED optics with integral electron gun, a quadrupole mass spectrometer (UTI 100C) for TPD and residual gas analysis, an ion sputter gun for sample cleaning, a leak valve (Varian) and an alkali dosing source (SAES). The 400 l/sec ion pump provided base pressures of 1×10^{-10} torr. The sample was mounted on an off axis (PHI) manipulator permitting resistive heating and liquid nitrogen cooling of the sample.

On all three apparatuses, gases are introduced into the chamber through variable leak valves connected to stainless steel gas manifolds. The manifolds are bakeable and pumped by a mechanical pump

and liquid nitrogen cooled sorption pumps, achieving typical pressures below 5×10^{-5} torr. Several gases are accessed to the manifold through gas regulators and metal sealed valves. The chamber could be rough pumped through the manifold via a right angle valve.

FIGURE CAPTIONS

Fig. 3.1 Schematic diagram of the UHV apparatus used for all Pt(111) HREELS experiments. The upper level permits AES, LEED and TPD analysis, the lower level allows surface vibrational spectroscopy to be performed. The pumping is positioned away from the main chamber to reduce magnetic fields near the HREEL spectrometer.

Fig. 3.2 (a) A schematic of the apparatus used for all vibrational studies on Rh(111). The circulation loop for reaction studies is also shown. The sample can be enclosed in a pressurizable cell while maintaining UHV in the excluded volume of the chamber. The cell is shown open with the sample in the vibrational analysis position. The ion and titanium sublimation pumping have been omitted for clarity. (b) Details are shown of how the pressure cell, when closed, can enclose the sample; the LEED/AES optics are in the retracted position.

Fig. 3.3 Schematic of the HREEL spectrometer as positioned inside the chamber in Fig. 3.1. The spectrometer and the entire inner chamber are lined with magnetic (μmetal) shielding as shown. The sample can be partially viewed to aid in sample positioning.

Fig. 3.4 Photograph of the UHV apparatus shown in Fig. 3.2. The main chamber, center, is mounted on a chassis which helps support the pumping devices; the diffusion pump is visible in the

lower right center; while the gas-inlet manifold and hydraulic pumping mechanism can be seen at the lower left.

Fig. 3.5 A close-up photograph of the extremely stable manipulator used on the chamber in Fig. 3.3 and 3.4. The long travel manipulator has travel dials for indicating the X-Y sample position.

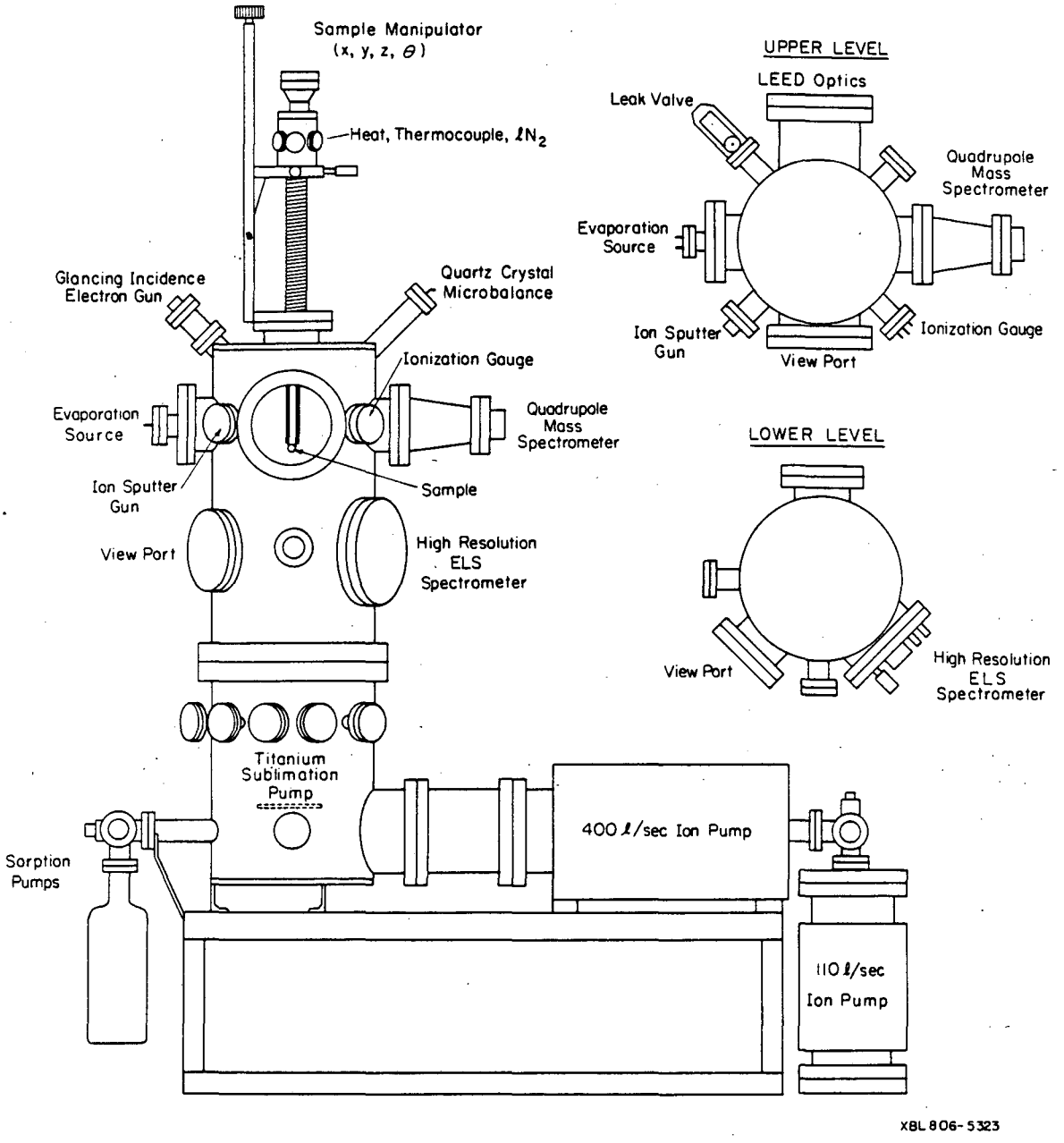
Sample Manipulator
(x, y, z, θ)
Heat, Thermocouple, ℓN2
Glancing Incidence
Electron Gun
Quartz Crystal
Microbalance
Ionization Gauge
Evaporation
Source
Quadrupole
Mass
Spectrometer
Ion Sputter
Gun
Sample
View Port
High Resolution
ELS
Spectrometer
Titanium
Sublimation
Pump
Sorption
Pumps
400 ℓ/sec Ion Pump
110 ℓ/sec
Ion Pump
UPPER LEVEL
LEED Optics
Leak Valve
Quadrupole
Mass
Spectrometer
Evaporation
Source
Ion Sputter
Gun
Ionization Gauge
View Port
LOWER LEVEL
View Port
High Resolution
ELS
Spectrometer
XBL806-5323

Figure 3.1

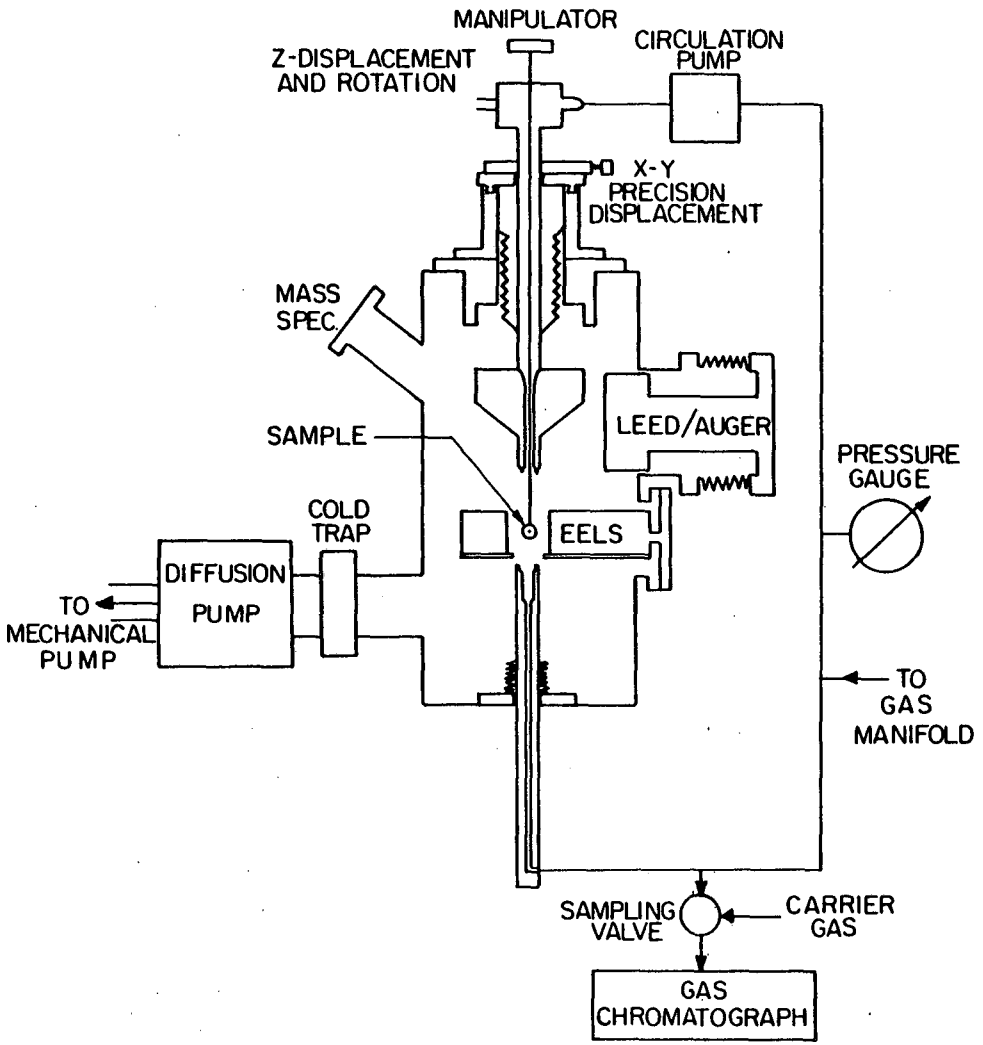

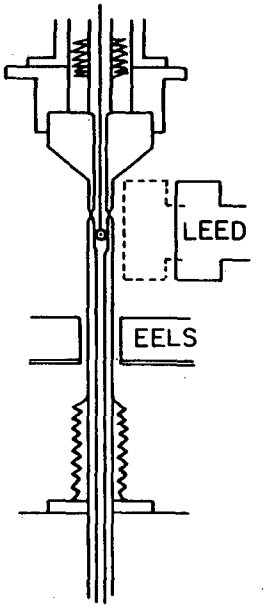

XBL 8111-6950

Figure 3.2

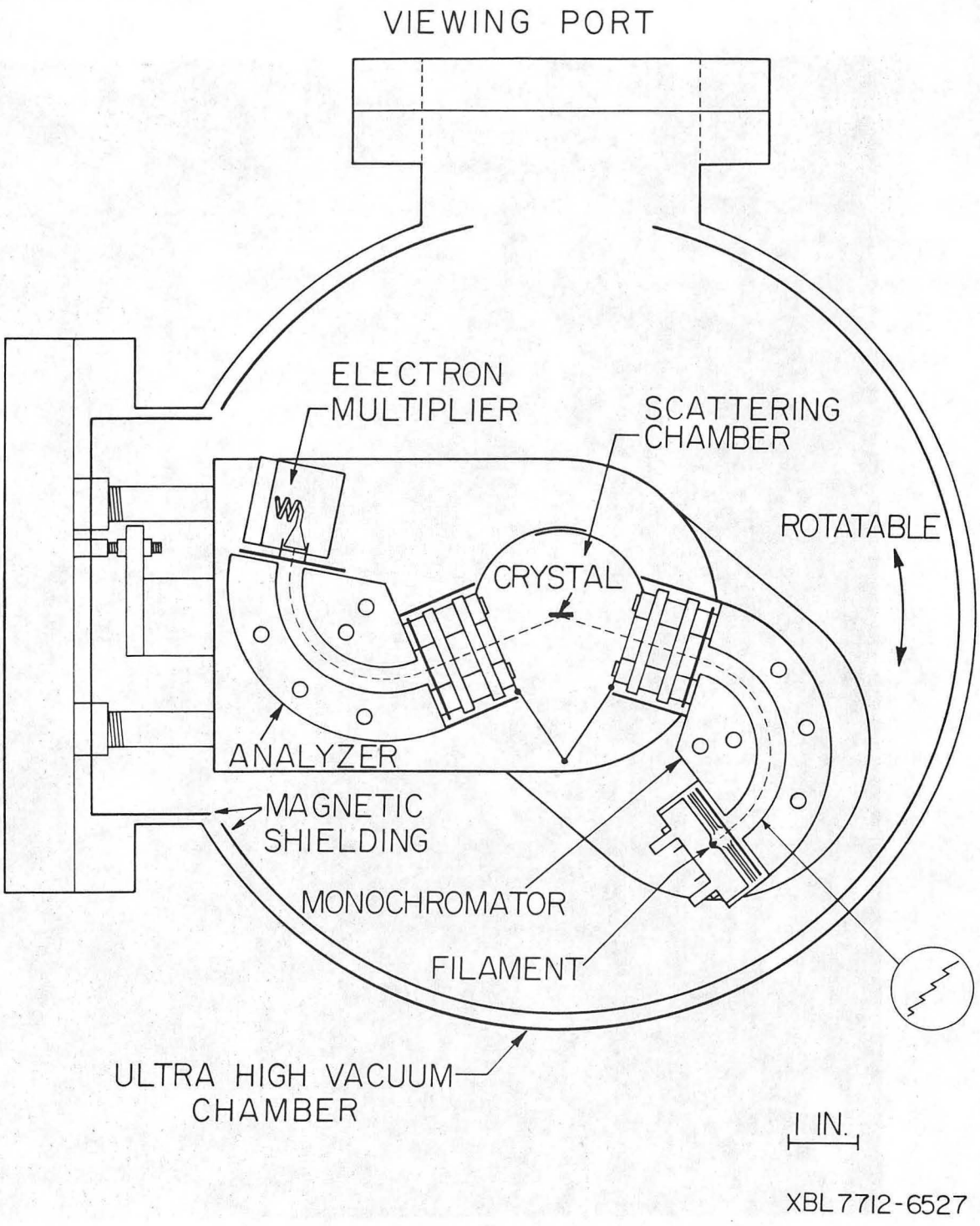
VIEWING PORT
ELECTRON MULTIPLIER
SCATTERING CHAMBER
ROTATABLE
CRYSTAL
ANALYZER
MAGNETIC SHIELDING
MONOCHROMATOR
FILAMENT
ULTRA HIGH VACUUM CHAMBER
1 IN.
XBL7712-6527

Figure 3.3

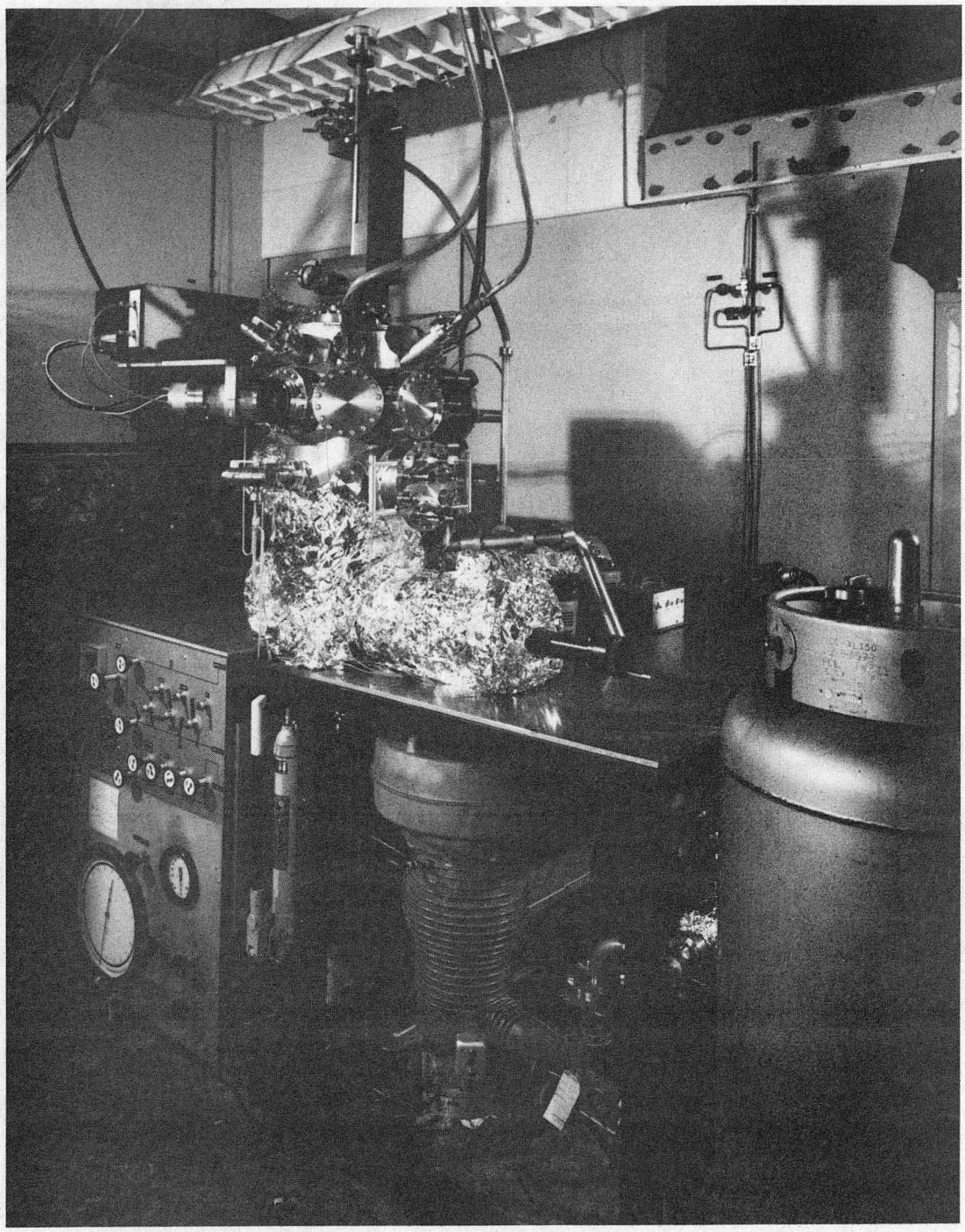

CBB 821-565

Figure 3.4

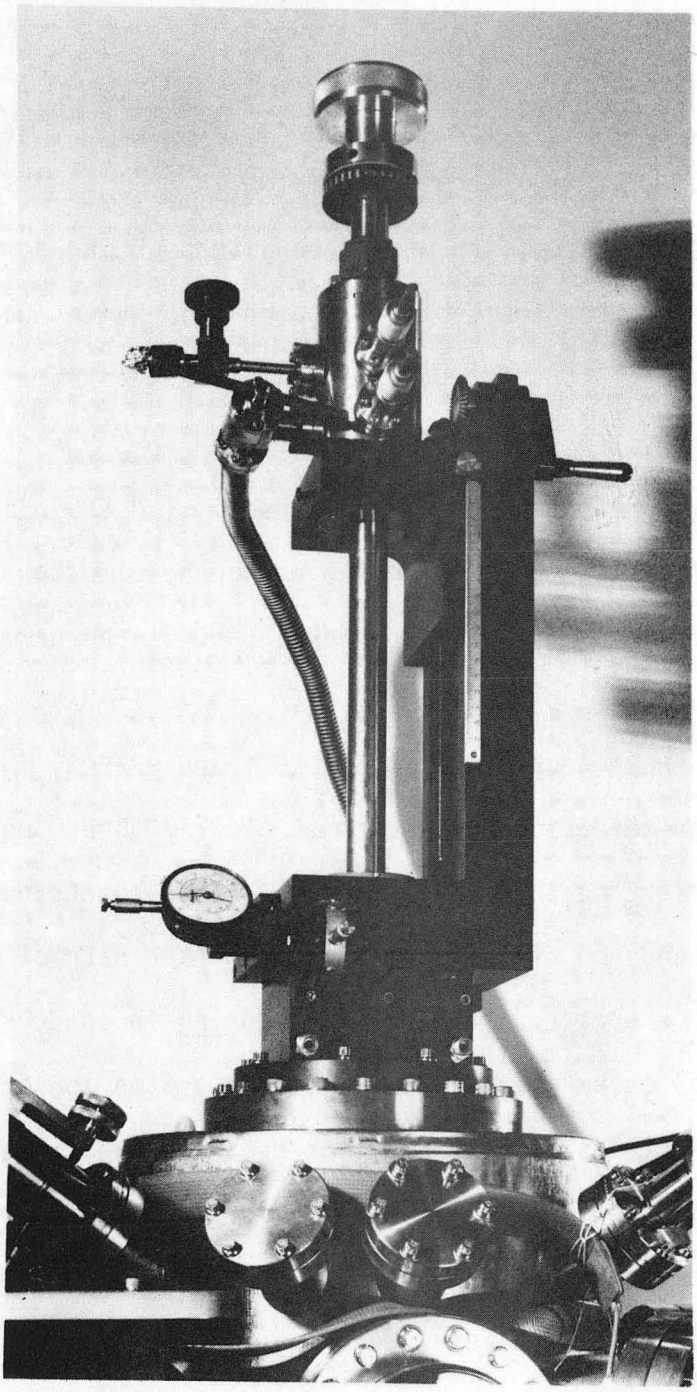

CBB 821-561

Figure 3.5

3.2 Surface Analysis Methods

The emphasis of the studies presented in this thesis is surface vibrational spectroscopy. However, only through the combined use of several different spectroscopies can a comprehensive understanding of the structural, electronic and chemical properties of a surface be obtained. The surface analysis methods used in these studies are high resolution electron energy loss spectroscopy (HREELS), low energy electron diffraction (LEED), Auger electron spectroscopy (AES), temperature programmed desorption (TPD), and second harmonic generatin (SHG).

Three of these techniques (AES, LEED, and HREELS) involve the generation and detection of electrons. In all three, use is made of the inherent surface sensitivity of low energy electrons. Figure 3.6 shows the dependence of the inelastic mean free path of electrons on their kinetic energy for inelastic scattering in condensed phases. This universal curve illustrates the large scattering cross section of low energy electrons: the penetration depth of electrons of low energy (10-500 eV) incident on solid surfaces is at most two or three atomic layers. Hence, for HREELS and LEED, the backscattered electrons carry information on the vibrational motion and atomic position of the atoms or molecules in the near surface region. Similarly, the escape depth of Auger electrons emerging from the surface in this energy range only occurs from the top most atomic layers.

Besides their surface sensitivity, electrons are also easily generated, collimated, and energy analyzed, as well as efficiently detected. The number of electrons emitted from a solid sample irradiated by a monoenergetic electron beam of energy Ep as a function of energy is shown schematically in Fig. 3.7. The very broad peak in the lowest energy range is due to secondary electrons created from a cascade process involving inelastic collisions between primary electrons and electrons bound in the solid. These can be used to measure work function changes. In the median energy range, secondary electrons generated in Auger processes are emitted, as shown in the derivative mode in insert (a). Closer to the specularly reflected beam, the 50 eV region below Ep is characterized by energy losses due to electronic excitations and ionization losses. The narrow peak with energy Ep is due to elastically diffracted electrons and contains structural information of the surface as in LEED (see insert (c)). Using higher energy analyzers, energy losses due to adsorbate or phonon vibrational excitations can be resolved, as shown in insert (b). Hence, electrons emitted from a surface are used to characterize the surface layer. The AES, LEED and HREEL spectra shown in the inserts (Fig. 3.7) are for ethylene adsorbed on Rh(111) in the c(4 x 2) structure, which loses a hydrogen atom to form ethylidyne (CCH_3) at 300K. These techniques, along with TPD and SHG, are used extensively in this thesis to characterize clear and adsorbate covered surfaces. Each is discussed briefly below.

Fig. 3.6 The inelastic mean free path for electrons as a function of their kinetic energy. The points represent individual measurements, the curve is often referred to as the "universal curve".

Fig. 3.7 A typical distribution [N(E)] of electrons observed after a sample is irradiated with a monoenergetic beam of electrons, shown as a function of energy. The solid (-) line shows the scattered (primary) electrons, the dashed (—) line shows the secondary electrons produced. The inserts show how these electrons are used for surface analysis. The inserts a, b and c show the AES, HREEL, LEED data observed for ethylene adsorption on Rh(111) at 300K.

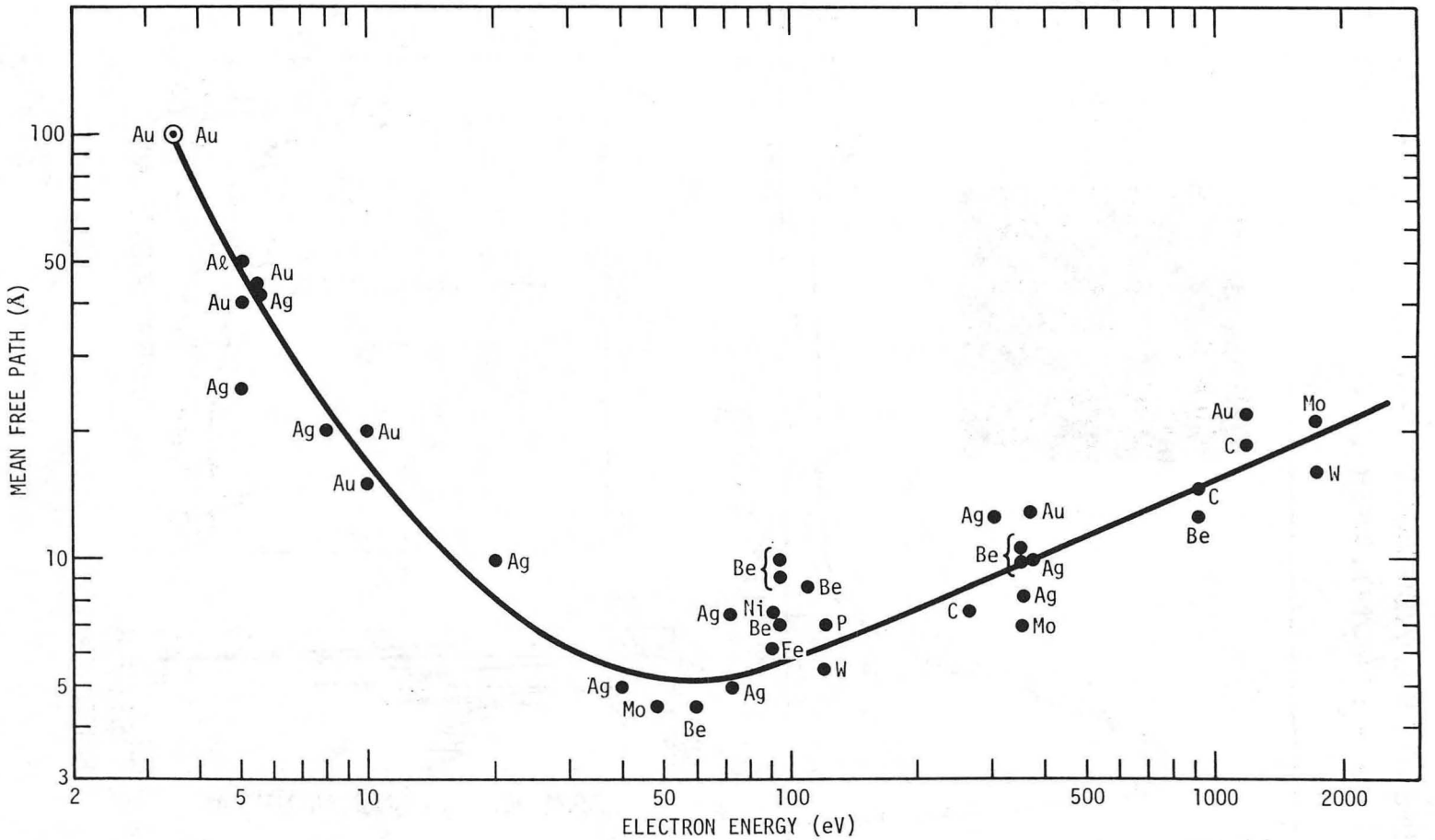

XBL 733-5917

Figure 3.6

ENERGY DISTRIBUTION OF SCATTERED ELECTRONS FROM A c(4x2) MONOLAYER OF C_2H_3 ON Rh(III) AT 300K

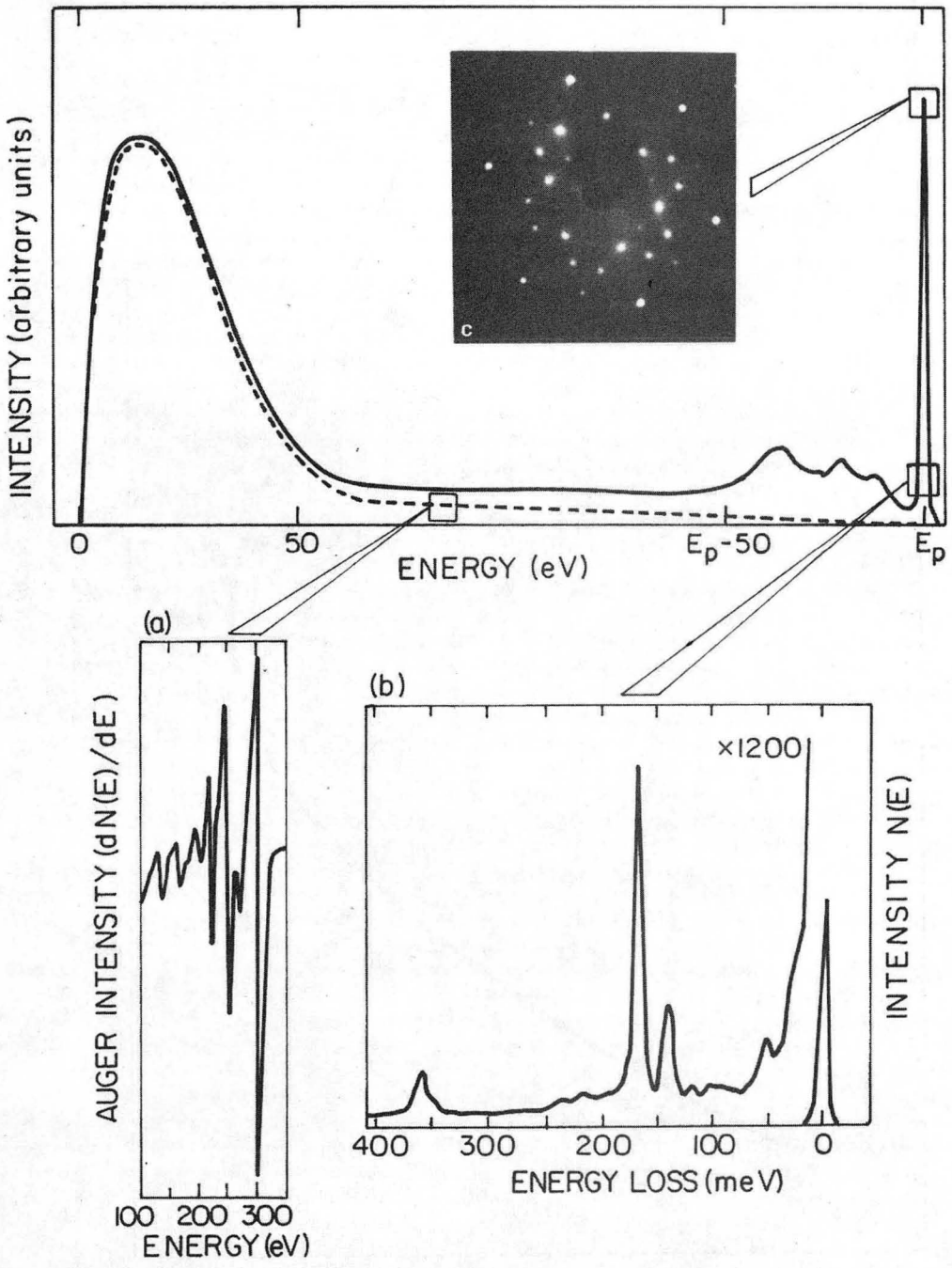

XBB 830-11012

Figure 3.7

3.2.1 HREELS

This technique is discussed in detail in Chapter 2. Briefly, electrons of monochromatic energy between typically 1-10 eV are scattered from a solid surface and energy analyzed to detect energy losses due to vibrational excitations of adsorbed atoms and molecules and of surface phonons. The electrostatic deflection HREEL spectrometer is run at sufficiently low pass energy (<1 eV) to allow energy resolution (FWHM) of 20-90 cm^{-1} (2.5-11 meV) at sufficiently high beam currents to produce good signal-to-noise levels. In this thesis, two HREEL spectrometers were used which differed markedly in their performance. The operating conditions and performance are described for each adsorption system in the chapters to follow. Briefly, all of the Rh(111) experiments were performed at an energy resolution between 20-60 cm^{-1} (2.5-7.5 meV) with 10^{-9}-10^{-11} Amps beam current at the crystal and 10^{5}-10^{7} elastically scattered electrons detected per second. The Pt(111) research was performed at similar beam currents but a resolution of 70-90 cm^{-1} and 10^{4}-10^{5} counts per second in the elastic peak intensity. Energy losses were typically measured between 200 and 4000 cm^{-1} (25-500 meV), although vibrations as low as 75 cm^{-1} were observed (see Chapter 4).

The angular dependence of the inelastically scattered electrons was also measured for several adsorption systems to determine surface orientation and site symmetry, as discussed in Chapter 2. In these experiments, the spectrometer was maintained at a fixed total scattering angle and the sample rotated in the scattering plane. This

permits measurement of the dipolar character of the observed vibrational mode, although the angle of incidence is also being varied. From a comparison of the number, frequency, and intensity of the observed modes with infrared and Raman spectra of known organic, inorganic and organometallic species and use of isotopic frequency shifts and the principles of group theory, the adsorption complex, its orientation and its symmetry can be identified.

All spectra in this thesis were made on an X-Y chart recorder by plotting the ratemeter output versus the electron energy loss (meV). Scan rate depended on the inelastic loss peak intensities, which in turn depended on the particular overlayer being studied, the detection angle (i.e., specular versus off-specular), the incident beam energy, and the spectrometer being used. All spectra are normalized to the elastic peak height shown, unless otherwise noted.

3.2.2 TPD

In temperature programmed desorption spectroscopy, a sample with an adsorbed layer is heated in a controlled manner and the desorbing species detected and analyzed. From a study of the desorption product(s) observed the nature of the adsorption state is inferred. Furthermore, one can also learn about the energetics of bonding, the chemical processes occurring at the surface, and the nature of adsorbate-adsorbate interactions. Specifically, TPD can be used to obtain thermodynamic, kinetic and dynamic quantities such as the activation energy and the pre-exponential factor of the desorption

rate, the kinetic order of the desorption process, the number and relative concentration of different binding states, the products of and mechanism for decomposition reactions, the identity and stability of adsorbed species, and the strength of lateral interactions.

In the experiments described here, TPD was used to help identify the surface species present, measure their population (either relative or absolute), and control their concentration. Kinetic information is obtained from an Arrhenius form of the desorption rate (R_d),

$$R_d = \frac{d\sigma}{dt} = \nu_n \, \sigma^n \exp(-E_d/RT)$$

where σ is the surface coverage, n is the desorption order, ν_n is the pre-exponential factor, E_d is the activation energy for desorption, and T is the desorption temperature. If one assumes that ν_n and E_d are independent of adsorbate concentration σ and time t, then E_d and ν_n can be determined as shown by Redhead [6] for first- and second-order desorption using

$$E_d/RT_p^2 = (\nu_1/\beta) \exp(-E_d/RT_p) \qquad \text{(1st order)}$$

and

$$E_d/RT_p^2 = (\nu_2\sigma_o/\beta) \exp(-E_d/RT_p) \qquad \text{(2nd order)}$$

where T_p is the temperature at which the rate of desorption is a maximum, β is the heating rate, and σ_o is the initial adsorbate coverage. As seen in these equations, t_p is independent of the surface coverage for a first-order desorption process but decreases with increasing σ_o for second-order desorption. Hence, the order of

the desorption process can be determined by plotting ln R_d versus ln σ_o. To determine E_d and ν_n one must vary β and σ_o independently. As this is often difficult experimentally, values are assumed for ν_n (specifically $\nu_1 = 10^{13}sec^{-1}$ and $\nu_2 = 10^{-2}cm^2sec^{-1}$) so that E_d can be determined. Other methods exist for determining ν_n and E_d from measurement of T_p and the peak width [7], but were not used here. E_d was determined by assuming a value for ν_n or using values previously determined from molecular beam scattering experiments or T_p and peak width measurements. Although these assumptions are not readily justified, they do permit relative changes and trends to be determined. As determined, E_d is the activation energy of desorption and equals the heat of adsorption ΔH_{ads} plus the adsorption activation energy E_a. If adsorption of the species is not activated, then E_d equals the heat of adsorption.

In all of the TPD results presented in this thesis, the crystal sample has been dosed to a measured exposure of gas at a controlled temperature. Subsequently, the sample is heated linearly (between 10 and 60 K/sec) and the desorbing species monitored line of site by a mass spectrometer. The change in pressure at a particular mass is recorded versus either time or sample temperature using an X-Y chart recorder or a microcomputer. Details of the microcomputer and software are discussed elsewhere [8]. The desorption rate was always much less than the pumping speed for the desorbing species such that the

desorption rate was proportional to pressure. The samples were mounted in such a way as to minimize support and edge effects and to permit resistive heating rates that were uniform and linear. The rates used are given for each experiment.

3.3.3 LEED

Low energy electron diffraction enables the structure of clean and adsorbate covered surfaces to be determined. This is because the de Broglie wavelength of electrons with energy 10-500 eV is comparable to the interatomic distances of most solids, varying between 3.9 and 0.64 Å. Hence, when an electron beam impinges on a crystal surface, a portion of these electrons are elastically scattered by the atomic cores producing wave interferences that depend on the atomic positions, thus providing structural information of the periodicity of the surface.

A schematic of the LEED experiment is shown in Fig. 3.8a. A variable, monoenergetic electron beam of energy 10-500 eV is incident on a crystal sample. The elastically backscattered electrons are filtered from the inelastically scattered electrons by a retarding field analyzer (see Fig. 3.8b), and post accelerated onto a phosphorescent screen for viewing (or photographing) the diffraction pattern. The overall intensities and sharpness of the diffraction spots depends strongly on the degree of microscopic order present on the surface. Furthermore, since the transfer width of most electron beam sources is rather small (ca. 50-100 Å) the diffracted beams have significant

intensity only if the region of well-ordered atoms are of the order of this transfer width or larger.

From the symmetry and position of the diffraction spots, the size and orientation of the 2D-surface unit cells can be determined. Hence, by following the diffraction pattern as a function of exposure or temperature, several features of the overlayer can be determined, including the presence of adsorbate-induced periodicity (superlattice) or reconstruction, attractive and/or repulsive interactions between adsorbates, order-disorder transitions, and the overlayer coverage (at least semi-quantitatively) [9]. From the variation in intensity of the diffracted beam as a function of electron beam energy, the precise position of the adsorbed atoms and molecules and the first two or three surface layers can be determined relative to one another (i.e., bond lengths and bond angles). However, due to the high scattering cross section of the electrons, multiple scattering is highly probable, significantly complicating the scattering theory necessary to determine the precise atomic positions (i.e., the 3-D structure).

In this thesis, only the symmetry and position of the diffracted beams were recorded. However, site symmetry and surface geometry of adsorbates as determined by HREELS for a particular surface structure (i.e., diffraction pattern) were used to suggest plausible surface configurations and aid surface structure calculations. Such combinations of surface spectroscopies are necessary to reduce the calculational effort needed for precise structural determinations to a manageable level. Benzene on Rh(111) (Chapter 6) provides a good example of the utility of LEED analysis.

3.2.4 AES

The elemental composition of the surface layer can be determined using Auger electron spectroscopy. AES is a two electron emission process that occurs after excitation, both the excitation and emission processes are shown schematically in Fig. 3.9(a) and (b). Impingement of the surface atoms by electrons, X-rays or ions of sufficient energy (1000-5000 eV) can create singly ionized, excited states caused by ejection of electrons from inner atomic levels of the atom. These electrons have binding energies less than the incident beam energy. A schematic of this excitation process is given in Fig. 3.9a. In $\sim 10^{-15}$ seconds, this singly ionized excited atom can de-excite by Auger electron emission, X-ray fluorescence, or a sequence of both. In the Auger process, de-excitation occurs when an outer shell electron fills the inner level vacancy and transfers the energy difference to a second outer shell electron that can be ejected (if the transferred energy exceeds the electrons binding energy). The result is a doubly ionized atom as shown in Fig. 3.9b. The energy of the ejected Auger electron is given by

$$E_{WXY}(Z) = E_W(Z) - E_X(Z) - E_Y(Z+\Delta) - e\phi_A.$$

The value $E_W - E_X$ is the energy difference between the two levels, but the electron must expend the energy $E_Y(Z+\Delta) + e\phi$ to escape the atom, where ϕ is the work function of the surface and $E_Y(Z+\Delta)$ is the binding energy of the ejected electron from the positively charged atom. The actual measured energy $E_{WXY}(Z)$ contains the additional

term $-(e\phi_A - e\phi)$ which is the difference between the work function of the energy analyzer (ϕ_A) and the sample (ϕ) (i.e., the work function of the sample is referenced to the vacuum level of the spectrometer) [10]. De-excitation via the Auger process is more probable for the lighter elements.

In all of the work reported here, the sample was irradiated with electrons (typically 2000 eV) at a glancing incidence of ~70° to the surface normal to minimize the penetration depth (5-20 Å). The Auger electrons were detected typically with a retarding field analyzer shown schematically in Fig. 3.8b. The analysis is achieved by applying a retarding DC ramp voltage to grids 2 and 3 (G2 and G3 in Fig. 3.9C), which are tied together. When the first and fourth grids are grounded, these LEED optics act as a high pass filter, the fluorescent screen acts as the electron collector when a 300V positive bias is applied. The spectra are recorded in the first derivative mode (dN(E)/dE) using electronic differentiation by applying a time varying voltage to the retarding grids (i.e. by superimposing an AC modulation voltage on the DC ramp voltage). The second harmonic of the modulation is detected then as a function of the DC ramp voltage using a phase-sensitive lock-in amplifier. If dependence on resolution is neglected, the second harmonic AC signal gives the first derivative Auger spectrum [10].

Since every element has a unique Auger spectrum, each transition observed can be associated with the presence of specific elements on/in the sample surface. As used here, AES permits quantification of

surface composition. Both the line shape and the core-level energy shifts of Auger transitions can be utilized to give additional chemical and electronic information [11], but were not utilized here.

3.2.5 SHG

Second harmonic generation is one of several nonlinear optical techniques that has undergone rapid development in recent years. Considerable effort has been made to apply these techniques to the study of surfaces and interfaces [12]. The appropriateness of SHG for studying surfaces arises from its intrinsic surface sensitivity: second-order nonlinear processes are (dipole) forbidden in media which possess a center of inversion [13]. Since the atomic and/or molecular surface layer has no inversion symmetry, the surface contribution can dominate over the bulk contribution, with the second harmonic signal coming mostly from the top one or two atomic layers [14].

The work reported here involves the first application of SHG to adsorption systems that are well characterized by surface sensitive techniques, namely using the four previously described spectroscopies [15]. Only those experiments involving the coadsorption with alkali (in this case sodium) are discussed here, more detailed discussion of the theory and experimental set-up can be found elsewhere [viz. 13,16]. Briefly, a Q-switched Nd:YAG laser was used to produce pulses with a ~10 nsec pulsewidth and ~6 mJ pulse energy at wavelengths of 0.532 or 1.06 μm. The laser pulses (with a repetition rate of 10 Hz) were p-polarized and incident on the crystal sample at 62.5° from the

surface normal with a beam diameter of 1 mm. The p-polarized second harmonic signal (at 0.27 or 0.53 μm, respectively) was collected with the appropriate optics and detected with a high-gain photomultiplier. The signal was recorded on an integrator with a gated electrometer.

Fig. 3.8 (a) Scheme of the low energy electron diffraction experiment from an idealized crystal lattice.

(b) Schematic of the LEED/AES analyzer. The potential on the analyzing grids (G2, G3) is controlled by the ramp generator and the programmable supplies. The audio-frequency generator provides the AC modulation while the diode arrangement allows for tuning the lock-in amplifier to 2ω for electronic differentiation. The shielding grids (G1, G4) can be biased to eliminate secondary electrons. The Auger electrons are collected by the fluorescent screen and detected with the lock-in amplifier.

Fig. 3.9 (a) Exciation of an atom to produce a singly ionized atom with a core hole.

(b) De-excitation of the ionized atom via emission of an Auger electron. After the two electron process, a doubly ionized atom is left.

(c) An example of a typical Auger electron spectrum, obtained for clean Pt(111).

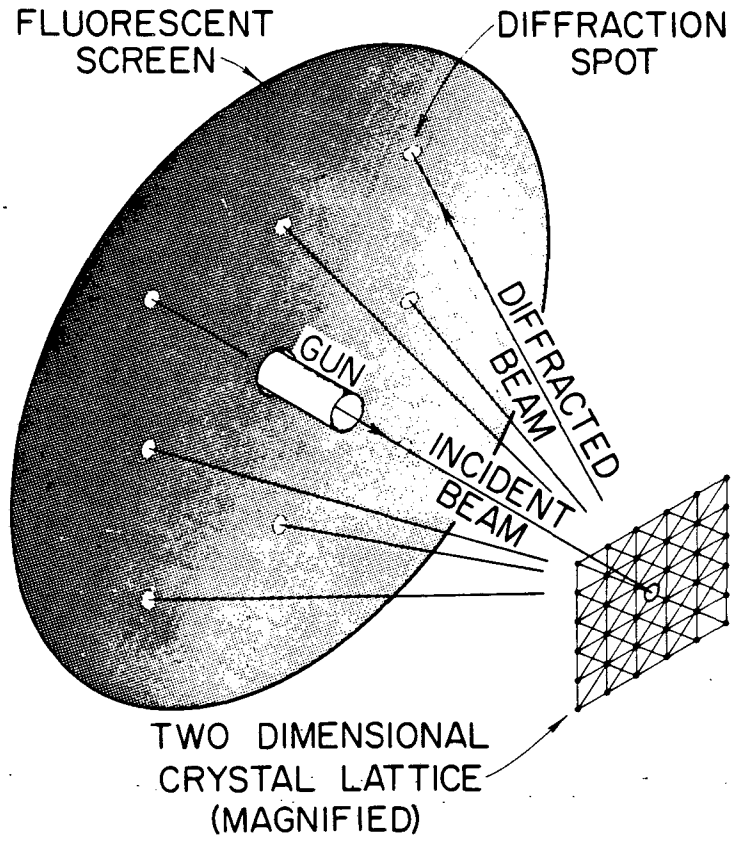
FLUORESCENT SCREEN
DIFFRACTION SPOT
DIFFRACTED BEAM
INCIDENT BEAM
GUN
TWO DIMENSIONAL CRYSTAL LATTICE (MAGNIFIED)

(a)

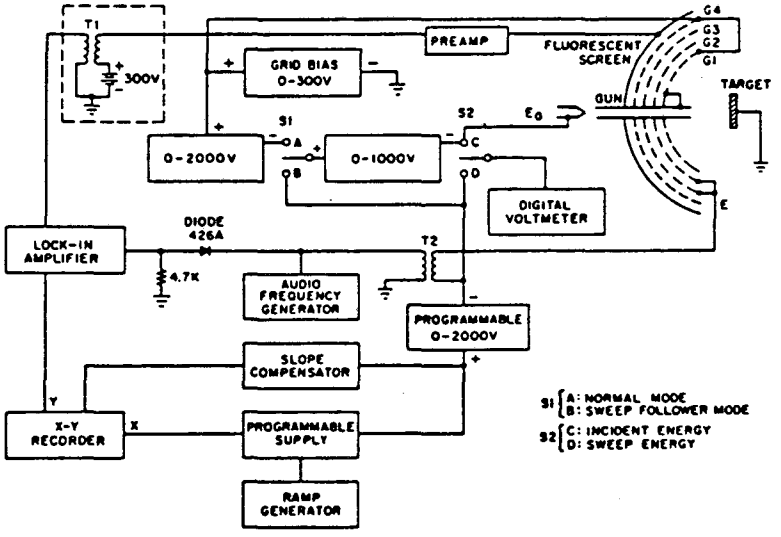
T1
300V
GRID BIAS 0-300V
PREAMP
FLUORESCENT SCREEN
G4
G3
G2
G1
TARGET
GUN
S1
S2
E_0
0-2000V
0-1000V
A
B
C
D
DIGITAL VOLTMETER
E
DIODE 426A
LOCK-IN AMPLIFIER
4.7K
T2
AUDIO FREQUENCY GENERATOR
PROGRAMMABLE 0-2000V
SLOPE COMPENSATOR
X-Y RECORDER
Y
X
PROGRAMMABLE SUPPLY
RAMP GENERATOR
S1 [A: NORMAL MODE, B: SWEEP FOLLOWER MODE
S2 [C: INCIDENT ENERGY, D: SWEEP ENERGY
XBL 8312-6874

(b)

Figure 3.8

AUGER ELECTRON EMISSION

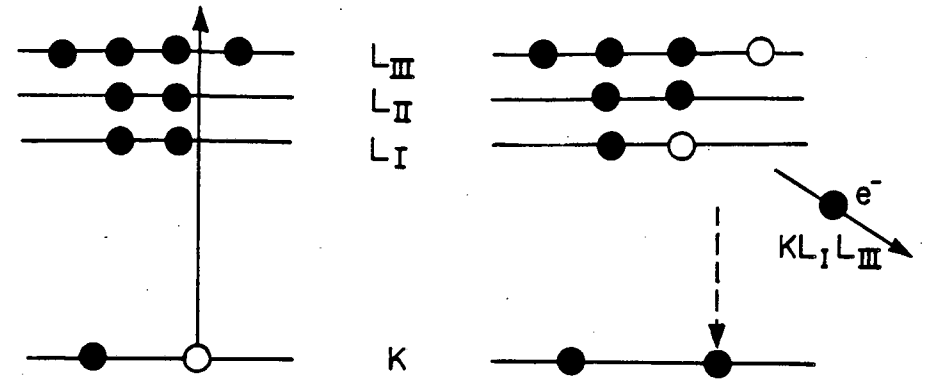

(a) EXCITATION (b) ELECTRON EMISSION

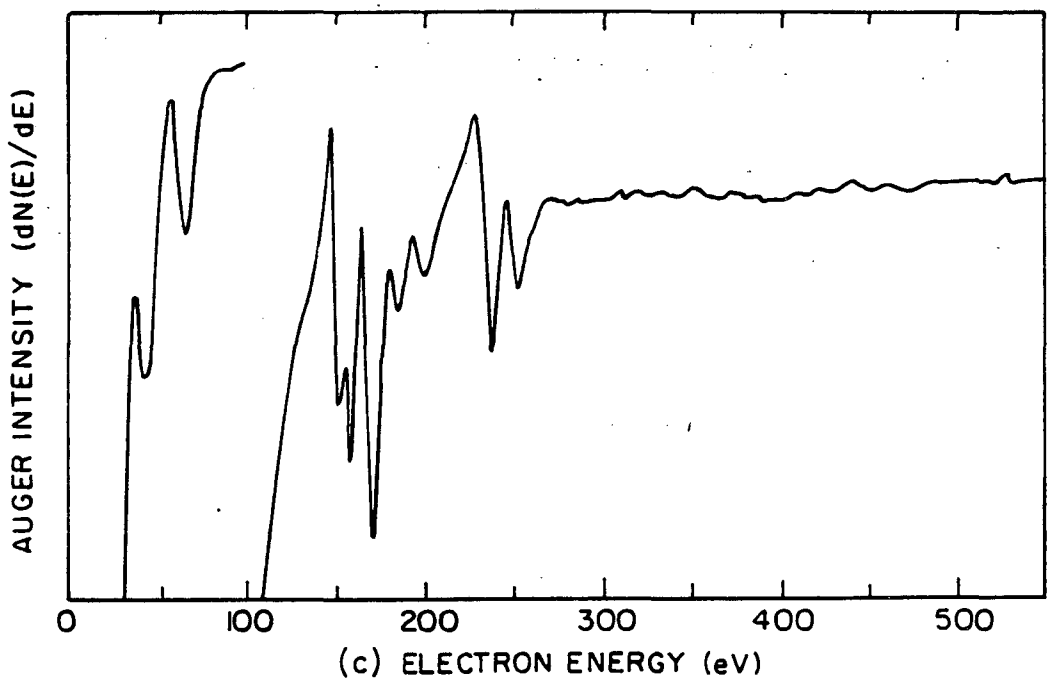

XBL8312-6679

Figure 3.9

3.3 Materials

3.3.1 Reagents

A listing of the reagents used in this thesis is given in Table 3.1. Liquid hydrocarbons (benzene and benzene-d_6) were stored in pyrex vacuum flasks fitted with O-ring sealed teflon stopcocks and stored over calcium hydride. These liquids were outgassed by repeated freeze-pump-thaw cycles at 77K prior to initial use. The isotopically labelled gases (^{13}CO, $C^{18}O$, and C_3D_6) were obtained in breakseal tubes adapted with vacuum stopcocks and used without further purification. The other gases were supplied in lecture bottles and used without further purification. However, before introduction into the vacuum system, all reagents excluding the hydrocarbons were passed through a liquid nitrogen trap (see Section 4.4.2).

Table 3.1 Sources, purities, and major contaminants of all reagents used.

REAGENT	SOURCE	PURITY (wt %)	CONTAMINANTS
Ar	LBL-Matheson	≥99.998	--
CO	LBL-Matheson	≥99.5	—
^{13}CO	Cambridge Isotope Lab.	≥99 atom % ^{13}C	CO
$C^{18}O$	Cambridge Isotope Lab.	≥99 atom % ^{18}O	CO
O_2	LBL-Matheson	≥99.9	CO
C_6H_6	Fischer	<99.9	—
C_6D_6	Norell Chemical	≥99 atom % D	C_6D_5H
C_3D_6	Merck	≥99 atom % D	C_3D_5H
H_2	LBL-Matheson	≥99.99	—
D_2	LBL-Matheson	≥99.5 D_2	HD, H_2
		≥99.95 D_2, HD, H_2	

3.3.2 Single Crystal Samples

Single crystal samples of platinum and rhodium with (111) orientation were used exclusively in this research. A total of five different samples were used, three platinum crystals and two rhodium crystals. All samples either existed on my arrival or were prepared by Wini Heppler of the LBL support staff. Both the platinum and rhodium single crystal rods were purchased at purities of at least 99.996 percent from the Materials Research Corporation (MRC). The single crystals were cut by spark erosion into thin ~1mm discs to within 1° of the (111) orientation as determined by Laue backreflection X-ray diffraction. The samples were mechanically polished to a mirror finish on both sides using standard procedures, finishing with an aqueous slurry of 0.05 μm alumina powder.

The samples were mounted on 0.51 mm (0.020 inch) mounting wires of either tantalum or platinum, which were attached to 3.18 mm (0.125 inch) tantalum rods. Care was taken to minimize the length of the mounting wires, and to achieve uniform heating. The temperature was measured with 0.13 mm (0.005 inch) chromel-alumel thermocouples spot welded to the edge or backface of the crystal.

3.4 Procedures

3.4.1 Cleaning the Single Crystal Surfaces

All the crystal samples were cleaned using a combination of chemical and mechanical treatment at elevated temperatures. The major impurities observed differed for the two metals but was similar for the different samples of each. The cleaning procedure used for each is discussed separately below.

The impurity levels in the Pt(111) samples varied from crystal to crystal, but at some point each had AES detectable levels of carbon, oxygen, sulfur, phosphorous, chlorine, calcium and silicon. The samples could be routinely cleaned, however such that no impurities were detectable by AES using a combination of treatments: heating in oxygen (1×10^{-7} torr O_2, 800-1200K), argon ion sputtering (0.5-1.5 keV, 5-10 μA crystal current) with repeated heat/cool cycles (viz. heated to 800-1300K for 5 min., cooled to ~300-500K for 5 min.), and annealing in vacuum at 1200-1400K. Initially several cycles of this treatments were necessary to obtain a clean sample. The high temperature oxygen treatment were necessary to segregate calcium and silicon to the surface as non-volatile oxides for removal by sputtering. Oxygen was occasionally added during ion sputtering to facilitate their removal. The impurity level of Ca and Si was easily monitored by AES and LEED. As these oxides formed ordered overlayers on the surface, the sensitivity of LEED to these small islands of impurities was often greater than that of AES.

For the Rh(111) samples, the impurities observed were carbon, oxygen, silicon, boron, chlorine and sulfur. Boron and sulfur were typically observed after repeated annealing and required prolonged ion sputtering to remove. The crystal was cleaned prior to experimentation in a similar manner as the Pt(111) samples. Routinely, a combination of oxygen treatment at 1-5 x 10^{-7} torr O_2 at 950-1250K, Ar^+ sputtering (0.5-1.0 keV, 6-8 μA), and annealing in vacuum at 1000-1400K were used to prepare a clean Rh(111) sample. AES, LEED, and HREELS were all used to insure the sample was clean and well-ordered (see Section 3.4.3). HREELS is especially sensitive to low levels of sulfur or boron oxide, and the sample was resputtered if these were observed.

All Ar^+ ion sputtering was performed at 4-6 x 10^{-5} torr Ar. On the UHV chamber containing only ion pumping, this was done in a static mode, all diffusion pumped apparatuses permitted flowing Ar during sputtering. A titanium film was always deposited with the TSP prior to sputtering to maintain gas purity. All chemical cleaning was done in flowing oxygen.

3.4.2 Gas and Alkali Dosing

Molecular gas dosing was achieved through a variable leak valve from the gas manifold into the vacuum chamber in one of three ways: either by backfilling the chamber, by introduction through a 3.18 mm (0.125 inch) O.D. tube doser or by introduction through a microchannel array nozzle doser. Both the tube and nozzle dosers were mounted within 2 cm of the sample to achieve local pressure enhancement at the

sample. For the condensible reagents used (C_6H_6, C_6D_6), the exposure rate was enhanced 5-fold using the nozzle doser. All exposures cited in this thesis are uncorrected for ion gauge sensitivity.

The gas manifold was typically maintained at $\leq 1 \times 10^{-5}$ torr by baking at ~450K at near weekly intervals. The manifold was flushed at least once with the gas to be used prior to storage. The gases were passed through a liquid nitrogen cooled trap prior to introduction into the chamber.

All alkali dosing was achieved by heating a commercial SAES Getter source which consists of a powdered mixture of potassium chromate and a zirconium-16 percent aluminum alloy getter, enclosed in a tantalum dispenser. The alkali dosers were positioned 3-8 cm from the sample (specifically 3-5 cm from the Pt(111) samples and 6-8 cm from the Rh(111) samples). Currents of 5-8 Amps were necessary to achieve dosing rates between 0.05 and 0.10 monolayers per minute (where one monolayer corresponds to one alkali atom per surface substrate atom). After an initial induction period when several impurities are additionally emitted by the source, pure neutral alkali is the only species emitted. The pressure increase typically observed during routine use of the sources was $1\text{-}2 \times 10^{-10}$ torr. Additionally, alkali layers with impurities present differed strongly in their chemisorption properties from pure alkali layers, making CO and oxygen impurities during dosing easy to detect.

3.4.3 Surface Characterization

Prior to gas or alkali adsorption, the sample was cleaned as described above. The surface cleanliness was determined by AES, LEED, and HREELS. Often, LEED and HREELS were more sensitive to low levels of impurities than AES, and once a reproducible cleaning procedure was established, these were used nearly exclusively to avoid possible decomposition of residual CO (the main contaminant in the vacuum chambers) caused by the 2 keV electron beam during AES analysis. Hence, after cleaning, if the surface possessed a sharp (1x1) diffraction pattern with little background intensity and showed energy losses due only to residual CO with low background and little tailing of the elastic peak, the sample was deemed clean. The sample was then flashed and exposed within 1-3 minutes.

The metal-adsorbate system was typically characterized by several techniques in succession, usually first by HREELS, then LEED, then either AES or TPD. The TPD experiments were also performed exclusively for a series of similar sample preparations, as were AES calibrations. All experiments were repeated to insure accuracy.

3.4.4 Tuning of the HREEL Spectrometer

As mentioned in section 3.2.1, the two spectrometers differed markedly in their performance. However, tuning of both spectrometers was very similar. Reference will be made here to typical voltages and currents observed as well as scanning and tuning time required for the newer spectrometer since it was used more extensively in this research.

Tuning of the spectrometer was fairly facile for any adsorption system once the proper sample position was determined and the approximate voltage settings decided for the lenses and sectors. Typically, once the sample was cleaned only a few minutes (5-15 minutes) were required to obtain good resolution (40-50 cm^{-1} FWHM) at counting rates of 10^5-10^6 cps. Similar tuning times were required after dosing the sample. Only slightly longer time (30-60 minutes) was required after baking the spectrometer and chamber, especially if the crystal sample was replaced or otherwise remounted. In this case, optimization of tuning and sample position could be accomplished after a small number of trial positions. As resolution was not sacrificed, this optimization only affected the intensity and tailing of the elastic peak.

One of the most important requirements for obtaining good quality spectra with minimum tuning effort is proper positioning of the sample. This is not always easy as the spectrometer and μmetal shielding surrounding it often limits or completely obstructs view of the sample. For the spectrometer used in the Pt(111) work (see Fig. 3.3) positioning of the sample was difficult since the sample was totally obscured by the spectrometer shielding plates and the X-Y axis of the manipulator could not be aligned with a defined X-Y plane of the spectrometer. In the other chamber (Fig. 3.4), both of these difficulties were corrected. The manipulator was aligned such that translation of the sample only changed the scattering point, not the scattering angle or path length of the electron beam. Furthermore,

the sample was readily visible through a 38 mm (1.5 inch) viewpoint. Markings on the B lenses' shields permitted proper z alignment. The crystal was easily positioned for specular scattering of the electron beam by rotating the sample until one's eye reflection could be viewed in the center of the viewport. Alternatively a strong light or laser beam could be used. The sample was then translated to the focal point of the spectrometer as close as possible optically. Since only one motion is undefined, this translation was then varied slowly once any signal was detected at the channeltron. This procedure resulted in optimum positioning of the sample for specular reflection experiments, the sample was simply rotated for off-specular measurements.

Tuning of the spectrometer is usually done in two stages: maximizing the current stepwise through the spectrometer until detection at the channeltron, followed by iterative voltage adjustment to maximize signal and resolution while maintaining peak shape and minimizing background. Voltages on the various lens elements often vary with similar spectral quality obtainable at many different voltage settings. Locating the elastically reflected beam at the detector can then be achieved by following a few guidelines. Initially one wants to detect current at the monochromator entrance aperture (or the collimating aperture, C1, if it is present). With an initial filament current of ~2 A, the repeller negative (typically -1V), voltages of 0-10, 20-50, 0-10V on A1, A2, and A3, respectively, and the ΔA difference (i.e., A_n left - A_n right) near zero, a current should be measurable with a picoammeter at the entrance aperture. The current

is maximized (~1-5 x 10^{-7} A) by adjusting the voltages within the prescribed ranges. Next the current should be maximized at the outer monochromator sector. The sector voltage separation should initially be large (ΔV ~0.5V) to permit high electron throughput. The voltage position of the entrance and exit apertures should be fixed according to the equation [17]

$$E(r) = \Delta V[\ln(r/R_{mean})]/[\ln(R_{outer}/R_{inner})]$$

where R_{mean}, R_{inner}, R_{outer} and r are the mean radius of the 127° sector, the radius of the inner and outer sector, and the radius of the sector whose voltage is to be determined, respectively. Inserting the dimensions of the spectrometer used here, these equations become

$$E_{outer} = -0.607\ \Delta V \qquad E_{inner} = 0.393\ \Delta V$$

for the voltage settings of the outer and inner sectors with respect to the aperture potential. Note that the difference between E_{inner} and E_{outer} is ΔV. Variation of the monochromator level changes both the aperture and sector voltages together; this should be adjusted along with the repeller, the filament, and the A lenses to maximize current at the monochromator outer sector. The monochromator aperture voltage should be maintained positive between 0-0.5V. The filament current should be adjusted between 1.8-2.3A to obtain a maximum in detected current.

Next, current at the crystal should be detected at a level of 10^{-10}-10^{-9}A by adjusting the previous lenses within their ranges, and B1 and B2. Voltages for B1 and B2 are between -2.0 and 2.0V. The voltage difference (ΔB_n) should be near zero. After this is achieved, current can be detected at the entrance aperture of the analyzer, but is somewhat difficult to measure due to its low level. Detection at the electron multiplier (channeltron) is also appropriate now by setting the analyzer and B_3 and B_4 voltages equivalent to their mirror image counterparts at the monochromator, and the collimating aperture (C2) set just positive of the analyzer aperture voltage. The slopes of the analyzer, which control the transmission of the analyzer, are adjusted to a setting of 1.0 (i.e., a 1 volt input sweeps all analyzer elements 1 volt). The elastic beam should be detectable by rastering the analyzer level between -0.1 and 0.1V of the monochromator level (viz., V(analyzer slit)-V(monochromator slit) = $\pm$0.1V).

Once the elastic beam is detected, the crystal position and voltages can be optimized simply by sweeping the elastic peak with either a computer generated stairstep ramp or a triangular wave generator, and displaying the output of the ratemeter on an oscilloscope. The intensity, resolution and peak shape are easily monitored as the voltages are varied within the above described ranges. The B lenses (especially B_2 and B_3), the sample position, the crystal bias, and the beam energy all strongly interact but are necessarily iterated to improve the peak shape. The resolution and

intensity depend on the pass energy, as noted in Chapter 2. By lowering the ΔV separation between the inner and outer sector, the resolution can be improved at the expense of count rate. Of course, the inner and outer sector voltages must be readjusted identically for both the monochromator and analyzer sectors as given by the above formula. Additionally, the aperture potentials should be made more negative as the ΔV separation decreases. Small adjustments in the other voltages, especially the beam energy and the B lenses, should maximize intensity and optimize peak shape.

REFERENCES

1. Except for the commercial equipment cited above, both apparatuses were custom built by the machine shops at the Department of Chemistry and Lawrence Berkeley Laboratories, including the chambers, the manipulators, and the HREEL spectrometers.
2. H. Froitzheim, H., Ibach, and S. Lehwald, Rev. Sci. Instrum. 46, 1325 (1975).
3. L. H. Dubois, Ph.D. thesis, University of California, Berkeley, 1980, unpublished.
4. The viton O-ring gate valves were baked slightly cooler at 400K while the HREEL spectrometer was usually baked at 525K.
5. A. L. Cabrera, N. D. Spencer, E. Kozak, P. W. Davies, and G. A. Somorjai, Rev. Sci. Instrum. 53, 1888 (1982).
6. P. A. Redhead, Vacuum 12, 203 (1962).
7. C. M. Chan, R. Aris, and W. H. Weinberg, Appl. Surface Sci. 1, 360 (1978).
8. E. L. Garfunkel, Ph.D. thesis, University of California, Berkeley, 1983, unpublished.
9. G. A. Somorjai, Chemistry in Two Dimensions: Surfaces, Cornell University Press, Ithaca, 1981.
10. C. C. Chang, in Characterization of Solid Surfaces, P. F. Kane and C. B. Larrabee, Eds., Plenum Press, New York, 1974.
11. J. C. Fuggle, in Electron Spectroscopy: Theory, Techiques and Applications, Vol. 4, C. R. Brundle and A. D. Baker, Eds., Academic Press, New York, 1981.

12. Y. R. Shen, in Novel Materials and Techniques in Condensed Matter, G. W. Crabtree and P. Vashishta, Eds., Elsevier, Amsterdam, 1982.

13. T. F. Heinz, Ph.D. thesis, University of California, Berkeley, 1982, unpublished.

14. N. Bluembergen, R. K. Chang, S. S. Jha, and C. H. Lee, Phys. Rev. 174, 813 (1968).

15. H. W. K. Tom, C. M. Mate, X. D. Zhu, J. E. Crowell, T. F. Heinz, G. A. Somorjai, and Y. R. Shen, Phys. Rev. Lett , submitted.

16. H. W. K. Tom, Ph.D. thesis, University of California, Berkeley, 1984, to be submitted.

17. M. E. Rudd, Low Energy Electron Spectrometry, K. D. Sevier, Eds., Wiley and Sons, Interscience, New York, 1972.

CHAPTER 4

POTASSIUM AND POTASSIUM PLUS OXYGEN ADSORPTION ON THE Pt(111) AND Rh(111) CRYSTAL SURFACES

4.1 Introduction

The adsorption of alkalis on metal surfaces has received considerable attention in the past since even small amounts of these adatoms can extensively modify the electron and ion emission properties of a metal surface [1]. Alkali adsorption on a metal surface typically lowers the work function dramatically. Preparation of these low work function surfaces has potential application in thermionic converters. In addition, as already discussed, alkali and alkali oxides and hydroxides are common additives in CO hydrogenation reactions, ammonia synthesis, and hydroformylation reactions. Hence, an investigation of their adsorption properties can have important ramifications in both heterogeneous catalysis and electronic device technology.

Since the physical and chemical properties of pure alkali overlayers differ markedly from that of alkali plus oxygen overlayers, they will be separately discussed.

4.2 Alkali Adsorption on Pt(111) and Rh(111)

Alkali adsorption has been characterized by TPD, AES, LEED, HREELS and SHG. Since the properties of potassium on Pt(111) and Rh(111) are very similar, they will be discussed together.

4.2.1 Work Function Changes

As mentioned above, one of the most important properties of alkali overlayers is their effect on the work function. The characteristic changes for alkali adsorption on a metal structure are: an initially rapid linear decrease in work function, reaching a minimum, then rising to the bulk alkali work function value at completion of the first layer. This behavior occurs because, upon adsorption, alkali adatoms transfer charge to the substrate, forming a positive alkali ion. This ion induces a screening charge, resulting in a net dipole moment, directed opposite to that of the pure substrate dipole layer. At low coverage, these dipoles form a continuous dipole layer decreasing the work function linearly with coverage. Interactions between adatoms (e.g. dipoles) reduce this effect at high coverage such that the work function eventually reaches a minimum and rises to the characteristic value of the bulk alkali [2]. The initial linear decrease in the work function gives the dipole field strength of the alkali atoms, and is governed by the Helmholtz equation (i.e. $\Delta\phi = 4\pi\mu N$, where μ is the dipole moment and N is the alkali surface adatom density). In this region, the alkali species are ionic. Once the minimum in work function is obtained, the slow increase in work function denotes the region where the alkali becomes metallic in nature. For potassium adsorption on Pt(111), the work function decreases up to 4 eV [3,4].

4.2.2 Low Energy Electron Diffraction Studies

A sequence of diffraction patterns observed for potassium adsorption on Pt(111) is shown in Fig. 4.1. The patterns are arranged in decreasing coverage as TPD was used to adjust the necessary coverage. Upon an exposure of potassium equal to completion of the first layer (as determined from TPD and AES measurements), an incommensurate hexagonally close packed ordered structure forms as shown in Fig. 4.1a. In this figure, it is evident that the potassium overlayer has its axis alligned with the substrate axis, but has a larger interatomic spacing (4.6 ± 0.1Å) than the platinum substrate spacing (2.78Å). Similar to K adsorption to Rh(111), this spacing is smaller than that observed for bulk potassium (4.70Å). The surface density is calculated to be 5.4×10^{14} K atoms/cm^2 assuming one K atom per unit cell; the coverage with respect to the Pt(111) surface density is $\theta_K = 0.36$ for this close packed overlayer.

As the potassium coverage is decreased, orientational reordering occurs, forming in sequence a ring structure which sharpens into split beams about the (1/3,1/3) spot position (see Fig. 4.1b and c). These coalesce into the $(\sqrt{3} \times \sqrt{3})R30^\circ$ structure. This occurs at $\theta_K = 0.33$. Similar behavior is seen on Rh(111) as discussed below. Noble gas and halogen adsorption systems show similar behavior [5,6]. No ordered structures were observed below $\theta_K = 0.33$ at temperatures as low as 270K.

On Rh(111), the sequence of LEED patterns observed for decreasing potassium coverage is shown in Fig. 4.2. The incommensurate hexagonally close packed overlayer observed at completion of the first layer (Fig. 4.2a) is nearly identical to that seen on Pt, and corresponds to an interatomic spacing of 4.45 ± 0.1Å compared to 2.68Å for Rh(111). The innermost ring of spots is due to second order diffraction. From the ordered structure observed and assuming one potassium atom per unit cell, the close packed potassium monolayer is calculated to have a surface density of 5.8×10^{14} atoms/cm^2, for a coverage of $\theta_K = 0.36$ as defined with respect to the Rh(111) surface density of 1.61×10^{15} atoms/cm^2. If additional potassium is added to the surface, the pattern becomes more diffuse as multilayers begin to grow. Figure 4.2b shows the additional structure that occurs upon decreasing the potassium coverage slightly. New spots at the (1/3,1/3) position begin growing in as the spots observed on axis move in toward the center and begin to split. The spacing observed for the (1/3,1/3) position implies a coverage of $\theta_K = .33$, while the interatomic spacing of 4.75 ± .1Å calculated for the on-axis spots indicates a coverage of $\theta_K = 0.32$, suggesting two domains are present. Upon further reduction of the coverage, a $(\sqrt{3} \times \sqrt{3})R30^\circ$ is exclusively present (Fig. 4.2C). As one approaches $\theta_K = 0.25$, a (2x2) structure begins to grow in with the $(\sqrt{3} \times \sqrt{3})R30^\circ$ pattern, forming hexagons about the (0,0) beam. Only a (2x2) pattern can be observed at slightly less coverages.

The absence of any structure at coverages less than $\theta_K = 0.25$ at temperatures as low as 140K suggest that no attractive interaction between adsorbed potassium adatoms exists. The structures observed provide additional coverage calibration points.

4.2.3 Potassium Uptake and Calibration

The potassium coverage on both surfaces was monitored in at least 3 ways: LEED structures, yields from thermal desorption measurements, and the Auger intensity ratios of the potassium (250 eV) and substrate (Pt 64, Rh 302 eV) transitions. Figure 4.3 shows the linear variation with θ_K of the Auger peak ratio for Rh up to completion of the first layer.

For the experiments on Rh, the coverage could also be calibrated by measuring the potassium flux using a line of sight mass spectrometer. Since the configuration was always the same and since the mass spectrometer was line of sight to the potassium source, these proved quite reliable for coverage determinations after the relationship to coverage was measured.

4.2.4 Temperature Programmed Desorption Studies

The thermal desorption spectra of potassium from Pt(111) and Rh(111) is shown as a function of coverage in Figures 4.4 and 4.5, respectively. On Pt(111), at low coverages, the maximum desorption rate of K occurs at ~1050K. With increasing K coverage, this peak shifts toward lower temperature in a smooth and pronounced way. At

completion rate of the first layer (θ_K = 0.36), the maximum desorption occurs near 400K. This behavior is common for alkali adsorption on transition metals. Similar spectra are seen for K on Rh(111). At low coverages, the maximum desorption rate occurs at ~1125K. This peak shifts to lower temperatures with increasing coverage until completion of the first layer, where it occurs at ~500K. This shift is believed to be due to repulsive interaction between the partially ionized alkali adatoms [1]. Multilayer desorption occurs at ~350K from Rh(111) and 380K for Pt(111). Assuming a pre-exponential factor of $1x10^{13}$ sec^{-1}, first order desorption kinetics, and using the Redhead equation, we obtain a desorption energy of 20 kcal/mole for both of these multilayer peaks. Figure 4.6 shows the variation in the heat of desorption as a function of K coverage. For Rh(111), these values vary from ~65 kcal/mole at the lowest coverages to 20 kcal/mole value at multilayer formation. This latter value agrees well with the heat of vaporization of potassium (18.9 kcal/mole). The same trend is seen for K adsorption on the Pt(111) surface. The shape of the curve is thought to be caused by depolarization of the surface dipoles at high coverage [7].

4.2.5 Second Harmonic Generation Studies

When any alkali is adsorbed onto a metal surface, the second harmonic signal varies drastically. Figure 4.7 shows a typical example of the large variation in signal with coverage, in this case for Na/Rh(111). Here saturation of the first layer occurs at $\theta = \theta_m = 0.5$

The variation in the SH signal is believed to be due to the ionic and metallic nature of an alkali as a function of coverage. The SH signal increases up to the point ($\theta \sim 0.5\theta_m$) where the minimum in work function is expected [8], indicating electron donation to the surface for the ionized alkali layer. At $\theta > 0.5\theta_m$ the SH signal decreases until $\theta \sim 0.9\theta_m$ subsequently increasing to 70 times the base Rh(111) metal value. Thos change suggests that as the Na layer becomes more metallic, it becomes much more free electron-like than Rh, giving rise to large second harmonic signals.

4.2.6 Vibrational Spectroscopy Studies

Figures 4.8 and 4.9 show the low frequency modes observable when potassium is adsorbed on Rh(111). The modes are very intense and their large tailing often obscures the weaker low frequency vibrations. The intensity of these modes increases when CO is coadsorbed with potassium; those spectra shown are for the coadsorption system. The most curious aspect of these modes is their variation with potassium coverage. The mode increases from 73 cm^{-1} to 129 cm^{-1} as θ_K varies from 0.03 to 0.25. Overtones or multiple losses are also observable for these losses. Their origin is either a surface phonon or a M-K stretching vibration. The vibrational frequency seems too low to be due to a ν_{M-K} but shifts in the expected direction for a surface phonon mode.

FIGURE CAPTIONS

Fig. 4.1. Sequence of LEED structures observed for K on Pt(111). (a) Close-packed K layer, θ_K = 0.36. (b) Annealed (a) to 330K. (c) Annealed (a) to 350K. (d) Annealed (a) to 400K.

Fig. 4.2. Progression of LEED patterns observed for potassium adsorption on Rh(111) as the coverage is decreased (a) θ_K = 0.36, saturation of the first layer. (b) After annealing (a) to 395K, (c) After annealing to 520K. (d) After annealing to 640K.

Fig. 4.3. Auger intensity ratio for K on Rh(111) as a function of the potassium coverage.

Fig. 4.4. TPD spectra for K on Pt(111) after adsorption at ~250K. The heating rate was 30K/s.

Fig. 4.5. TPD spectra for K on Rh(111) after adsorption at 290K. The heating rate was 15K/s.

Fig. 4.6. The heat of desorption of potassium on Rh(111) versus K coverage.

Fig. 4.7. Variation in the second harmonic as a function of Na coverage. The inset shows the low coverage region on an expanded scale.

Fig. 4.8. Vibrational spectra of the low frequency modes observed only in the presence of K, as a function of K coverage.

Fig. 4.9. Vibrational spectra of the K-induced modes shown on an expanded scale, as a function of coverage or temperature.

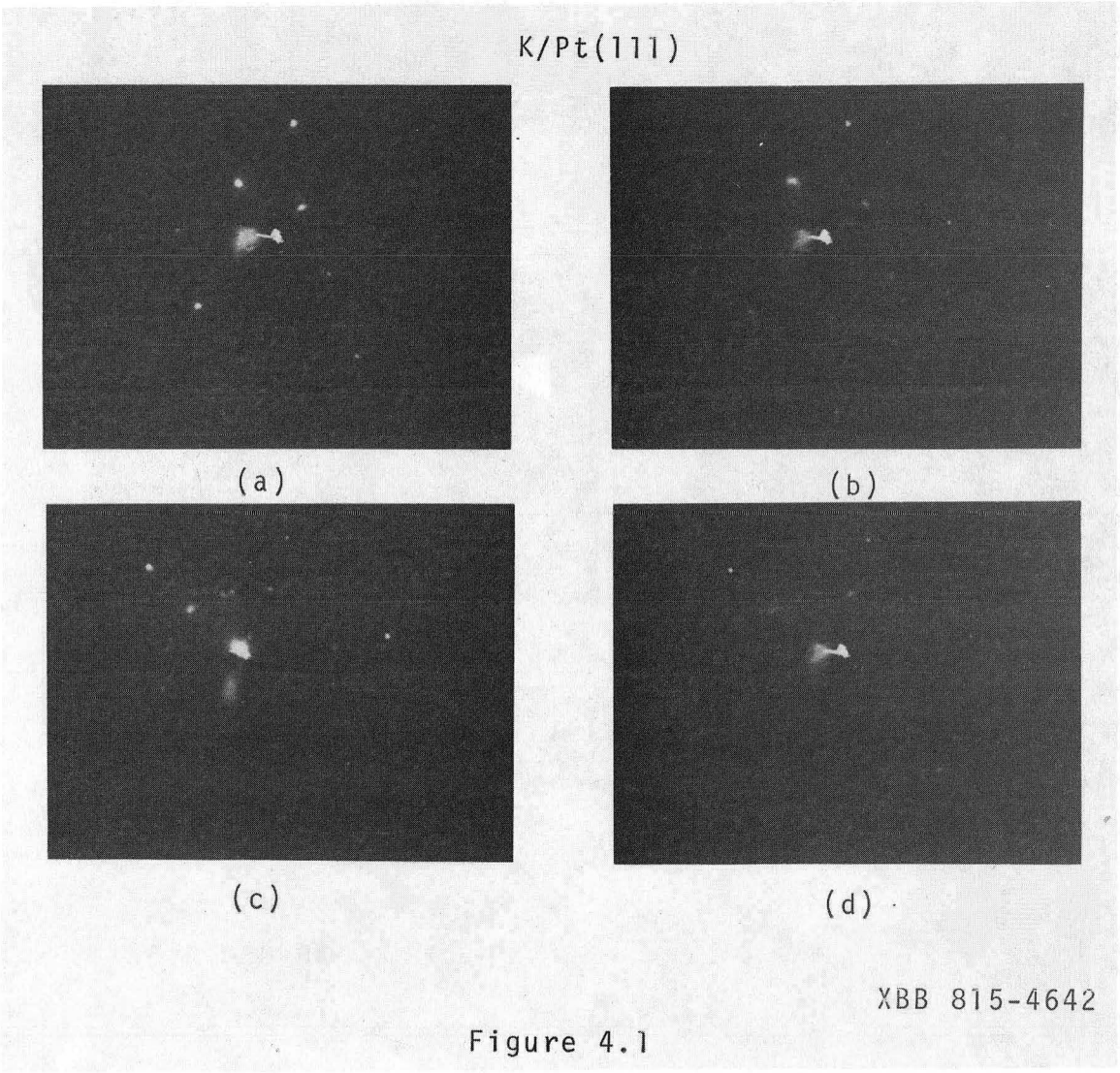

Figure 4.1

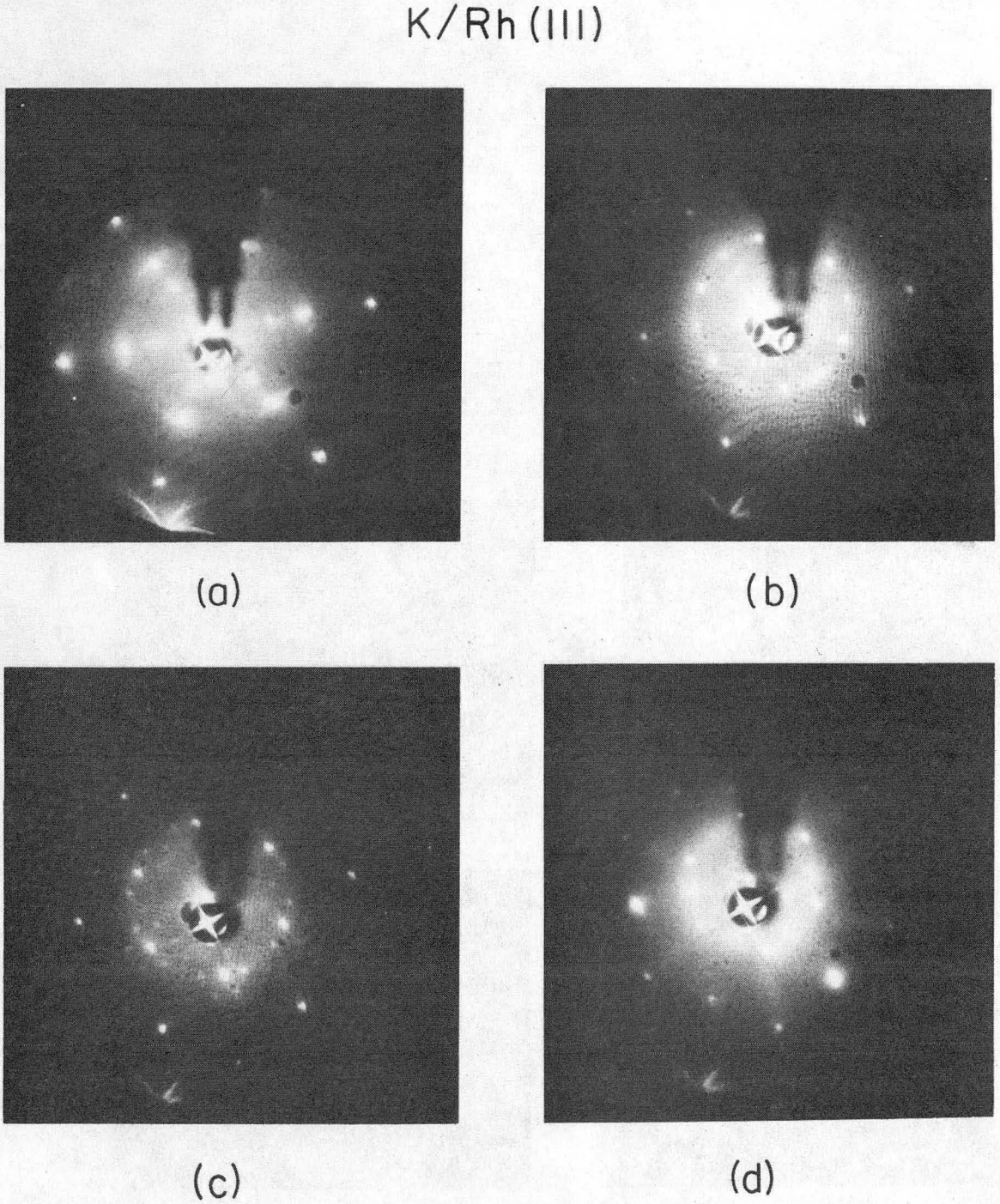

XBB 830-9567

Figure 4.2

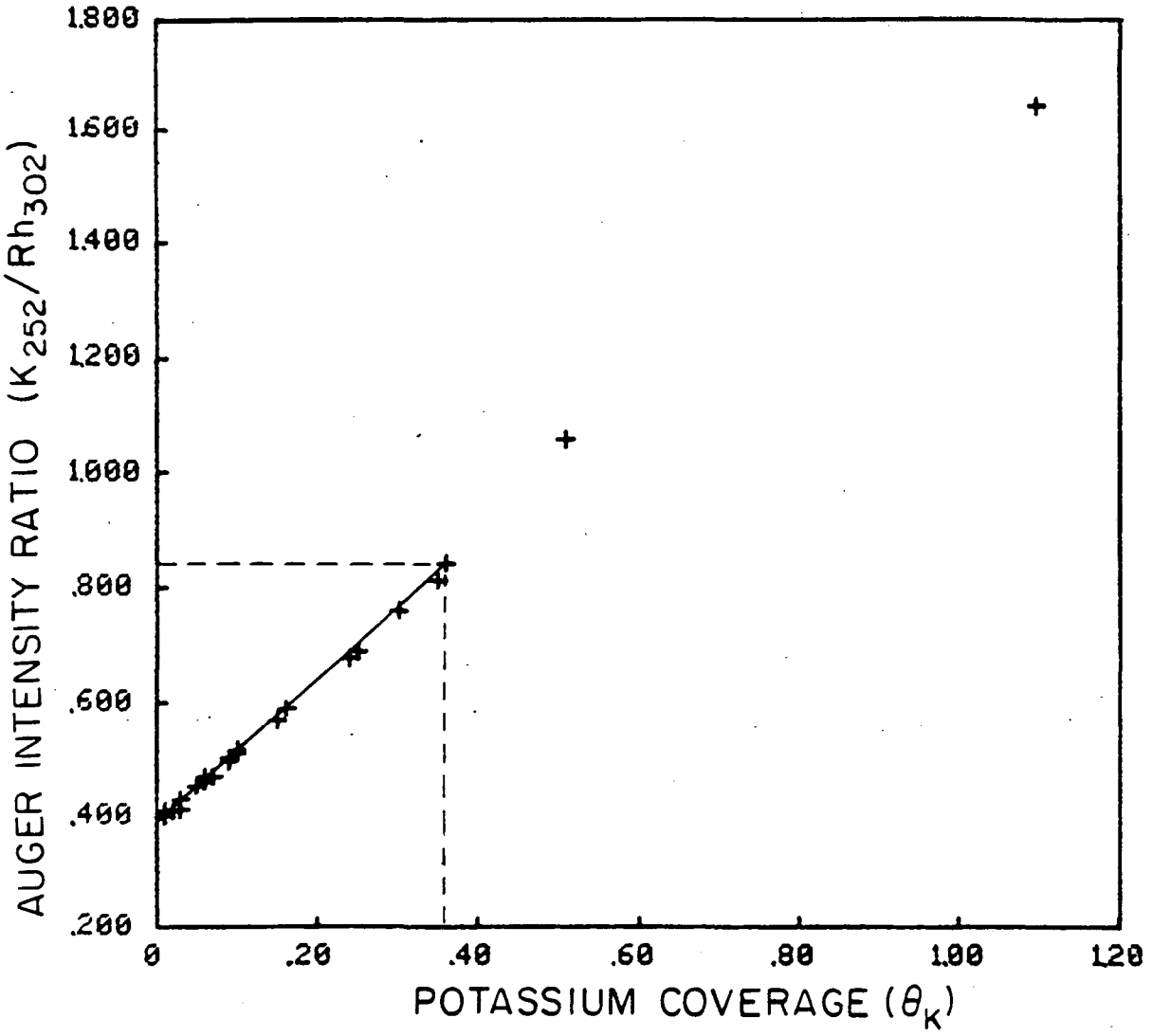
1.800
1.600
1.400
1.200
1.000
.800
.600
.400
.200
AUGER INTENSITY RATIO (K_{252}/Rh_{302})
0
.20
.40
.60
.80
1.00
1.20
POTASSIUM COVERAGE (θ_K)
X8L8310-6564

Figure 4.3

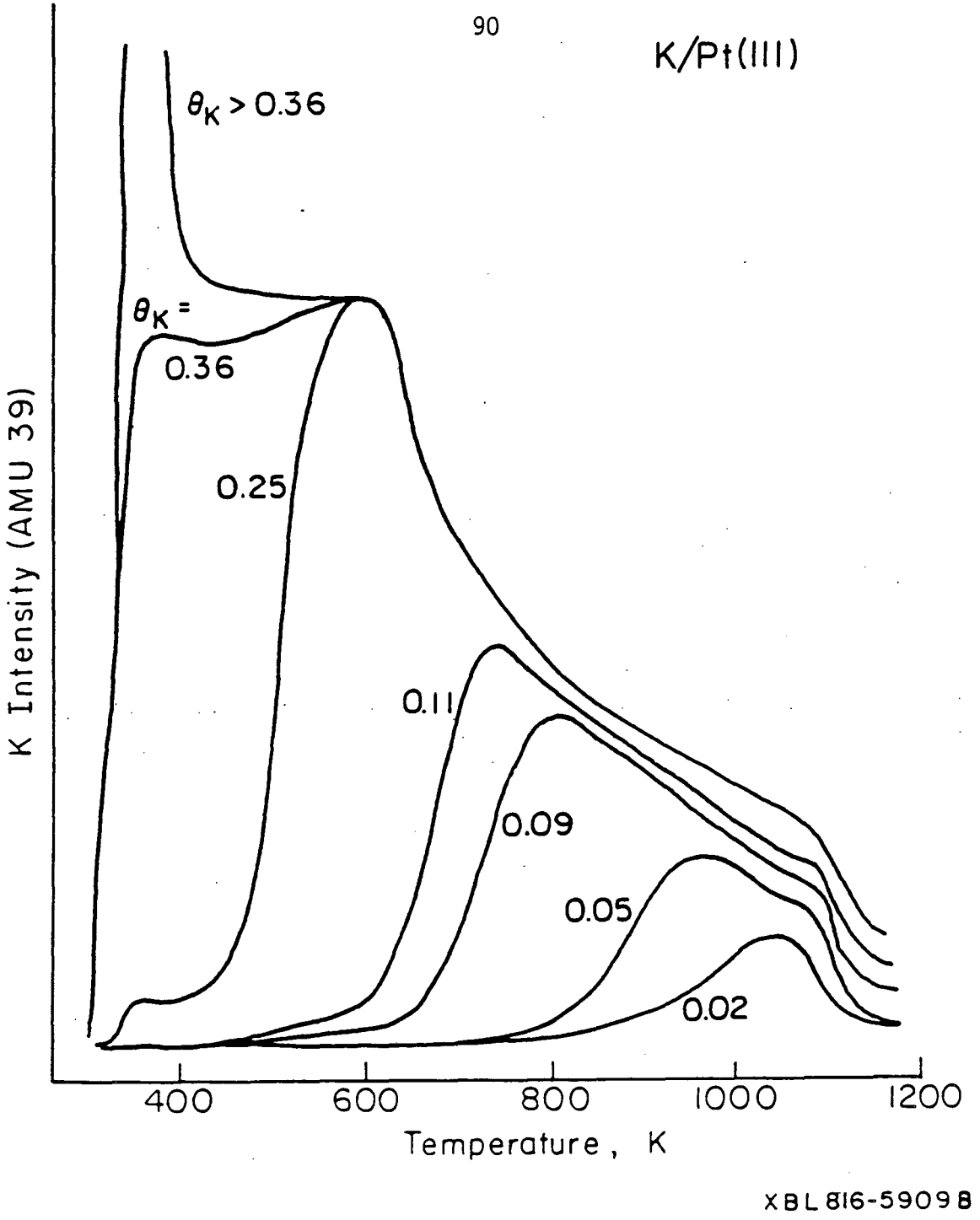
K/Pt(111)
$\theta_K > 0.36$
$\theta_K =$
0.36
0.25
0.11
0.09
0.05
0.02
K Intensity (AMU 39)
400
600
800
1000
1200
Temperature, K
XBL816-5909B

Figure 4.4

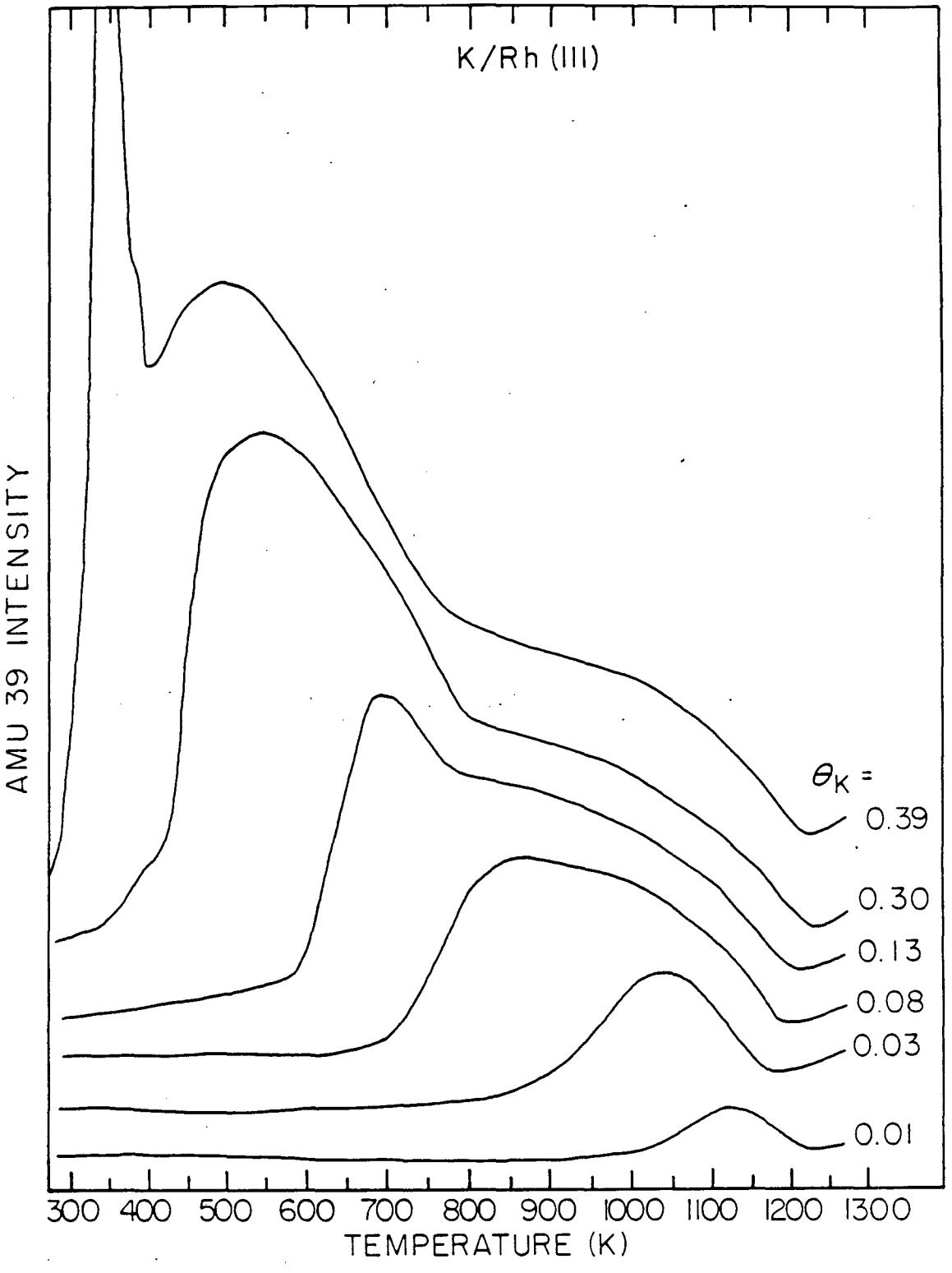
K/Rh (111)
AMU 39 INTENSITY
θ_K =
0.39
0.30
0.13
0.08
0.03
0.01
300 400 500 600 700 800 900 1000 1100 1200 1300
TEMPERATURE (K)
XBL 8310-6554

Figure 4.5

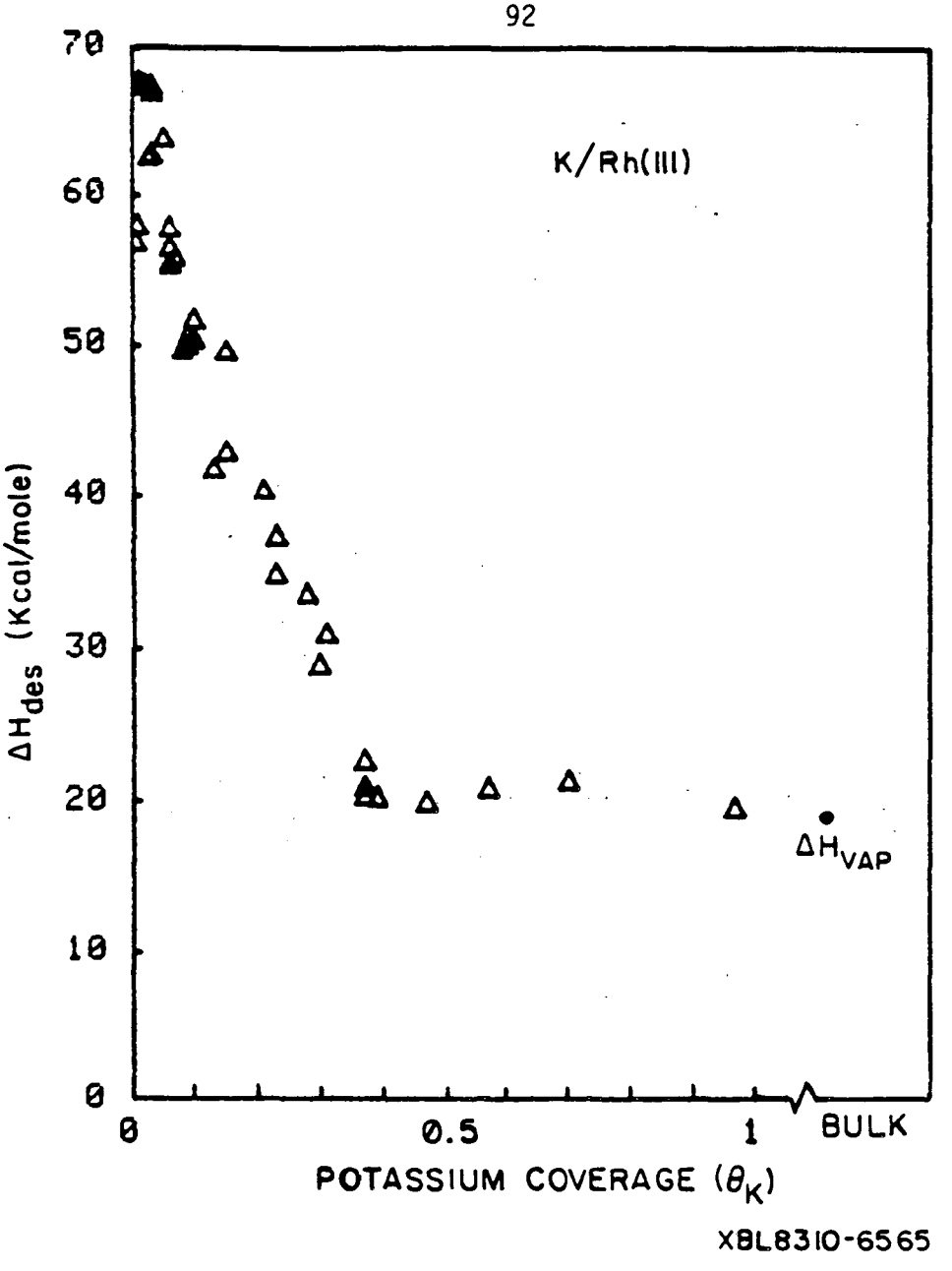
70
60
50
40
30
20
10
0
K/Rh(111)
ΔH_{des} (Kcal/mole)
ΔH_{VAP}
0
0.5
1
BULK
POTASSIUM COVERAGE (θ_K)
X8L8310-6565

Figure 4.6

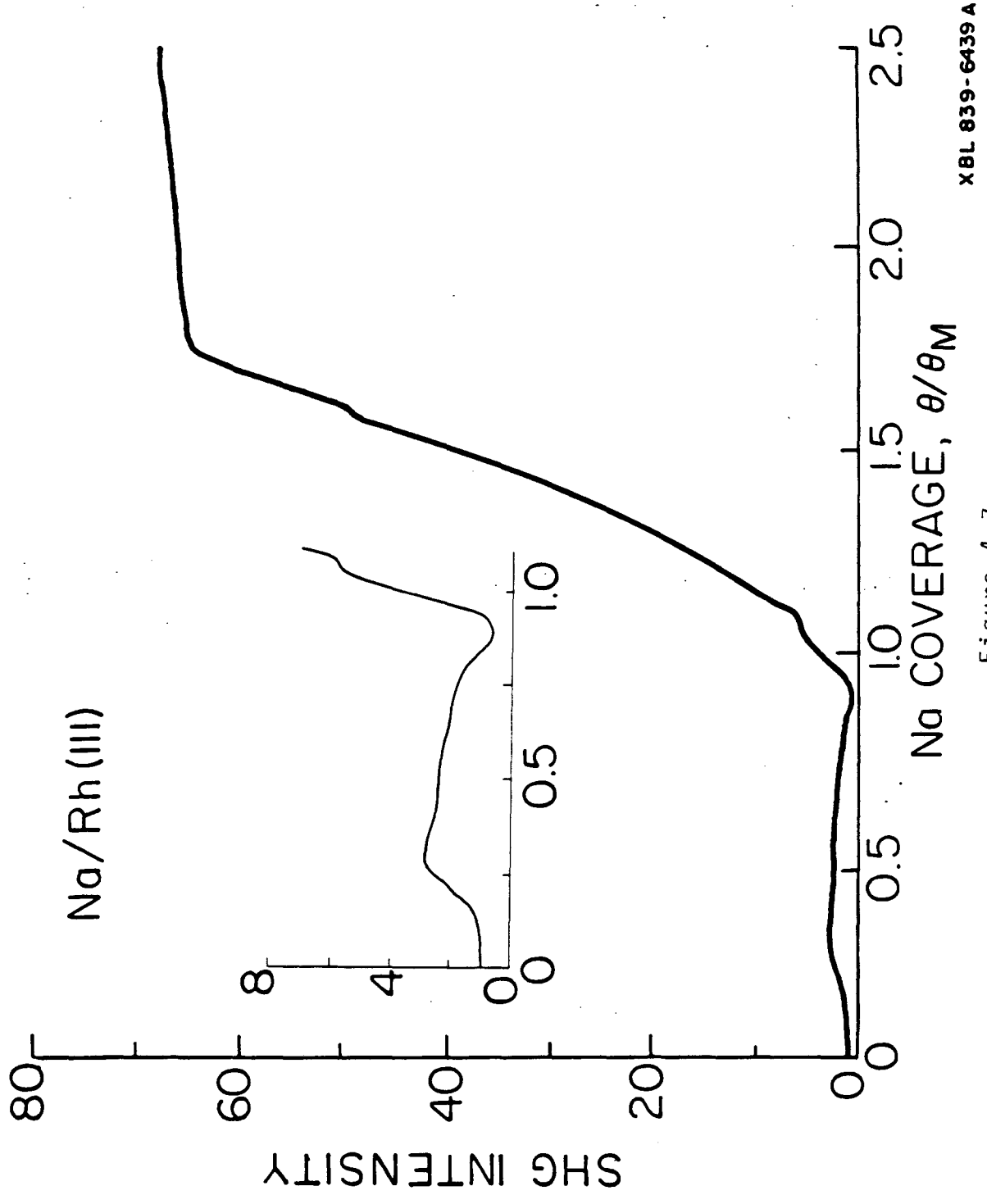
Na/Rh(111)
SHG INTENSITY
Na COVERAGE, θ/θM
0
20
40
60
80
0
0.5
1.0
1.5
2.0
2.5
0
4
8
0
0.5
1.0
XBL 839-6439A

Figure 4.7

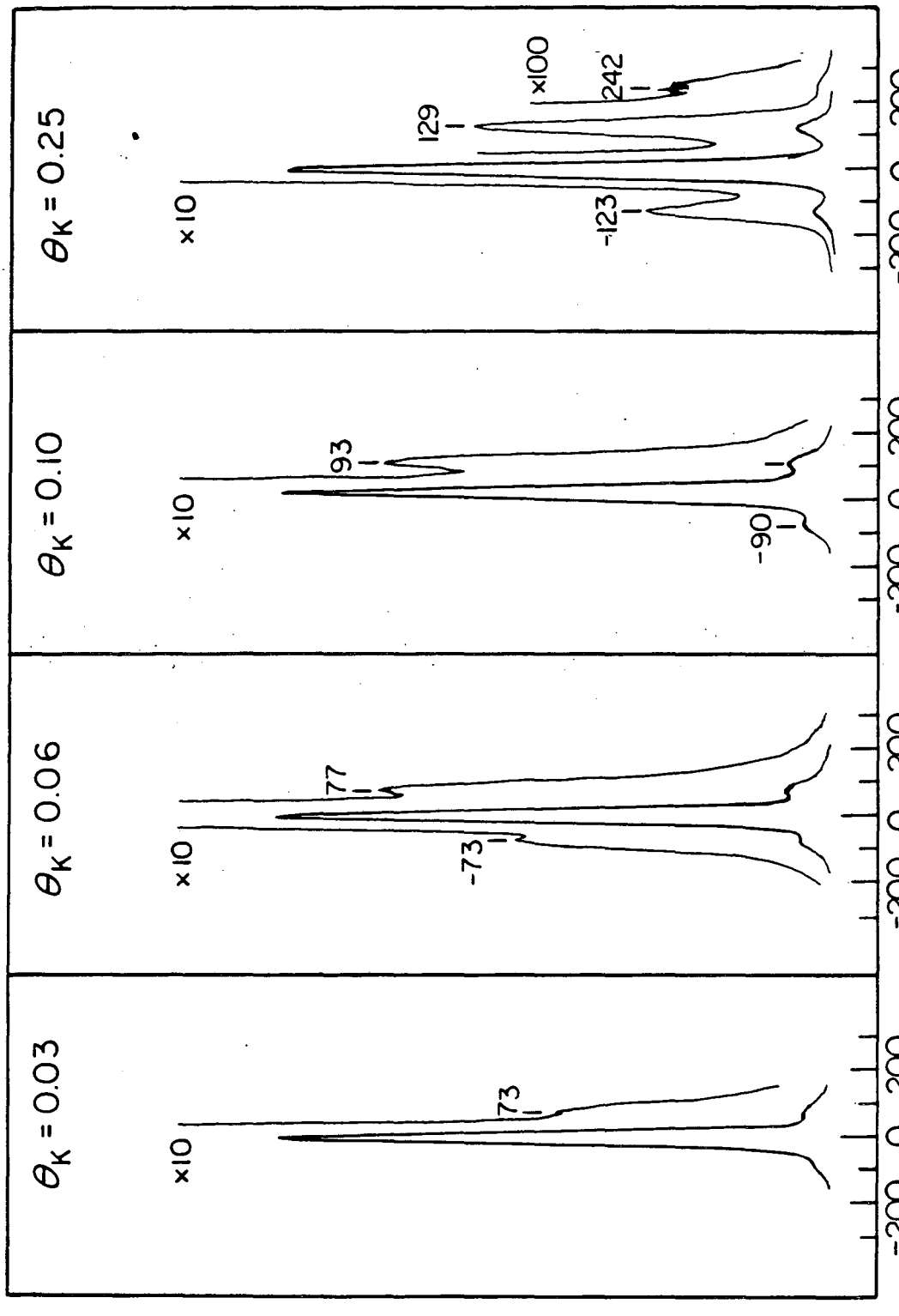
CO/K/Rh(111)
θK = 0.03
θK = 0.06
θK = 0.10
θK = 0.25
×10
×100
73
77
-73
93
-90
129
242
-123
-200 0 200
ENERGY LOSS (cm-1)
INTENSITY (ARBITRARY UNITS)
XBL 8310-6550

Figure 4.8

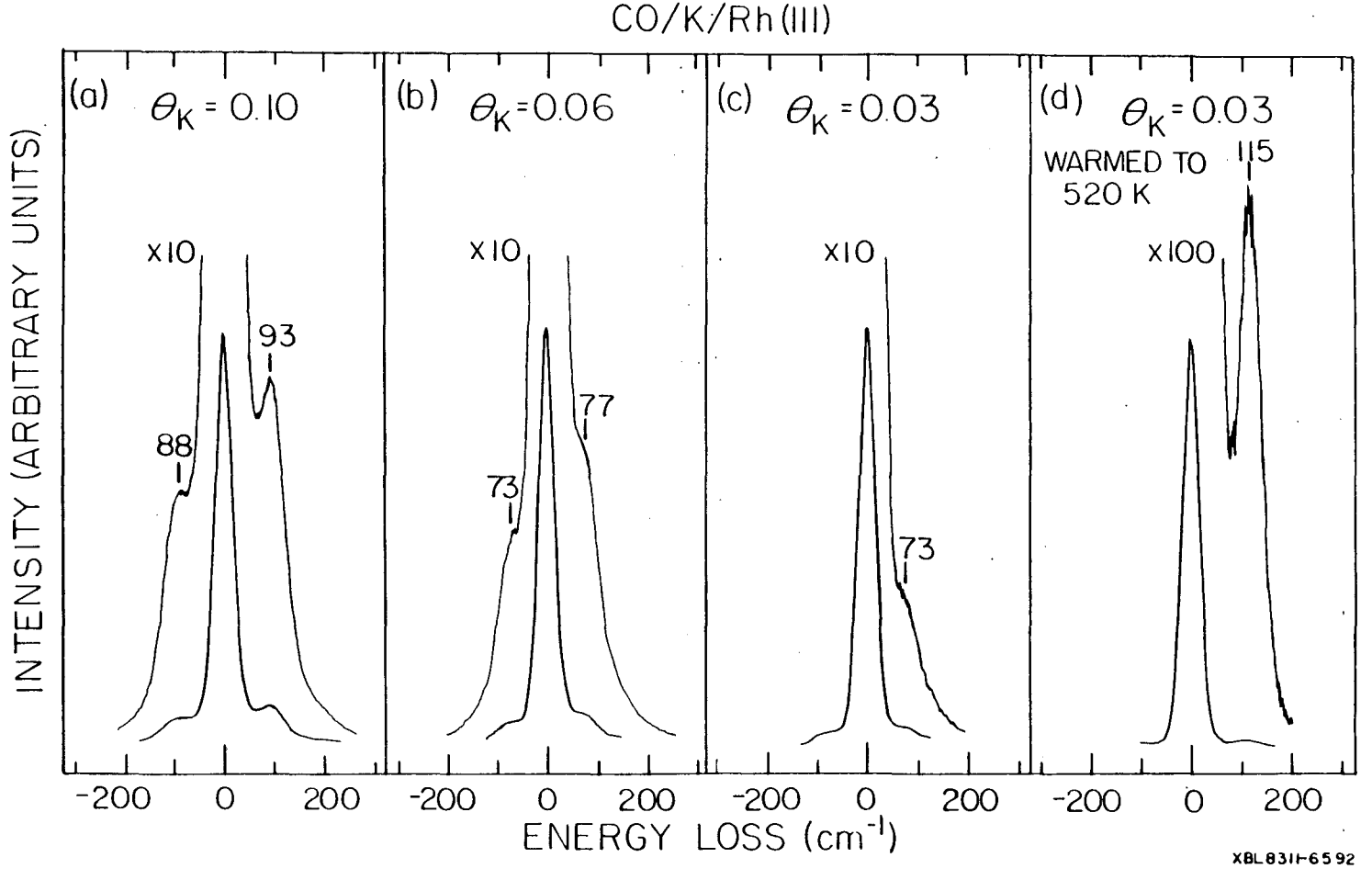
CO/K/Rh(111)
(a) θ_K = 0.10
(b) θ_K = 0.06
(c) θ_K = 0.03
(d) θ_K = 0.03
WARMED TO 520 K
x10
x10
x10
x100
88
93
73
77
73
115
INTENSITY (ARBITRARY UNITS)
-200
0
200
ENERGY LOSS (cm^{-1})
XBL831I-6592

Figure 4.9

4.3 Oxygen Adsorption on Potassium Dosed Rh(111)

In the previous section it was shown that potassium layers have similar physical and chemical properties on different surfaces. The same is true for potassium layers dosed with oxygen. The TPD spectra reported here for O_2/K/Rh(111) are very simlar to that found by Garfunkel and Somorjai for the O_2/K/Pt(111) adsorption system [7].

Figure 4.10 shows the thermal desorption spectra for K with coadsorbed oxygen (20L) on Rh(111). The nature of the desorption is changed drastically from that of pure K desorption (Section 4.2.4). The coadsorbed oxygen adatoms strongly modify the heat of adsorption of K on Rh(111), increasing it by over 30 kcal/mole from that seen for multilayer K desorption. At low K coverages, O_2 desorbs at a lower temperature than K. The temperature differences of the peak desorption maxima decreases, until at K coverages greater than $\theta_K = 0.2$, O_2 and K desorb simultaneously, indicating surface complex formation. This is shown in Fig. 4.11 for $\theta_K = 0.8$. Similar behavior is seen for CO on K dosed Rh(111) as discussed in Chapter 5. No KO, K_2O or KO_2 species were detected for this adsorption system, suggesting that such complexes dissociate in the ionizer of the mass spectrometer. The simultaneous desorption of O_2 and K strongly suggests such complex formation.

As already mentioned, small potassium coverages do not perturb the desorption of oxygen or vice-versa. This is because all of the O_2 desorbs from the surface prior to any potassium desorption. Vibrational spectra of these layers are only slightly shifted from the

clean surface vibrational frequencies, as shown in Fig. 4.12. Oxygen adsorption on Rh(111) is dissociative [9], with a Rh-O stretching vibration occurring between 525-550 cm^{-1}. As seen in Fig. 4.12, low potassium coverages do not affect this vibration, although at θ_K = 0.10 the mode does increase in frequency, indicating stronger bonding between Rh and $O_{(a)}$, as indicated by the increase in the temperature of the oxygen desorption rate maximum with K adsorption. The surface phonon mode at 210 cm^{-1} broadens and increases in frequency with oxygen coadsorption. The 1430-1460 cm^{-1} vibrations are due to residual CO adsorption, as described in the next chapter.

FIGURE CAPTIONS

Fig. 4.10. TPD spectra for potassium desorption from Rh(111) after oxygen (20L) was coadsorbed at 300K. The heating rate was 15K/s.

Fig. 4.11. TPD spectra for both potassium and oxygen after adsorption of 20L O_2 onto a potassium dosed Rh(111) surface. The heating rate was 60 K/s.

Fig. 4.12. Vibrational spectra for oxygen adsorption on a potassium predosed Rh(111) surface.

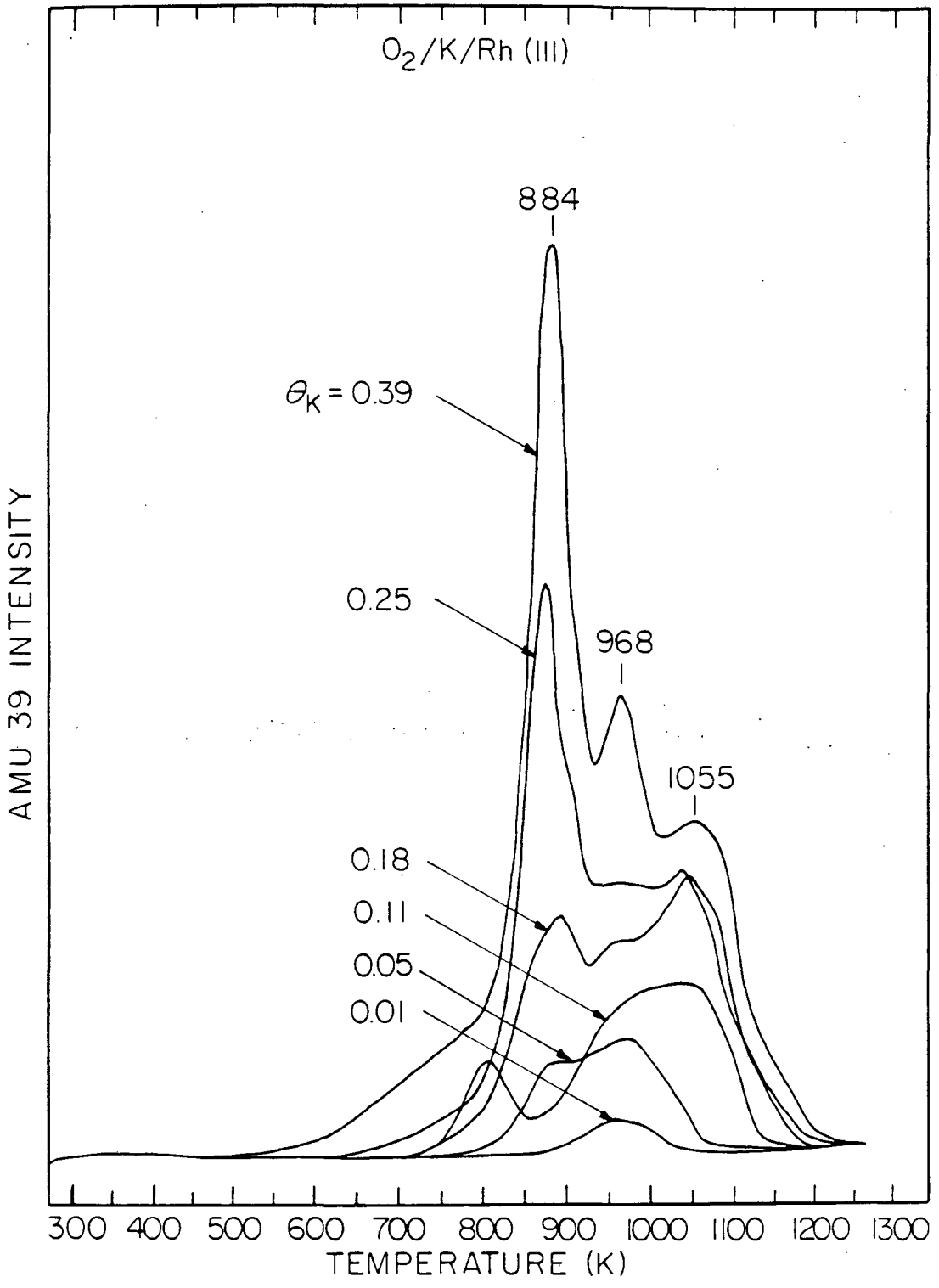

Figure 4.10

xBL 8310-6553

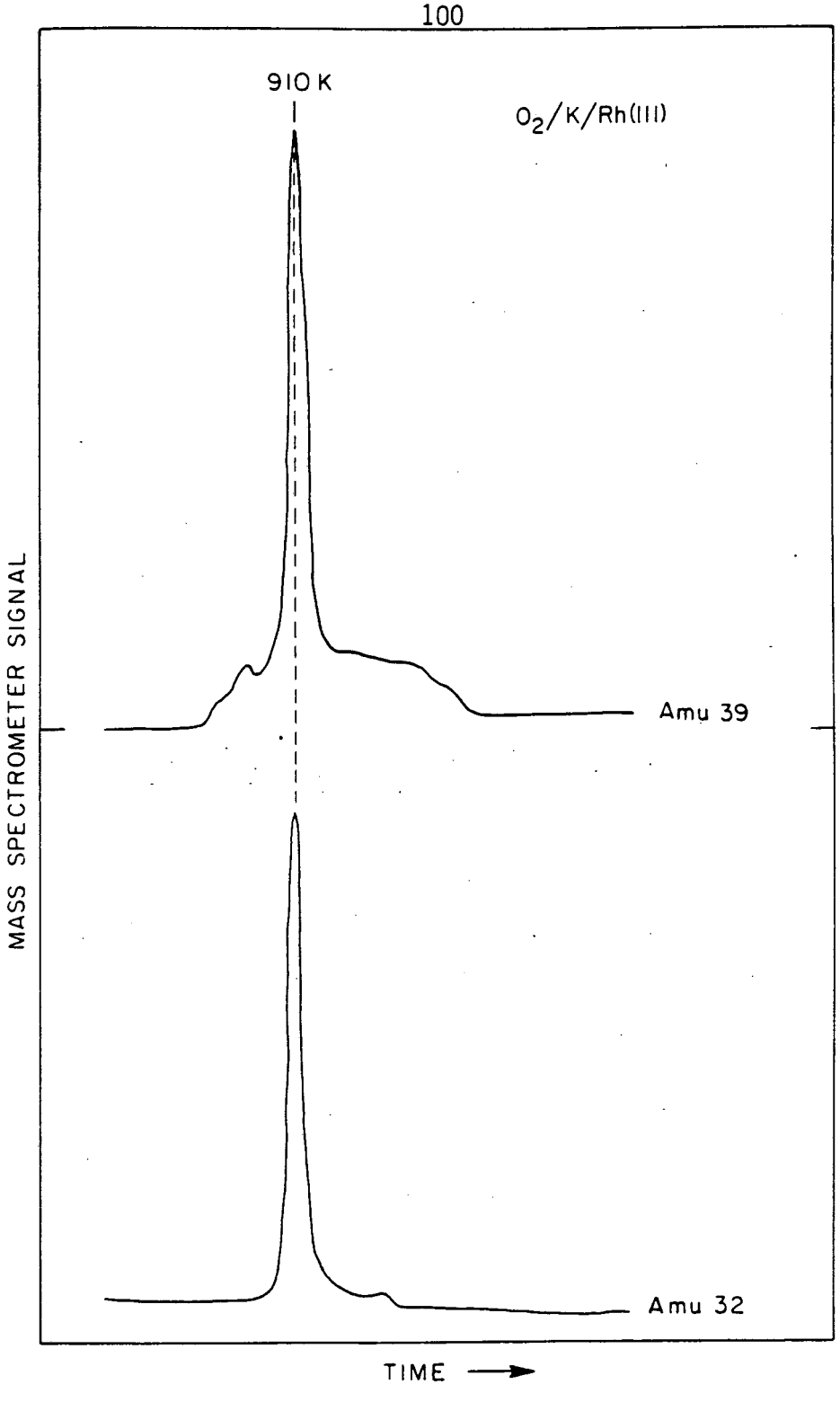
910 K
O_2/K/Rh(111)
Amu 39
Amu 32
MASS SPECTROMETER SIGNAL
TIME
X8L8312-6689

Figure 4.11

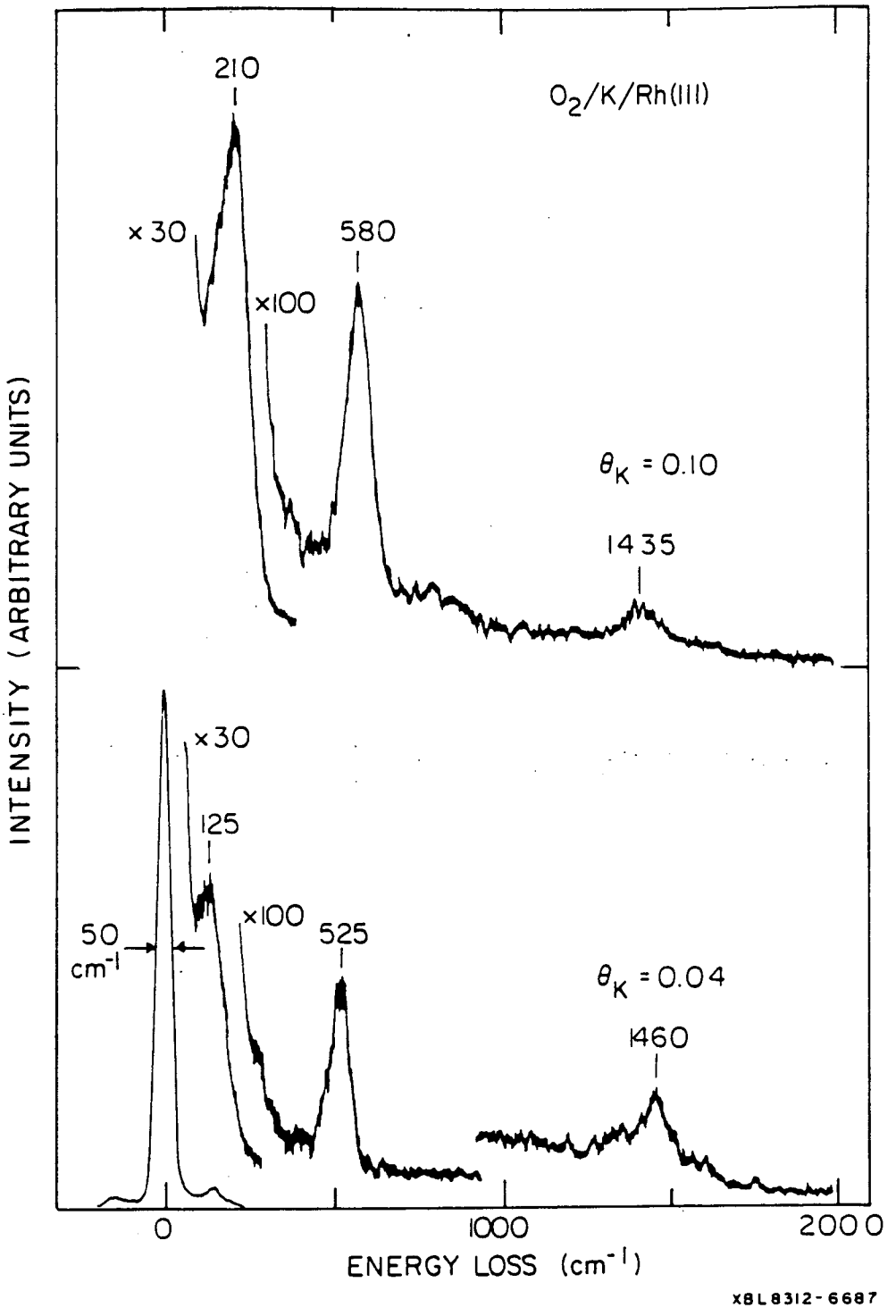
210
O_2/K/Rh(111)
×30
580
×100
θ_K = 0.10
1435
INTENSITY (ARBITRARY UNITS)
×30
125
50
cm⁻¹
×100
525
θ_K = 0.04
1460
0
1000
2000
ENERGY LOSS (cm⁻¹)
XBL8312-6687

Figure 4.12

REFERENCES

1. R. L. Gerlach and T. N. Rhodin, Surface Sci. 17, 32 (1969).
2. J. W. Gadzuk, "Proceedings of NATO Advanced Research Institute, Atomistics of Fracture", Corsica (1981).
3. E. L. Garfunkel, Ph.D. Thesis, University of California, Berkeley, 1983, unpublished.
4. J. E. Crowell, E. L. Garfunkel and G. A. Somorjai, Surface Sci. 121, 303 (1982).
5. A. D. Novaco and J. P. McTague, Phys. Rev. Lett. 38, 1286 (1977).
6. U. Bardi and G. Rovida, "Proceedings of ICSS-4 and ECOSS-3", Cannes (1980).
7. E. L. Garfunkel and G. A. Somorjai, Surface Sci. 115, 441 (1982).
8. S. A. Andersson and U. Jostell, Surface Sci. 46, 625 (1974).
9. J. T. Yates, Jr., P. A. Thiel, and W. H. Weinberg, Surface Sci. 82, 45 (1979).

CHAPTER 5

THE ADSORPTION OF CARBON MONOXIDE ON THE CLEAN AND POTASSIUM DOSED Pt(111) AND Rh(111) CRYSTAL SURFACES

5.1 Overview

The influence of potassium on the chemisorptive properties of CO is daramatic, and is one of the most important and interesting examples of the ability of additives to modify the chemical properties of surfaces. Clearly, transition metal-CO chemistry is of enormous technological importance in catalysis: the Fischer-Tropsch synthesis, hydroformylation reactions, and methanation reactions all involve the catalytic conversion of CO to needed fuels and feedstocks, specifically alcohols and aldehydes, hydrocarbons, and methane. Likewise, the significance of alkalis in catalysis and thermionic emission was noted in the preceding chapter. Since potassium influences the rate and product distribution of these catalytic reactions, an investigation into the chemical interaction of CO and alkalis is of obvious significance.

An understanding of the interaction of CO with potassium dosed surfaces, besides being of consequence in catalysis, can lead to a better description of CO bonding to transition metals. Due to the rich and extensively studied quality of CO-transition metal chemistry [1], improving one's understanding of the nature of the metal-CO interaction is of momentous value to the field of surface chemistry. Since the two

metal surfaces exhibited unique attributes in their chemisorption behavior, they will be discussed separately. A general comparison of the two surfaces will follow in the conclusions (section 5.4).

5.2 CO and K Coadsorption on Pt(111)

5.2.1. Introduction

The use of platinum in various catalytic processes has inspired considerable interest in platinum chemistry, making the CO on platinum adsorption system one of the most widely studied of all in catalysis and surface science. In contrast, the coadsorption of CO with alkalis on platinum or any other transition metal has received very little attention, despite the promoter action of alkalis in the catalytic hydrogenation of carbon monoxide. Dry and coworkers [2] found, using calorimetry, that the heat of adsorption of CO increased 5 kcal/mole on an iron catalyst in the presence of potassium oxide (K_2O). Ten years later, Broden, Gafner and Bonzel [3] found a similar increase in the heat of adsorption of CO with potassium coadsorption on Fe(110). More importantly, they showed that upon heating, the probability of adsorbed CO dissociating increases with increasing potassium coverage. Similarly, Benziger and Madix [4] studied the effect of potassium on the adsorption of CO and H_2 on Fe(100). They showed that potassium increased the binding energy of both CO and H_2, and enhanced CO dissociation. They also performed LCAO (linear combination of atomic orbitals) calculations that suggested that donation of the potassium

4s electron into the iron d-band enhanced the metal electron back-donation into the $2\pi^*$ level of CO, thereby increasing the CO heat of desorption and increasing the dissociation probability. In a study on Ni(100), Kiskinova [5] found that preadsorbed alkalis (Na, K and Cs) increased both the adsorption energy of molecularly adsorbed CO and the fraction of dissociated CO. The dissociation probability was found to increase with increasing alkali coverage, and depended on the alkali itself, in the sequence Na < K < Cs. These four studies on Fe and Ni all found that alkalis cause CO to bond more strongly to the metal surface, and enhance dissociation on these transition metals (which incidentally, already dissociate CO on their own). The effect of potassium on surfaces that do not dissociate CO independently was unexplored at this point, as were the changes induced in the C-O bond itself. Our study of CO and K on Pt(111) using vibrational spectroscopy (HREELS), heat of desorption measurements (TPD), diffraction studies (LEED), and work function changes was aimed at exploring the influence of potassium on molecular CO chemisorption and elucidating the nature of their interaction.

5.2.2. Results and Interpretation

In the previous chapter the chemisorption properties of potassium overlayers and the potassium coverage calibrations have been discussed in detail. On Pt(111), a hexagonal close packed overlayer completely covering the platinum surface forms at a K coverage of 5.5×10^{14} atoms/cm^2, corresponding to a coverage of $\theta_K = 0.36$ (i.e., 0.36

potassium atoms per surface platinum atom corresponds to saturation of the first layer). Detailed here are the properties of CO adsorption on the clean and potassium-dosed Pt(111) surface.

5.2.2a. CO Adsorption on Clean Pt(111)

The adsorption of CO has been extensively studied [6-12]. Representative TPD and HREEL spectra recorded as a function of CO exposure at 300K are shown in Figures 5.1 and 5.2. These spectra agree well with other studies of this system [10-12]. As shown in Fig. 5.1, the desorption of CO from Pt(111) is characterized by a single desorption state whose peak maximum shifts to lower temperature and broadens with increasing coverage. The HREEL spectra in Fig. 5.2 shows vibrational features at 1870 and 2110 cm^{-1}, characteristic of CO bonded carbon end down in a bridged and atop bonding configurations [13]. However, these two binding sites are not resolved in the desorption spectrum (see Fig. 5.1). Norton et al. [8], using dynamic measurement of the surface work function changes with desorption, deconvoluted a similar desorption spectrum for CO on Pt(111) at 298K into bridge, atop and step/defect site components. They determined that the atop species had an ~0.9 kcal/mole higher binding energy than the bridge site. If we assume the recently derived [7] pre-exponential factor of 10^{13} sec^{-1} for CO adsorption on Pt(111) and ignore the small binding site differences, we cab estimate that the heat of adsorption varies from 30-32 kcal/mole at low coverage to 25-27 kcal/mole at saturation coverage at 300K.

The vibrational spectra in Fig. 5.2 show that the atop species is thermally more stable than the bridge species, in agreement with the measurements by Norton et al. Consequently, it was found that the atop site fills first, followed by population of the bridge site. The metal-carbon stretching vibrations (ν_{M-C}) for these two molecular adsorption sites differ by 120 cm^{-1}, occurring at 360 and 480 cm^{-1} for the bridge and atop sites, respectively. The bridge ν_{M-C} mode is only discernible at relatively high coverages. The atop site adsorption frequency decreases with decreasing coverage. This shift is attributed to dipole-dipole coupling between adsorbed molecules as determined by Crossley and King [10] using mixtures of isotopically labelled CO.

Two surface structures were observed for CO adsorption, a diffuse $(\sqrt{3} \times \sqrt{3})R30^\circ$ and a c(4x2) structure. Recent work by Steininger et al. [14] shows that at low temperature the diffuse $(\sqrt{3} \times \sqrt{3})R30^\circ$ structure is really a superposition of two complicated structures resembling this structure. They also show that these structures are associated with CO on atop sites only, while the c(4x2) structure has CO on both atop and bridge sites. We observe a similar vibrational frequency and site occupation dependence here for the two LEED structures seen.

5.2.2b. CO Adsorption on Potassium Dosed Pt(111)

The pre-adsorption of potassium strongly modified the chemisorption properties of CO, as evidenced by the substantial changes in the desorption and vibrational spectra.

The TPD spectra for a saturation CO exposure (10L) of the Pt(111) surface as a function of potassium pre-adsorption is shown in Fig. 5.3. Already at $\theta_K = 0.02$, the CO desorption peak maximum is shifted toward higher temperatures, above the 400K peak maximum observed for the clean surface. As the potassium coverage is increased to $\theta_K = 0.07$, the peak maximum continues to shift to higher temperatures as the desorption broadens substantially toward higher temperatures. By $\theta_K = 0.11$, the desorption peak width (FWHM) is 200K, with desorption continuing beyond 600K. The desorption peak maximum reaches 610K near $\theta_K = 0.18$, but the saturation CO coverage decreases (as measured from the TPD peak area). The CO coverage continues to decrease with further K exposure, as no CO adsorbs onto the potassium multilayers. For $\theta_K = 0.33$ (i.e., 90 percent of saturation of the first layer), very little CO can adsorb. This CO desorbs at 610K exclusively, the same peak maximum observed for a much lower potassium coverage [15]. Assuming a pre-exponential factor of 10^{13} sec^{-1} and first-order desorption kinetics, similar to the clean surface [7], we find that an increase in the desorption rate maximum from 400K to 610K corresponds to an increase in the heat of adsorption from 25 to 36 kcal/mole. No significant irreversible CO dissociation was evident as no carbon or oxygen was found to remain on the surface by AES after heating to 650K.

Vibrational spectra for these overlayers are shown in Fig. 5.4. Here the room temperature HREELS vibrational spectra for saturation coverages ($\geq$10L) of CO are shown as a function of potassium coverage.

Potassium coverages were achieved by depositing a monolayer or more of potassium, then heating the surface to achieve the desired coverage by desorption. The indicated potassium coverages were monitored by both TPD and AES [16].

Figure 5.4 demonstrates the marked effect that even a small addition of potassium has on the CO vibrational spectrum. As seen in this figure, three major changes occur in the spectra as a function of increasing potassium coverage: the relative intensity of the two vibrational states varies continuously, the peak frequency of both sites decreases, and the vibrational features broaden substantially. Specifically, a coverage of $\theta_K = 0.02$ can already increase the intensity of the bridge site relative to the atop site. By $\theta_K = 0.04$, the peak heights are nearly equal. The bridge site loss intensity becomes more than twice that of the atop site at $\theta_K = 0.11$, nearly the inverse of the ratio found for the potassium free surface. We interpret this shift in intensity as a shift in CO occupation from the atop site to the bridge site. This trend continues with increasing potassium coverage until only bridged CO sites are occupied at $\theta_K = 0.22$.

In addition to the change in site occupancy, the vibrational peak frequency for both adsorption sites decreases with increasing potassium coverage. Already by $\theta_K = 0.04$, the bridged CO stretching frequency has decreased by 100 cm^{-1} while the atop site vibration has decreased by 65 cm^{-1}. Gradually, the atop vibration shifts to 2000 cm^{-1} at $\theta_K = 0.11$, substantially lower than the 2120 cm^{-1} potassium free value. The bridge bonded CO species decreases even more dramatically

to 1565 cm^{-1}, although by this coverage (θ_K = 0.22), the saturation CO coverage is about one-half that of the other five spectra, adding to the frequency shift.

Finally, these peaks broaden, especially to the low frequency side, as the potassium coverage increases. This suggests inhomogeneity in the CO overlayer. Also, note that the Pt-C stretching modes are partly obscured due to potassium induced modes of high intensity at frequencies less than 250 cm^{-1} (see chapter 4). However, no vibrations between 500-1000 cm^{-1}, due to Pt-O or K-O vibrations as a result of CO dissociation, were ever observed.

The TPD spectra for various CO exposures on Pt(111) at a constant potassium coverage of θ_K = 0.11 are shown in Fig. 5.5. At low CO exposures ($\leq$ 0.1L), the temperature of the CO desorption peak is centered between 580-600K. As the coverage is increased, the CO desorption peak broadens to lower temperature. After CO exposures $\geq$ 2.0L, the peak width (FWHM) expands to 200K, compared to only 80K for the clean surface. Curiously, the desorption spectra broaden continously and do not indicate two distinct peaks. At higher potassium coverages, the peak maxima begin at 600K at low CO exposures but do not broaden as much since the saturation CO coverage at 300K is less. At lower predosed potassium coverages, the maximum coverage attainable and the general desorption behavior with CO coverage are the same (Fig. 5.5). However, the CO desorption maxima at low exposures gradually shifts to lower temperature with decreasing potassium coverage, as expected from Fig. 5.3. Hence the maximum peak

width (FWHM) continues to decrease from 200 to 80K as θ_K decreases from 0.11 to zero [17,18]. The mechanism responsible for the broad desorption peak will be discussed below.

Figures 5.6 through 5.9 show the comparable changes in the vibrational spectrum as the CO coverage is varied at a constant potassium coverage. All spectra were obtained at 300K. The reported temperatures indicate the temperature at which the crystal was annealed for several seconds prior to recording the spectra. This annealing process is used to vary the CO coverage: the higher the annealing temperature, the lower the CO coverage (the actual coverage was not determined). Since the partial monolayer potassium coverages were obtained by annealing a monolayer of potassium to at least 700K (e.g., annealing to 700K produced $\theta_K \simeq 0.11$), no noticeable potassium desorption was detected during the CO desorption.

In Fig. 5.6 we show the vibrational spectra as the CO coverage is varied for $\theta_K = 0.02$. In the 300K spectrum, both peaks are shifted slightly from the potassium free saturation CO coverage values. The bridged species is most strongly affected, having shifted by 65 cm^{-1} down from 1870 cm^{-1}. As the temperature is increased up to 400K, only slight shifts occur in the vibrational frequency. Between 400 and 425K however, a larger proportion of the CO begins to desorb, mainly from the atop adsorption site. By 425K both the atop and bridged species have the same peak height. On the potassium free Pt(111) surface only the atop species would be present near this temperature. Hence, desorption of CO from the atop site becomes equal

or favored over that of the bridged site for even very small levels of potassium.

At a potassium coverage of θ_K = 0.03, shown in Fig. 5.7, similar trends with CO coverage occur. However, the thermal stability of the bridged site continues to increase. At this potassium coverage, parity of the vibrational peak intensities is achieved at 410K. As the coverage is decreased, the peak height of the atop species continues to decrease faster than that of the bridged site species. But, the peak maximum of the stretching vibration has decreased more substantially for the bridged site than for the atop site (115 cm^{-1} vs. 25 cm^{-1}).

The trend of decreasing stretching frequencies and higher bridge site occupation continues for θ_K = 0.04 (Figure 5.8). In this case, the atop and bridge site peak heights are nearly the same at saturation exposure, certainly so after a small fraction of CO desorbs. The bridged site then dominates at lower coverages as the CO preferentially desorbs from the atop site upon heating. The C-O stretching vibration decreases to a low of 1715 cm^{-1} for the bridge-bonded molecules with no species in atop sites present after heating to 435K. The broad feature near 700 cm^{-1} that dominates after annealing to 450K is likely due to oxygen impurities, possibly caused by diffusion from the near surface region.

Figure 5.9 shows the HREEL spectra for θ_K = 0.11. At this potassium coverage, most of the CO adsorbs in bridge sites. Occupation of the atop site is relatively small and occurs only at near saturation

exposure. By 400K, only a broad, strongly shifted bridge site C-O stretching mode is present. This mode continues to shift to lower frequency as the CO coverage is decreased. Notice that this shift is continuous with increasing temperature, but here the desorption process occurs over a broad temperature range, as evident in the corresponding TPD curves shown in Fig. 5.5. The asymmetric broadening of these modes as the CO coverage decreases suggests some inhomogeneity in the nature of the adsorbed CO. This may indicate that the proximity of the C-O molecules to the potassium atoms affects the vibrational frequency and is heterogeneous, or that additional adsorption sites, such as 3-fold hollows, may be occupied. After further heating, a C-O stretching frequency of 1400 cm^{-1} is observed. No spectra were taken above 525K where further decreases in the stretching frequency might occur. The 1400 cm^{-1} frequency, the weakest CO stretching vibration observed for this adsorption system, is characteristic of a CO molecule with a bond order of 1.2 - 1.5, compared to a bond order of 2.4 for free CO [19]. The data indicates that the presence of potassium considerably weakens the C-O bond without inducing dissociation.

By measuring the cutoff energy of the secondary electron emission (in this case, after excitation of the surface layer with ultraviolet radiation), the work function change can be obtained. As discussed in Chapter 4, the work function of the clean Pt(111) surface decreases by as much as 4 eV upon adsorption of potassium [17]. After adsorption of enough potassium to cause a 4 eV work function decrease, CO was

coadsorbed. The work function was observed to increase by 1.5 eV at saturation CO exposure [18]. Such a work function shift indicates a change in the surface dipole field strength, suggesting charge transfer occurs.

Figure Captions

Fig. 5.1. TPD spectra of CO on Pt(111) as a function of CO exposure. The heating rate was linear at 30 K/s.

Fig. 5.2. HREEL spectra of CO on Pt(111) as a function of CO coverage. The coverage was varied by dosing to saturation and then desorbing CO by heating to the temperature indicated.

Fig. 5.3. Carbon monoxide TPD spectra after saturation CO exposure of a Pt(111) crystal predosed with potassium, as a function of the potassium coverage.

Fig. 5.4. Vibrational spectra for saturation CO exposure at 300K of a Pt(111) crystal predosed with potassium, as a function of potassium coverage.

Fig. 5.5. TPD spectra of CO on Pt(111) predosed with potassium ($\theta_K \sim 0.11$), as a function of CO exposure.

Fig. 5.6. Vibrational spectra of CO chemisorbed on Pt(111) predosed with potassium at $\theta_K = 0.02$, as a function of annealing temperature (i.e., CO coverage).

Fig. 5.7. Vibrational spectra of CO chemisorbed on Pt(111) predosed with potassium at $\theta_K = 0.03$, as a function of annealing temperature (i.e., CO coverage).

Fig. 5.8. Vibrational spectra of CO chemisorbed on Pt(111) predosed with potassium at $\theta_K = 0.04$, as a function of annealing temperature (i.e., CO coverage).

Fig. 5.9. Vibrational spectra of CO chemisorbed on Pt(111) predosed with potassium at $\theta_K = 0.11$, as a function of annealing temperature (i.e., CO coverage).

Fig. 5.10. (a) A schematic of the molecular orbitals believed to interact most strongly when CO bonds to a metal.

(b) A model depicting the enhanced electron density near the surface caused by adsorption of potassium atoms, which induces enhanced electron donation from the substrate to the coadsorbed CO.

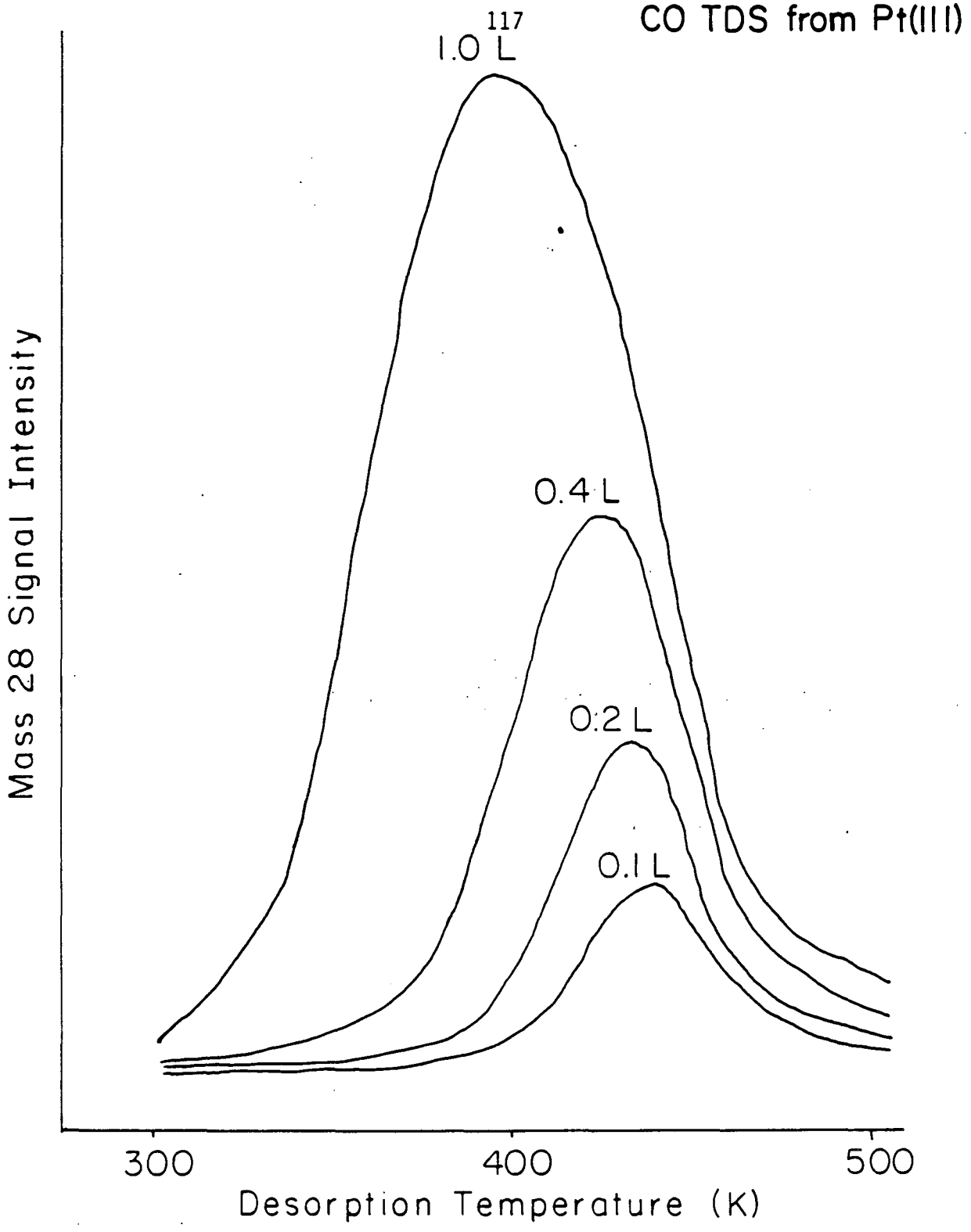

Figure 5.1

XBL 819-6465 A

CO ON Pt(111)

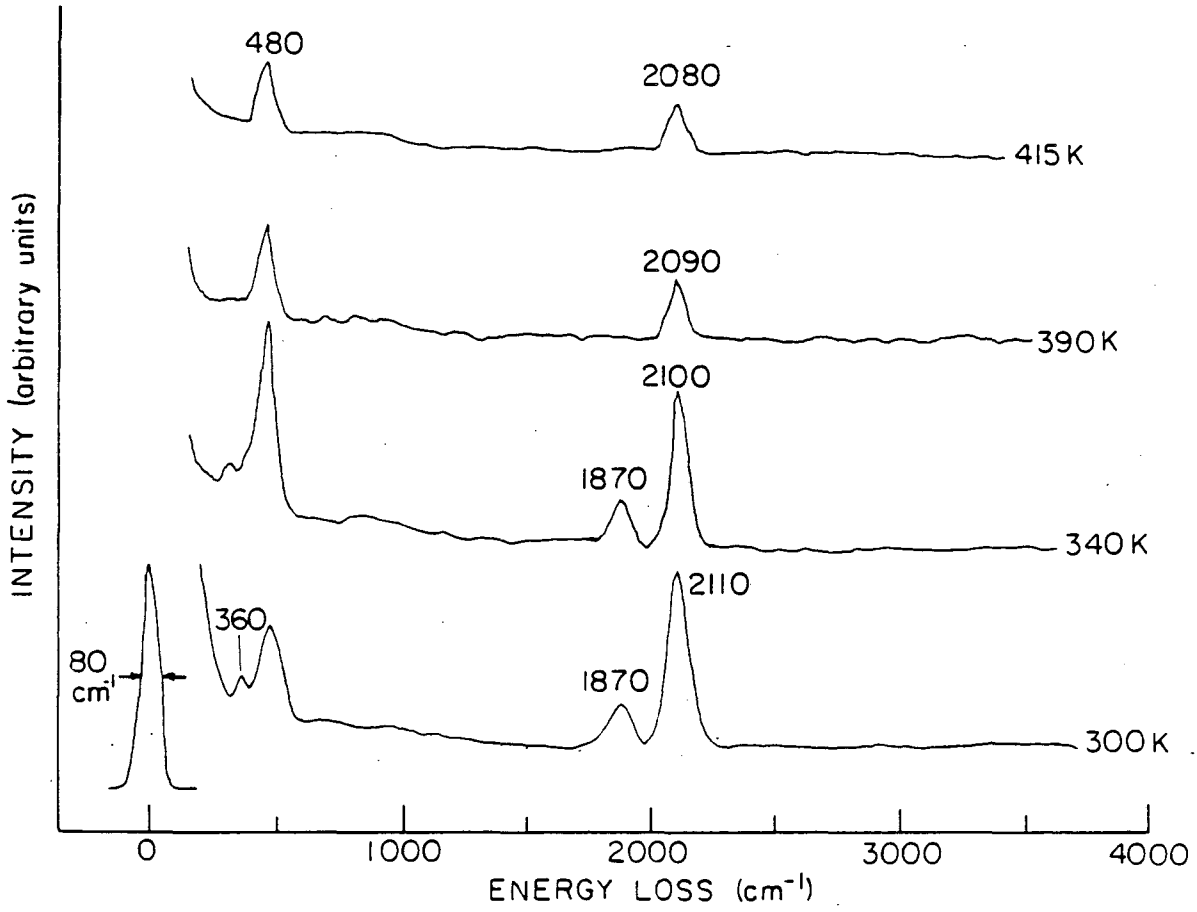

XBL 823-5454

Figure 5.2

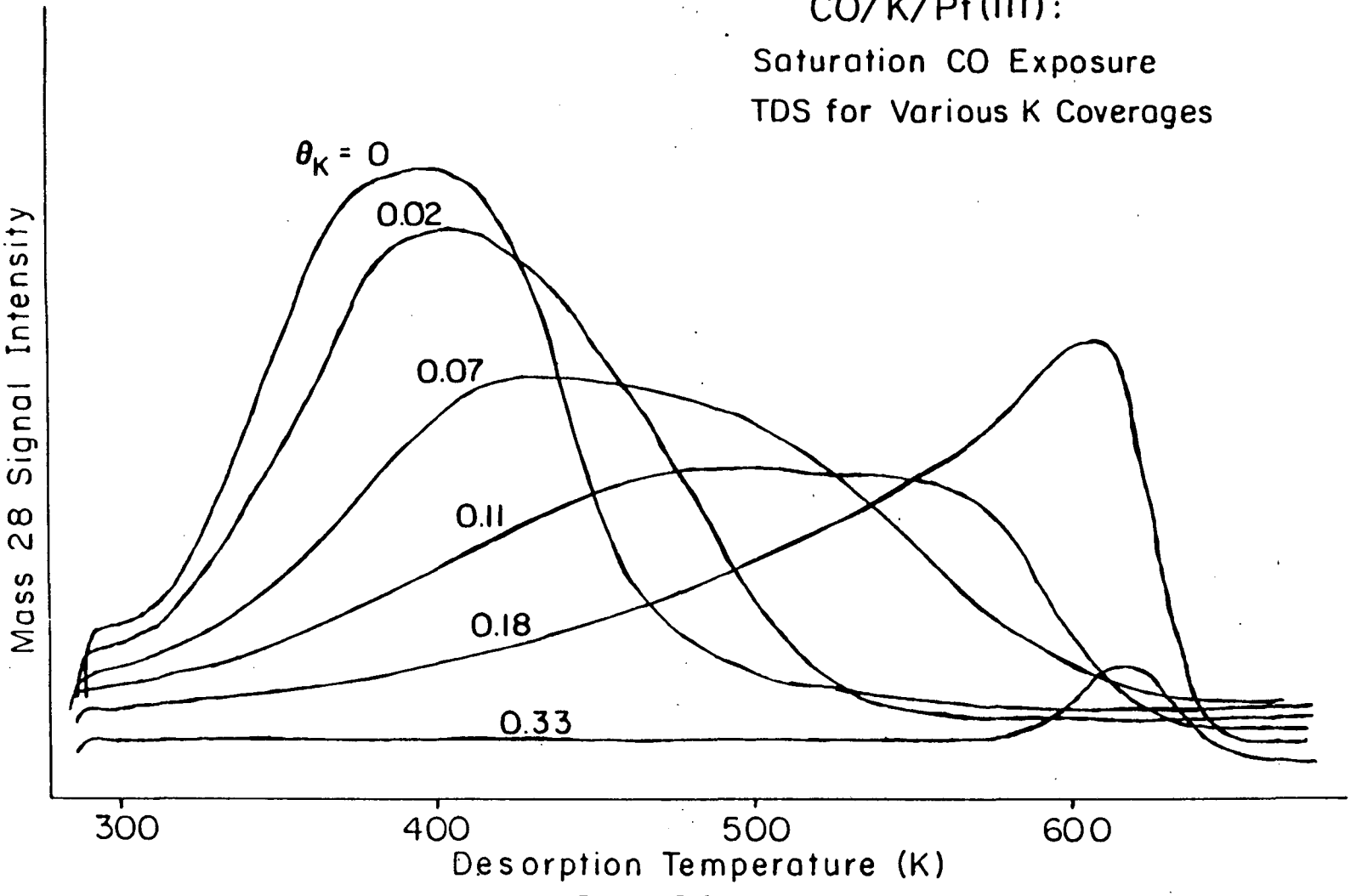

Figure 5.3

XBL 819-6461 C

SATURATION CO COVERAGE (T=300K) ON Pt(111)/K

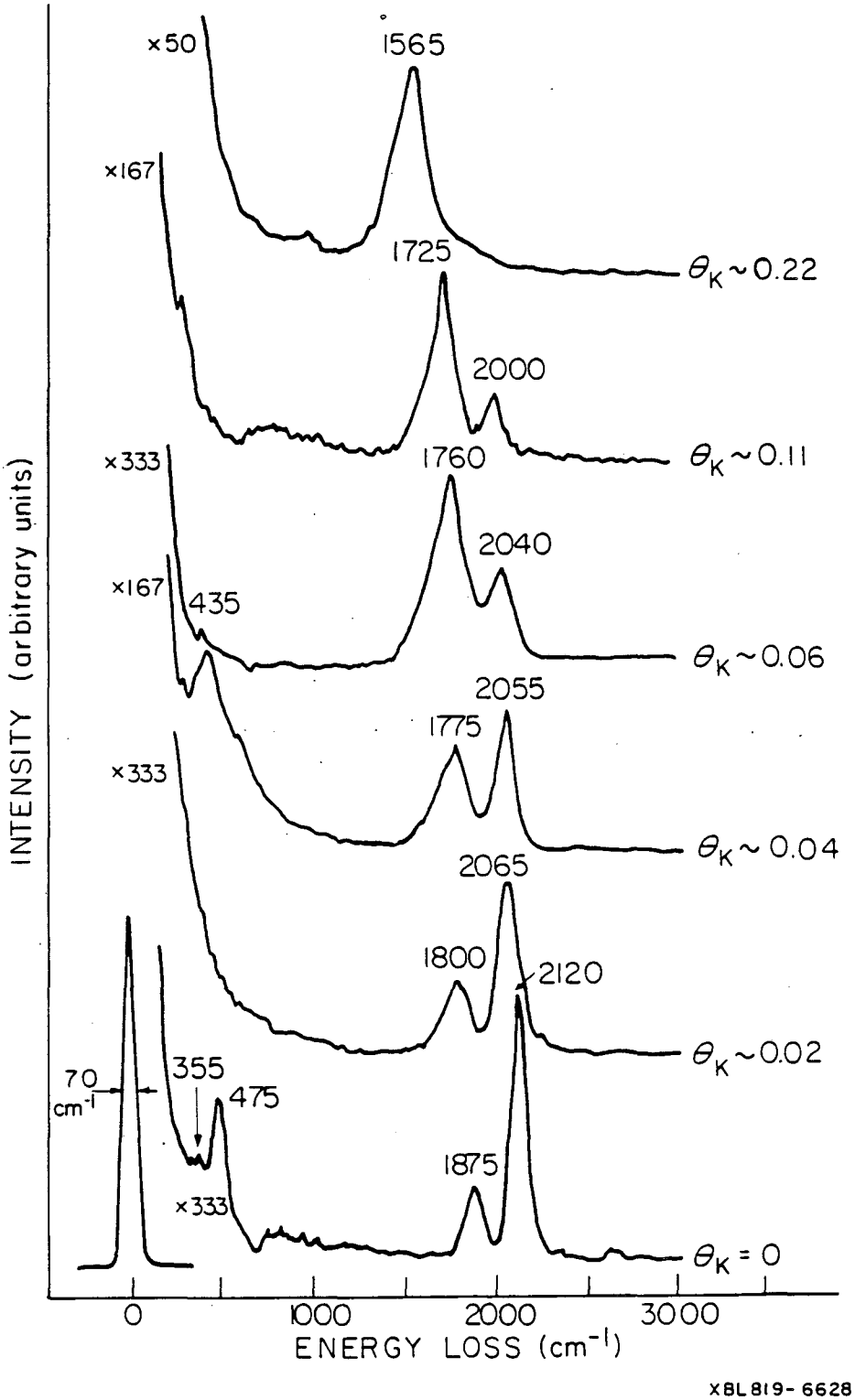

XBL819-6628A

Figure 5.4

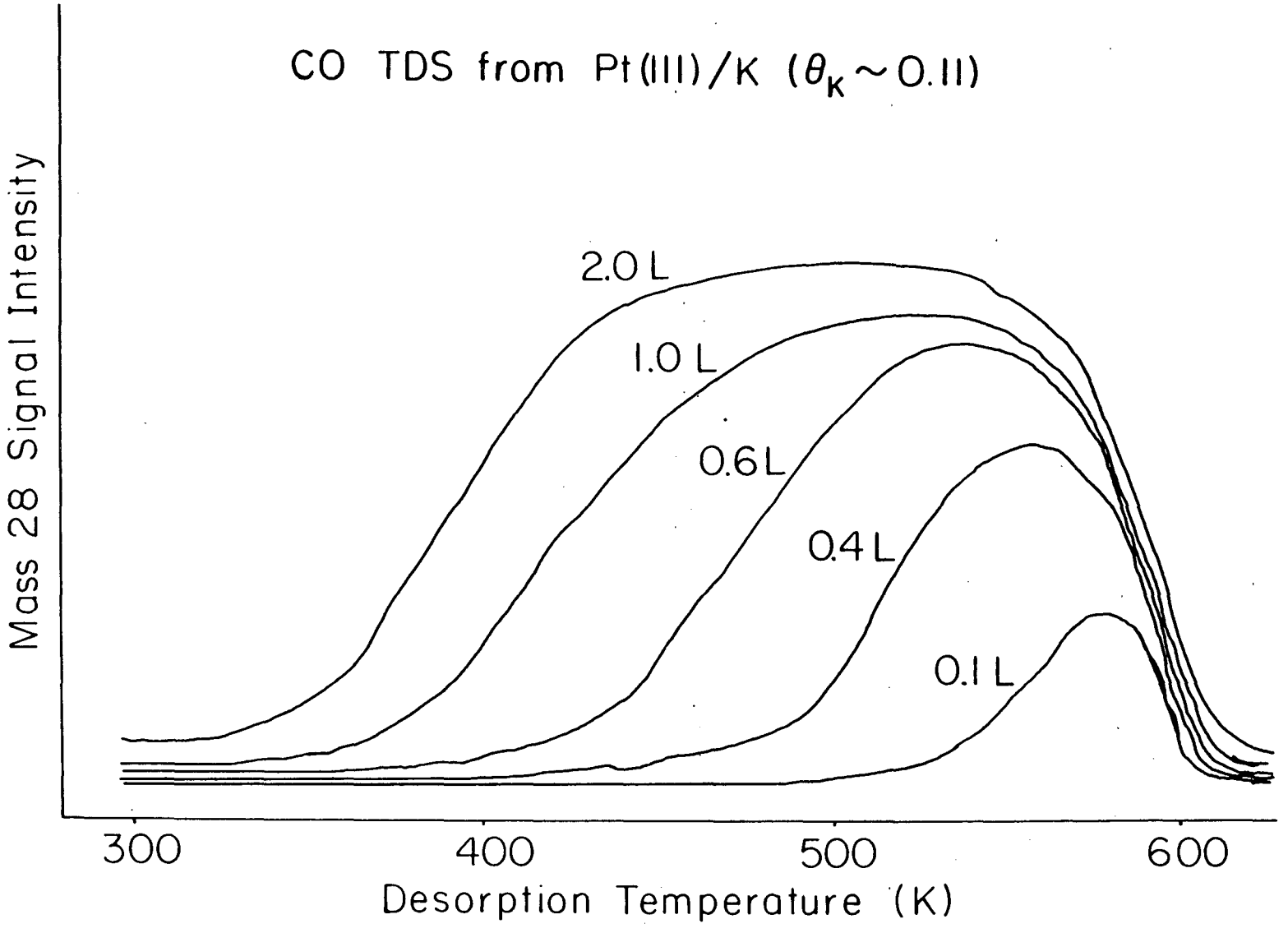

Figure 5.5

XBL819-6462B

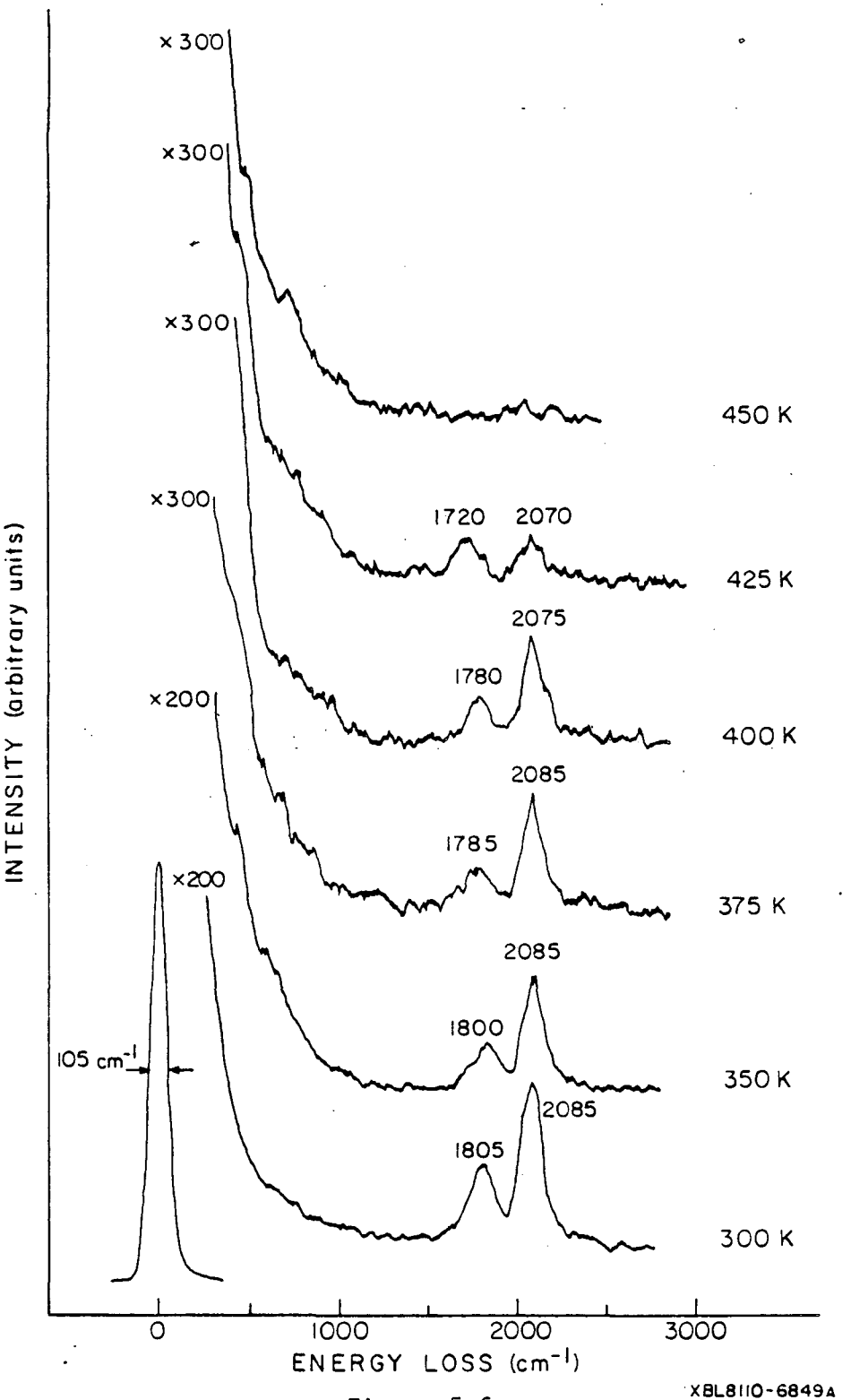
COVERAGE DEPENDENCE OF CO ON Pt(111)/K AT θ_K~0.02
×300
×300
×300
×300
×200
×200
450 K
425 K
400 K
375 K
350 K
300 K
1720
2070
2075
1780
2085
1785
2085
1800
2085
1805
105 cm⁻¹
INTENSITY (arbitrary units)
0
1000
2000
3000
ENERGY LOSS (cm⁻¹)
XBL8110-6849A

Figure 5.6

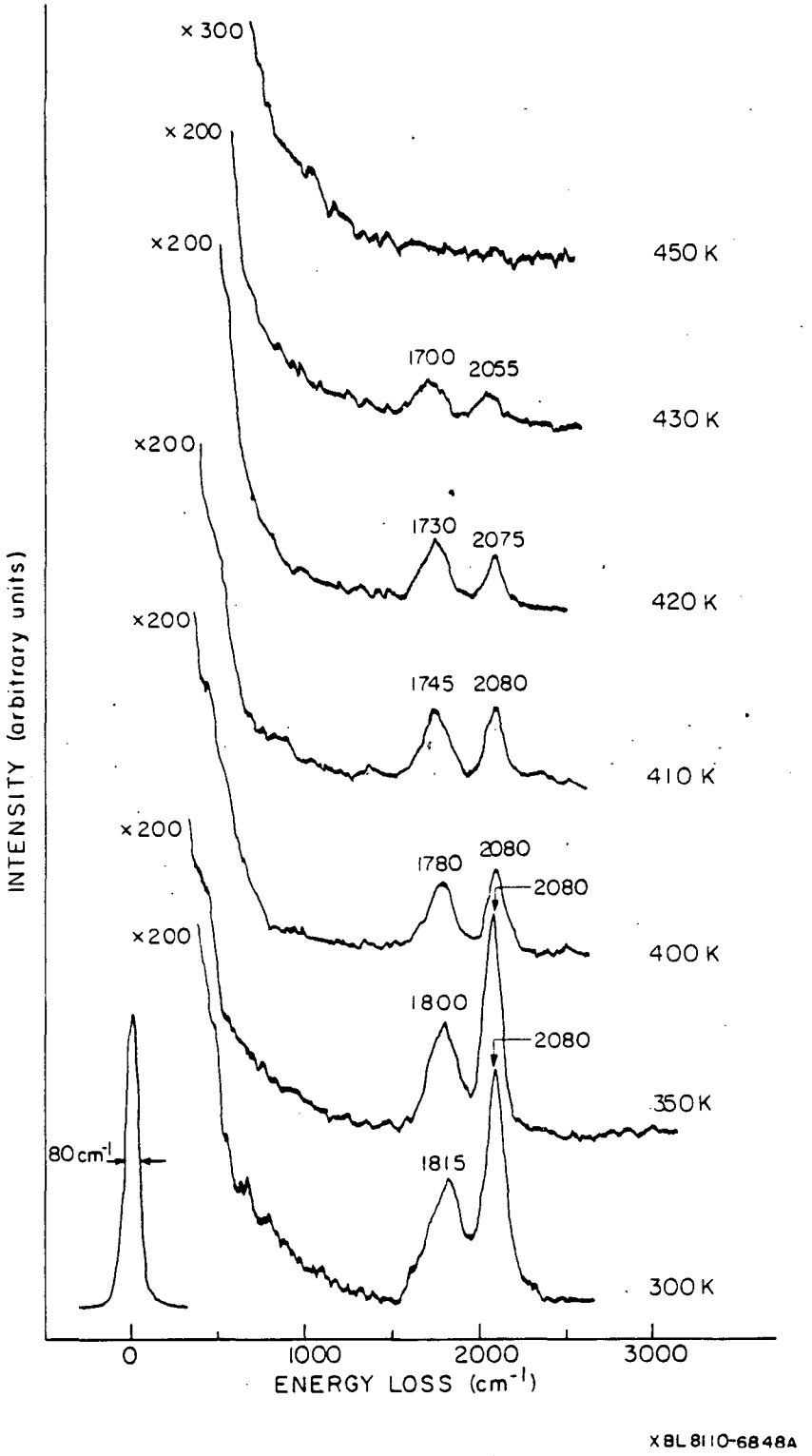
COVERAGE DEPENDENCE OF CO ON Pt(111)/K AT $\theta_K \sim 0.03$
×300
×200
×200
1700
2055
450 K
430 K
×200
1730
2075
420 K
×200
1745
2080
410 K
×200
1780
2080
2080
400 K
×200
1800
2080
350K
80 cm⁻¹
1815
300 K
INTENSITY (arbitrary units)
0
1000
2000
3000
ENERGY LOSS (cm⁻¹)
X8L8110-6848A

Figure 5.7

COVERAGE DEPENDENCE OF CO ON Pt(111)/K AT $\theta_K \sim 0.04$

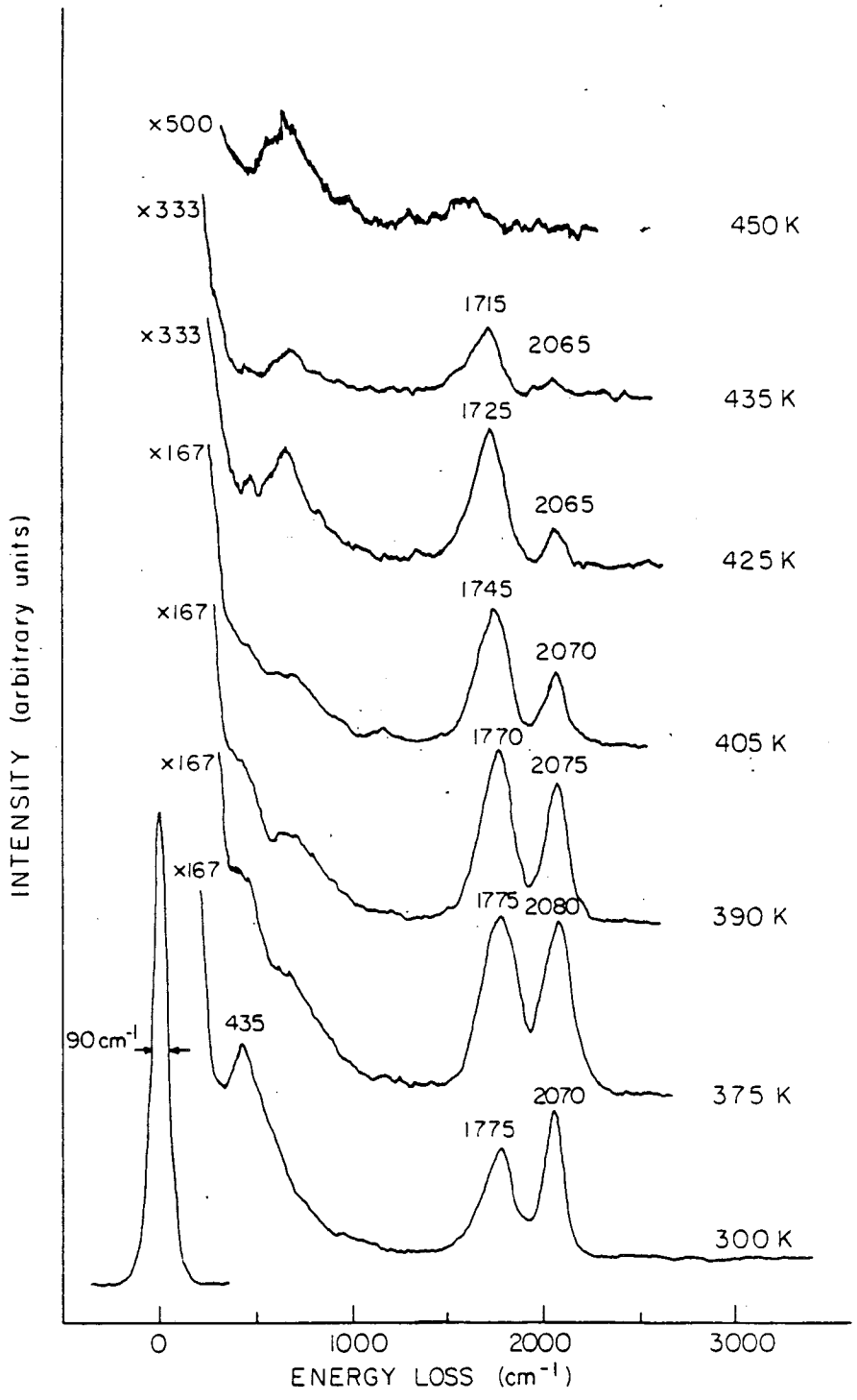

Figure 5.8

XBL 8110-6847A

CO COVERAGE DEPENDENCE ON Pt(111)/K (θ_K~0.11)

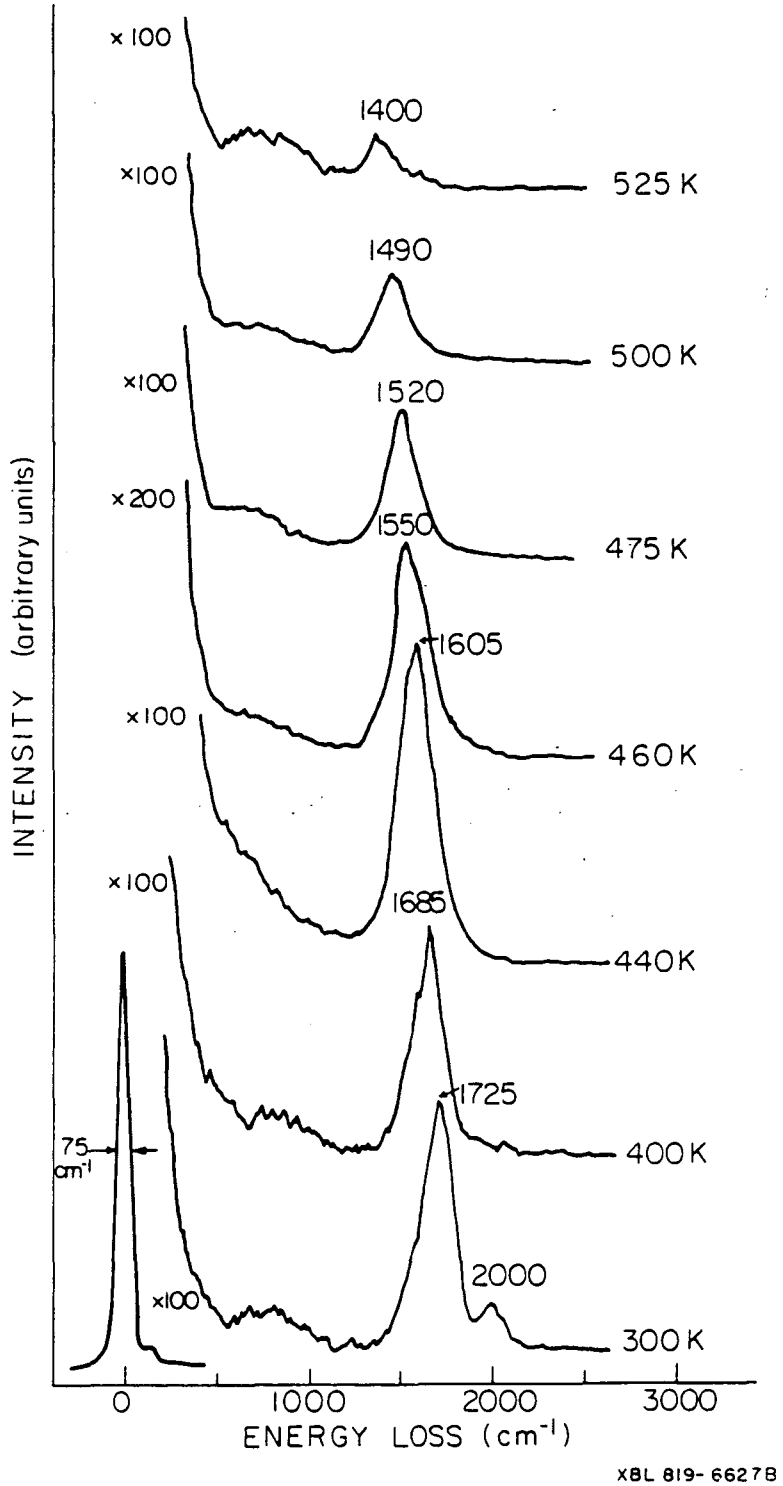

Figure 5.9

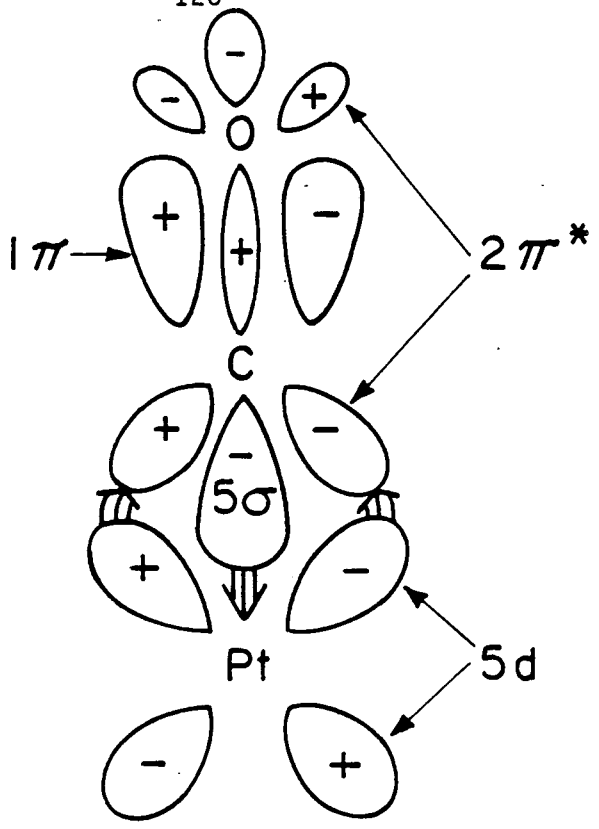

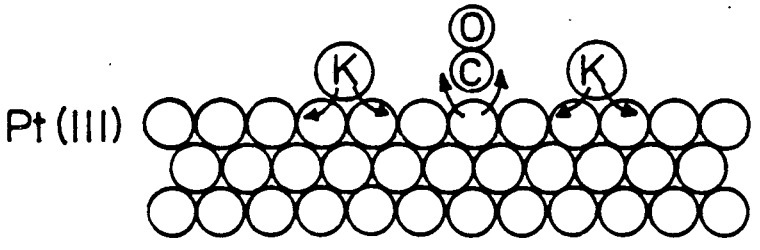

XBL823-8332

Figure 5.10

5.2.3. Discussion

The preadsorption of potassium has marked effects on the adsorption of CO on Pt(111). The major experimental findings can be summarized as follows:

i) The addition of submonolayer amounts of potassium continuously increases the heat of adsorption of CO on Pt(111) from 25 kcal/mole for clean Pt(111) to 36 kcal/mole for potassium coverages nearing completion of the first layer ($\theta_K \sim 0.36$).

ii) Associated with the increase in heat of adsorption is a 310 cm^{-1} decrease in the C-O stretching frequency of the bridge bonded CO molecules from 1870 cm^{-1} on clean Pt(111) to 1560 cm^{-1} with 0.22 monolayers of K coadsorbed.

iii) The CO thermal desorption peak broadens continuously to a maximum of 200K (FWHM) at saturation CO coverages as the potassium coverage is increased.

iv) At a constant potassium coverage, the C-O vibrational frequencies for both atop and bridge adsorption sites decrease substantially with decreasing CO coverage.

v) On the potassium free Pt(111) surface, CO prefers to occupy atop adsorption sites while on the potassium covered surface CO adsorbs preferentially on bridged sites.

vi) The C-O stretching frequencies broaden asymmetrically in the presence of coadsorbed potassium.

vii) The work function of the Pt(111) surface decreases by 4 eV upon the adsorption of 0.12 monolayers of potassium, but increases by 1.5 eV when CO is dosed to saturation at 300K.

By examining the electron acceptor character of CO (i.e., its Lewis acidity) and the changes in charge density at the platinum surface as potassium is adsorbed (i.e., the change in surface basicity upon alkali adsorption), we can understand the bonding changes induced by coadsorbed potassium better.

The bonding of CO to transition metal surfaces is believed to be synergistic with electron donation from the 5σ orbital of CO to partially empty metal orbitals, and simultaneous backdonation of charge from metal orbitals into the empty $2\pi^*$ orbitals of CO. The σ bonding strengthens both the M-C and C-O bonds, while the backdonation strengthens the M-CO interaction but weakens the C-O bonding. This is shown schematically in Fig. 5.10(a). On surfaces, the metal-carbonyl vibrational frequencies and bond energies depend on the crystallographic orientation of the metal (i.e., the site symmetry), the metal work function (a measure of the surface basicity), and the CO coverage [20]. Enhanced backdonation decreases the C-O stretching frequency, increases the M-CO stretching frequency, and strengthens the CO adsorption energy. Additionally, backdonation requires suitably oriented d orbitals on the metal; recent studies indicate that bridge sites have better π orbital overlap with CO, allowing greater backdonation [14,21,22]. Specifically, work function measurements for CO on Pt(111) show an abrupt change from decreasing to increasing work function with initial population of bridge sites in addition to atop sites [14], while calculations suggest $d_M - 2\pi^*_{CO}$ overlap is greater for bridge sites [21,22].

Potassium, a strong electron donor, can change the basicity of the Pt(111) surface, thus inducing changes in the extent of backdonation to adsorbed CO. It is clear that charge is transferred from the potassium to platinum, with electrostatic screening of the resultant positive charge on potassium by metal electrons. This polarization is displayed by the 4 eV drop in work function upon potassium adsorption. Then, upon CO coadsorption, an enhancement (relative to clean platinum) of backdonation into CO occurs as a result of the potassium induced surface charge density changes. This is depicted in Fig. 5.10(b).

The mechanism by which the CO molecules come to have greater electron occupancy of their $2\pi^*$ levels is not well understood. Possibly potassium shifts the molecular CO levels while changing the occupancy of the platinum valence band, allowing greater occupancy of the conjugate $d_{Pt} - 2\pi^*_{CO}$ orbitals. Likewise, one could imagine that this conjugate orbital is fully occupied upon adsorption but the spatial distribution of charge is determined by the surface dipole component of the work function. Hence in the absence of potassium, the work function is large, and the electrons are localized on the platinum atoms. When potassium is adsorbed, the work function decreases, and the electrons become localized on the adsorbed CO molecule, giving the conjugate $d_{Pt} - 2\pi^*_{CO}$ orbital more $2\pi^*_{CO}$ character. Both mechanisms give rise to enhanced backdonation which results in a stronger Pt-C bond and a weaker C-O bond. Both of these are observed experimentally: the CO adsorption energy increases by 11 kcal/mole with potassium coadsorption, and the

C-O vibrational frequency for a saturation CO coverage decreases by 310 cm^{-1} for the bridge adsorption site as the preadsorbed potassium coverage is increased to 0.22 monolayers.

Quite dramatically, both the atop and bridge site vibrational frequencies decrease continuously as the CO coverage is decreased at a constant potassium coverage (viz. Figures 5.6-5.9). A plausible rationale for the gradual, yet large frequency shift with CO coverage is that the adsorbed CO molecules compete for the excess platinum valence electrons provided by the fixed number of potassium adatoms. At low CO coverages, each CO molecule may interact with a larger fraction of the excess electron density, leading to more backdonation per CO molecule. This explanation is also supported by the TPD results observed. At low CO coverages (viz. Fig. 5.5) the adsorption energy of CO is quite strong. As the coverage increases, the desorption broadens up to 200K (FWHM) at saturation exposure for θ_K = 0.11. The adsorption energy of CO varies seemingly over a range of 10 kcal/mole. However, a single vibrational mode is observed, not a collection of modes expanding the entire 325 cm^{-1} range traversed as a function of CO coverage. This is because at any point during the CO desorption process, those CO molecules which remain on the surface become more tightly bound as the electron density per CO increases. Hence, the CO molecules left have a higher desorption temperature, broadening the peak across the full temperature range. As surface electron processes occur quite rapidly ($\sim 10^{-14}$-10^{-15} sec^{-1}), such a response to the surface layer during the desorption process is

quite reasonable. Alternatively, electrostatic interactions between CO and K could enhance electron backdonation between the surface and the CO molecule, and could vary as a function of CO coverage, accounting for the changes observed [21]. Regardless, both rationale suggest backdonation is the prevailing mechanism changing the M-C and C-O bond strengths.

Of course, contributions to this 325 cm^{-1} frequency shift due to dipole-dipole interactions between the adsorbed CO molecules cannot be distinguished from backbonding effects. The decrease observed for clean Pt(111) as the CO coverage varies is 40 cm^{-1} [10]. Hence, although dipole interactions may be important, the dominant contribution accounting for these large frequency shifts with CO coverage is increased backdonation.

The 1.5 eV increase in the work function suggests that suitable sites permitting backdonation are occupied. Several recent studies [14,21,22] suggest bridge sites permit better overlap between the metal and the $2\pi^*$ orbital of CO. The striking change in adsorption site occupation from atop to bridge positions with increasing potassium coverage is expected for this low work function surface.

The occupation of three-fold sites by CO molecules cannot be ruled out for these potassium dosed surfaces at low CO coverages. However, one would expect observation of two sites occupied simultaneously at some CO coverage, giving rise to a very broad band, as seen for CO on Pd(111) [23]. No such evidence for three-fold site occupancy has been observed here.

The question of local versus nonlocal interactions of CO with potassium is difficult to answer. Clearly, very small coverages of potassium strongly perturb the stretching frequency of several CO molecules, many more than just those within one or two interatomic distances of the potassium adatoms. Hence, long range interactions are indicated. However, the vibrational features are broad and asymmetric, suggesting that the local proximity of a CO molecule to the K adatom also affects its vibrational frequency. Thus some evidence for both short and long range interactions exist, but generally, all CO molecules on the surface interact with approximately the same altered substrate. The TPD results support these observations, as only continuous desorption spectra are observed. Furthermore, direct K-CO interactions seem unlikely since (1) no K-O vibrations are observed, and (2) discrete TPD desorption states do not exist.

The delocalization of interaction appears not to occur for other similar systems which have recently been studied. Multiple sites have been shown to exist in thermal desorption and photoelectron spectroscopy studies of CO on alkali covered Ni(100) [5] and Fe(110) [3], N_2 on K covered Fe(111) and Fe(100) [24], and NO on K covered Pt(111) [25]. However, in most of these cases dissociative adsorption occurs first, followed by molecular adsorption on the remaining surface sites. While we find that the adsorption of CO on the potassium covered platinum surface increases the work function, CO was found to decrease the work function of the potassium covered Fe(110)

surface [3]. We believe that this effect in the CO/K/Fe adsorption system is most likely due to the formation of potassium oxide islands after the dissociation of CO. The interpretation of electron backdonation into CO is much more complex in the presence of dissociative adsorption and surface chemical reactions, both of which are absent for the CO/K/Pt adsorption system.

5.3 CO and K Coadsorption on Rh(111)

5.3.1 Introduction

The interaction of CO with transition metals shows empirical trends in both adsorption energy and dissociation behavior [26]. In particular, for a given row, the farther to the left in the periodic table a transition metal lies, the greater is the probability that CO will dissociate on this surface. Furthermore, the borderline or transition from dissociative to molecular adsorption moves to the left as one moves down the periodic table [27]. In the preceding section, we showed that CO chemisorption on Pt(111) is strongly affected by coadsorbed potassium. The binding energy increases dramatically with increasing potassium coverage (as indicated by changes in the CO stretching frequency). Concurrent with these metal-CO bonding changes was a shift in site occupancy of the CO molecules from predominantly single metal atom coordination sites to predominantly multiply coordinated adsorption sites. However, no evidence for CO dissociation was seen. The work reported here involves a similar study of the coadsorption of CO and K on Rh(111) using principally TPD

and HREELS, but also employing LEED, SHG and isotopic scrambling measurements. The rationale for investigating Rh(111) is that this surface does not dissociate CO at low pressures [28], but its position in the periodic table suggests that the nature of CO adsorption on this surface, associative or dissociative, may be extremely sensitive to alkali promotion.

5.3.2 Results and Interpretation

The chemisorption of CO on the clean and potassium pre-dosed Rh(111) crystal surface has been studied in detail. In order to facilitate the presentation and discussion of the most important features, the data has been divided into 3 categories: CO adsorption on clean rhodium, isotopic exchange measurements on the clean and potassium modified surface, and vibrational spectroscopy of CO on the rhodium surface in the presence of potassium.

Similar to that seen on Pt(111), a monolayer of potassium on Rh(111) corresponds to a surface density of 5.8×10^{14} atoms/cm^2, or $\theta_K = 0.36$ potassium atom per surface rhodium atom. Potassium coverage calibrations are discussed in Chapter 4.

5.3.2a CO Adsorption on Clean Rh(111)

The desorption of CO from Rh(111), shown in Fig. 5.11, is characterized by a single desorption peak. The peak maximum decreases as a function of CO exposure from 516K at low exposures to 482K at near-saturation exposures (at a linear heating rate of 15K/s). At

high coverages, a low temperature shoulder develops. This desorption behavior of decreasing desorption temperature and observation of a low temperature shoulder with increasing coverage has been observed previously [29,30] and is believed to be due to repulsive lateral interactions between the CO molecules and population of lower energy binding sites at high coverage. Using the recently derived [29] pre-exponential value of 4×10^{13} sec^{-1}, the low coverage activation energy for desorption is calculated to be 32.0 kcal/mole, in good agreement with the zero coverage limit value of 31.6 kcal/mole [29].

Vibrational spectroscopy using electron energy losses shows that at low exposures only a single C-O stretching vibration with a frequency characteristic of CO adsorption on an atop site is observed. This is shown in Fig. 5.12. Associated with this 2016 cm^{-1} vibration is a low frequency mode at 468 cm^{-1} due to a metal-carbon stretch of this linearly-bonded molecule. Bonding at a bridge site begins to populate at higher exposures with an initial C-O stretching frequency of 1835 cm^{-1}. Both sites continue to populate with increasing exposure, and quickly a new vibration assigned to the metal-carbon stretching mode of the bridge bonded species becomes discernible at 383 cm^{-1}. Note that both C-O stretching vibrations increase in frequency with increasing exposure; this has been shown for a number of systems to be due predominately to dipole-dipole coupling [10]. Similar vibrational spectra for this system have been seen previously [31,32].

Additional vibrational modes can be observed for adsorbed CO if the magnification is increased, as is shown in Fig. 5.13. Three modes can be distinguished with frequencies between that of the Rh-C and the C-O fundamental vibrations, while four modes are visible at frequencies greater that the C-O fundamentals. The lower spectrum has been recorded at a lower resolution (65 cm^{-1}) to enhance the signal to noise ratio. All of these additional vibrations can be assigned to either overtones of fundamentals, combination bands, or multiple losses. The mode at 900 cm^{-1} is assigned to either the double loss or the overtone of the dominant Pt-C stretching vibration at 452 cm^{-1}. It is uncertain which mechanism gives rise to this mode since it is generally difficult to distinguish between the two (i.e. independent multiple scattering events versus multiphonon processes such as overtones or combination bands caused by anharmonicity) when the frequency shift due to anharmonicity is small [14]. The modes at 735 and 815 cm^{-1} are assigned to the overtones of the bending modes for CO molecules adsorbed in bridge and atop sites, respectively. The fundamental of these bending modes or frustrated rotations are expected at 360 and 410 cm^{-1} for the bridge and atop bonded molecules, respectively. These vibrations are dipole forbidden as are the fundamentals for perpendicularly bonded CO molecules, but the first overtones (and any even harmonic) of these modes are totally symmetric and hence dipole allowed in HREELS. The loss at 2490 cm^{-1} is either a double loss or a combination band from ν_{Rh-C} and ν_{CO} (445 + 2065 cm^{-1}), and the 4140 cm^{-1} loss is an overtone of the

fundamental (ν_{CO} at 2065 cm^{-1}) or a double loss of this vibration. The losses at 2300 and 3900 cm^{-1} are multiple excitations of, respectively, the atop site ν_{Rh-C} and the bridge site ν_{CO}, and the two stretching frequencies (ν_{CO}) of CO in atop and bridge sites. Similar vibrational modes have been observed for CO chemisorbed on Pt(111) [33].

A series of ordered superstructures form when CO is adsorbed on Rh(111). Initially a diffuse ring develops which sharpens into a $(\sqrt{3} \times \sqrt{3})R30^\circ$ structure, as shown in Fig. 5.14b. These spots blurr with further exposure and a split (2x2) pattern appears and becomes sharp (see Fig. 5.14c). As the coverage is increased further, the split spots coalesce into the half-order beams of a (2x2) pattern, which develops at saturation. The (2x2) structure, and hence saturation, is not reached at 300K unless the CO pressure is maintained at greater than 4×10^{-5} torr. Alternatively, this coverage can be obtained at <10L exposure, if the sample is less than 140K. Hence, the 300K adsorption temperature used for Fig. 5.11-5.13 resulted in saturation CO coverages ~0.8 θ_{max}. The $(\sqrt{3} \times \sqrt{3})R30^\circ$ is characterized by only atop-bonded CO, while both sites are occupied at higher CO coverages. The $(\sqrt{3} \times \sqrt{3})R30^\circ$ structure corresponds to $\theta_{CO} = 0.33$, and the (2x2) is a coverage of $\theta_{CO} = 0.75$. Van Hove, Koestner, and Somorjai [34,35] have used LEED intensity analysis to calculate the position of the CO molecules for these two structures, their result is shown in Fig. 5.15. For the $(\sqrt{3} \times \sqrt{3})R30^\circ$ structure, one CO molecule per unit cell is present, occupying only

atop sites, as observed here by HREELS. The (2x2) structure has three CO molecules per unit cell with one molecule occupying a bridged site and two molecules in asymmetric near top sites. No vibrational spectra at this coverage have been recorded here; the canted position suggested by the LEED calculations would mean that the 360 and 410 cm^{-1} bending vibrations would be dipole allowed at this coverage.

The changes induced by CO adsorption in the second harmonic intensity is shown in Fig. 5.16 as a function of CO coverage. The second harmonic signal decreases nonlinearly, with a distinct change in slope at $\theta_{CO} \sim 1/3$. Optical second harmonic generation is sensitive to the nonlinear susceptibility of the surface [36]. Furthermore, the delocalized surface electrons of the metal seem responsible for the SHG signal as opposed to charge-transfer resonances or the adsorbate since the second harmonic signal does not depend critically on the incident pulse wavelength (0.53 vs. 1.06 μm), and does exhibit a similar magnitude of intensity variation for either CO or oxygen adsorption. Hence, the second harmonic signal decreases upon CO adsorption since the localization of electrons upon chemisorption decreases the number of delocalized electrons near the surface. The near-linear variation with coverage in the second harmonic signal changes abruptly at the point where bridge site occupation have been shown to begin. This suggests that the nonlinear polarizability of CO bonded to a bridge site is different from an atop site. This curve demonstrates that indeed a change in the number of delocalized surface electrons occurs at $\theta_{CO} \sim 0.33$, suggesting that the localization of charge differs for the two sites.

FIGURE CAPTIONS

Fig. 5.11. TPD spectra of CO on Rh(111) following adsorption near 300K measured as a function of CO exposure. The heating rate used was linear at 15K/sec.

Fig. 5.12. Vibrational spectra obtained using HREELS for CO chemisorbed on Rh(111) at 300K, recorded as a function of CO exposure.

Fig. 5.13. Vibrational spectra obtained after a 10L CO exposure of Rh(111) at 300K, showing additional modes due to fundamental overtones, combination bands and multiple losses.

Fig. 5.14. Diffraction pattern observed using LEED for CO adsorption on Rh(111). The photographs are for (a) the clean Rh(111) substrate, (b) the $(\sqrt{3} \times \sqrt{3})R30^{\circ}$ structure, (c) the split (2x2) overlayer, and (d) the (2x2) structure observed at saturation.

Fig. 5.15. The position of the CO overlayer (filled circles) for the two distinct structures observed. Positions are those determined from LEED intensity analysis (taken from Dubois and Somorjai [31]).

Fig. 5.16. Variation in the second harmonic intensity for CO adsorption on Rh(111), plotted as a function of CO coverage.

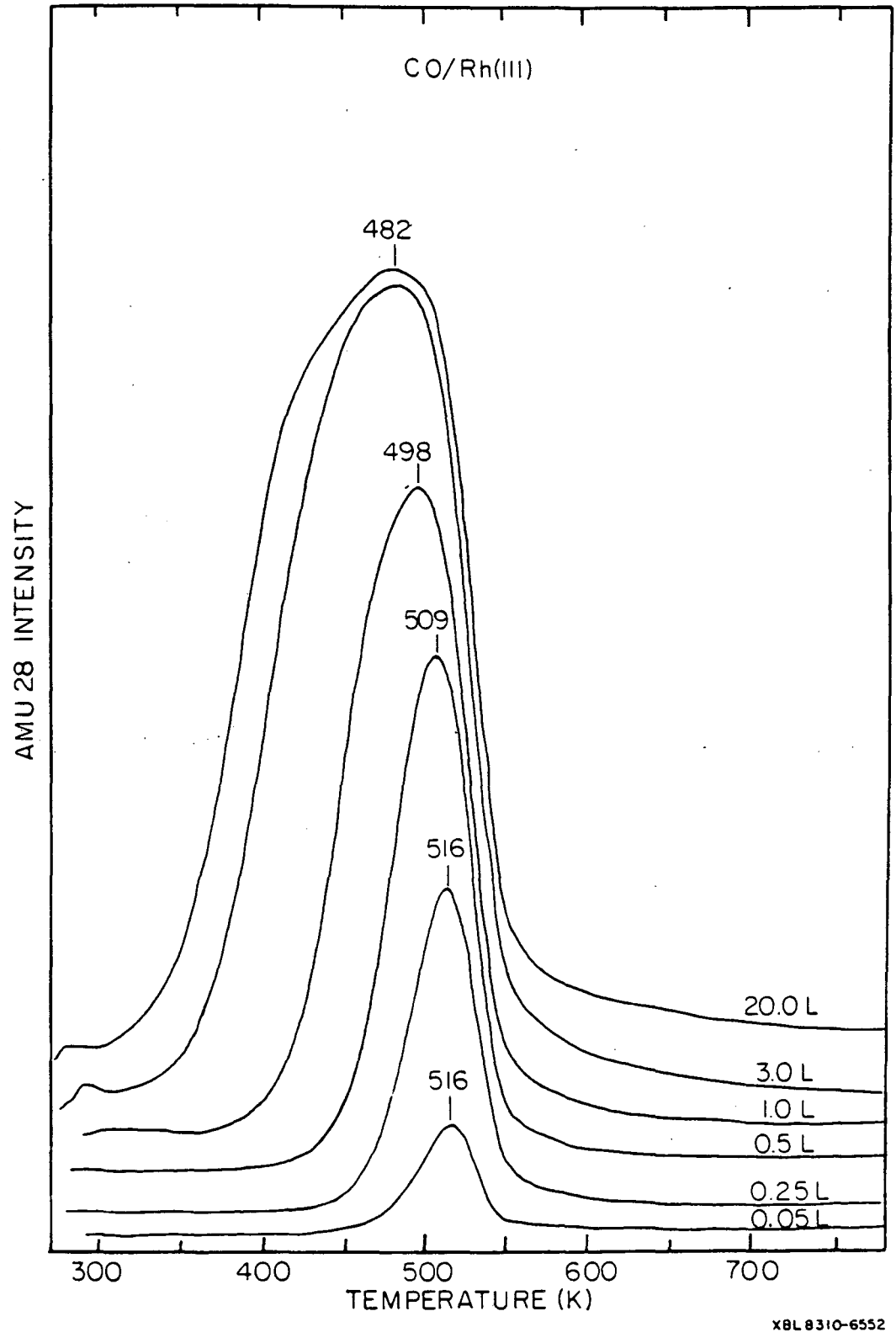
CO/Rh(111)
482
498
509
516
516
20.0 L
3.0 L
1.0 L
0.5 L
0.25 L
0.05 L
AMU 28 INTENSITY
300
400
500
600
700
TEMPERATURE (K)
XBL 8310-6552

Figure 5.11

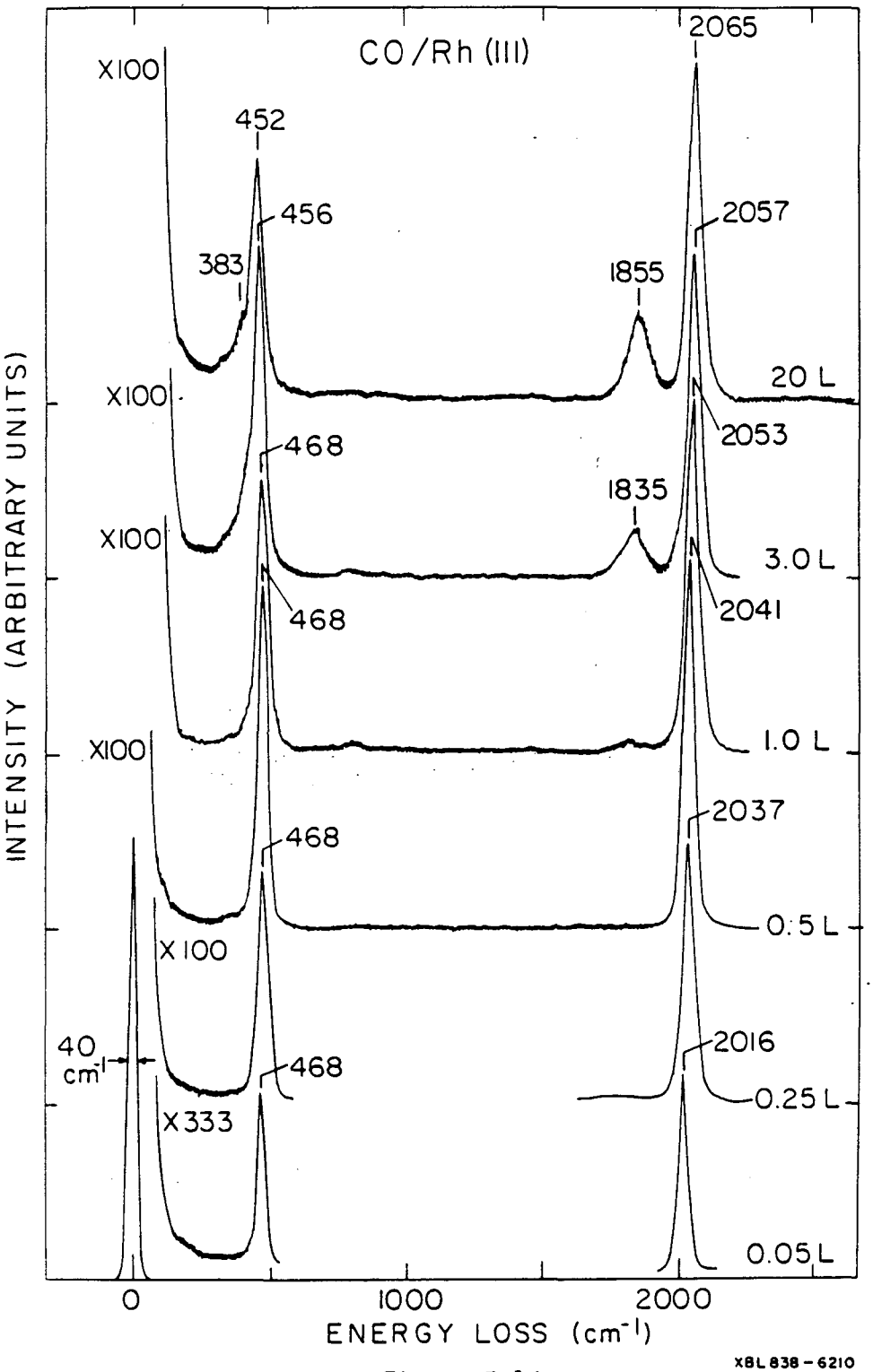
CO/Rh (111)
X100
452
456
383
2065
2057
1855
20 L
X100
468
2053
1835
3.0 L
X100
468
2041
1.0 L
X100
468
2037
0.5 L
X 100
40 cm⁻¹
468
2016
X333
0.25 L
0.05 L
INTENSITY (ARBITRARY UNITS)
0
1000
2000
ENERGY LOSS (cm⁻¹)
XBL 838-6210

Figure 5.12

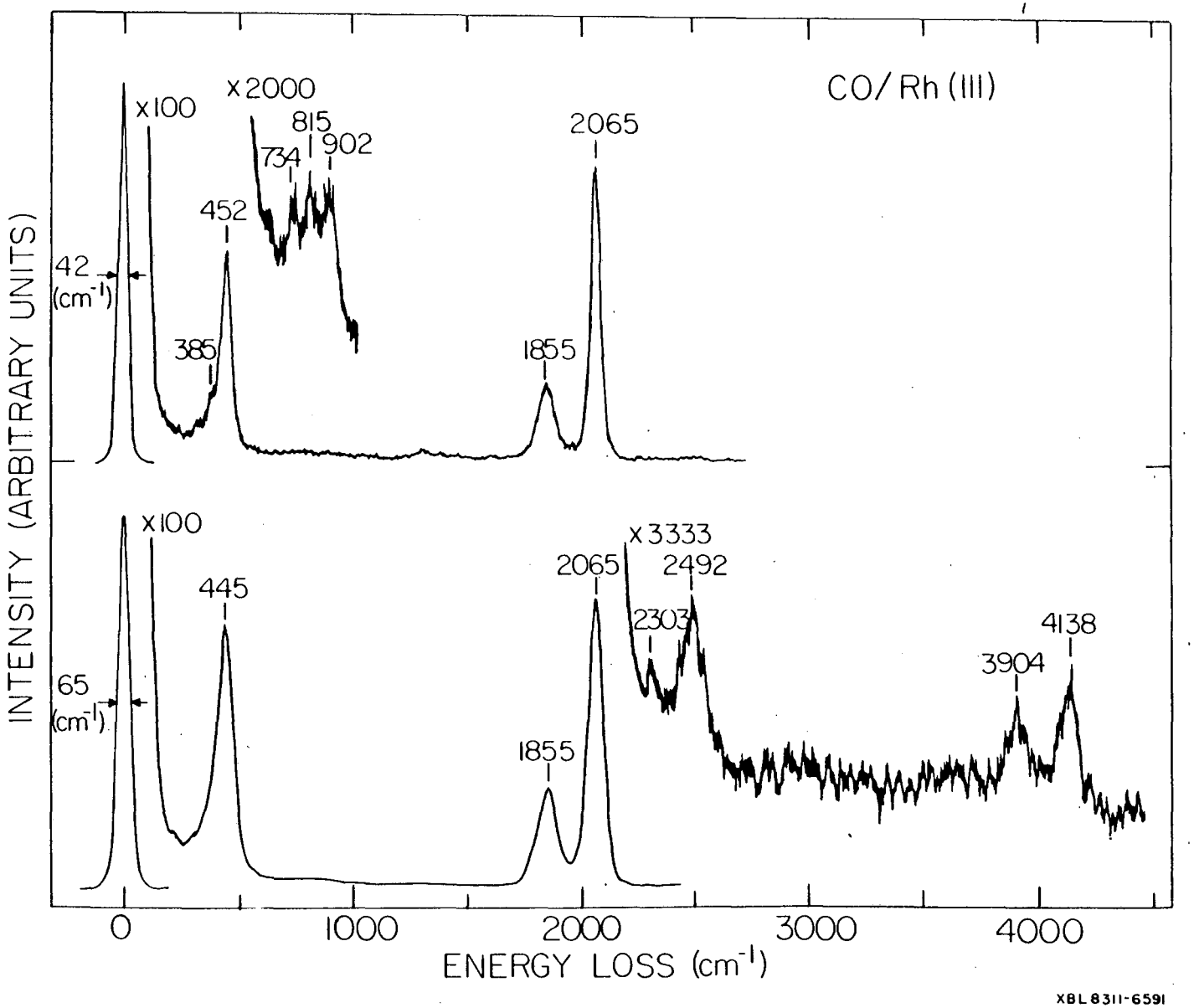
CO/Rh (111)
x100
x2000
815
902
734
2065
452
42
(cm⁻¹)
385
1855
x100
x3333
2065
2492
445
2303
4138
3904
65
(cm⁻¹)
1855
INTENSITY (ARBITRARY UNITS)
0
1000
2000
3000
4000
ENERGY LOSS (cm⁻¹)
XBL8311-6591

Figure 5.13

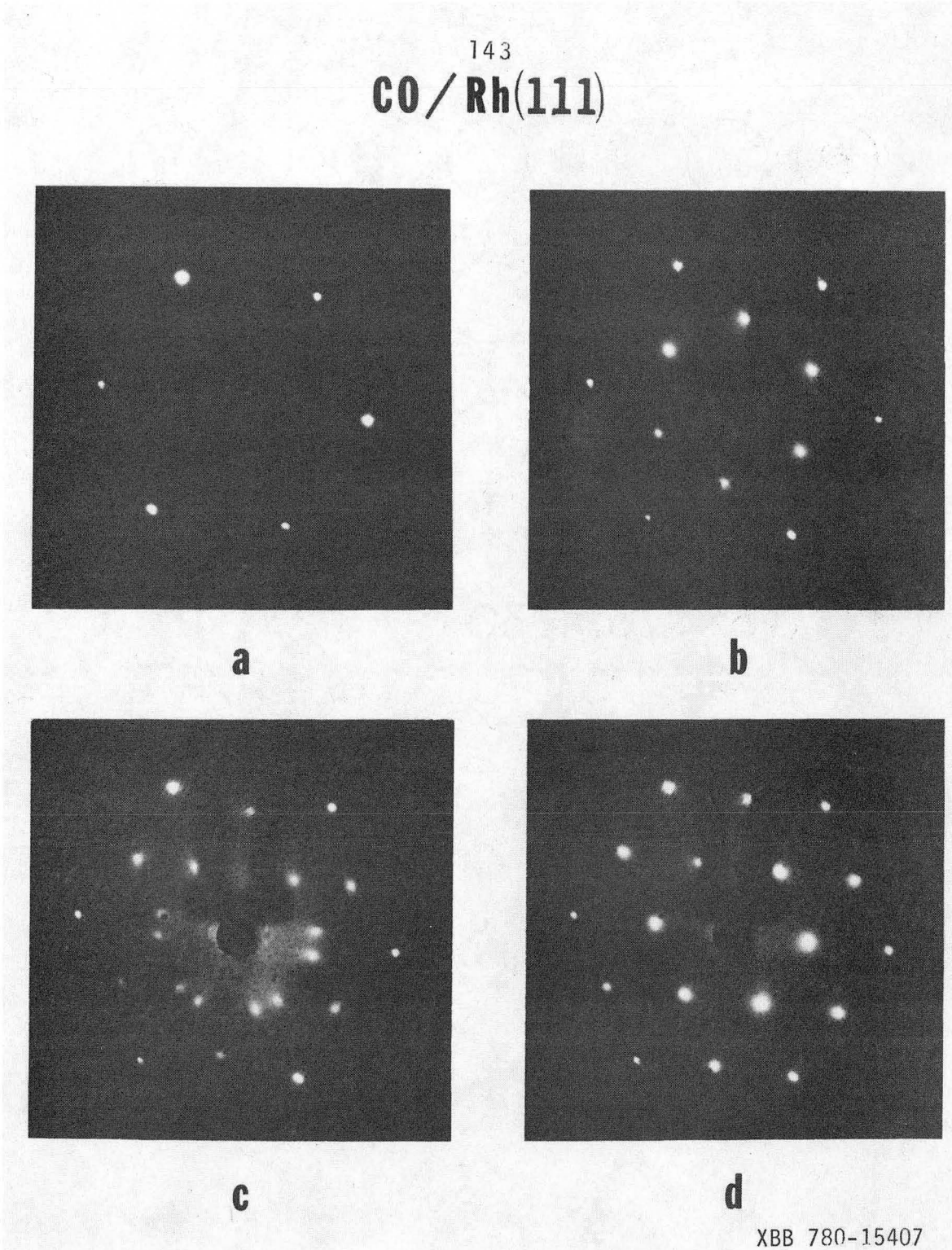

Figure 5.14

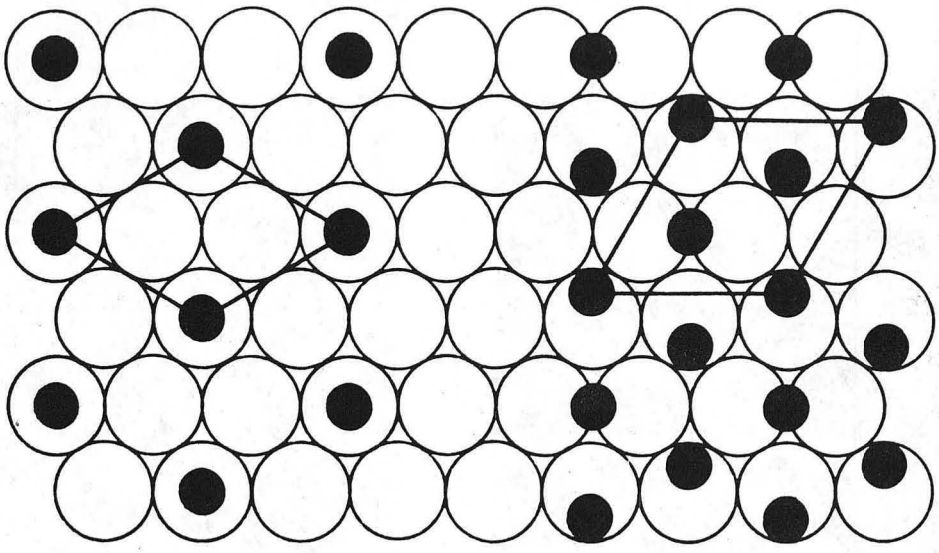

Figure 5.15

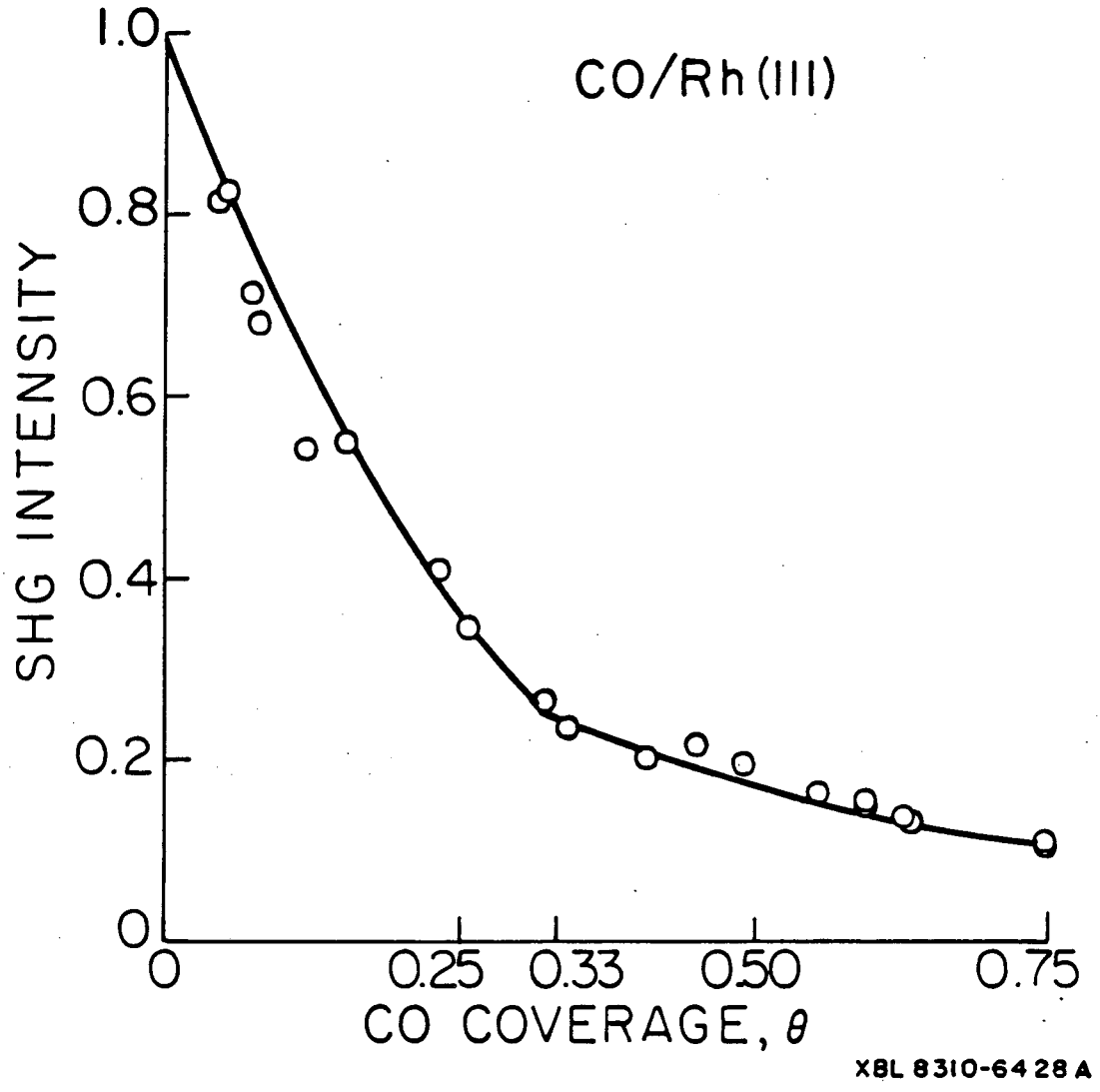
CO/Rh(111)
SHG INTENSITY
1.0
0.8
0.6
0.4
0.2
0
0
0.25
0.33
0.50
0.75
CO COVERAGE, θ
XBL 8310-6428A

Figure 5.16

5.3.2b CO ISOTOPIC MIXING MEASUREMENTS ON CLEAN AND POTASSIUM DOSED Rh(111)

When CO is adsorbed onto a potassium predosed Rh(111) surface, dramatic changes in the CO TPD spectra occur. In Fig. 5.17 representative TPD spectra are shown for saturation CO exposure on Rh(111) at 300K as a function of predosed potassium coverage. In these experiments the back face of the crystal was masked by adsorbing multilayers of potassium prior to CO exposure; CO does not adsorb on pure potassium multilayers (see Chapter 4). When the Rh(111) surface is predosed with small amounts of potassium ($\theta_K < 0.10$), the CO desorption spectra only broaden to higher temperature. The degree of broadening is dependent on the potassium coverage. Once a critical potassium coverage is reached ($\theta_K \approx 0.10$), two new desorption states at 630 and 700K become populated. These new states are present in addition to the broadened lower temperature state such that CO desorbs continuosuly from 325 to 725K at this potassium coverage. New states at 630 and 700K continue to grow in intensity with increasing potassium coverage as the lower temprature state(s) dramatically decrease in intensity. At potassium coverages near saturation (e.g. see $\theta_K = 0.33$ in Fig. 5.17), only desorption from the 700K state occurs. This state decreases further with increasing potassium coverage. No CO desorption is seen for this exposure (10L) at $\theta_K \geq 0.36$.

As discussed in the previous section, CO adsorption on clean Rh(111) is molecular. Yates and coworkers [28] have shown that below

800K, CO does not dissociate on the clean Rh(111) surface at low pressures ($\leq 2 \times 10^{-6}$ torr CO). Hence, the low temperature desorption peak is clearly due to first order molecular desorption. In order to elucidate the nature of the high temperature desorption states observed at large potassium coverages, and we have recently adsorbed isotopically labelled CO and followed any isotopic mixing that occurs as a function of CO exposure, potassium coverage, heating rate [37]. In this experiment, a mixture of $^{13}C^{16}O$ and $^{12}C^{18}O$ is adsorbed on the potassium dosed Rh(111) surface at 140K. The desorption of several species, including all possible CO isotopes (i.e., amu 28, 29, 30 and 31) are followed as the sample is heated linearly. If CO does dissociate on the potassium dosed surface, we expect scrambling of the isotopes to occur, according to the reaction

$$^{13}C^{16}O + {}^{12}C^{18}O \longrightarrow {}^{13}C^{18}O + {}^{12}C^{16}O.$$

Hence, in addition to the isotopes adsorbed, two new species can be produced. Figure 5.18 shows typical desorption spectra observed after adsorption of a mixture of $^{13}C^{16}O$ and $^{12}C^{18}O$ onto a Rh(111) surface predosed with potassium. Here the back face was not masked (cf. Fig. 5.17) to demonstrate the changes seen with preadsorbed potassium. For potassium coverages large enough so that the 630 and 700K states are populated ($0.10 \leq \theta_K \leq 0.30$), we observe enhanced desorption of the mixed products $^{13}C^{18}O$ and $^{12}C^{16}O$ from these states. This does not occur for the lower temperature states, nor

does it occur for the clean surface or for low coverages of potassium. Since the 31 amu and the 28 amu spectra contain the same scrambling information, desorption spectra for both should be identical. However, as the major contaminant in the vacuum chamber is $^{12}C^{16}O$, background and support effects are largest for this amu. Consequently amu 28 desorption has been omitted for clarity. Notice that some desorption at 31 amu occurs near 500K, the state due to desorption of CO from the clean surface. This is due to a small fraction of $^{13}C^{18}O$ in the adsorption mixture. The ratio of desorption yield from the 630 and 700K state versus the 500K state is clearly greater than one for amu 31, whereas this ratio is less than one for the isotopes adsorbed (e.g. $^{13}C^{16}O$ and $^{12}C^{18}O$).

On the right side of Fig. 5.18 we see desorption spectra at $\theta_K = 0.32$. When the potassium coverage is between 0.30 and 0.36, desorption only occurs from the 700K state. The 500K state is due solely to the backface. We see that considerable scrambling occurs from this state. The scrambling is not complete (i.e., statistically, equal quantities of each isotope should be observed for total scrambling of an equimolar adsorption mixture, if total mobility on the surface is assumed). This implies that the mobility of the adatoms is small such that they have a higher probability of recombining with the atom to which they were originally attached. Reasons for the reduced mobility will be discussed below.

When the higher temperature states become populated in the CO TPD spectra, significant changes also occur in the potassium desorption

behavior. Potassium TPD on Rh(111) has been discussed in Chapter 4 and compared to other surfaces. Briefly, it is characterized by a desorption maximum near 1100K at low coverages ($\theta_K < 0.20$). The maximum desorption rate shifts rapidly to lower temperature with increasing coverages and peaks at 500K at the completion of the first monolayer. The second layer desorption maximum then begins growing in at 350K. When CO is coadsorbed with small potassium coverages, this desorption behavior is unchanged as all the CO desorbs prior to any potassium desorption. However, once a critical potassium coverage is obtained such that the two high temperature CO desorption states are present, no potassium desorbs until 700K. This is in contrast to potassium desorption without coadsorbates, where desorption at much lower temperature occurs. Curiously, for larger potassium coverages, all the additional desorption intensity grows in sharply into this narrow desorption state near 700K. Figure 5.19 shows a typical desorption spectrum observed in this potassium coverage range. the desorption maximum is identical to that of the highest CO desorption state, and suggests that potassium and either carbon or oxygen are associated with one another. This surface complex decomposes then, giving rise to the autocatalytic desorption. The surface complex is likely K_xO_y, possibly K_2O although none of these species (KO, K_2O or KO_2) were observed to desorb using the mass spectrometer.

The near simultaneous desorption of these species can also be followed using second harmonic generation. In this case however, sodium was the alkali used. Isotopic scrambling experiments on sodium

predosed Rh(111) are very similar to that of potassium on this surface. Figure 5.20 shows the variation in the SHG signal for exposure of CO to sodium predosed Rh(111), and the subsequent desorption of both species. The SHG signal shows that upon desorption, the alkali and CO species desorb at similar temperatures, although CO seems to desorb completely prior to alkali desorption. In contrast to the adsorption of CO on clean Rh(111), the initial slope of the adsorption curve for the sodium predosed surface is zero. The data shows that sodium modifies the adsorption properties of CO at low coverages, possibly by keeping the near surface free electron density constant by becoming more ionized as CO is adsorbed.

Let us turn our attention back to the changes in the alkali TPD spectrum with coverage and post adsorption of CO. Figure 5.19 shows behavior that must obviously depend on the ratio of alkali and CO atoms on the surface. For K on Rh(111) at near saturation of the first layer of potassium, much less CO can be adsorbed so desorption maxima at both 500K (i.e. clean surface behavior) and 700K (i.e. coadsorbed CO behavior) are observed in the potassium TPD spectrum. Similar behavior has been seen with coadsorbed oxygen, both on Rh(111) and Pt(111) [16]. These results suggest a strong interaction at higher coverages between potassium and certain coadsorbates.

The major conclusion from the isotopic mixing reaction study is that the higher temperature desorption states, only present at relatively high potassium coverages, are due to recombination of carbon and oxygen atoms on the surface, produced from the dissociation of adsorbed CO.

FIGURE CATPIONS

Fig. 5.17. TPD spectra of CO following saturation adsorption at 300K on a Rh(111) surface predosed with the potassium coverage specified. The heating rate used was linear at 15K/sec. A coverage of θ_K = 0.36 potassium atom per surface rhodium atom corresponds to a surface density of 5.8×10^{14} atoms/cm^2.

Fig. 5.18. TPD spectra at amu 29, 30 and 31 following exposure of potassium dosed surfaces to a nearly equal mixture of $^{13}C^{16}O$ and $^{12}C^{18}O$.

Fig. 5.19. TPD spectrum for potassium desorption from Rh(111) after saturation adsorption of CO.

Fig. 5.20. Variation in the second harmonic signal during (a) CO exposure of a sodium predosed Rh(111) sample, and (b) desorption of both CO and Na upon heating the layer in (a) after a 15L CO exposure.

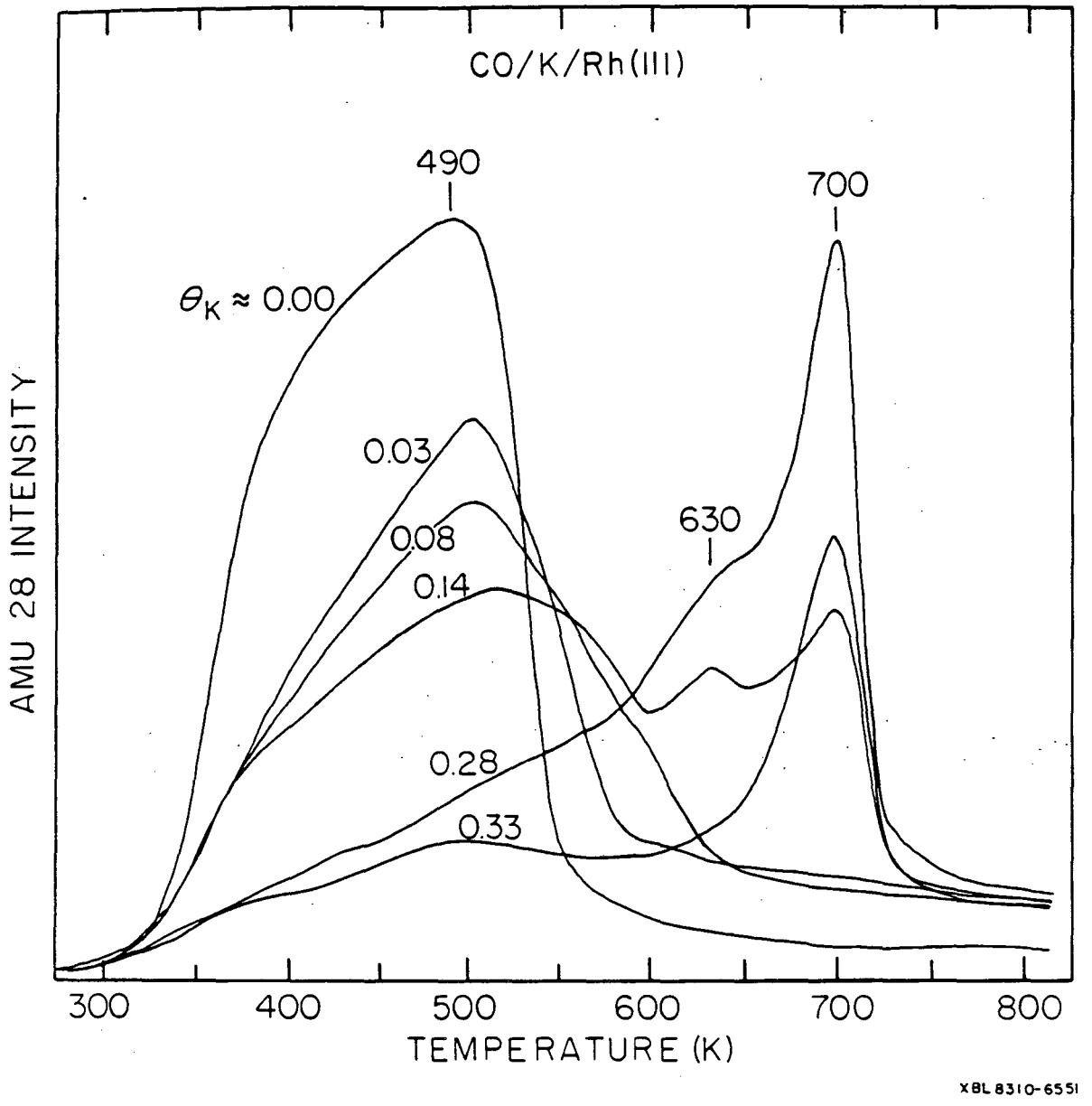
CO/K/Rh(111)
490
700
$\theta_K \approx 0.00$
0.03
0.08
630
0.14
0.28
0.33
AMU 28 INTENSITY
300
400
500
600
700
800
TEMPERATURE (K)
XBL 8310-6551

Figure 5.17

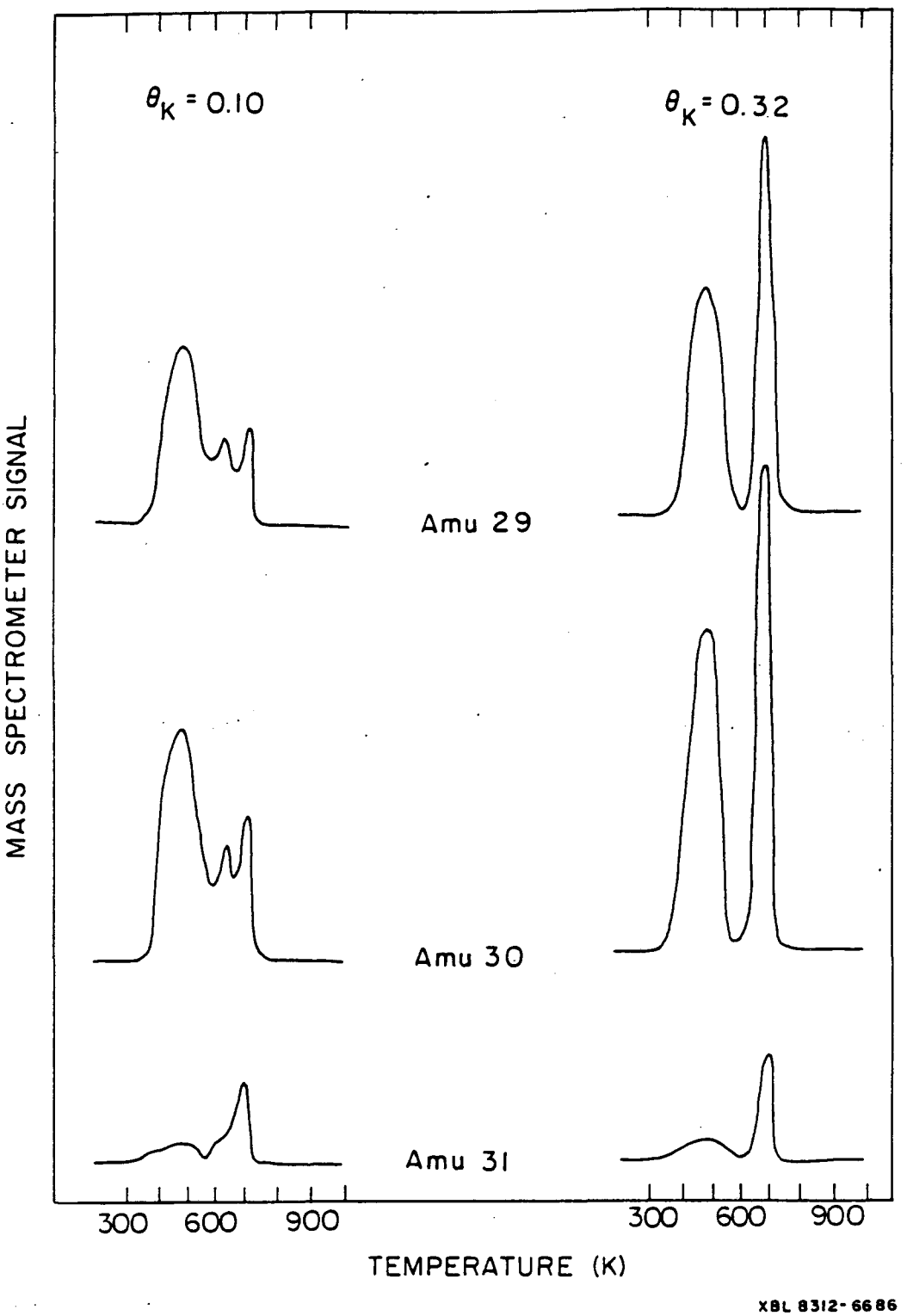
10L CO/K/Rh(111)
θ_K = 0.10
θ_K = 0.32
Amu 29
Amu 30
Amu 31
MASS SPECTROMETER SIGNAL
300
600
900
300
600
900
TEMPERATURE (K)
XBL 8312-6686

Figure 5.18

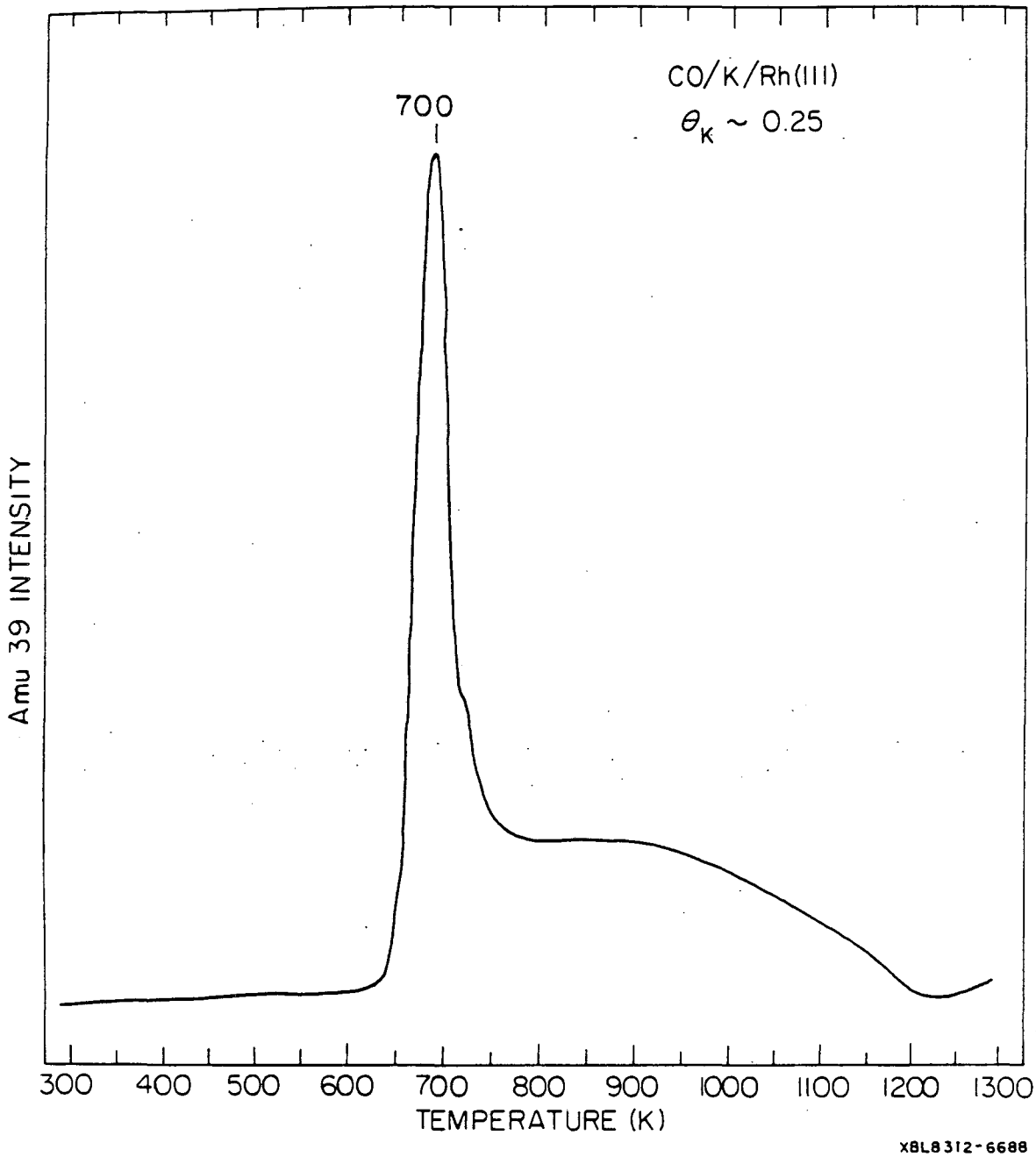
CO/K/Rh(111)
$\theta_K \sim 0.25$
700
Amu 39 INTENSITY
300
400
500
600
700
800
900
1000
1100
1200
1300
TEMPERATURE (K)
XBL8312-6688

Figure 5.19

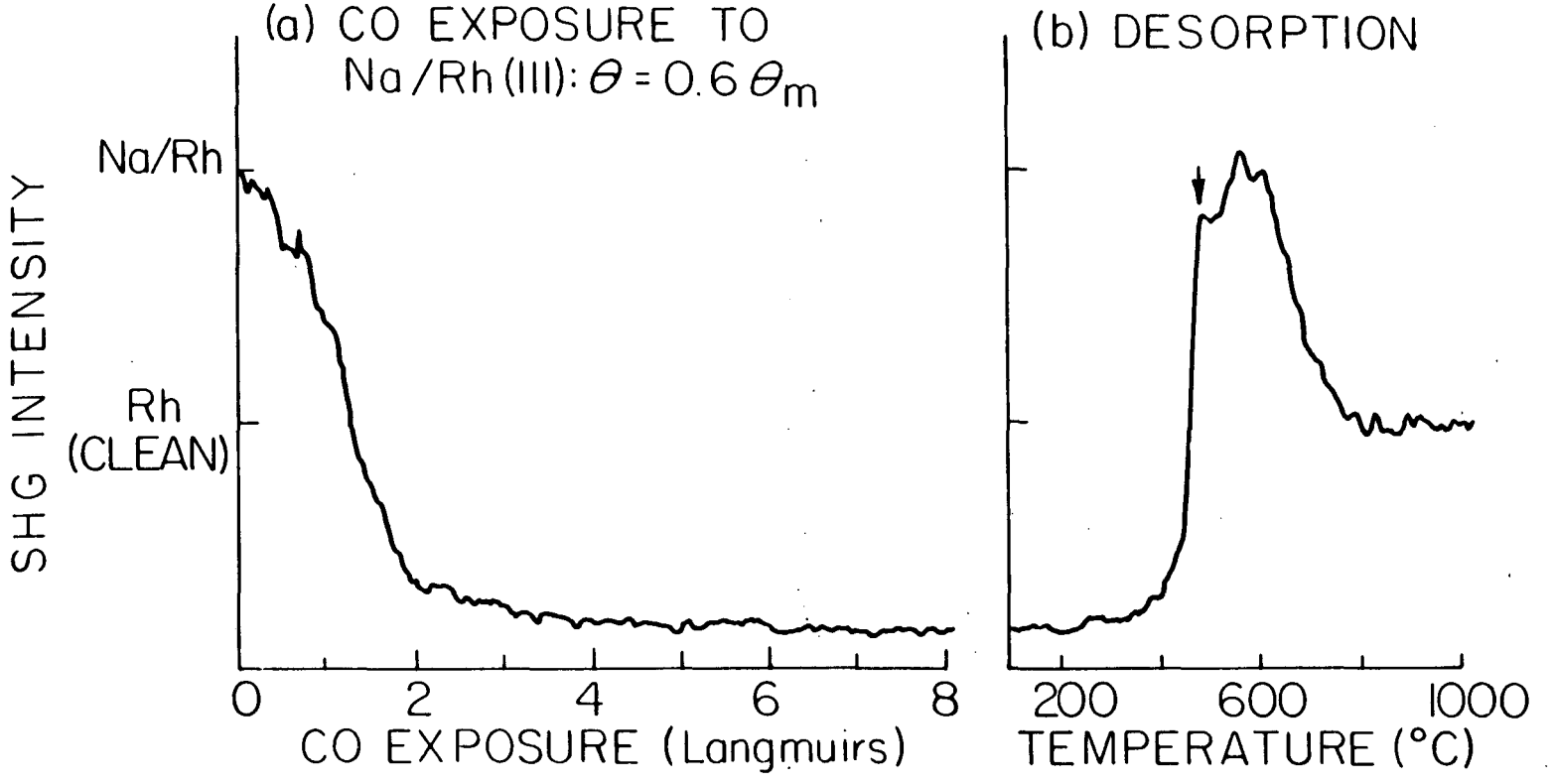

Figure 5.20

XBL 8310-6427A

5.3.2c Vibrational Spectroscopy of CO Adsorbed on Potassium Dosed Rh(111)

The effect of potassium on the adsorption of CO has also been studied by vibrational spectroscopy, as shown in Fig. 5.21. These spectra are for saturation CO exposure of a predosed potassium overlayer at 300K. One of the most striking features seen with even very small potassium coverages is the increased intensity in the bridge site CO stretching frequency. This trend continues with increasing coverage such that the bridge site intensity dominates and very little of the atop species is populated at large potassium coverage (cf. $\theta_K = 0.25$). In addition, the frequency of the C-O stretching vibrations decrease as the potassium coverage increases. This shift is fairly uniform with potassium coverage, although at very small coverages only relative populations change. The frequency shift is more pronounced for the bridged species, decreasing by 145 cm^{-1} compared to 65 cm^{-1} for the atop site. The average metal-carbon vibration also decreases in frequency with increasing potassium coverage, although only by 17 cm^{-1} up to $\theta_K = 0.25$. Furthermore, the intensity of all the CO vibrations decrease with increasing potassium coverage, as indicated by the relative scaling factors. This intensity decrease is more pronounced for the metal-carbon vibrations. From Fig. 5.12 we note that the intensity and frequency of the bridge bonded metal-carbon stretch are significantly less than that of the atop site, hence both changes seen with potassium coadsorption (i.e., decreased intensity and frequency of the observed

ν_{M-C} mode) are consistent with increased population of a bridge bonded species. Hence, the change in site occupation dominates over the change in M-CO bond strength as the average single M-C vibration is observed to decrease slightly with potassium, rather than increase as expected.

One also sees in Fig. 5.21 that the width at the base of the CO stretching vibrations increase significantly with increasing potassium coverage. This is seen more clearly in Fig. 5.22 where the M-C and C-O stretching vibrations are shown on an expanded scale. Note that even for very small potassium coverages there is considerable broadening near the base of the peaks, especially on the low frequency side of the peaks. As the potassium coverage increases, this trend continues, and as the average frequencies of the peaks decrease, the broadening is seen to be extended to the high frequency side of the peak maxima as well. This broadening of the basewidth can be attributed to either population of additional sites, such as 3-fold hollow sites, or to the inhomogeneity in the bond strength of the CO molecules due to their proximity to the potassium adatoms.

Figures 5.23 shows the vibrational spectra for CO with a small fixed potassium concentration as a function of CO exposure. Initial CO adsorption on a θ_K = 0.02 potassium layer has a stretching frequency that is quite low, 1530 cm^{-1}, but the vibrational mode is broad and asymmetric. At slightly higher CO exposure (0.7L), modes near 1600 cm^{-1} populate in addition to those at 1530 cm^{-1}. Compared to the clean Rh(111) case, the CO stretching region becomes

quite broad even at this low coverage. With further CO exposure these modes remain populated as additional modes at higher frequency begin growing in. At this point (2.0L), similar behavior begins for the atop site (i.e. more than one vibrational mode becomes visible near 2000 cm^{-1}). However, as more CO is adsorbed, the intensities of the initially filled low frequency modes seem to decrease as the average peak frequencies begin to increase. This trend continues with further exposure as the atop site predominantly fills. These spectra indicate that the first CO molecules on the surface feel a much greater perturbation due to the potassium adatoms, with a large inhomogeneity in the CO bond strength. As the CO coverage increases, this inhomogeneity increases, indicating that the proximity of the CO molecules to the K adatoms strongly affects its bond strength. As additional CO adsorb, these low frequency modes decrease in intensity while further increases in the average CO frequency occur, indicating the effect per CO is decreasing. Interestingly, a metal-carbon mode does not become visible until the atop sites begin to be significantly populated. The dynamic dipole moment of the metal-carbon stretch perpendicular to the surface is expected to decrease as the bond strength increases for a bridge or multiply coordinated CO molecule. This may explain why the metal-carbon vibration for the strongly perturbed CO molecule is difficult to observe.

A region of the vibrational spectrum for a coverage series similar to Fig. 5.23 is shown in Fig. 5.24. Here the C-O stretching frequency region is shown on an expanded scale as a function of CO coverage at a

predosed potassium coverage of θ_K = 0.03. At low exposure, the stretching vibration is quite broad, extending from 1500-1700 cm^{-1}. At 0.7L exposure, the stretching vibration becomes quite asymmetric, as modes near 1655 cm^{-1} begin to populate. The relative intensity of the most strongly perturbed CO molecules begins to decrease with increasing exposure, as shown at 1.7 and 20L. The peak maxima also shift considerably. similar trends, though less dramatic, occur for the atop site vibrations. These spectra, like those in Fig. 5.23, suggest both local and nonlocal intractions. The local interactions dominate at small CO exposures, as evidenced by the asymmetric band filling sequence and the strongly perturbed vibrational frequencies observed. Nonlocal interactions are apparent at large CO exposures, indicated by large continuous shifts in the peak frequency and dramatic reduction in the intensity of the most strongly perturbed CO molecules.

At a larger potassium coverage (θK = 0.10), the local effects are not nearly so dramatic, as shown in Fig. 5.25. The major change observed as the CO coverage increases is a continuous increase in the CO stretching frequency, shifting from 1500 to 1790 cm^{-1}. As this shift occurs, little broadening occurs, suggesting that the inhomogeneity in the CO frequencies is much less. Similar to that seen in Fig. 5.23, a metal-carbon vibration does not become distinguishable until an atop site stretching vibration is observed.

Figure 5.26 shows the vibrational spectrum of CO on a potassium predosed surface for both specular and off-specular scattering. In

moving from specular to 20° off-specular, the 445, 1830 and 2035 cm^{-1} modes all decrease by factors of 8.5-10.5, while the specular beam decreases by a factor of 70. This suggests these modes are caused by dipole scattering, as suspected. The lack of any additional modes in the off-specular spectrum indicate the orientation of CO in the presence of potassium is similar to that of CO on the clean surface, i.e., the molecules are standing upright.

FIGURE CAPTIONS

Fig. 5.21. HREEL spectra for saturation CO adsorption at 300K on a Rh(111) surface predosed with varying amounts of potassium.

Fig. 5.22. Portions of the vibrational spectrum obtained on an expanded scale for saturation CO adsorption at 300K on a Rh(111) surface predosed with potassium. Three different potassium coverages are shown.

Fig. 5.23. HREELS spectra of CO adsorbed on a potassium predosed Rh(111) surface obtained as a function of CO exposure at a constant potassium coverage.

Fig. 5.24. Vibrational spectra of CO adsorbed at 300K on a Rh(111) surface predosed with potassium, as a function of CO exposure. The CO stretching vibrations are shown on an expanded scale.

Fig. 5.25. HREELS spectra of varying exposures of CO on a Rh(111) surface predosed with potassium.

Fig. 5.26. Specular and off-specular spectra for CO adsorption on a potassium dosed Rh(111) surface.

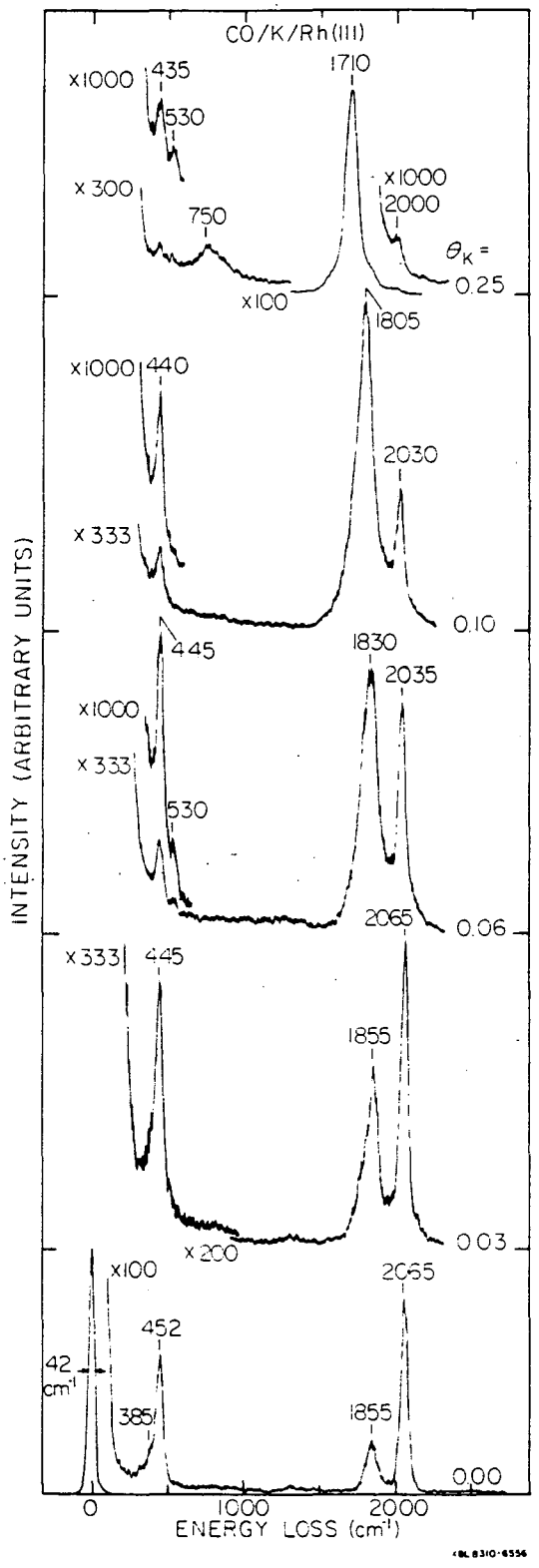
CO/K/Rh(111)
x1000
435
530
1710
x300
750
x100
x1000
2000
θK = 0.25
1805
x1000
440
2030
x333
0.10
445
1830
2035
x1000
x333
530
2065
0.06
x333
445
1855
x200
0.03
x100
2065
452
42 cm-1
385
1855
0.00
INTENSITY (ARBITRARY UNITS)
0
1000
2000
ENERGY LOSS (cm-1)

Figure 5.21

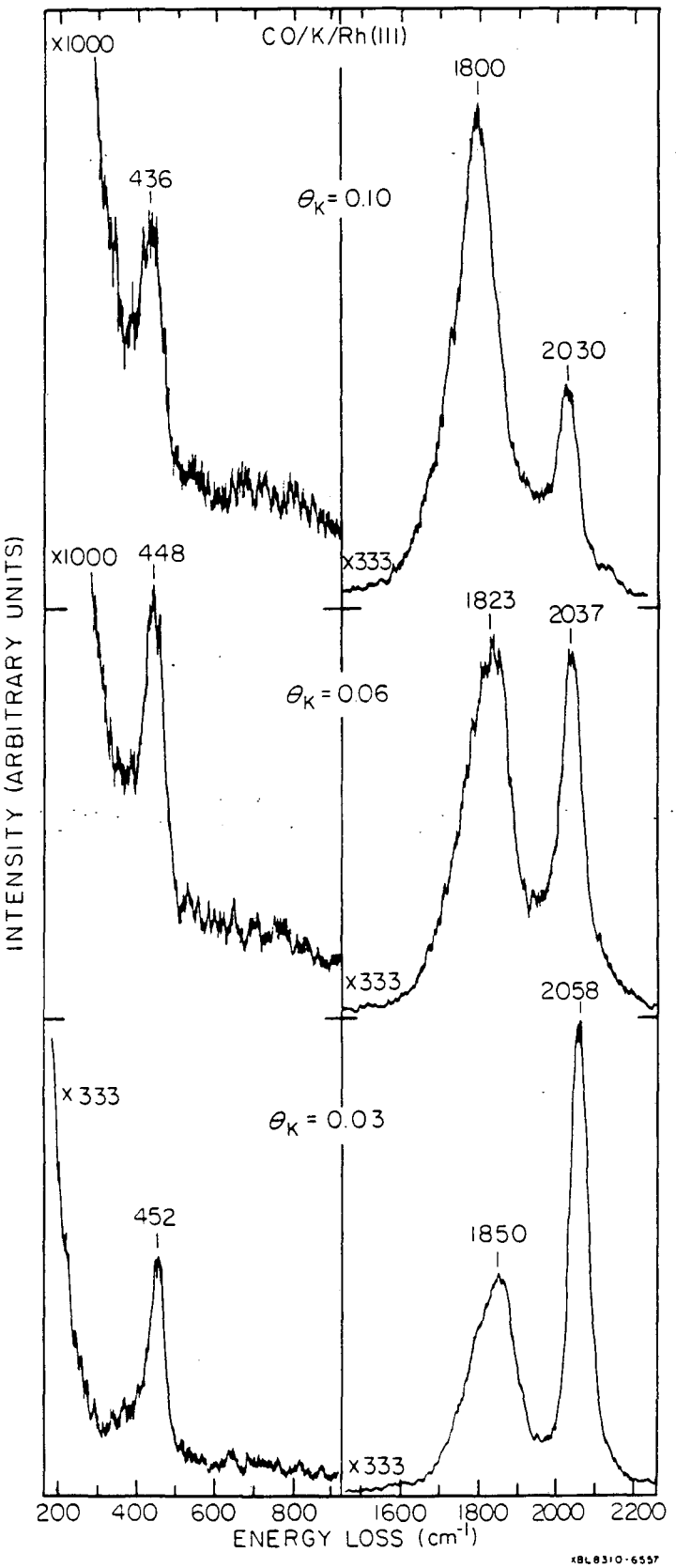
CO/K/Rh(111)
x1000
436
1800
2030
θK = 0.10
x333
x1000
448
1823
2037
θK = 0.06
x333
2058
x 333
θK = 0.03
452
1850
x333
INTENSITY (ARBITRARY UNITS)
200
400
600
800
1600
1800
2000
2200
ENERGY LOSS (cm-1)
XBL8310-6557

Figure 5.22

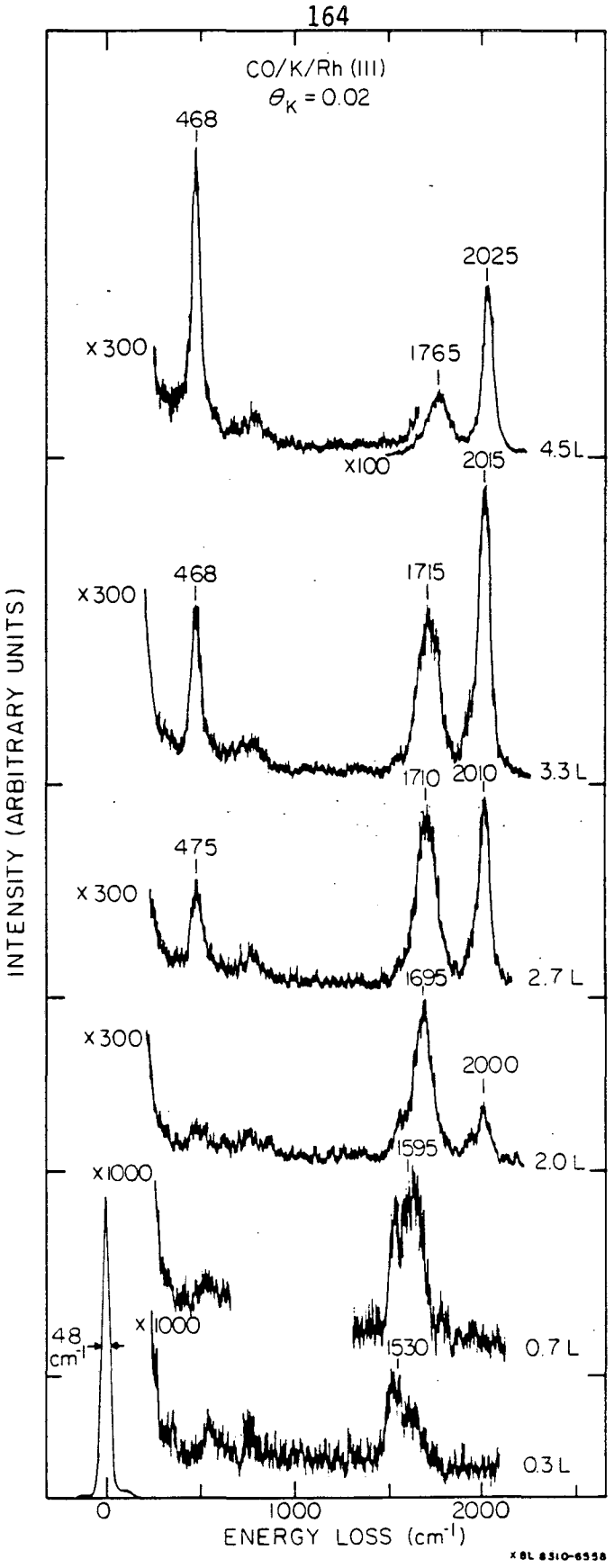
CO/K/Rh (111)
θ_K = 0.02
468
2025
x300
1765
x100
2015
4.5 L
468
1715
x300
1710
2010
3.3 L
475
x300
1695
2.7 L
x300
2000
1595
2.0 L
x1000
x1000
48 cm^{-1}
1530
0.7 L
0.3 L
INTENSITY (ARBITRARY UNITS)
0
1000
2000
ENERGY LOSS (cm^{-1})

Figure 5.23

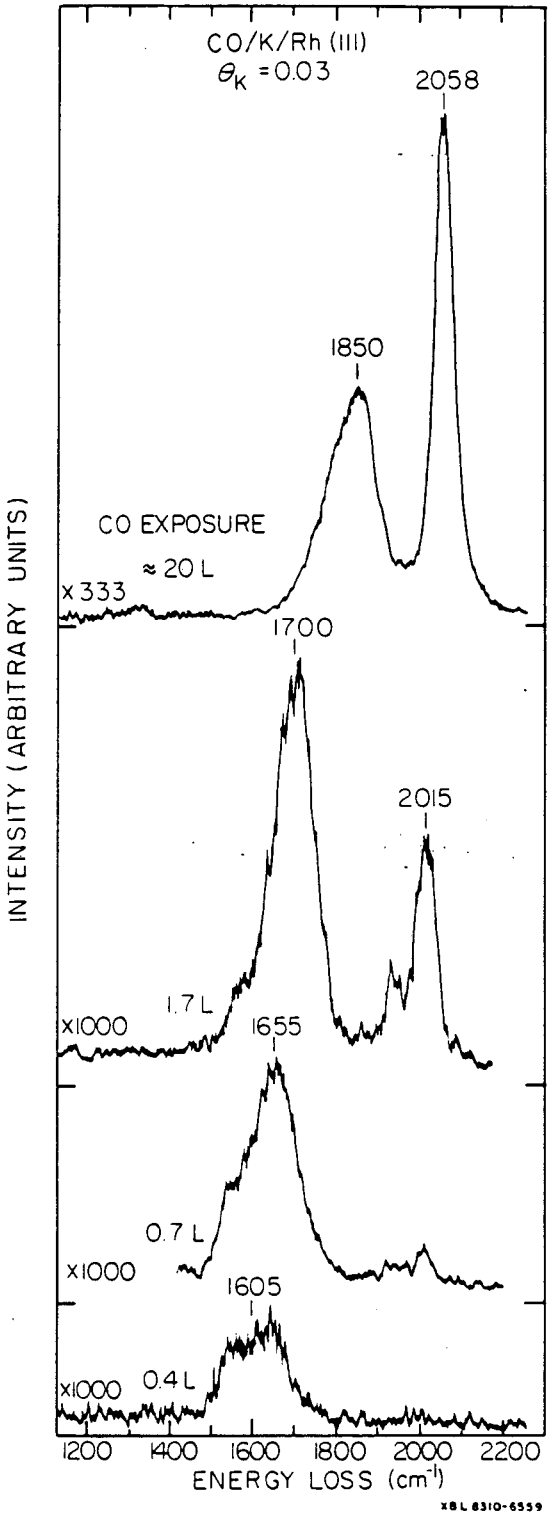
CO/K/Rh (111)
θ_K = 0.03
2058
1850
CO EXPOSURE
≈ 20 L
x 333
1700
2015
1.7 L
x1000
1655
0.7 L
x1000
1605
x1000
0.4 L
INTENSITY (ARBITRARY UNITS)
1200
1400
1600
1800
2000
2200
ENERGY LOSS (cm^{-1})
XBL 8310-6559

Figure 5.24

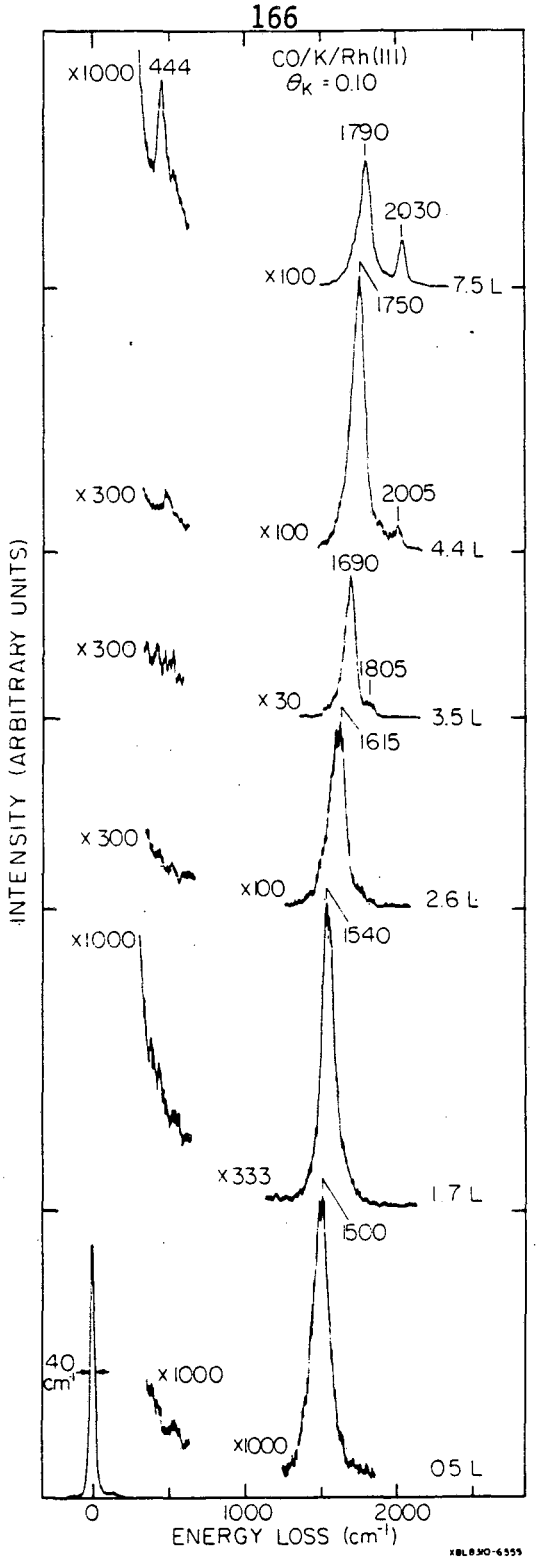
CO/K/Rh(111)
θ_K = 0.10
x1000
444
1790
2030
x100
7.5 L
1750
x300
2005
x100
4.4 L
1690
x300
1805
x30
3.5 L
1615
x300
x100
2.6 L
x1000
1540
x333
1.7 L
1500
40 cm^{-1}
x1000
x1000
0.5 L
INTENSITY (ARBITRARY UNITS)
0
1000
2000
ENERGY LOSS (cm^{-1})
XBL830-6555

Figure 5.25

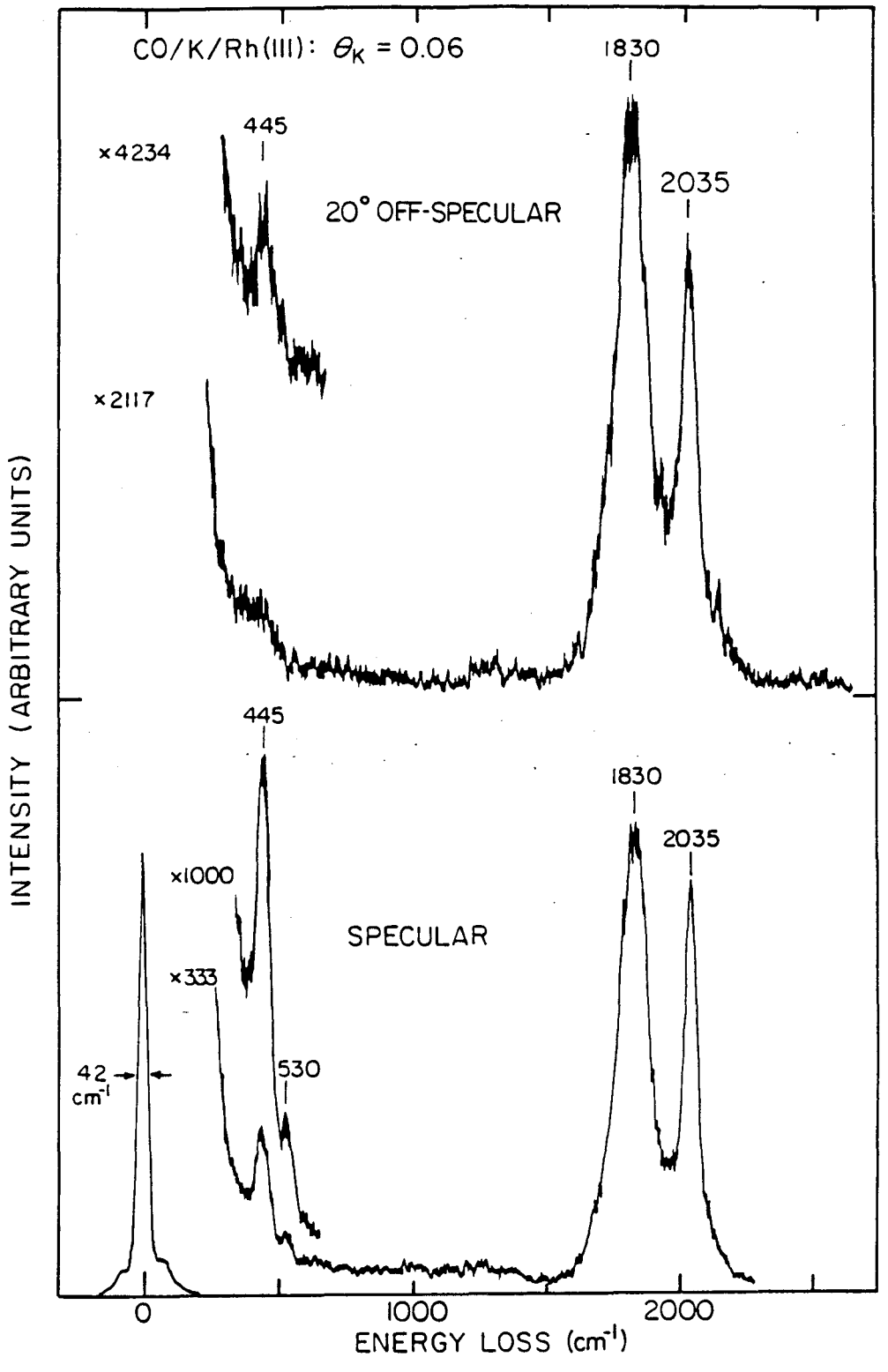
CO/K/Rh(111): θ_K = 0.06
1830
445
×4234
2035
20° OFF-SPECULAR
×2117
445
1830
2035
×1000
SPECULAR
×333
42
cm⁻¹
530
INTENSITY (ARBITRARY UNITS)
0
1000
2000
ENERGY LOSS (cm⁻¹)
XBL 8310-6549

Figure 5.26

5.3.3 DISCUSSION

Preadsorbed potassium dramatically affects the chemisorption behavior of CO on Rh(111), as evidenced by the changes seen in the TPD and HREEL spectra. The most significant results are summarized as follows:

(i) The CO desorption spectrum broadens up to 100K higher temperature as a function of potassium coverage, for $\theta_K < 0.10$.

(ii) For $0.10 < \theta_K < 0.36$, two new desorption maxima at 630 and 700K are observed and are due to recombination of carbon and oxygen produced by dissociation of adsorbed CO.

(iii) The presence of CO alters the desorption behavior of potassium for $\theta_K > 0.10$, increasing the potassium binding energy by as much as 12 kcal/mole. Nearly simultaneous desorption of CO and K occurs for the 700K CO state.

(iv) As the potassium coverage increases from zero to 0.25 of a monolayer, the CO stretching modes at saturation coverage decrease by 145 cm^{-1} for the bridge site and 65 cm^{-1} for the atop site. Concurrently, the broad single M-CO vibration decreases by 17 cm^{-1}.

(v) The relative occupancy of the two adsorption sites changes considerably with increasing potassium coverage, favoring the bridge site over the atop site.

(vi) The width at the base of the stretching vibrations increase as the potassium coverage increases.

(vii) The CO stretching vibration observed at submonolayer CO coverages in the presence of low concentrations of potassium

($0.02 < \theta_K < 0.10$) is 335 cm^{-1} less than the lowest vibration observed for CO adsorption on clean Rh(111). Dramatic broadening and asymmetry is also observed at these low CO and potassium coverages.

As discussed in Section 5.2.3, the bonding of carbon monoxide to metal atoms involves a synergistic electron transfer from the highest occupied molecular orbitals of CO (5σ) to the metal, and in turn metal electrons are backdonated into the lowest unoccupied molecular orbital ($2\pi^*$) of CO. The backdonation of metal electrons into the $2\pi^*_{CO}$ orbital leads to a simultaneous strengthening of the M-C bond and a weakening of the C-O bond, as seen in Figure 5.10(a).

The large changes in the desorption behavior, the vibrational frequencies, and the site occupancy of adsorbed CO in the presence of potassium can all be attributed to enhanced backdonation of electrons from the metal into the $2\pi^*$-orbital of CO. Potassium is expected to lower the work function of the rhodium surface. This allows a greater electron spillover into the backbonding orbital [20], of which bridge sites permit more extensive $d_M - 2\pi^*_{CO}$ orbital overlap [14,21,22]. Enhanced electron density into this conjugate orbital increases the metal-carbonyl bond strength, increasing both the CO heat of desorption and the ν_{M-CO} vibrational frequency. Enhanced occupancy of this orbital also weakens the C-O bond, leading to a decrease in the ν_{CO} frequencies. Whether the enhanced backdonation is due solely to electrostatic effects [21,38], or involve primarily other contributions [22] is not directly measured here; the results only indicate the strength of the bonds involved. Recent metastable

quenching experiments [39] also indicate enhanced occupation of the $2\pi^*$-orbital of CO in the presence of potassium.

In a recent photoemission study, Kiskinova et al. [40] suggest that potassium strongly influences neighboring CO molecules, decreasing the C-O stretching frequency of atop bonded molecules to frequencies near and below that of bridge bonded CO in the absence of potassium. They observed two O(1s) and C(1s) binding states which occur at nearly identical energies for both CO on clean Pt(111) and CO on K dosed Pt(111). For the clean metal case, the two states are assigned to atop and bridge adsorption sites, in agreement with vibrational analysis. For the K dosed surface, where $\Delta\phi$ and UPS measurements indicate enhnaced backdonation, these are assigned to clean and K promoted atop adsorption sites. As similar vibrational spectra are observed for Pt(111) and Rh(111) with coadsorbed potassium, their suggested assignment applies to this study as well; namely that the increased intensity between 1700-1850 cm^{-1} is due to a K influenced linearly bonded CO molecule. The gradual shift of the frequency with potassium coverage, and the above mentioned calculations [14,21,22], strongly suggests a bridge site CO molecule gives rise to these features. Furthermore, the absence of any intense modes between 1850 and 2000 cm^{-1} with coadsorbed potassium is quite conspicuous. The vibrational data for both adsorption systems (CO and K coadsorbed on Pt(111) and Rh(111)) strongly indicates that bridge sites are preferably occupied in the presence of potassium.

An important aspect of the effects seen with additives such as potassium or sulfur is the spatial extent of the interaction. The results presented here provide evidence for both short and long range electronic effects. The results presented in Figures 5.23 and 5.24 strongly suggest that local or even direct interactions occur for initially adsorbed CO. The asymmetry and broadening also seen at relatively small CO and potassium coverages indicate further that the proximity of the CO molecules to the potassium adatoms is important: the closer the species are, the more pronounced is the perturbation. Once a significant amount of CO has been adsorbed at these low potassium coverages, additionally adsorbed CO molecules can no longer occupy sites closer than a few interatomic spacings, yet their frequency is strongly altered. Furthermore, the intensity of initially occupied sites decrease with increasing CO coverage (cf. the vibrations between 1530 and 1590 cm^{-1} decrease in intensity as the CO exposure in increased from 2.0 to 3.3L in Fig. 5.23). Both these results can be explained by suggesting that potassium can affect more than its nearest and next-nearest neighbors. Furthermore, it is difficult to explain the gradual frequency shift observed with increasing CO coverage seen in Figures 5.23-5.25 without invoking long range interactions. Note that some broadening occurs with increasing CO coverage, but much less than expected if the additional CO molecules did not strongly influence the already adsorbed CO vibrational frequencies. The HREELS data discussed here and the gradual broadening seen as a function of CO coverage in TPD [37]

strongly indicate that nonlocal electronic changes occur, and that as additional CO molecules are adsorbed, the effect of potassium per CO decreases.

Each additional CO molecule adsorbed is perturbed by potassium, and either through changes in the polarization or electron density at the surface, modifies the extent of perturbation felt by the already adsorbed molecules. This suggests that a competition for the available surface electron density exists. These conclusions are based on both the TPD and HREELS data. Changes in the electron scattering cross section or in the shape of the CO molecular potential well with CO coverage or in the presence of potassium are not well understood, but could possibly account for the vibrational data. However, these changes would not additionally account for the dramatic changes seen in the TPD spectra.

It is curious that no strong evidence for the dissociation of CO is found using HREELS. This suggests that dissociation occurs during the desorption process. In fact, recent metastable quenching experiments by Metiu and coworkers [41] indicate that dissociation occurs just below the onset of desorption on Ni(111). However, heating a CO plus potassium overlayer sequentially to 700K (total desorption) only produced vibrational spectra characteristic of a gradual reduction in CO coverage. TPD experiments to determine at which temperature CO dissociates are currently being investigated.

Another curious aspect of the CO plus K adsorption system is the lack of a metal-carbon stretching vibration at low CO coverages on

both Pt(111) and Rh(111). Similar behavior has also been seen recently for CO and K on Ru(001) [42]. It has been proposed [42] that the low frequency C-O vibrations observed for these systems between 1400-1600 cm^{-1} and the lack of any detectable M-C vibration is caused by CO being side-on bonded. Such bonding would certainly lead to higher dissociation probabilities. Due to the uncertainty in adsorption site determination for CO species on metal surfaces, such a bonding configuration is feasible.

5.4 CONCLUSIONS

Potassium preadsortion on Pt(111) and Rh(111) has been shown to significantly alter the chemisorptive properties of CO. For both surfaces, the heat of desorption increases while the C-O stretching frequencies decrease in the presence of preadsorbed potassium. Additionally, a dramatic shift in intensity from the atop to the bridge site occurs with increasing potassium coverage. The site-filling sequence observed as a function of CO exposure is also altered even for very low levels of coadsorbed potassium. The changes observed suggest enhanced occupation of the $2\pi^*$-orbital of CO in the presence of potassium, leading to a weakening of the C-O bonding with simultaneous strengthening of the M-C bonding. Occupation of higher coordination sites leads to better d_M-$2\pi^*_{CO}$ orbital overlap, and is common for low work function surfaces. Local interactions seem to be evident at low CO coverages, but the entire CO layer is affected at even small potassium coverages, suggesting long-range electronic effects. For a fixed potassium coverage, the CO molecules appear to compete for the excess surface charge available due to the presence of potassium.

The effects seen for CO and potassium on Rh(111) are not as large in magnitude of frequency shifts and heat of adsorption changes as seen on Pt(111), although the trends are quite similar. However, unlike that seen for Pt(111), CO does dissociate on potassium promoted Rh(111), if the potassium coverage is high enough.

The role these additives play in promoting CO hydrogenation reactions is clearly complicated. Potassium certainly enhances CO dissociation in some cases, leading to reduced methanation and higher molecular weight products [43]. But CO insertion reactions are also more facile in the presence of alkalis in homogeneous catalysis [44], and may also be an important mechanism in heterogeneous Fischer-Tropsch reactions, as alkalis also enhance the formation of olefins and oxygenated molecules [45,46]. For either mechanism, a change in relative concentraions of CO and H on the surface will alter product distribution.

REFERENCES

1. J. T. Yates, Jr., T. E. Madey, and J. C. Campuzano, in The Physics and Chemistry of Solid Surfaces and Heterogeneous Catalysis, D. A. King and D. P. Woodruff, Eds., in press.
2. M. E. Dry, T. Shingles, L. J. Boshoff and G. J. Oosthuizen, J. Catalysis 15, 190 (1969).
3. G. Broden, G. Gafner, and H. P. Bonzel, Surface Sci. 84, 295 (1979).
4. J. Benziger and R. J. Madix, Surface Sci. 94, 119 (1980).
5. M. P. Kiskinova, Surface Sci. 111, 584 (1981).
6. C. T. Campbell, G. Ertl, H. Kuipers, and J. Segner, Surface Sci. 107, 207 (1981).
7. D. H. Winicur, J. Hurst,, C. A. Becker and L. Wharton, Surface Sci. 109, 263 (1981).
8. R. P. Norton, J. W. Goodale and E. B. Selkirk, Surface Sci. 83, 189 (1979).
9. G. Ertl, M. Neumann and K. M. Steit, Surface Sci. 83, 189 (1979).
10. A. Crossley and D. A. King, Surface Sci. 95, 131 (1980).
11. H. Froitzheim, H. Hopster, H. Ibach and S. Lehwald, Appl. Phys. 13, 147 (1977).
12. A. M. Baro and H. Ibach, J. Chem. Phys. 71, 4812 (1979).
13. N. Sheppard and T. T. Nguyen in Advances in Infrared and Raman Spectroscopy, Vol. 5, R. J. H. Clark and R. E. Hester, Ed., Heyden and Son, London, 1968.

14. H. Steininger, S. Lehwald, and H. Ibach, Surface Sci. 123, 264 (1982).

15. Desorption of CO at 420K with a peak area ~5 percent of saturation, which was shown to be due to crystal back, edge, and/or support effects, has been subtracted from all spectra in Fig. 5.3.

16. E. L. Garfunkel and G. A. Somorjai, Surface Sci. 115, 441 (1982).

17. E. L. Garfunkel, Ph.D. Thesis, University of California, Berkeley, 1983, unpublished.

18. J. E. Crowell, E. L. Garfunkel and G. A. Somorjai, Surface Sci. 121, 303 (1982).

19. L. Pauling, The Nature of the Chemical Bond, Cornell University Press, Ithaca, N.Y., 1960.

20. B. E. Nieuwenhuys, Surface Sci. 105, 505 (1981).

21. R. A. van Santen, in press.

22. N. K. Ray and A. B. Anderson, Surface Sci. 125, 803 (1983).

23. A. M. Bradshaw and F. M. Hoffman, Surface Sci. 72, 513 (1978).

24. G. Ertl, M. Weiss and S. B. Lee, Chem. Phys. Lett. 60, 391 (1979).

25. E. L. Garfunkel, J. J. May, J. C. Frost, M. H. Farias, and G. A. Somorjai, J. Phys. Chem. 87, 3629 (1983).

26. W. Andreoni and C. M. Varma, Phys. Rev. B23, 437 (1981).

27. G. Broden, T. N. Rhodin, C. Brucker, R. Benbow, and Z. Hurych, Surface Sci. 59, 593 (1976).

28. J. T. Yates, Jr., E. D. Williams, and W. H. Weinberg, Surface Sci. 91, 562 (1980).

29. P. A. Thiel, E. D. Williams, J. T. Yates, Jr., and W. H. Weinberg, Surface Sci. 84, 54 (1979).

30. D. G. Castner, B. A. Sexton, and G. A. Somorjai, Surface Sci. 71, 519 (1978).

31. L. H. Dubois and G. A. Somorjai, Surface Sci. 91, 514 (1980).

32. S. Semancik, G. L. Haller and J. T. Yates, Jr., J. Chem. Phys. 78, 6970 (1983).

33. S. Lehwald, H. Ibach and H. Steininger, Surface Sci. 117, 342 (1982).

34. R. J. Koestner, M. A. Van Hove, and G. A. Somorjai, Surface Sci. 107, 439 (1981).

35. M. A. Van Hove, R. J. Koestner, and G. A. Somorjai, Phys. Rev. Lett. 50, 903 (1983).

36. T. F. Heinz, Ph.D. Thesis, University of California, Berkeley, unpublished.

37. J. E. Crowell, W. T. Tysoe and G. A. Somorjai, to be submitted.

38. H S. Luftman and J. M. White, submitted to Surface Sci.

39. J. Lee, C. R. Hanrahan, J. Arias, R. M. Martin and H. Metiu, Phys. Rev. Lett. 51, 1803 (1983).

40. M. Kiskinova, G. Pirug and H. P. Bonzel, Surface Sci. 133, 321 (1983).

41. H. Metiu, private communication.

42. F. M. Hoffmann, private communication.

43. C. T. Campbell and D. W. Goodman, Surface Sci. 123, 413 (1982).

44. J. P. Collman, R. G. Finke, J. N. Cawse, and J. I. Bramman, J. Am. Chem. Soc. 100, 4766 (1978).

45. G. Henrici-Olive and S. Olive, J. Mol. Catal. 16, 187 (1982).

46. H. Orita, S. Naito and K. Tamaru, Chem. Lett. 1161 (1983).

CHAPTER 6

THE ADSORPTION OF BENZENE ON THE CLEAN AND POTASSIUM DOSED Rh(111) CRYSTAL SURFACE

6.1 Overview

A molecular scale understanding of the chemical bonding of aromatic molecules to metal surfaces is obtainable by employing high resolution electron energy loss spectroscopy (HREELS) and low energy electron diffraction (LEED). Detailed scrutiny of the bonding and reactivity at these metal-organic interfaces could help in unraveling the reaction steps during the catalytic conversion of aromatic molecules and could provide the molecular basis for adhesion and lubrication.

In this chapter we examine the simplest aromatic molecule, benzene, on the (111) crystal face of rhodium [1]. HREELS and LEED were employed to study the molecular structure and bonding of benzene adsorbed on this transition metal surface. Use of the surface selection rule in conjunction with detailed angular profile measurements allow for a bonding site determination to be made and compared to the surface structure obtained from dynamic LEED calculations [2].

A characteristic of benzene and arenes in general is their ability to form π bonds with transition metals. The nature of this interaction is dependent on the π donor character of the transition metal, and hence the transition metal itself. Potassium strongly perturbs the basicity of metal surfaces, as characterized by the large work function

change. Consequently, preadsorbed potassium should alter the bonding of benzene to a metal surface. The coadsorption of benzene and potassium has been studied here to explore these bonding changes.

In addition, by using vibrational spectroscopy in combination with temperature programmed desorption (TPD) studies, we can explore C-H and C-C bond activation. Catalytic reactions depend on the nature of C-C and C-H bond breaking and bond formation processes. By characterizing the decomposition of benzene on the clean and potassium dosed Rh(111) surface, a partial understanding of these processes in ultra high vacuum has been obtained.

The chapter is divided as follows: in Section 6.2 the adsorption of benzene on clean Rh(111) is described, along with its structure determination and the nature of benzene decomposition. Section 6.3 examines how benzene adsorption and decomposition are affected by preadsorbed potassium; the overall conclusions from these studies appears in Section 6.4.

6.2 Benzene Adsorption on Clean Rh(111)

6.2.1. Introduction.

Benzene is typically chemisorbed on transition metal surfaces with its ring plane parallel to the surface plane as concluded in several spectroscopic studies [3-19]. Several angle-resolved photoemission studies [3-6] show that the flat lying benzene bonds predominately through π orbitals. Temperature programmed desorption (TPD) studies [7-12] indicate that on most transition metal surfaces, benzene

adsorption is associative at 300K, with only partial reversibility. Vibrational spectroscopy of benzene chemisorbed on both single crystal [10-16] and supported metal surfaces [17-19] conclude that benzene is indeed oriented with its ring plane parallel to the surface plane and is only weakly distorted from its gas phase molecule structure through interaction with the metal, indicating π bonding. A comparison of the surface chemistry of benzene on Rh(111) as obtained in this HREELS study with those of the previously mentioned studies on other surfaces leads to important correlations.

In addition, vibrational spectra have been obtained of ordered benzene overlayers for which LEED intensity-voltage curves have been measured [24]. From a correlation of the vibrational spectroscopy data with the dynamical LEED intensity analyses [2], a comprehensive picture of the adsorption site symmetry and bonding configuration is obtained. Furthermore, from a comparison with disordered benzene overlayers, the influence of ordering on this adsorption geometry has been determined.

The decomposition of benzene adsorbed on the Rh(111) crystal face has also been explored as a function of temperature in the range of 300-800K. The sequential hydrogen evolution that accompanied the decomposition of this organic molecule was monitored by TPD. The disordered carbonaceous fragments produced on the surface were studied by HREELS as a function of decomposition temperature. The species produced are compared to those formed from thermal decomposition of acetylene and ethylene on other transition metal surfaces.

The vibrational spectra recorded here were obtained at an incident energy of ~4 eV referenced to the sample fermi level. The total scattering angle was fixed at 120°, so for specular reflection $\theta_i = \theta_s = 60°$ from the surface normal. Off specular measurements ($\theta_i \neq \theta_s$) were performed by rotation of the sample about an axis perpendicular to the scattering plane. Off-specular measurements varied up to 20° from specular reflection, with θ_i varying between 55 and 70°.

6.2.2 Results and Interpretation

6.2.2a. Benzene Adsorption on Rh(111) at 300K.

Benzene adsorption occurs on Rh(111) at 300K with an initial sticking coefficient of near unity, as indicated by AES and TPD. The sticking coefficient is constant ($S = S_0$) for coverages less than 85 percent of the saturation amount. Saturation benzene coverage is nearly reached after 5L exposure, but the coverage can be increased about 15 percent by exposures of 70L. The saturation benzene coverage ($\theta_{C_6H_6}$) on Rh(111) at 300K and at 5×10^{-10} torr is 0.125 ML (ML = monolayers, defined relative to the surface Rh atom density of 1.60×10^{15} atoms/cm^2), or a carbon atom coverage (θ_C) of 0.75 ML [24]. This coverage was determined from the LEED pattern observed assuming one molecule per unit cell.

The chemisorption of benzene at less than about 25 percent of saturation coverage ($\theta_{C_6H_6} < 0.03$ ML) is totally irreversible. Evidence for this is shown in Fig. 6.1, where no detectable molecular

benzene thermal desorption occurs, only dehydrogenation yielding H_2 desorption and an adsorbed hydrocarbon fragment. Figure 6.1 shows TPD spectra for (A) C_6H_6 desorption after C_6H_6 exposure and (B) D_2 desorption following C_6D_6 exposure of Rh(111) at 300K. Some reversible benzene chemisorption occurs for exposures larger than 2L, and with increasing exposure the fraction of benzene chemisorption that can be reversibly desorbed increases. AES, along with supporting evidence from HREELS and LEED, indicates that heating the saturation covered surface to 380K (which removes one-half of the molecular benzene state) reduces the adsorbate coverage less than 10 percent. Therefore, along with dehydrogenation, molecular benzene desorption becomes significant at high coverages during heating of the surface, but still accounts for less than 0.02 ML C_6H_6.

For exposures greater than 2L (Fig. 6.1(A)), molecular benzene desorption occurs immediately upon heating and continues until 500K. A broad benzene desorption peak is observed at 415K after 5L exposure which shifts to 395K after saturation exposure. TPD spectra for desorption of C_6D_6 from Rh(111) after C_6D_6 exposure are identical to those in Fig. 6.1(A). Repulsive interactions between benzene molecules at high coverages could account for reducing the adsorption energy with increasing coverage, but we cannot rule out the existence of several overlapping desorption states with different desorption energies.

Figure 6.1(B) shows the TPD spectra for D_2 following C_6D_6 exposure to Rh(111) at 300K. TPD spectra for H_2 after C_6H_6

exposures were qualitatively the same. An isotope effect was apparent for the largest desorption peak (473K) which occurred at 20K lower temperature for H_2 evolution. Also, some small amount of contaminant coadsorbed hydrogen was observed for small benzene coverages that desorbed near 370K. In Fig. 6.1(B), at low exposures, several D_2 desorption states are observed between 430-540K. With increasing exposure, the dominant peak at 495K continued to increase in size and, at coverages greater than 50 percent of saturation, shift gradually to lower temperatures. A minimum of 475K was reached at saturation. Also, with increasing exposure, the peak at 540K grows in intensity and broadens to higher temperatures. At saturation coverage, D_2 desorption continues to nearly 800K, with a slight peak near 695K.

The dominant desorption peak corresponds to initial dissociation of hydrogen from molecular benzene; the tail of continuous hydrogen evolution following this peak is due predominately to hydrogen dissociation from the remaining hydrocarbon fragments. The broadening of this desorption state to higher temperatures with increasing benzene coverage is likely due to higher dissociation energy for C-H bond scission as more dissociation sites become occupied.

Adsorption of benzene on Rh(111) between 270-320K initially produces only a weak, diffuse LEED pattern. Increasing exposure (1-3L) causes new diffuse fractional-order spots to appear, but a large background intensity is present indicating considerable disorder. The fractional-order spot intensity increased with further exposure so that

after 10L, several ordered LEED structures are visible. The quality of the pattern seen can often be improved by large exposures of 30-70L and annealing. The particular pattern observed depends sensitively on the benzene coverage which is a function of the benzene exposure, benzene background pressure, and sample temperature. We have observed patterns denoted as $(2\sqrt{3} \times 3)$-rect, $(\sqrt{7} \times \sqrt{7})$R 19.1°, (3 x 3), and c$(2\sqrt{3} \times 4)$-rect. In matrix notation, these LEED patterns are labelled respectively:

$\begin{pmatrix} 3 & 3 \\ 2 & 2 \end{pmatrix}$, $\begin{pmatrix} 3 & 2 \\ 1 & 3 \end{pmatrix}$, $\begin{pmatrix} 3 & 0 \\ 0 & 3 \end{pmatrix}$, and $\begin{pmatrix} 3 & 1 \\ 1 & 3 \end{pmatrix}$. The patterns are all related by small changes in coverage. These results are consistent with previous results reported by Lin et al. [24] where they discuss in detail the c$(2\sqrt{3} \times 4)$-rect and (3 x 3) structure, and did not choose to discuss the other less well-ordered structures sometimes encountered.

The HREEL spectra of benzene adsorbed on the Rh(111) crystal face shown in Fig. 6.2 were obtained for specular scattering at a saturation benzene coverage under conditions that produced a well ordered c$(2\sqrt{3} \times 4)$-rect LEED pattern. The dominant features are the 345 and 810 cm^{-1} losses observed for C_6H_6 (Fig. 6.2A) and the 330 and 565 cm^{-1} losses observed for C_6D_6 (Fig. 6.2B). From the isotopic shifts observed for these spectra, the losses at 810, 1130, and 3000 cm^{-1} are identified as C-H vibrations and those at 345, 550, 1320 and 1420 as Rh-C and C-C vibrations. Contamination of the Rh(111) surface by 0.01 ML CO coadsorption produced a loss peak near 1660 cm^{-1}, which is assigned to the CO stretching frequency of bridge-bonded CO [25].

Representative specular and off-specular HREEL spectra for adsorbed benzene that yields the c $(2\sqrt{3} \times 4)$-rect surface structure are shown in Fig. 6.3. The off-specular spectrum shown in Fig. 6.3 was taken after a 7.5° rotation of the Rh(111) surface normal towards the analyzer, which corresponds to 15° off-specular scattering ($\theta_i - \theta_s = 15°$). The purpose of examining the distribution of scattered electrons as a function of angle and energy is to differentiate between the two inelastic scattering processes which can be responsible for the observed electron energy losses: dipole scattering and impact scattering [26]. Losses that are the result of dipole scattering satisfy a surface dipole selection rule that only vibrational modes with dynamic dipole components perpendicular to the metal surface are observed as dipole-active. Dipole scattering produces a scattering lobe which is sharply peaked in the specular direction. Near the specular, dipole scattering is usually much more intense than impact scattering. However, for adsorbed hydrocarbons, it is possible for impact and dipole scattering contributions to be of comparable magnitude for a particular loss peak in the specular direction [27]. Thus, the observation of a weak mode on-specular does not mean that it is dipole active, and also the observation of a loss peak off-specular does not necessarily mean that the mode is not dipole-active. Detailed angular dependent studies are needed to distinguish the spectral contributions of the two inelastic scattering mechanisms in order to determine surface geometry and site symmetry.

The results for such an angular profile study of the vibrational frequencies of benzene adsorbed on Rh(111) are shown in Fig. 6.4 for the same c($2\sqrt{3}$ x 4)-rect structure. Typical changes observed are similar to those depicted in Fig. 6.3: in moving from specular to 15° off-specular, the 1130, 1320, 1420 and 3000 cm^{-1} modes decrease in intensity by factors of 1.3-2.6, while the modes at 345, 550, and 810 cm^{-1} decrease by factors of 8-18, compared to a decrease of 150-170 in the elastic peak. From the intensity variation of these losses with angle, it is clear that all seven losses have dipole scattering contributions. However, all modes, except possibly the 550 cm^{-1} vibration, also have impact scattering contribution. Furthermore, this impact contribution is substantial for the modes occurring at 1130, 1320, 1420 and 3000 cm^{-1}, as is evident in Fig. 6.4.

We can determine the adsorption geometry of the benzene molecule from these figures (Figs. 6.2, 6.3, and 6.4) by comparing these spectra with the spectrum of benzene in the gas phase [28] or liquid phase [29], and by using the surface dipole selection rule in conjunction with principles of group theory. In the gas phase, benzene has 20 fundamental vibrational frequencies, of which 10 are doubly degenerate. However, only 4 of these modes are IR active: 3 involving dipole moment changes parallel to the ring plane of the molecule (E_{1u} symmetry modes ν_{12}, ν_{13}, and ν_{14}), and one involving changes perpendicular to the ring plane (A_{2u} symmetry mode ν_4). Upon adsorption, the benzene molecule becomes fixed in space, removing the translational and rotational degrees of freedom, resulting in six additional vibrational

modes. Two of these new modes are IR active: one involving dipole moment changes perpendicular (A_{2u} symmetry mode T_z) and one involving dipole moment changes parallel (E_{1u} symmetry degenerate modes T_x and T_y) to the ring plane.

The most intense loss, already shown to be due to a C-H vibration, is assigned to the out-of-plane CH bending mode (γ_{CH}). This feature, coupled with the absence of any intense E_{1u} modes and the several other vibrations expected for upright or tilted benzene, (i.e. the A_{1g}, B_{1u} and E_{2g} modes), allow us to conclude that the benzene molecule is adsorbed with the ring plane parallel to the Rh(111) surface at 300K. The full assignment of the adsorbed benzene spectrum is given in Table 6.1. The other two modes having very strong dipolar origin (345 and 550 cm^{-1}) which shift little with deuteration, are assigned to rhodium-carbon vibrations (ν_{Rh-C}). These correspond to the vibration of the whole molecule against the surface. The remaining modes with dipolar contribution are due to motions in the ring-plane of the molecule and have relatively less intensities: 1130 cm^{-1}, C-H bend (δ_{CH}, ν_{10}); 1320 cm^{-1}, ring stretch (ν_{cc}, ν_9); 1420 cm^{-1}, ring stretch and deformation (ν_{cc}, ν_{13}); and 3000 cm^{-1}, C-H stretch (ν_{CH}, ν_1). An additional mode, visible at 835 cm^{-1} in the deuterated benzene spectrum (Fig. 6.2), is too intense to be exclusively due to the δ_{CD} mode (ν_{10}), and is assigned additionally to a molecular ring stretch (ν_{cc}, ν_2) [31]. The ν_2 vibration for C_6H_6 is difficult to see on-specular since it is under the intense γ_{CH} vibration, but is visible off-specular at 880 cm^{-1} in

Fig. 6.3. Additional modes, only visible off-specular, probably account for the additional intensity seen, especially at 780 and 990 cm^{-1}. These principally impact active modes are not assigned in Table 6.1.

As described earlier, near saturation benzene adsorption on Rh(111) at 300K can produce a variety of ordered structures. However, the vibrational spectra are very similar irrespective of the degree of ordering or the ordered structure present. For example, the C_6H_6 spectrum shown in Fig. 6.2(A) is for a well-ordered c($2\sqrt{3}$ x 4)-rect structure while the specular spectrum of Fig. 6.3 is for a less well-ordered c($2\sqrt{3}$ x 4)-rect structure. It is typical that upon partial ordering, the only change occurring is in the relative intensity of the observed losses, especially those at 1130, 1320 and 1420 cm^{-1}, which increase with increasing disorder. Figure 6.5 shows the vibrational spectra of benzene adsorbed in the c($2\sqrt{3}$ x 4)-rect and (3 x 3) structures. However, neither layer was well-ordered. The (3 x 3) layer was obtained by momentary warming of the c($2\sqrt{3}$ x 4)-rect benzene layer to 393K and waiting several hours in vacuum. Besides small changes in relative intensities and an overall decrease in total intensity for the (3 x 3) layer, no significant changes occur in the vibrational spectra as the surface structure is altered. The increase in frequency of the C-O stretch for bridge-bonded CO from 1660 to 1710 cm^{-1} and the additional C-O stretch at 1960 for linearly-bonded CO

Table 6.1. Assignment of the observed vibrational frequencies for benzene chemisorbed on Rh(111). The gas phase frequencies for C_6H_6 and C_6D_6 are included for comparison. All frequencies are given in units of cm^{-1}.

mode number (Herzberg [30]) and representation		Mode type	Gas phase frequencies [28] $C_6H_6(C_6D_6)$	C_6H_6/C_6D_6 Ratio	Chemisorbed Frequencies $C_6H_6(C_6D_6)$	C_6H_6/C_6D_6 Ratio
ν_1	A_{1g}	CH stretch	3062(2293)	1.34	3000(2250)	1.33
ν_2	A_{1g}	ring stretch	992(943)	1.05	880(835)	1.05
ν_3	A_{2g}	CH bend	1326(1037)	1.28	--	--
ν_4	A_{2u}	CH bend	673(497)	1.35	810(565)	1.41
ν_5	B_{1u}	CH stretch	3068(2292)	1.34	--	--
ν_6	B_{1u}	ring deform.	1010(969)	1.04	--	--
ν_7	B_{2g}	CH bend	995(827)	1.20	--	--
ν_8	B_{2g}	ring deform.	703(601)	1.17	--	--
ν_9	B_{2u}	ring stretch	1310(1286)	1.02	1320(1320)	1.00
ν_{10}	B_{2u}	CH bend	1150(824)	1.40	1130(835)	1.35
ν_{11}	E_{1g}	CH bend	849(662)	1.28	--	--
ν_{12}	E_{1u}	CH stretch	3063(2287)	1.34	--	--
ν_{13}	E_{1u}	ring str. and deform.	1486(1335)	1.11	1420(1365)	1.04
ν_{14}	E_{1u}	CH bend	1038(814)	1.28	--	--
ν_{15}	E_{2g}	CH stretch	3047(2265)	1.35	--	--
ν_{16}	E_{2g}	ring stretch	1596(1552)	1.03	--	--
ν_{17}	E_{2g}	CH bend	1178(867)	1.36	--	--
ν_{18}	E_{2g}	ring deform	606(577)	1.05	--	--
ν_{19}	E_{2u}	CH bend	975(795)	1.23	--	--
ν_{20}	E_{2u}	ring deform	410(352)	1.16	--	--
		RhC stretch	---	--	550(550)	1.00
		RhC stretch	---	--	345(330)	1.05

occur because the surface was exposed to the background (mostly CO) for a prolonged period, and additional clean surface sites become available as molecular benzene desorbs upon warming the surface to 393K (see Fig. 6.1(A)). The small changes in frequency observed for the benzene modes are also seen for unstructured layers produced at subsaturation exposures, as is evidenced in Fig. 6.6.

Vibrational spectra obtained at benzene coverages less than saturation show important differences when compared to the saturation spectra of Figs. 6.2 and 6.3. This is evident in Fig. 6.6 where the HREEL spectra for benzene adsorption on Rh(111) is plotted as a function of coverage. Most prevalent in the spectra at 0.5 and 1.5L are the linearly-bonded CO stretching vibrations at 2030-2015 cm^{-1}, and the Rh-CO stretching vibrations at 485 cm^{-1}. The mode at 550 cm^{-1} is partially obscured by the ν_{Rh-CO} mode at 485 cm^{-1}, but does seem to increase in intensity with coverage. The lowest energy ν_{Rh-C} mode, occurring at 345 cm^{-1} for saturation benzene coverage, is shifted to 340 cm^{-1} at 1.5-3.0L and to 330 cm^{-1} at 0.5L. Associated with this increase in frequency with coverage are frequency shifts of similar magnitude for the modes near 810 and 3000 cm^{-1}. At low coverage, the ν_{CH} loss peak occurs at 3030 cm^{-1} and has a FWHM near the instrumental resolution of the elastic peak, which is much narrower than this same mode at saturation coverage where ν_{CH} broadens to 97 cm^{-1}, twice that of the instrumental resolution used. Similar changes are seen for the γ_{CH} loss, although the frequency here increases with coverage. A high frequency shoulder exists on

this peak, which grows with increasing coverage and dominates the spectrum by saturation. Figure 6.7 shows that at saturation, the peak labeled at 810 in Figs. 6.2 or 6.3 is actually composed of two peaks of frequencies 776 and 819 cm^{-1}, when observed with a resolution of 27 cm^{-1} (FWHM). At low coverage the intensity ratio (I_{776}/I_{819}) is clearly greater than 4, but decreases to 0.3 at saturation (see Fig. 6.7). This ratio changes again to 1.6 as the saturation layer is warmed to 390K. The changes observed imply no large variation in bonding with benzene exposure, however, the presence of two kinds of chemisorbed benzene are indicated by the data. The other loss peaks in the spectra of Fig. 6.6 are quite weak and change little in vibrational energy or relative intensity as a function of coverage.

FIGURE CAPTIONS

Fig. 6.1. Temperature programmed desorption (TPD) spectra of (A) C_6H_6 and (B) D_2 following adsorption of (A) benzene or (B) benzene-d_6 on Rh(111) near 300K measured as a function of benzene exposure. The heating rate used was linear at 15 K/sec.

Fig. 6.2. Vibrational spectra obtained by HREELS in the specular direction for a saturation coverage of benzene chemisorbed on Rh(111) at 300K for a well-ordered c($2\sqrt{3}$ x 4)-rect surface structure: (A) C_6H_6; (B) C_6D_6.

Fig. 6.3. HREEL spectra obtained for specular and 15° off specular scattering angles (i.e. $\theta_i = \theta_s = 60°$ and $\theta_i = 67.5°$, $\theta_s = 52.5°$, respectively). The Rh(111) surface was saturated with benzene (C_6H_6) to produce the c($2\sqrt{3}$ x 4)-rect structure, but in this case the pattern was not so well-ordered as for Fig. 6.2.

Fig. 6.4. Absolute intensities of the vibrational frequencies observed for saturation benzene adsorption on Rh(111) at 300K, plotted as a function of $\theta_s-\theta_i$. The elastic peak angular dependence is shown for comparison. Both the incident and the scattered angles are changed equally in magnitude but in opposite direction from the specular geometry of $\theta_i=\theta_s = 60°$ (i.e. the total scattering angle is fixed at 120°).

Fig. 6.5. Vibrational spectra for two of the structures produced after benzene adsorption on Rh(111): (A) c($2\sqrt{3}$ x 4)-rect, after saturation adsorption at 300K, (B) (3 x 3), after warming the layer in (A) to 393K and waiting several hours.

Fig. 6.6. HREEL spectra obtained at 300K as a function of benzene exposure. Large variations in the scattered elastic peak intensity were observed as a function of benzene coverage.

Fig. 6.7. HREEL spectra obtained at 27 cm^{-1} resolution for the ν_{CH} mode of benzene adsorbed at (A) 300K and (B) after heating to 390K. Spectra were recorded on an expanded scale.

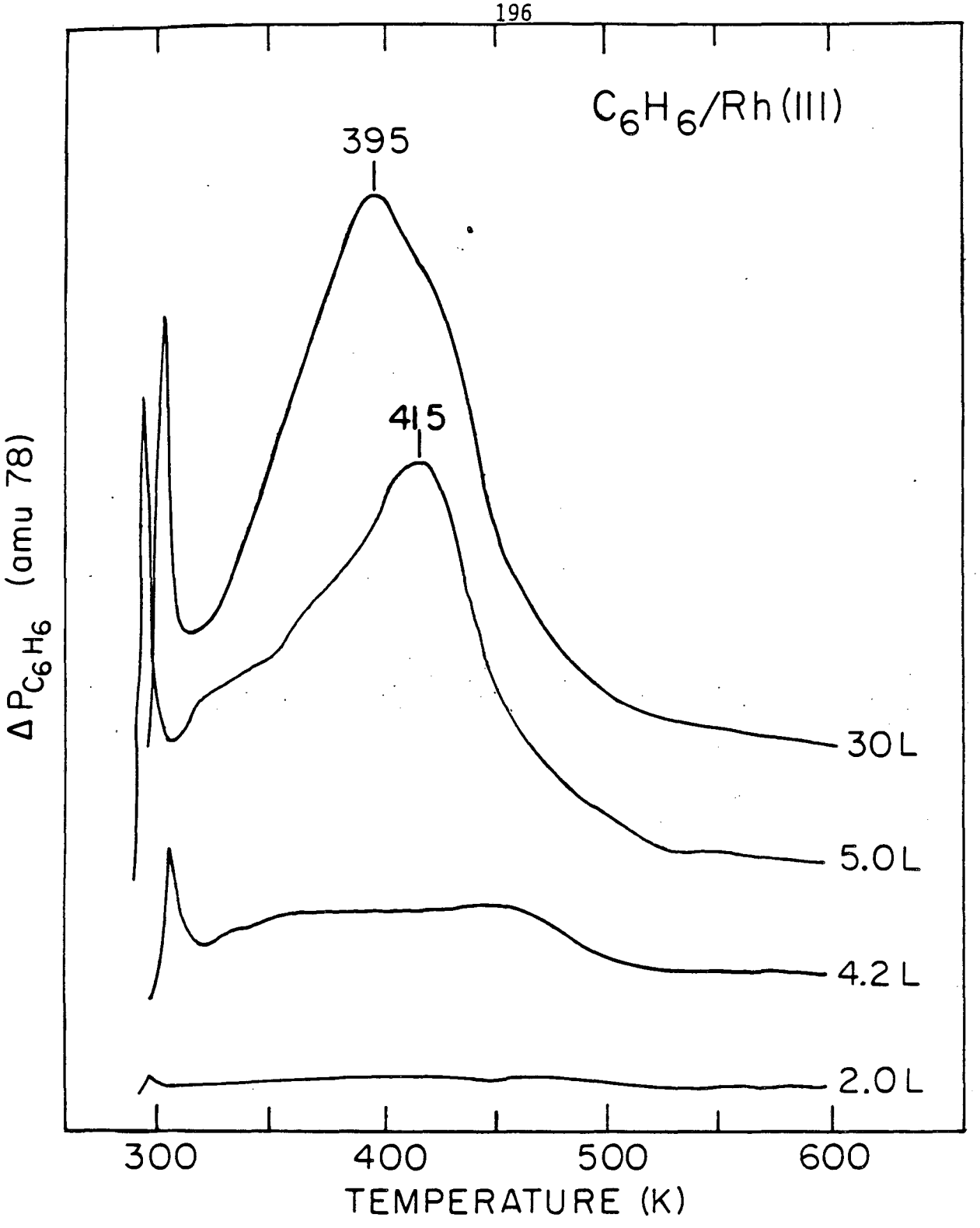

Figure 6.1A

XBL838-6201

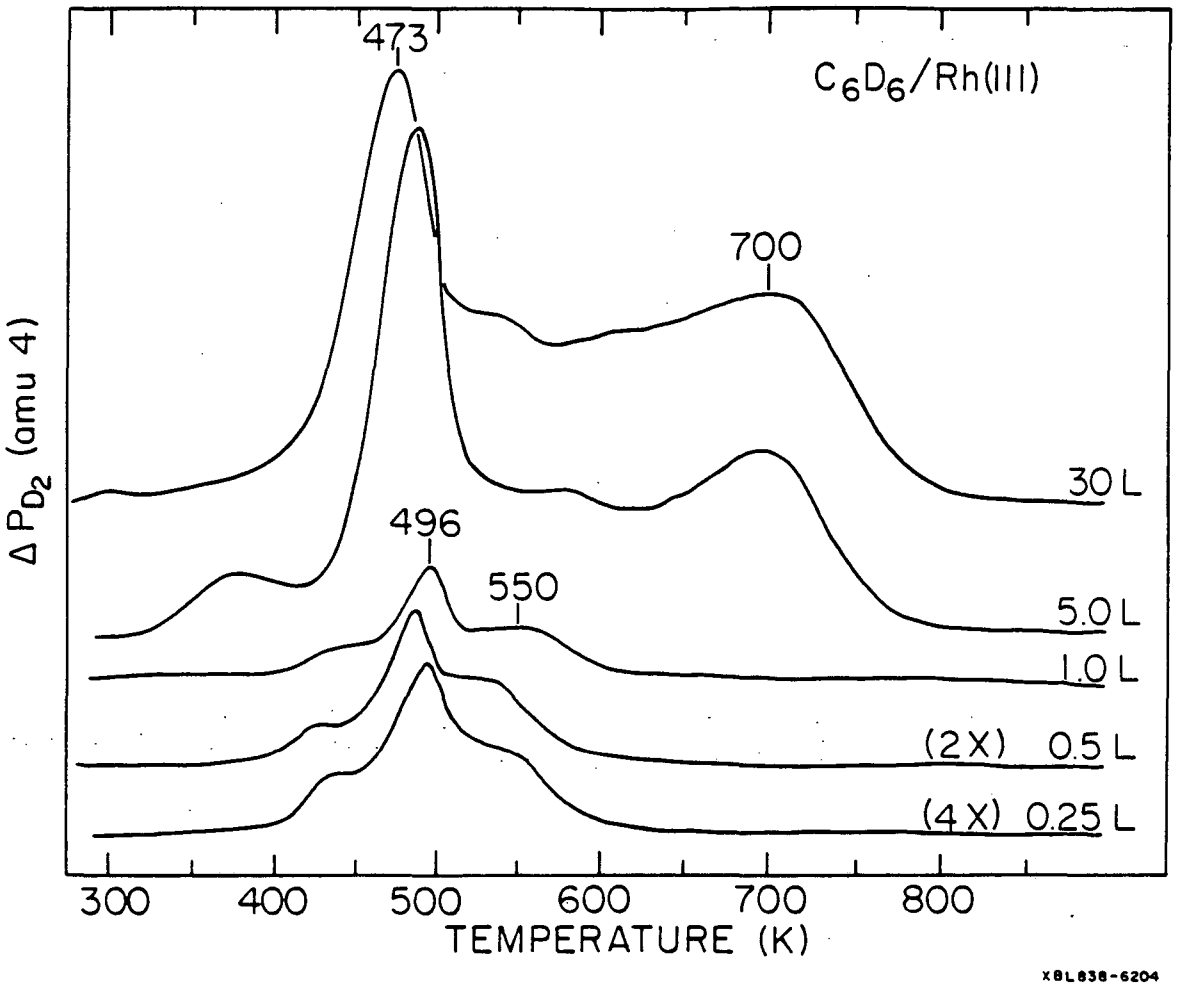
473
700
496
550
C_6D_6/Rh(111)
30 L
5.0 L
1.0 L
(2X) 0.5 L
(4X) 0.25 L
ΔP_{D_2} (amu 4)
300
400
500
600
700
800
TEMPERATURE (K)
XBL838-6204

Figure 6.1B

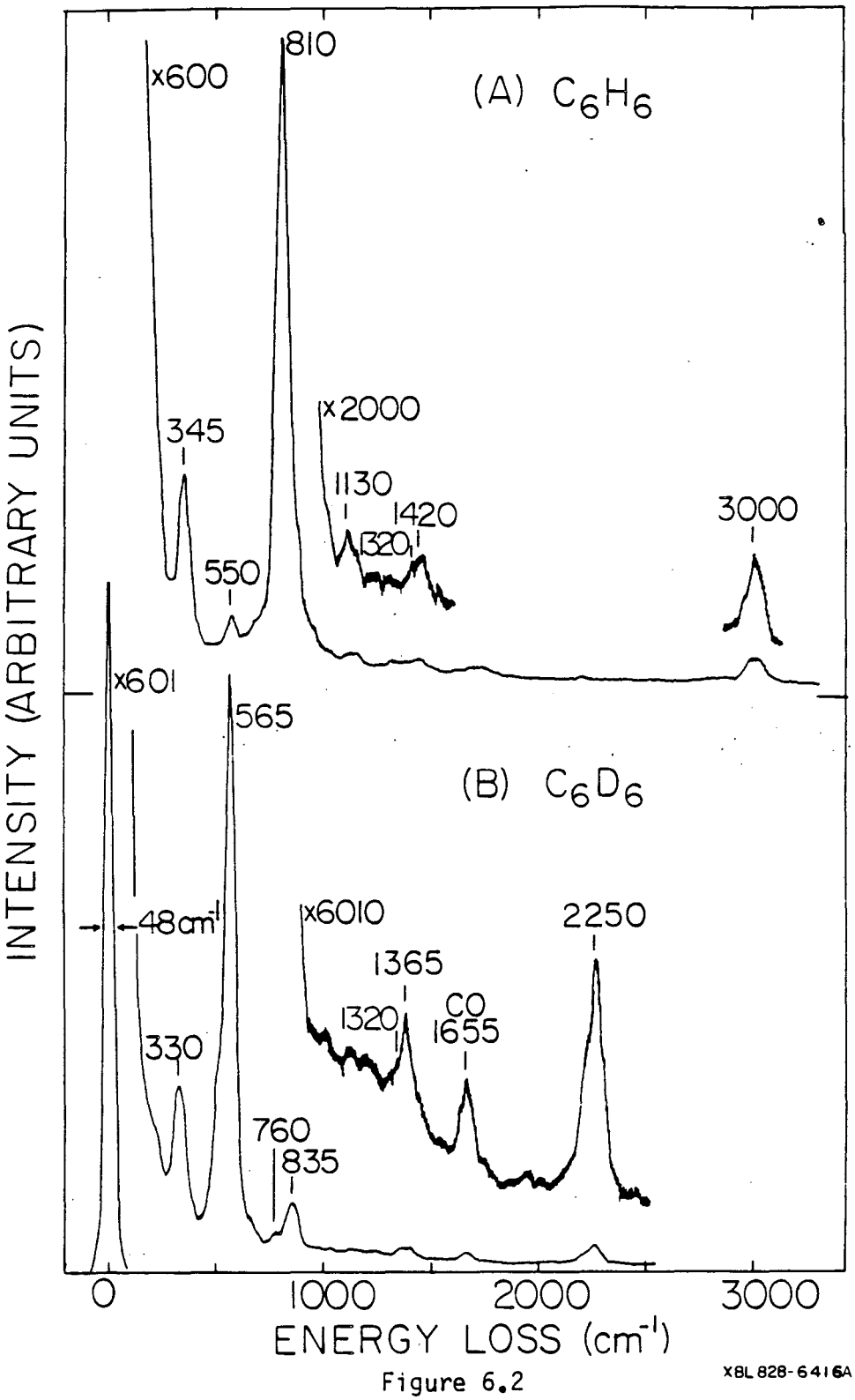
(A) C_6H_6
x600
810
345
550
x2000
1130
1420
1320
3000
(B) C_6D_6
x601
565
48cm⁻¹
330
760
835
x6010
1365
1320
CO
1655
2250
INTENSITY (ARBITRARY UNITS)
0
1000
2000
3000
ENERGY LOSS (cm⁻¹)
X8L828-6416A

Figure 6.2

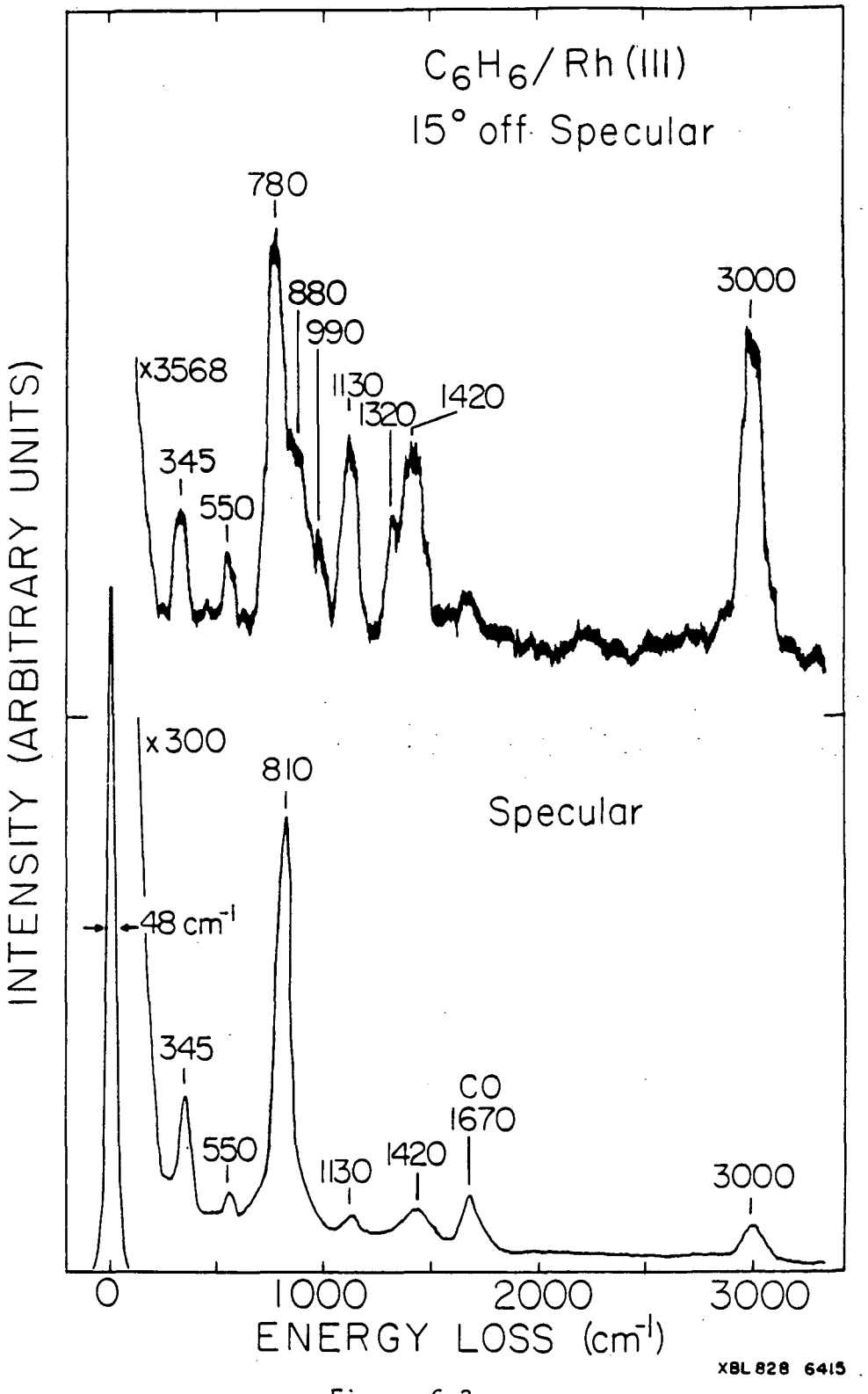
C6H6/Rh(111)
15° off Specular
780
880
990
1130
1320
1420
3000
x3568
345
550
x300
810
Specular
48 cm-1
345
550
1130
1420
CO
1670
3000
INTENSITY (ARBITRARY UNITS)
0
1000
2000
3000
ENERGY LOSS (cm-1)
XBL 828 6415

Figure 6.3

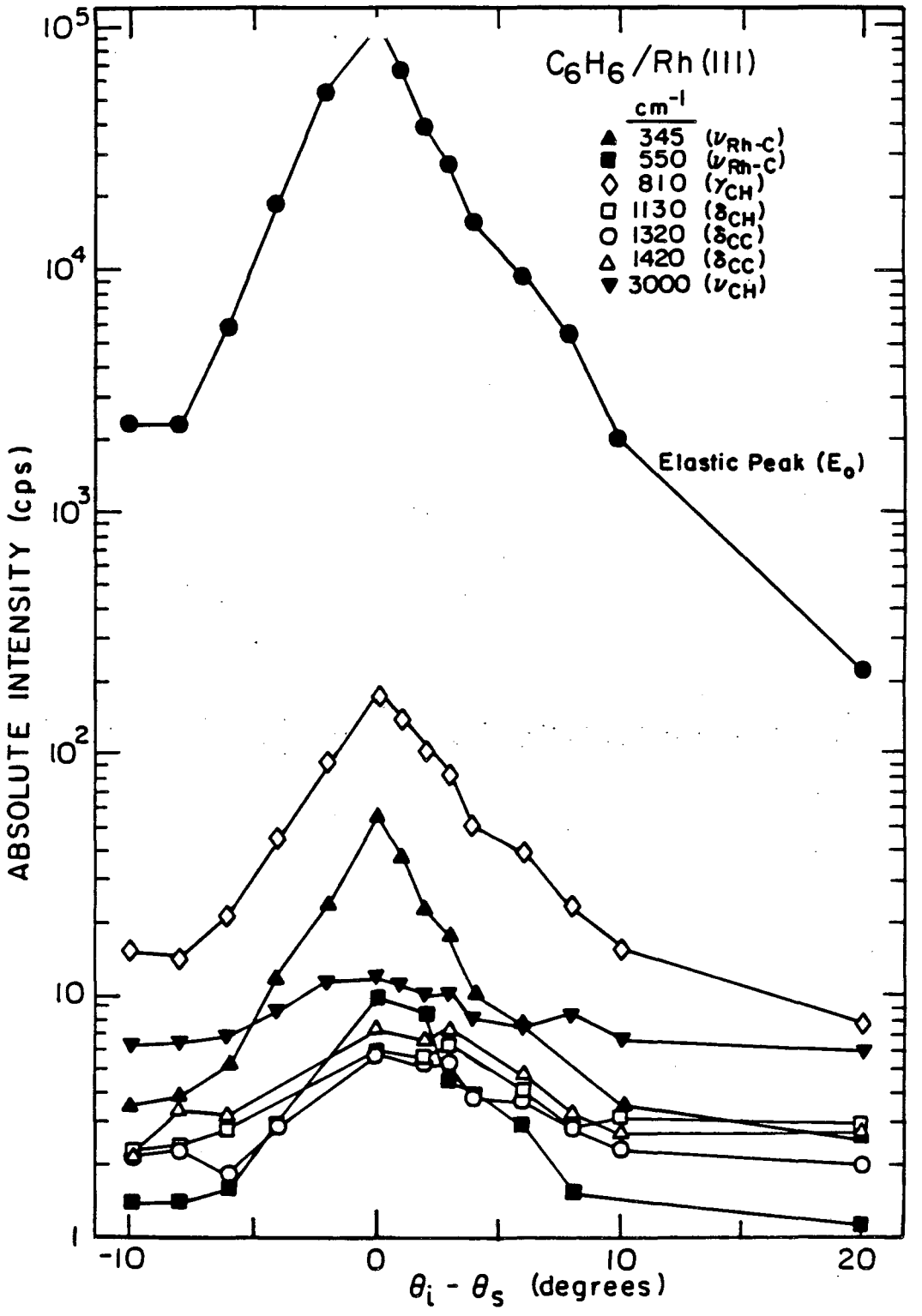

Figure 6.4

XBL 838-6208

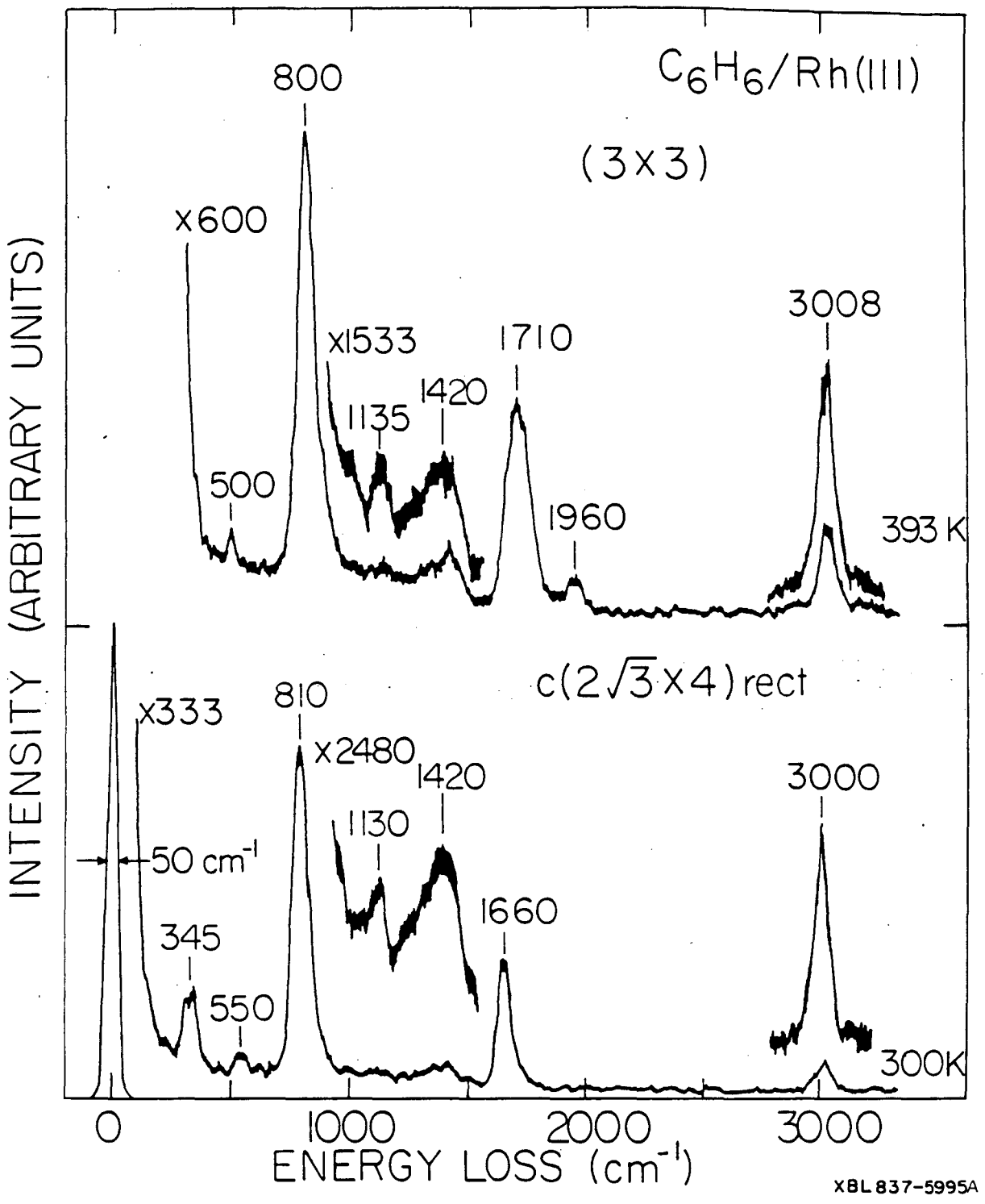
C6H6/Rh(111)
(3x3)
800
x600
500
x1533
1135
1420
1710
1960
3008
393 K
c(2√3x4)rect
x333
810
x2480
1130
1420
1660
3000
50 cm-1
345
550
300K
INTENSITY (ARBITRARY UNITS)
0
1000
2000
3000
ENERGY LOSS (cm-1)
XBL837-5995A

Figure 6.5

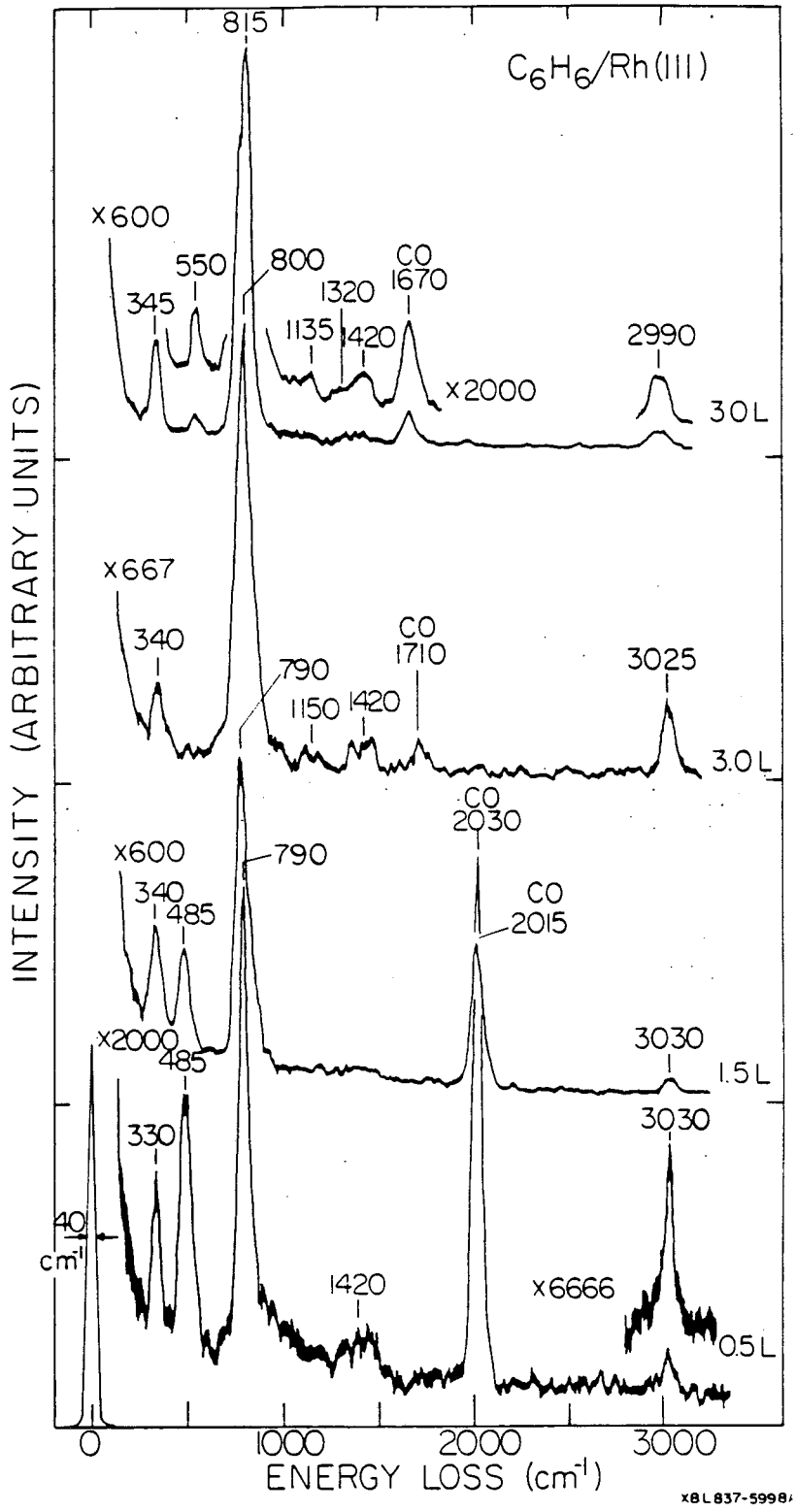
815
C6H6/Rh(111)
x600
550
800
CO
1670
345
1320
1135
1420
2990
x2000
3.0 L
x667
340
CO
1710
790
3025
1150
1420
3.0 L
CO
2030
x600
790
340
485
CO
2015
x2000
485
3030
1.5 L
330
3030
40
cm-1
1420
x6666
0.5 L
INTENSITY (ARBITRARY UNITS)
0
1000
2000
3000
ENERGY LOSS (cm-1)
XBL837-5998

Figure 6.6

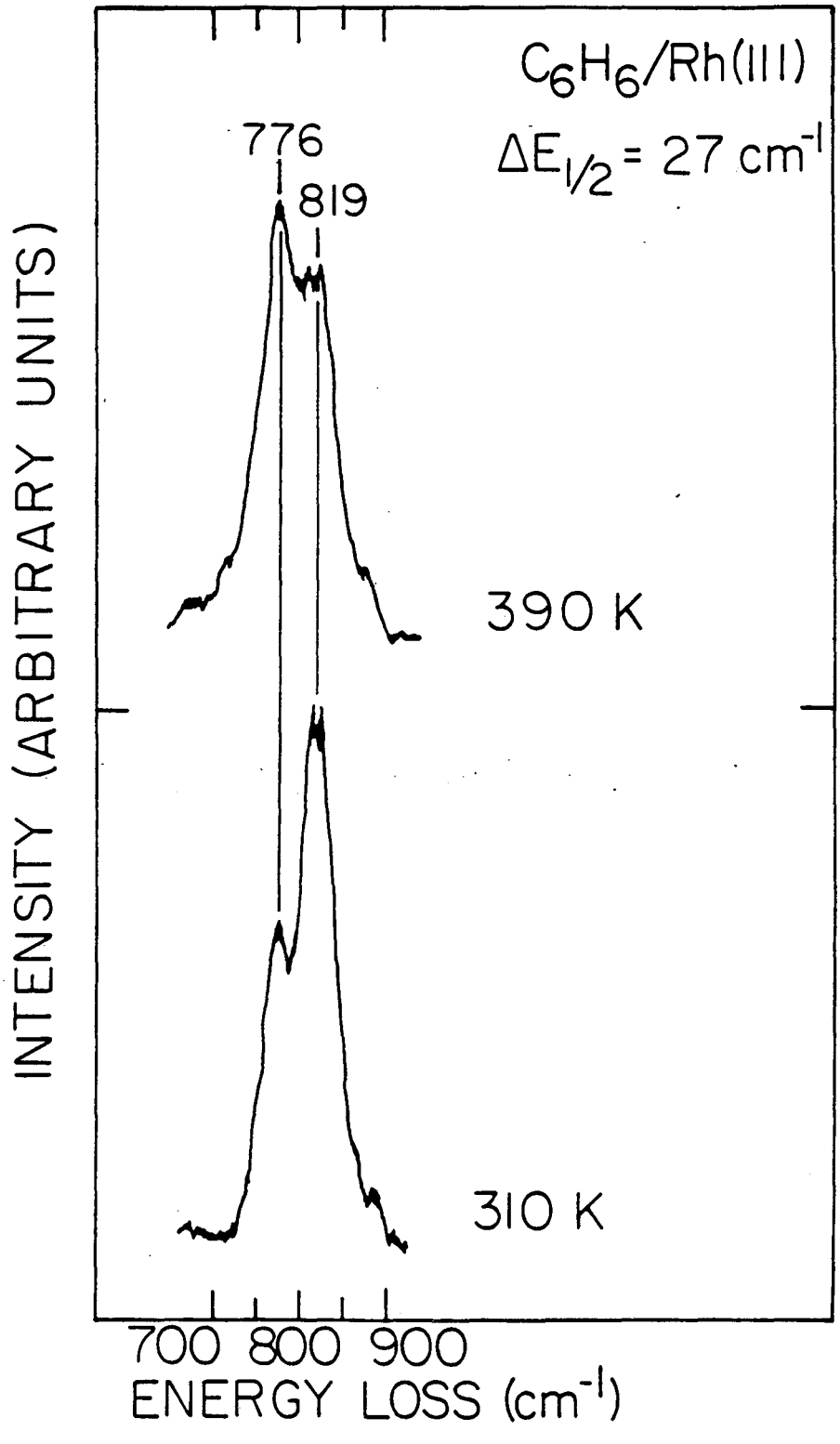

XBL 837-5996

Figure 6.7

6.2.2b. Thermal Decomposition of Adsorbed Benzene on Rh(111).

The c($2\sqrt{3}$ x 4)-rect structure of benzene was stable up to 360K. Near 363K the structure would start to disorder, or form a mixed phase between the c($2\sqrt{3}$ x 4)-rect and a new (3 x 3) structure. Near 390K, a diffuse (3 x 3) structure was occasionally produced. Heating above 395K caused complete disordering in all cases. This behavior is consistent with the results reported by Lin et al. [24] for preparation of the c($2\sqrt{3}$ x 4)-rect structure. However, they report the preparation of a single phase that gave a well-ordered (3 x 3) structure at 363K, a similarly well-ordered (3 x 3) phase was not produced in this study.

The disordering of the LEED pattern at 393K coincides with the onset of the H_2 desorption state with T_p = 450K and gives the temperature where significant benzene dehydrogenation begins. For instance, 40 percent of the surface hydrogen originating from benzene decomposition can be removed by momentary warming of the sample to 420K, as measured from TPD peak areas. This leaves only the high temperature H_2 desorption states at 500-700K, and a layer with a stoichiometry of C/H = 2. The C/H ratio of this layer can be steadily increased by increasing the temperature, and as shown in Fig. 6.1. dehydrogenation occurs until 800K where all hydrogen has been removed leaving only a carbon covered surface.

Figures 6.8 and 6.9 show a series of HREEL spectra taken sequentially after a saturation coverage of benzene on Rh(111) was warmed stepwise to 800K. The crystal was allowed to cool to 300K

during the time the spectra were obtained. Vibrational spectra were obtained approximately every 20K, from 290K to 390K. Only slight changes occur up to 390K. Specifically, the strong γ_{CH} peak at 815 cm^{-1} shifts apparently to 810 cm^{-1}, due to the decreased intensity of the 819 cm^{-1} loss relative to the 776 cm^{-1} loss, as shown in Fig. 6.7. For an ~10 percent decrease in benzene coverage caused by heating to 390K (Fig. 6.1(A)), we would expect an increase in the intensity ratio I_{776}/I_{819} if the intensity variations seen with increasing coverage (Fig. 6.6) were reversible. The magnitude of this shift (I_{776}/I_{819} changes from 0.3 to 1.6 as one heats from 310 to 390K) seems larger than expected for a 10 percent change in coverage, probably due to the onset of decomposition for which a new mode grows in at this frequency. This will become evident below. The ν_{CH} peak at 2988 cm^{-1} does not change measurably in width or position [32]. The contaminant CO peak increases slightly in intensity consistent with the TPD results indicating a small amount of C_6H_6 desorption is occurring.

Heating to 410K causes significant benzene dehydrogenation. TPD shows that the largest H_2 desorption state at 450K is completely removed by momentary warming to 420K, as shown in Fig. 6.11. Changes seen in the HREEL spectrum (Fig. 6.9) indicate partial formation of C_xH fragments (where x = 1, 2). In particular, the dominant peak in the spectrum is now centered at 790 cm^{-1}. This peak still may have significant contributions from molecular benzene (γ_{CH}), but is also attributed to the CH bending mode (δ_{CH}) of C_xH species produced

from benzene dehydrogenation. Concurrently, the CH stretching vibration broadens to lower frequency as a new ν_{CH} loss begins to grow in. This can be seen more clearly in Fig. 6.10 where the ν_{CH} vibrations are shown on an expanded scale. As seen here, π-bonded benzene at saturation coverage has ν_{CH} at 2988 cm^{-1} with the full width at half maximum twice that of the instrumental resolution. Upon warming this layer to 410K, two losses are seen in this region at 2928 and 3008 cm^{-1}. We assign both of these losses to ν_{CH} modes of C_xH fragments, although a significant contribution may still exist from molecular benzene. Clearly, the other modes expected for benzene still exist at 339, 524, 1113, 1330 and 1428 cm^{-1}, although shifted from their higher coverage position. Finally, the appearance of CO in on-top sites (ν_{CO} = 1936 cm^{-1}) indicates a chemical change on the surface. With further heating (not shown in Fig. 6.9), a 60 cm^{-1} shift in ν_{CO} for bridge-bonded CO occurs accompanied by a large shift in population to the on-top site. One explanation for these changes is that the π donation of the benzene molecule to the Rh(111) surface, responsible for the perturbation of the CO bonding, has dramatically decreased.

The rationale for the above assignments becomes more understandable as the layer is heated to 470K. This causes further hydrogen evolution, pushing the onset of hydrogen desorption to higher temperature similar to that shown already in Fig. 6.11. At this point molecular benzene desorption is complete, and the remaining layer has lost more than 50 percent of the surface complex hydrogen. Hence, we

assume that every benzene molecule which did not desorb molecularly has undergone partial dehydrogenation. Inspection of Figs. 6.9 and 6.10 show that vibrational losses exist at 476, 807, 1363, 2928 and 3008 cm^{-1}. The loss at 807 cm^{-1} has certainly broadened to higher energy with further heating and more clearly consists of two vibrations. The off-specular spectrum, shown in Fig. 6.12 in comparison to the reproduced specular spectrum, permits better separation of these δ_{CH} losses at 766 and 831 cm^{-1}. Additionally, Fig. 6.10 shows that the relative intensity of the ν_{CH} mode at 2928 cm^{-1} has increased. Since chemisorbed benzene no longer exists on the surface, all four of these vibrations (i.e. the two δ_{CH} losses at 766 and 831 cm^{-1} and the two ν_{CH} losses at 2928 and 3008 cm^{-1}) must be due to fragments produced from benzene dehydrogenation. From a comparison with the vibrational spectrum of $HCCo_3(CO)_9$ [33], which has two CH modes (δ_{CH} at 850 cm^{-1} and ν_{CH} at 3041 cm^{-1}), we conclude these observed losses are due to C_xH species. Curiously, the two vibrations at 831 and 2928 cm^{-1}, which grow in upon heating from 410 to 470K, seem to be correlated. These peaks are shifted in frequency in different directions with respect to the vibrations at 766 and 3008 cm^{-1}. This shift can be associated with a slight increase in hybridization. Such a change is expected if further C-C bond scission occurs upon heating to 470K, reducing some C_2H fragments to CH species. These frequency shifts can alternatively be rationalized in terms of a change in bonding to the metal through an increase in coordination.

The vibrations at 323 and 476 cm^{-1} are assigned to ν_{Rh-C} modes, yet are shifted from the frequencies at 410K. The broad peak centered near 1363 cm^{-1} may be decomposed into two peaks, as shown in the off-specular measurement of Fig. 6.12. This mode (1363 cm^{-1}) is likely due to ν_{CC} vibrations, but the origin of the remaining vibrations not associated with C_xH fragments is less obvious. The formation of a CH_2 group from the self-hydrogenating disproportionation of adsorbed CH species has been postulated previously [34], and could account for the observed vibrations. However, the extremely weak intensity of these modes indicates that CH (and/or C_2H) is the dominant fragment(s) produced.

Upon heating to 570K, the δ_{CH} losses both decrease in intensity. Furthermore, the peak width of the combined vibrations decreases, although the peak position remains constant (δ_{CH} = 807 cm^{-1} in Fig. 6.9). The 2928 cm^{-1} CH stretching vibration has decreased dramatically with the observed loss increasing to 3020 cm^{-1}. The broad ν_{CC} mode is still present, shifted to 1290 cm^{-1}, while the M-C vibration decreases in intensity at 490 cm^{-1}. A change in bonding is indicated by the frequency shifts, but the two dominant modes observed still indicate that CH species are present and are resistive to dehydrogenation at this temperature.

The adsorbed layer totally dehydrogenates upon heating to 800K, as evidenced by TPD (Fig. 6.11) and the lack of any CH stretching vibrations (Fig. 6.9). Only a broad shoulder from 350-650 cm^{-1} and a broad peak centered at 1265 cm^{-1} are observed. The broad bands

are characteristic of the carbonaceous residue formed from alkene decomposition [35]. In addition, these same broad bands are observed from ordered incommensurate graphitic overlayers formed on Rh(111). Such an overlayer, formed by exposing Rh(111) to deuterated propylene-d_6 (C_3D_6) at 1075K, then flashing momentarily to 1075K to remove any additional hydrocarbons adsorbed from the background, is shown in Fig. 6.13. The high background intensity is typical for high carbon-covered overlayers. Graphite formation from a single hydrocarbon monolayer is difficult due to dissolution of carbon into the bulk on Rh(111) at these temperatures. Hence, prolonged exposure at 800K was needed to produce the graphite layer.

It is interesting to follow the ν_{CC} frequency in Fig. 6.9 all of the way from molecular benzene to the carbonaceous residues. Upon the initiation of dehydrogenation, the ν_{CC} mode at 1420 cm^{-1} broadens to lower temperature, indicating an increase in hybridization toward sp^3 for the ring carbon atoms. Heating to 470K, which removes more than 50 percent of the surface complex hydrogen, as measured from TPD peak areas, causes a shift to 1363 cm^{-1}. No molecular benzene remains, but a ν_{CC} peak is clearly present and well-defined. Heating to 800K broadens this peak and shifts the center of the loss to 1265 cm^{-1}. The position of ν_{CC} after heating to 470K or above agrees well with spectra from alkene decomposition. One explanation for the broadening and shift of the ν_{CC} mode is that at temperatures near 470K, Rh-C interactions dominate the structure of the adlayer and the ν_{CC} modes are well-defined. Above 500K, C-C interactions become

dominant and the adlayer structure becomes incommensurate with the substrate allowing for a variety of chemical environments for the carbon atoms. This broadens the ν_{CC} loss, shifts it to lower frequency, and decreases the intensity (due to weaker Rh-C coupling).

FIGURE CAPTIONS

Fig. 6.8 HREEL spectra taken following step-wise warming of the surface after a saturation coverage of benzene had been obtained on Rh(111) at 300K. The surface layer was momentarily warmed to the temperature indicated, then allowed to cool to 300K. All spectra were recorded near 300K.

Fig. 6.9. HREEL spectra recorded near 300K following step-wise warming of a saturation benzene overlayer, identical to that in Fig. 6.8.

Fig. 6.10. The ν_{CH} region shown on an expanded scale, for heating of the benzene monolayer as in Fig. 6.8 and 6.9.

Fig. 6.11. TPD spectra obtained for H_2 desorption from Rh(111): (A) after benzene adsorption at 300K and (B) after benzene adsorption at 300K followed by momentary warming of this layer to 420K.

Fig. 6.12. HREEL spectra recorded after momentary warming a Rh(111) surface saturated with benzene at 300K to 470K: obtained at (A) specular and (B) 20° off-specular scattering angles. All spectra were recorded at 300K.

Fig. 6.13. HREEL spectrum of a graphitic overlayer on Rh(111) at 300K. The ordered (12 x 12) incommensurate graphite layer was produced by exposing the clean Rh(111) sample maintained at 1075K to 2 x 10^{-7} torr C_3D_6 for 10 minutes. After achieving ultra-high vacuum pressure and a crystal

temperature of 300K, the graphitic layer was warmed momentarily to 1075K to remove C_3D_6 adsorbed from the background.

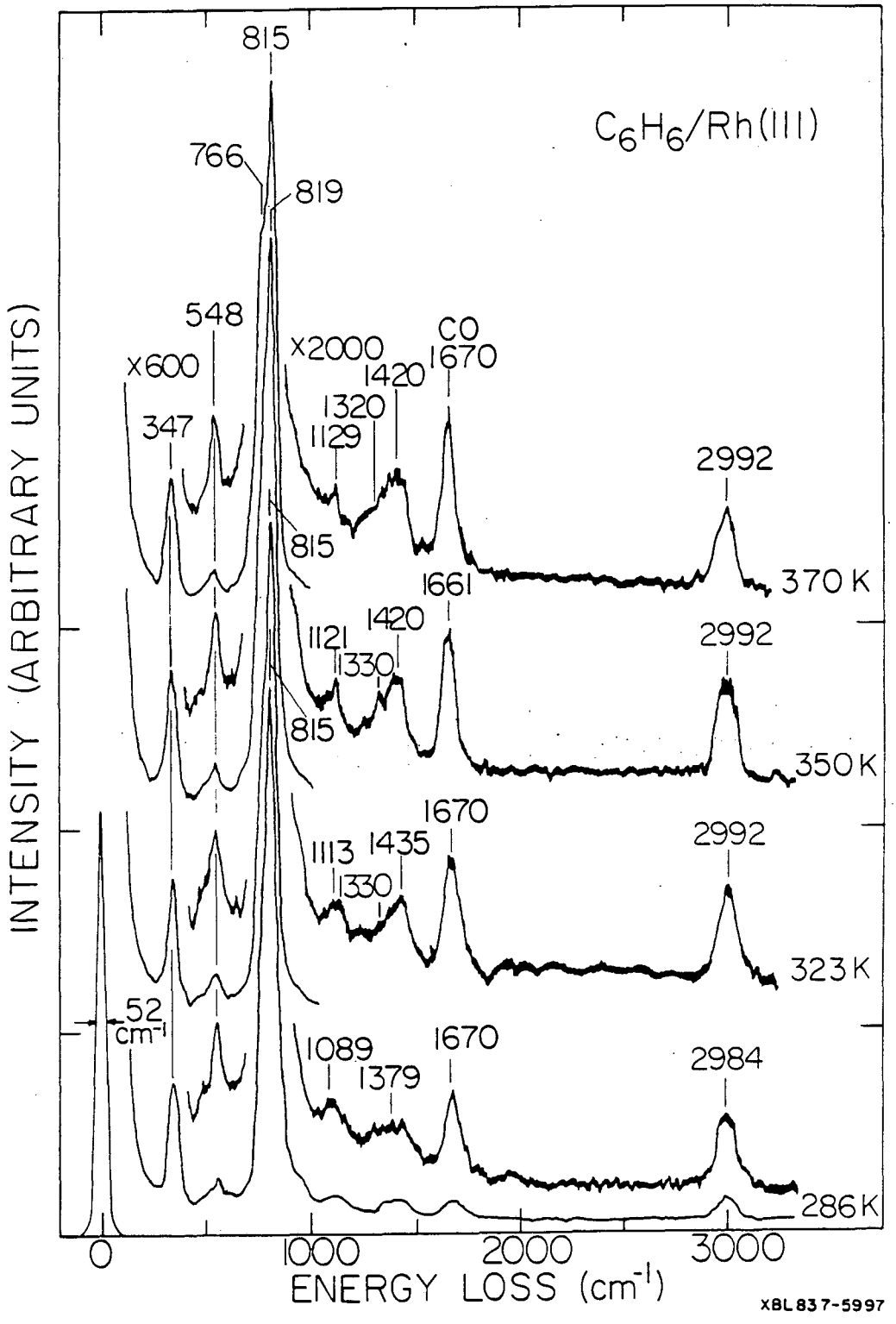
815
766
819
548
x600
x2000
CO
1670
1420
1320
1129
347
2992
815
370 K
1661
1420
1121
1330
2992
815
350K
1670
1113
1435
1330
2992
323K
52
cm⁻¹
1089
1670
1379
2984
286K
0
1000
2000
3000
ENERGY LOSS (cm⁻¹)
INTENSITY (ARBITRARY UNITS)
C6H6/Rh(111)
XBL837-5997

Figure 6.8

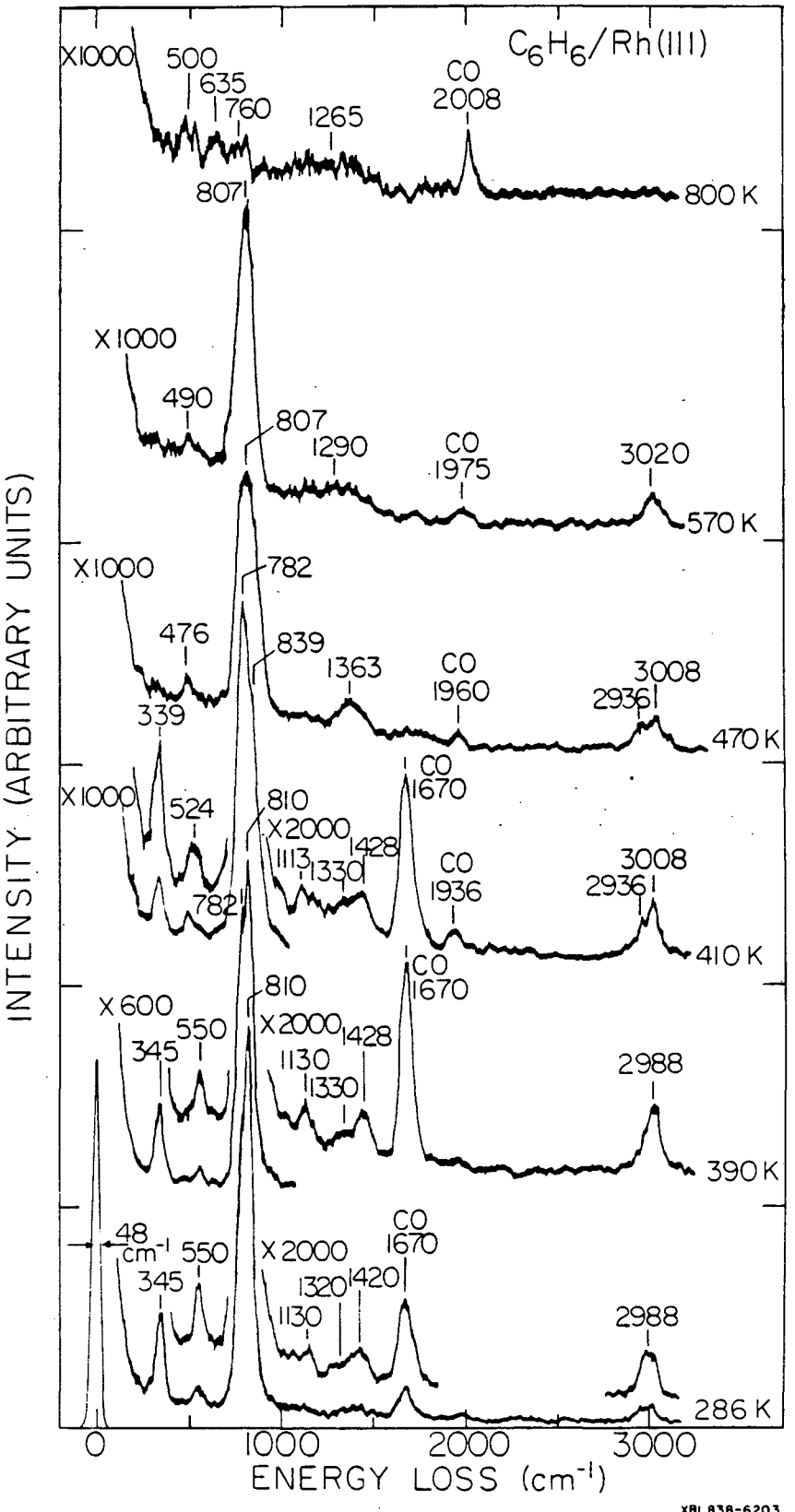
C6H6/Rh(111)
X1000
500
635
760
1265
CO
2008
807
800 K
X1000
490
807
1290
CO
1975
3020
570 K
X1000
782
476
839
1363
CO
1960
3008
2936
339
470 K
X1000
524
810
X2000
1113
1330
1428
CO
1670
CO
1936
3008
2936
782
410 K
X600
550
345
810
X2000
1428
1130
1330
CO
1670
2988
390 K
48 cm-1
550
345
X2000
CO
1670
1320
1420
1130
2988
286 K
INTENSITY (ARBITRARY UNITS)
0
1000
2000
3000
ENERGY LOSS (cm-1)
XBL838-6203

Figure 6.9

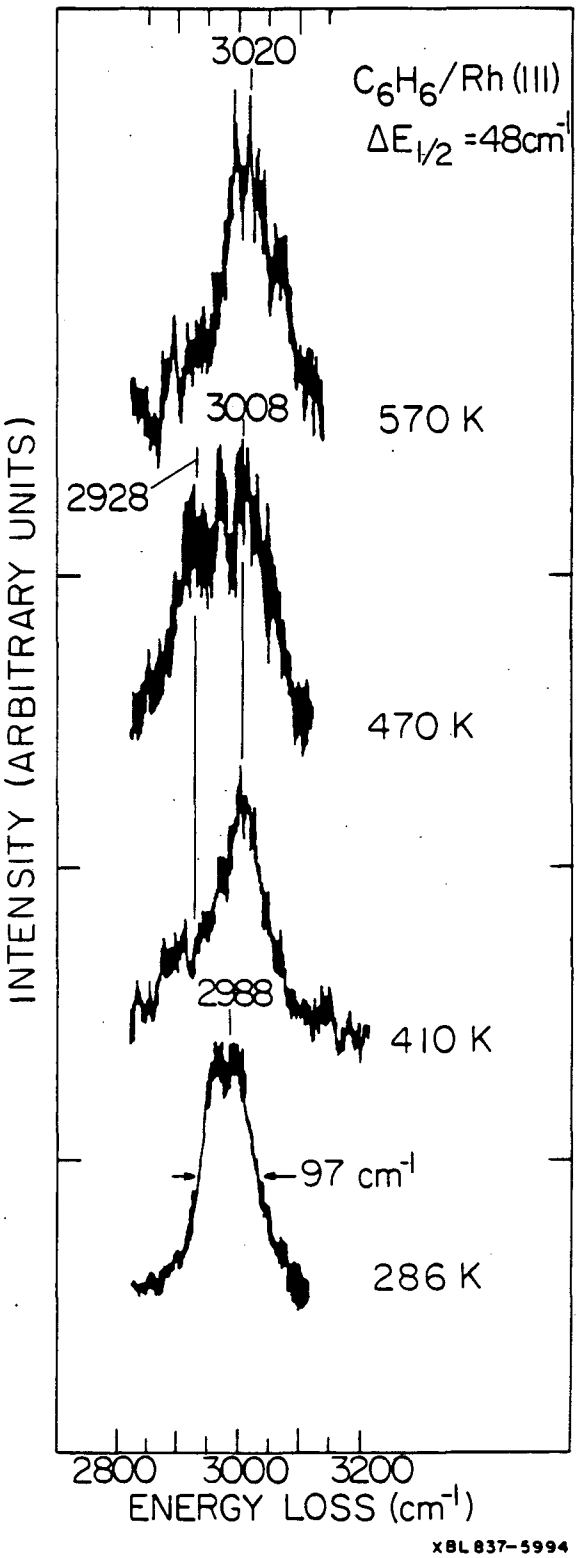
3020
C_6H_6/Rh (111)
$\Delta E_{1/2}$ =48cm^{-1}
3008
570 K
2928
470 K
2988
410 K
97 cm^{-1}
286 K
INTENSITY (ARBITRARY UNITS)
2800
3000
3200
ENERGY LOSS (cm^{-1})
XBL 837-5994

Figure 6.10

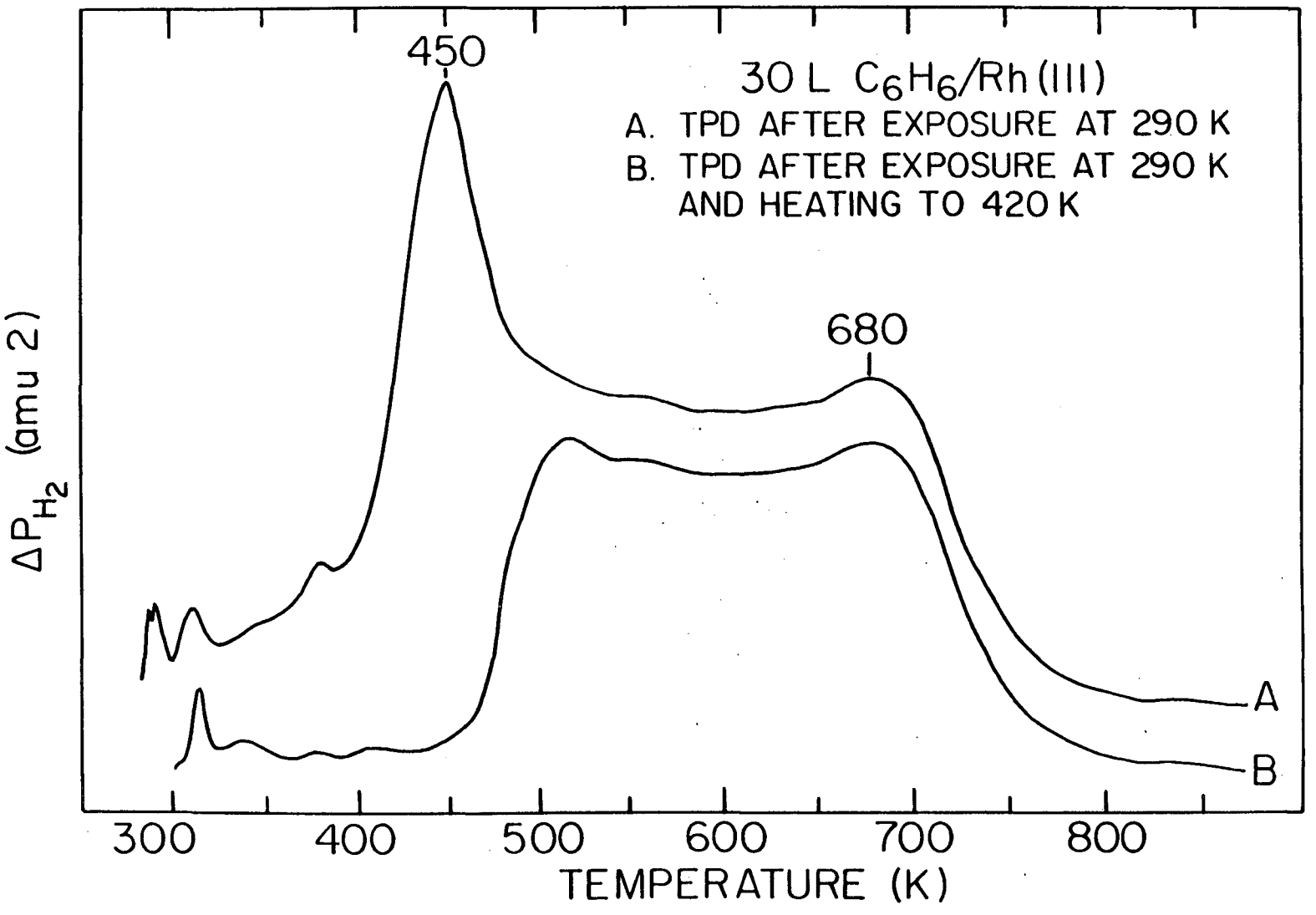

Figure 6.11

XBL838-6205

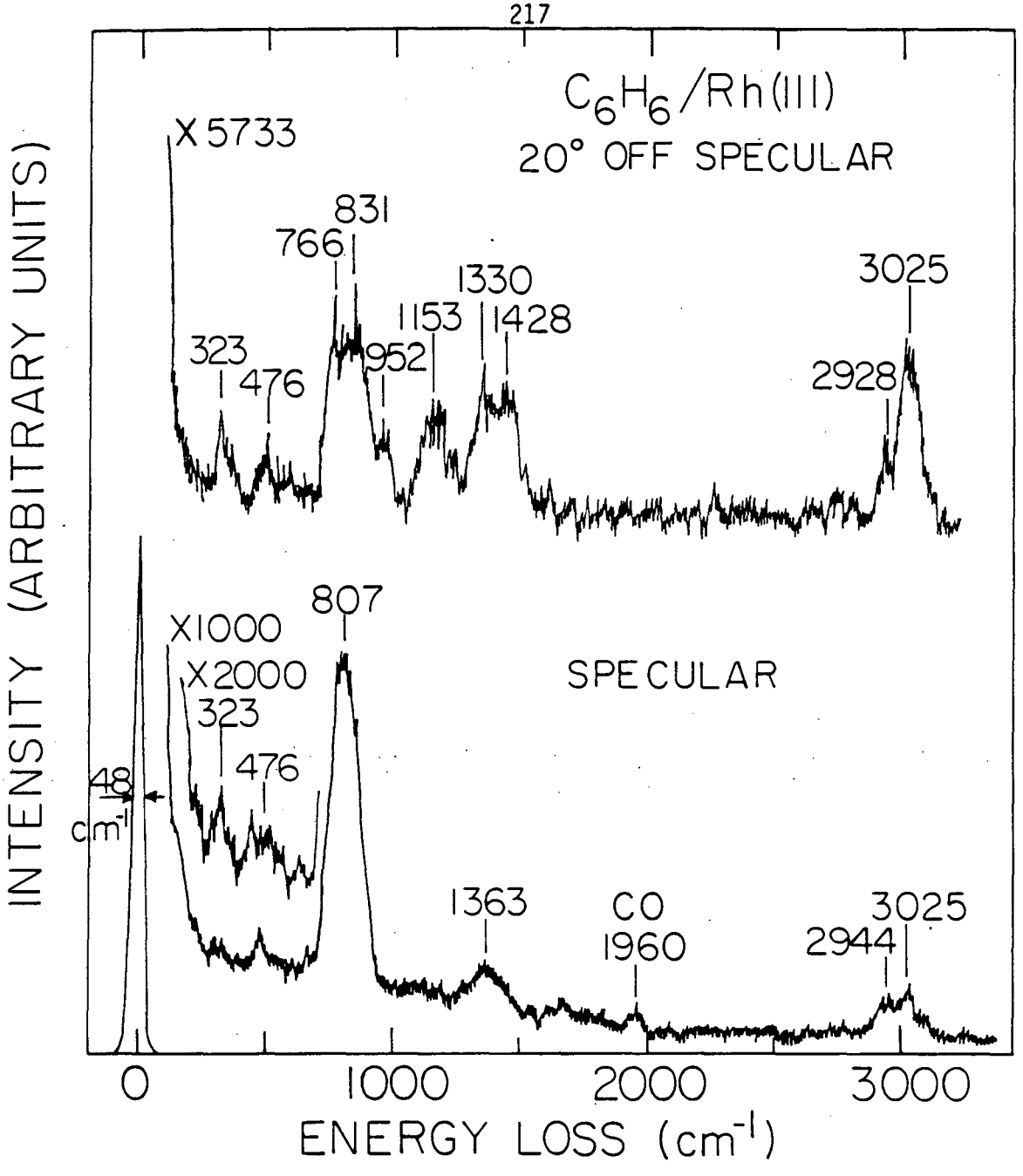

XBL 838-6207

Figure 6.12

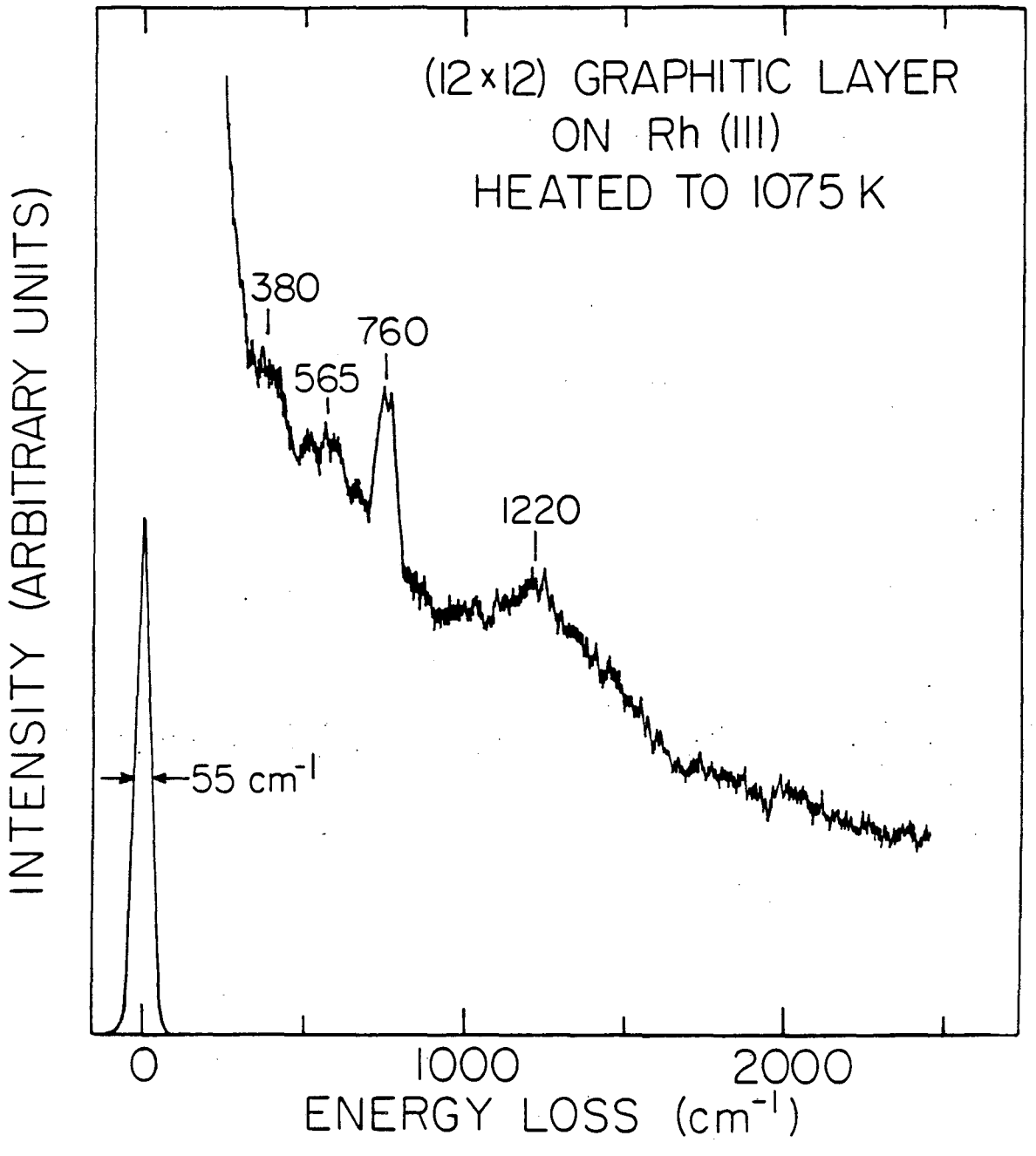
(12×12) GRAPHITIC LAYER
ON Rh (111)
HEATED TO 1075 K
380
565
760
1220
55 cm⁻¹
INTENSITY (ARBITRARY UNITS)
0
1000
2000
ENERGY LOSS (cm⁻¹)
XBL 838-6206

Figure 6.13

6.2.3 DISCUSSION

6.2.3a. The Structure of Benzene Adsorbed on Rh(111).

The surface chemistry of benzene with Rh(111) is very similar to that observed previously on Pt and Ni surfaces. There are some important differences, but an accurate representative picture of Group VIII metal-arene chemistry may be obtained by a detailed study of one of these systems.

On Rh(111), benzene chemisorbs irreversibly at low coverages upon exposure at 300K. This is also seen for benzene adsorption on several other transition metal surfaces including Ni(111) [7], Pt(111) [8], Pt(100) [9], Ni(110) [11] and $Pt_{10}Ni_{90}$(111) [11]. This state, however, is molecularly adsorbed, as evidenced by the HREEL spectra [36]. At higher coverages, a reversible chemisorption state can be populated. The only difference in the chemisorption bonding of these two states detected by HREELS is the presence of two γ_{CH} vibrations with varying intensity ratios. The dependence of the relative intensity of these vibrations on coverage and temperature suggests that benzene adsorbs on two different sites. Further evidence for this interpretation is provided by the infrared spectra of metal-arene complexes formed by co-condensing transition metal vapors with benzene at 77K or in argon matrices at 10K [37]. When benzene was attached to small metal aggregates instead of a single metal atom, decreases in the frequency of the γ_{CH} mode of 15-45 cm^{-1} were observed. This suggests that the lower frequency γ_{CH} mode, which initially populates at low coverage, is due to benzene adsorption in a higher coordination site.

A detailed study of benzene adsorption on Ni(111) and Pt(111) also indicates two site adsorption with strong reversible temperature and coverage dependence [15]. On Rh(111), the two γ_{CH} modes are separated by 43 cm^{-1} with the low frequency mode populating first. Similar behavior is seen on Ni(111) where the two γ_{CH} modes are separated by 90 cm^{-1} with the lower frequency mode populating faster at low coverages. This behavior is not observed on Pt(111) however. On Pt(111), the two γ_{CH} modes, separated by 90 cm^{-1}, populate equally at low coverages. TPD shows benzene to both decompose and desorb molecularly from a single high temperature state at 473-493K [8]. At high coverages, the lower frequency mode is four times more intense than the higher frequency mode while benzene now desorbs with an additional molecular desorption state at 373-403K. Note that the chemical behavior of benzene on Rh(111) is most similar to that on Ni(111), both in γ_{CH} frequencies (see Table 6.2) and in coverage dependence.

The bending vibration for CH groups present in gas phase molecules is a strong function of the hybridization of the carbon atom, increasing in frequency with increasing hybridization (e.g. $sp < sp^2 < sp^3$) [28]. A similar trend occurs on metal surfaces where the CH out-of-plane bending frequency increases as the metal-benzene interaction becomes stronger. This is evident in Table 6.2 where the vibrational data for benzene adsorption on several

Table 6.2. A comparison of vibrational frequencies (cm^{-1}) observed by HREELS for benzene chemisorbed on single crystal metal surfaces with the gas phase values. Frequencies are grouped by mode assignments; original assignments, when different, are given in parentheses.

Crystal Surface	ν_{M-C}	ν_{M-C}	γ_{CH} (ν_4,A_{2u})	δ_{CH} (ν_{10},B_{2u})	δ_{CC} (ν_{13},E_{1u})	ν_{CH} (ν_1,A_{1g})
gas phase[a]			673	1150	1486	3062
Ag(111)[b]			675	1155	1480	3030
Ni(111)[c]	320		730,820	1130	1430(ν_9)	3000
[d,e]	290		745,845(ν_2)	1110	1420	3020
Ni(110)[e]			735,845(ν_2)	1110*	1420*	3020
Ni(100)[d]	360		750,845(ν_2)	1115	1425	3025
Rh(111)[f]	345	550	776,819	1130	1420	3000
$Pt_{10}Ni_{90}$(111)[e]			800,845(ν_2)	1110*	1420*	3050
$Pt_{78}Ni_{22}$(111)[g]			835,910	1130*	1385*	3010
Pt(110)[h]	340*	565*	830*,910*	1120*	1435*	3025
Pt(111)[c]	360	570	830,920	1130	1402(ν_9)	3000

* indicates vibrations not assigned to specific modes.

a) Shimanouchi (ref. 28)

b) Avouris and Demuth (ref. 14)

c) Lehwald et al. (ref. 15)

d) Bertolini and Rousseau (ref. 10)

e) Bertolini et al. (ref. 11)

f) This study.

g) Massardier et al. (ref. 12)

h) Surman et al. (ref. 16)

single crystal surfaces is summarized. The table illustrates that the perturbation from gas phase benzene increases as one moves down the table, toward higher frequency γ_{CH} vibrations. Similar trends are seen in metal-benzene complexes where the γ_{CH} frequency was found to increase in the order: nickel < cobalt < iron < chromium [37]. In addition, the magnitude of the frequency shifts in this mode for these complexes is similar to that seen for benzene chemisorption on metal surfaces. For example, in Table 6.2 the frequencies for γ_{CH} range from 675 to 920 cm^{-1}, while $(C_6H_6)_2$ Cr has a γ_{CH} frequency of 795 cm^{-1}. Although this CH out-of-plane bending mode shifts by as much as 247 cm^{-1} upon chemisorption, the number and frequency of the other vibrational modes observed confirm that the adsorbed benzene is π-bonded on the surfaces listed in Table 6.2. Similarly, the complexes described above [37] are known to have benzene π-bonded to the metal atom(s). Furthermore, direct hydrogen-metal interaction does not occur since a large decrease in the CH stretching vibration is typically associated with such an interaction, and this is not observed for benzene adsorption (cf. ν_{CH} for organometallics containing C-H-M bonding occurs between 2350 and 2700 cm^{-1} [38]). Hence, the frequency of the γ_{CH} mode is sensitive to both the strength of the metal-benzene interaction and the adsorption site. The extent of the metal-benzene interaction may also account for the differences in C-H bond breaking activity. This will be discussed more below.

Inspection of Table 6.2 shows that in addition to the γ_{CH} vibrations, both M-C stretching vibrations increase as the interaction with the surface increases. A similar trend was also reported for benzene π-complexed to nickel, cobalt, iron, and chromium [37], with the interaction between benzene and the metal atom (and ν_{M-C}) increasing in the order given. The remaining three modes in Table 6.2 all decrease from their gas phase values. The magnitude of this decrease grows as one moves down the table, again indicating larger deviation from the gas phase with stronger adsorption. Some discrepancies exist in this trend partially due to the resolution used to measure these weak, broad vibrations. However, the trend is clear, and the frequencies observed for these modes give further information on the extent of rehybridization. The ring stretch and deformation mode (ν_{13}) decreases by 30-40 cm^{-1} for benzene π-complexed to the metal atoms mentioned previously [37], and between 45-60 cm^{-1} typically for all but Ag(111) in Table 6.2. Furthermore, the CH stretching mode decreases by 30-60 cm^{-1} typically for adsorbed benzene from the gas phase value (3062 cm^{-1}). Comparing these values to the ν_{CH} of gas phase cyclohexane (2930 cm^{-1}) [28] and adsorbed cyclohexane on Ni(111) and Pt(111) (2900 cm^{-1} on both surfaces [39]) we conclude that benzene is rehybridized but still retains principally sp^2 character.

The frequency of the metal-ring vibration (i.e. ν_{M-C}) is a good measure of the strength of the metal-benzene interaction, and is well correlated with frequency shifts of the other dipole-active modes of

adsorbed benzene. The CH out-of-plane bending mode is the most intense in the spectrum and undergoes substantial shifts, hence this bend has been used previously as an indirect means of relating metal-ring bond strengths for both arene- and cyclopentadienyl-metal complexes [40]. In an attempt to extend this correlation to metal surfaces, the heats of desorption for molecular benzene and the decomposition product hydrogen have been calculated and are given in Table 6.3. For comparison, the values are determined from the desorption temperature using first order desorption kinetics and an assumed preexponential factor of 10^{13} sec^{-1} [42]. As shown in Fig. 6.14, for the limited number of metals studied, the heat of desorption of molecular benzene correlates reasonably well with the observed frequency shifts.

The degree of interaction between benzene and the first row transition metal atoms has also been correlated to the ability of these metals to serve as acceptors of π-electron density [41]. This ability can be related to the electronegativity of the metal, the surface equivalent of which is the work function. Such a correlation does exist for benzene adsorption: the work function of the clean metal surface increases, in general, as one moves down Table 6.2 as shown in Fig. 6.15. These simple arguments provide reasonable rationale for the trends observed, but the ability of the metal to backdonate into antibonding π^* orbitals of benzene can lead to deviations. In general, however, the bond-strength between benzene and a metal surface increases for higher work function surfaces, as can be indirectly measured from the increase in the CH out-of-plane bending frequency.

Table 6.3. Desorption temperatures (K) for benzene and hydrogen evolution from chemisorbed benzene on single crystal fcc(111) surfaces. The heats of desorption (kcal/mole) are given for relative comparisons as determined using the Redhead formula [42] assuming first order desorption kinetics and a preexponential factor of 10^{13} sec^{-1}.

Crystal Surface	H_2 Desorption	$\Delta H_d(H_2)$	C_6H_6 Desorption	$\Delta H_d(C_6H_6)$
Ni(111)[a]	453	26.3	388-398	22.4-23.0
Rh(111)[b]	450,670	26.6,40.1	395-415	23.2-24.4
$Pt_{10}Ni_{90}(111)$[c]	448,583	26.8,35.2	368,423	21.9,25.3
$Pt_{78}Ni_{22}(111)$[d]	none	---	365,445	21.7,26.6
Pt(111)[e]	543,653	31.7,38.3	373-403, 473-493	21.5-23.3, 27.5-28.7

a) Friend and Muetterties (ref. 7); heating rate = 25K/sec

b) This study; heating rate = 15K/sec

c) Bertolini et al. (ref. 11); heating rate = 10K/sec

d) Massardier et al. (ref. 12); heating rate = 10K/sec

e) Tsai and Muetterties (ref. 8); heating rate = 25K/sec.

These correlations (between the CH out-of-plane bending mode and either the π-acceptor character of the metal or the heat of desorption of molecular benzene from the metal) are not as simple as one would like; the γ_{CH} frequency is sensitive to both the strength of the metal-benzene interaction and the nature of the adsorption site. On

Rh(111) for example, the lower frequency γ_{CH} mode populates at low coverages, while the higher frequency γ_{CH} mode dominates at high coverages. Based on the correlations described above, we would conclude that the benzene initially adsorbed was more weakly bound than that at saturation. However, TPD shows that the initial benzene is irreversibly adsorbed, and with increasing coverage a more and more weakly bound reverisble adsorption state is populated. This observation of stronger bonding at low coverages is typically seen for most chemisorption systems. Hence, from the TPD data we would come to the opposite conclusion that the benzene initially adsorbed was more strongly bound than that at saturation. This discrepancy could be rationalized by attributing the changes seen in TPD with coverage to a higher activation energy barrier to CH bond scission as more sites are occupied. However, it is more likely that while a general trend of higher γ_{CH} frequency with greate metal-benzene interaction exists from metal to metal (as seen in Figures 6.14 and 6.15), the γ_{CH} frequency also depends on the nature (e.g., coordination number) of the adsorption site.

Structural information regarding the adsorption geometry and the symmetry of the adsorbed complex can be obtained by comparing the number, frequency, and intensity of the dipole active modes observed with the correlation table of the point group for the gas phase molecule [43]. Benzene in the gas-phase has D_{6h} symmetry. The presence of a strong A_{2u} mode and the absence of the E_{1u} modes confirms that the molecule is lying flat and that the ring plane is

not tilted from the surface plane (i.e. the skeletal carbon ring is planar with the surface; the hydrogen atoms can be bent out of this plane). Hence, only a select number of subgroup symmetries are possible and these are reproduced in Table 6.4. This correlation table makes use of the relationship between the representations of D_{6h} and its subgroups. Only those modes which belong to totally symmetric representations are observed for dipole scattering, hence, the modes whose frequencies are given in the table should be present for that particular adsorption symmetry. Planar adsorption on the Rh(111) surface removes at least the σ_h symmetry plane. As a result, the highest symmetry point group for the adsorbate complex is C_{6v}, that is if adsorption is centered over a single Rh atom and if second layer interactions are not important (which gives the substrate surface 6-fold rather than 3-fold symmetry). If second layer interactions are important or if the adsorption is centered over a hollow or top site, one must consider the C_{3v} point group. The symmetry is reduced even further to C_s or C_{2v} if adsorption is centered over a bridged site and second layer interactions are or are not important, respectively. Lower symmetry can result if the molecule is asymmetrically distorted due to bonding or centered over a less symmetric site.

The off-specular measurements allow symmetry groups lower than C_{3v} to be ruled out (Table 6.4) since only 7 vibrational modes are observed to have a dipole contribution. Clearly the number and frequencies of the observed vibrations favor the C_{3v} point groups.

Table 6.4. Correlation table for the symmetries of the point group D_{6h} with those of the subgroups C_{6v}, $C_{3v}(\sigma_d)$, $C_{3v}(\sigma_v)$, and C_{2v}. The vibrational frequencies for gas phase benzene are given for those modes which are active for dipole scattering using HREELS (i.e. for those modes which belong to the totally symmetric representations A_1, A' and A).

D_{6h}	C_{6v}	$C_{3v}(\sigma_d)$	$C_{3v}(\sigma_v)$	C_{2v}
A_{1g}	A_1(992,3062*)	A_1(992,3062*)	A_1(992,3062*)	A_1(992,3062*)
A_{1u}	A_2	A_2	A_2	A_2
A_{2g}	A_2	A_2	A_2	A_2
A_{2u}	A_1(673*,T_z)	A_1(673*,T_z)	A_1(673*,T_z)	A_1(673*,T_z)
B_{1g}	B_2	A_1(no vib.)	A_2	B_2
B_{1u}	B_1	A_2	A_1(1010,3068*)	B_1
B_{2g}	B_1	A_2	A_1(995*,703*)	B_1
B_{2u}	B_2	A_1(1150*,1310)	A_2	B_2
E_{1g}	E_1	E	E	B_2+B_1
E_{1u}	E_1	E	E	B_2+B_1
E_{2g}	E_2	E	E	A_2+A_1(606,1178* 1596, 3047*)
E_{2u}	E_2	E	E	A_2+A_1(410*,975*)

* indicates modes due to C-H vibrations.

The dipolar contribution to the modes at 1130 and 1320 cm^{-1} leads to the conclusion that the adsorption site symmetry is $C_{3v}(\sigma_d)$. This point group implies that the symmetry planes of the Rh(111) substrate bisect the dihedral angles between planes that include adjacent CH bonds of the ring.

Lehwald et al. [15] also concluded that benzene adsorbed on Ni(111) and Pt(111) occupied adsorption sites of C_{3v} (σ_d) symmetry. A similar conclusion was reached for benzene on Ag(111) [14], while Haaland [17] suggests benzene symmetrically distorts to this geometry on alumina supported platinum, rather than strictly adsorbing on a site of this symmetry. An inspection of Table 6.2 suggests that C_{3v} (σ_d) adsorption symmetry is reasonable for all the metal surfaces studied to date. Clearly such symmetry is not possible for adsorption on either Ni(100) or Ni(110). The correlation table (Table 6.4) shows that several additional modes should be seen on specular for C_{2v} symmetry (the highest symmetry point group expected on these crystallographic orientations). Why these modes are not seen is yet to be understood.

A model for the structure of the benzene monolayer deduced from dynamical low energy electron diffraction calculations of the I-V profiles of the c($2\sqrt{3}$ x 4)-rect LEED pattern is shown in Fig. 6.16 [2]. This model is supported by our determination of the adsorption geometry with the benzene ring parallel to the surface with an adsorption complex symmetry C_{3v} (σ_d). The calculations indicate bonding on a 3-fold hollow site with a second layer atom directly underneath (i.e. the hcp-type hollow), while the HREELS data indicates two adsorption sites of C_{3v} (σ_d) symmetry. Taken together, the data suggests two of the three possible adsorption sites having C_{3v} (σ_d) symmetry are occupied, with most of the benzene molecules centered over hcp-type hollow sites at saturation (i.e. a larger

fraction of molecules have ν_{CH} = 819 cm^{-1} at saturation coverage). The remaining benzene (with ν_{CH} = 776 cm^{-1}) occupy either an fcc-type hollow or a top site. In addition, an in-plane distortion of the benzene ring, as shown at right in Fig. 6.16, gave the best fit between dynamic LEED theory and the experimental I-V profiles. Such a symmetric distortion is not inconsistent with the HREELS data. In fact, the vibrational spectra of benzene and the low temperature phase of acetylene are quite similar for several metal surfaces [27,44,45]. Lehwald et al. [15] have pointed out that the π/di-σ bonding of acetylene over hollow sites found on Pt(111) [44], and now on Pd(111) [27], puts the C and H atoms into the same local geometry as expected for benzene over hollow sites, possibly with the same distortion. Furthermore, the observed production of benzene upon trimerization of acetylene on Ni [45] and Pd [46] surfaces gives additional support for the distortion calculated.

The close similarity in the vibrational spectra for differently ordered structures or totally disordered layers produced from near saturation benzene coverages indicates that adsorbate-adsorbate interactions, either direct or thru-metal, are responsible for the order-order transitions rather than major changes in the bonding mode or geometry at the surface. Explanation of minor changes in intensity of some modes involves weak breakdown of the symmetry of the surface complex or perhaps the presence of surface species with different symmetries (e.g. some small fraction of molecules inclined slightly from the surface plane). Spectra taken at very large exposures (300L)

show that (1) no compressional phase transition, such as that observed for pyridine on Ag(111) [47], occurs for our conditions to produce two different bonding geometries of benzene near 300K, and that (2) no evidence was found for benzene adsorbed with its ring inclined to the surface, as suggested might be possible on Pt(111) for the benzene $(2\sqrt{3} \times 5)$ structure obtained after similar large exposure [48].

Fig. 6.14. The CH out-of-plane bending mode frequency (γ_{CH}) for benzene adsorbed on several metal surfaces plotted as a function of the calculated heat of desorption for molecular benzene from that metal surface. The data is taken from Tables 6.2 and 6.3. The frequency used in the correlation is the dominant frequency observed in the coverage range that a particular desorption state is present.

Fig. 6.15. The CH out-of-plane bending mode frequency (γ_{CH}) for benzene adsorbed on several metal surfaces plotted as a function of the corresponding clean metal work function. The frequencies are taken from Table 6.2; the work functions are obtained from ref. 54 and 55. The dominant frequency observed near saturation exposure is correlated with the work function.

Fig. 6.16. Structural model based on LEED and HREELS results for benzene adsorbed in the c($2\sqrt{3}$ x 4)-rect ordered structure. The benzene molecules are centered over hcp-type hollow sites and positioned with $C_{3v}(\sigma_d)$ symmetry. Van der Waals radii of 1.8 and 1.2 Å for C and H, respectively, are included to demonstrate packing density. The right hand benzene molecule shows the in-plane symmetric distortion preferred from dynamic LEED calculations [2]. The side view in the top panel includes possible CH bending away from the surface. A unit cell is outlined in the bottom panel.

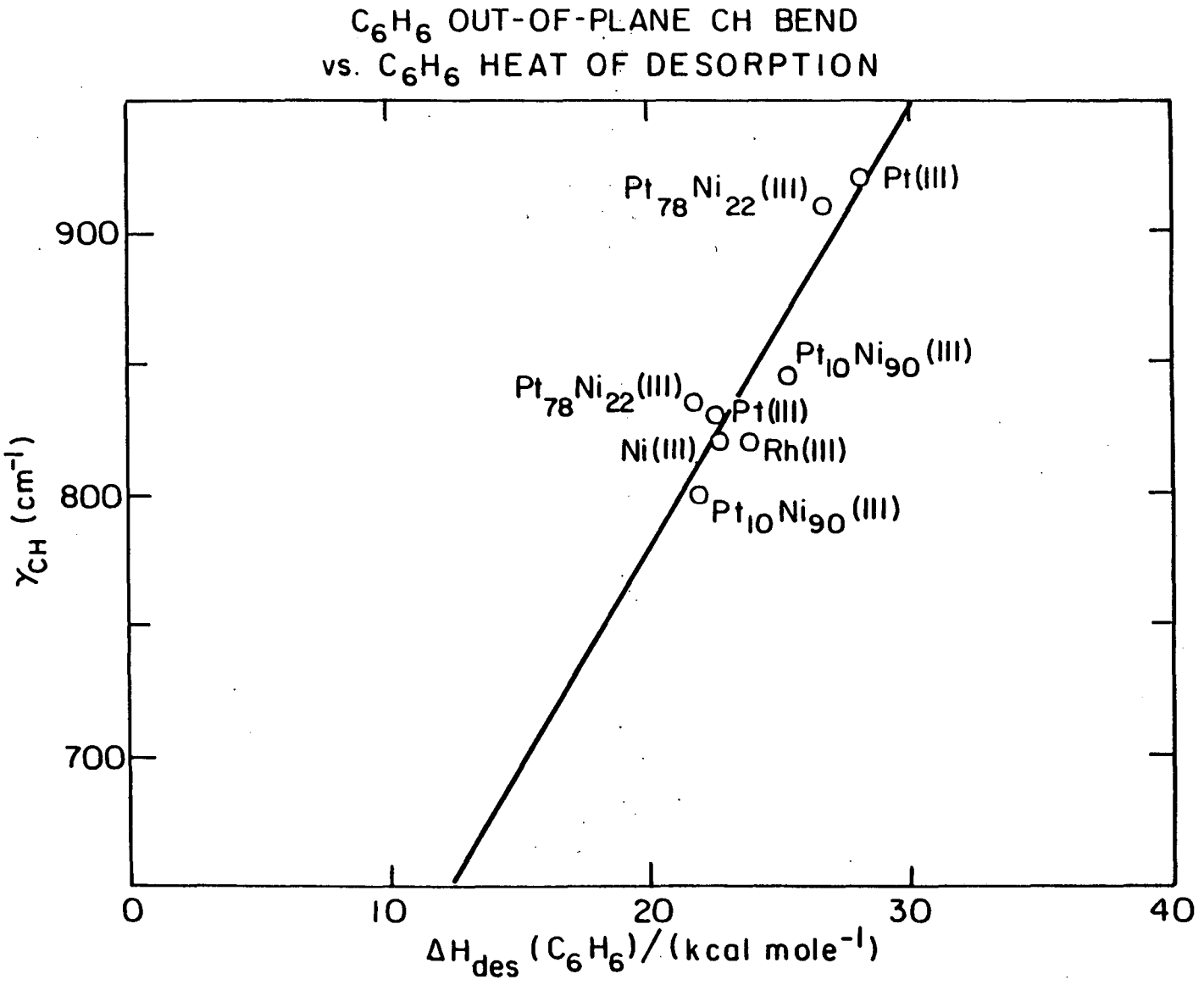

Figure 6.14

XBL8311-6594

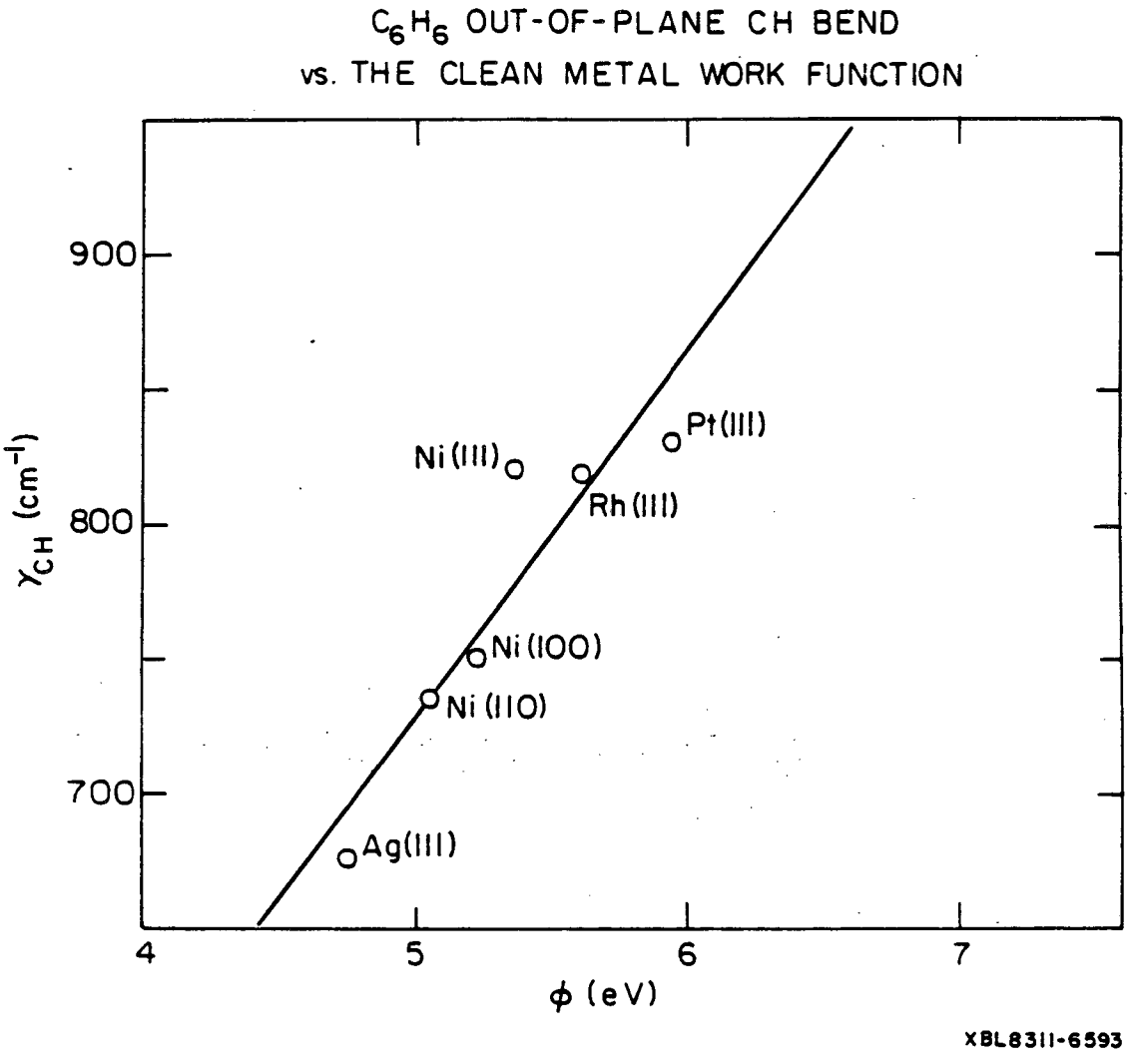
C_6H_6 OUT-OF-PLANE CH BEND
vs. THE CLEAN METAL WORK FUNCTION
900
800
700
γ_{CH} (cm^{-1})
Ni(111)
Pt(111)
Rh(111)
Ni(100)
Ni(110)
Ag(111)
4
5
6
7
ϕ (eV)
XBL8311-6593

Figure 6.15

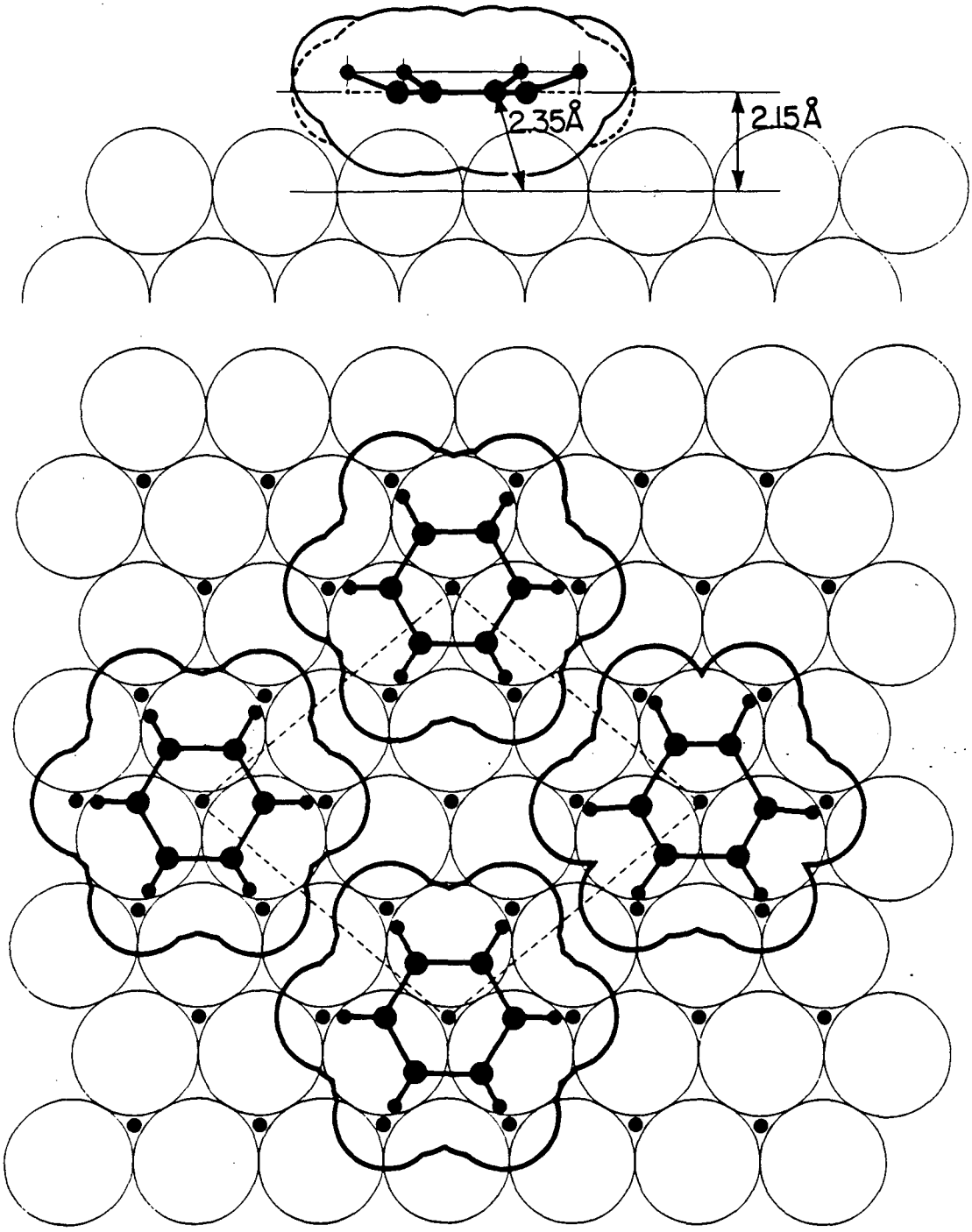

$Rh(111)-\begin{pmatrix} 3 & 1 \\ 1 & 3 \end{pmatrix} C_6H_6$

Figure 6.16

XBL 835-198

6.2.3b The Nature of Benzene Decomposition. Upon heating the benzene layer, two competing processes occur: reversible molecular benzene desorption and irreversible benzene decomposition. The changes observed as a function of coverage were already discussed, only the nature of the decomposition layer will be discussed here. A comparison of TPD data reported for near saturation benzene adsorption on fcc(111) single crystal surfaces is given in Table 6.3. No decomposition occurs for the platinum-rich alloys (and most likely not for Ag(111)). However, the TPD desorption maximum occurs at ~450K for $Pt_{10}Ni_{90}$(111), Ni(111), and Rh(111). This maximum is ~100K higher on Pt(111).

The temperature where significant C-H bond breaking occurs has also been measured, occurring for $T \geq 373K$ on Ni(111) [7], $T \geq 393K$ on Rh(111), and $T > 473K$ on Pt(111) [8]. This indicates that benzene adsorption and decomposition behavior on Rh(111) is between that of Ni(111) and Pt(111), but most similar to Ni(111).

The point where C-C bond breaking occurs is more difficult to determine, and has not been examined for benzene decomposition on any other surface than Rh(111). From the production of CH fragments already at 410K we deduce that significant C-C bond breaking occurs by this temperature. Additional evidence on Rh(111) has been observed in this laboratory recently where CH formation is observed from heating the ethylidyne species (M_3CCH_3, produced at 300K from ethylene adsorption) to 410K [35]. For ethylene adsorption, the point where C-C bond scission occurs is more easily determined since the ethylidyne

and CH vibrational modes do not overlap. Scission of C-C bonds of hydrocarbons other than benzene have been studied on a few surfaces. On Ni(111), C-C bonds are broken for di-σ/π bonded acetylene at 400K as evidenced by CH formation [49]. On Pt(111), significant C-C bond cleavage occurs at 470K, where CH fragments are produced after ethylidyne formation. Additional evidence verifying the interpretation of the HREELS data was shown recently by Creighton and White, who observed predominately CH^+ ions at 500K in a static SIMS experiment, suggesting CH species on the surface at this temperature [50]. Again, the reactivity for C-C bond breaking on Rh(111) is between that of the (111) faces of Ni and Pt, and very similar to the reactivity of Ni.

The vibrational frequencies observed for CH species produced from alkene, alkyne, or benzene decomposition on several surfaces are compared in Table 6.5. Comparing the observed frequencies to those of several gas phase molecules [26,28], we conclude all the surface species are between sp^2 and sp^3 hybridized, base on the ν_{CH} vibrations. However, the CH bending vibrations suggest a hybridization between sp and sp^2. Comparison with the cluster compound $HCCo_3(CO)_9$ suggests the former interpretation is the correct one. Curiously, the (111) faces of Rh, Ni and Pd are very similar in frequencies, indicating similar adsorption, while the CH species seems to be more strongly bound to Pt(111).

Table 6.5. A comparison of vibrational frequencies (cm^{-1}) assigned to adsorbed CH species with the cluster compound $HCCo_3(CO)_9$. The CH species are produced by thermal decomposition of acetylene [b,d,e], ethylene [f], or benzene [c] on the surfaces given below. Frequencies for the highest temperature species are reported.

Mode	$HCCo_3(CO_9)$[a]	W(110)[b]	Rh(111)[c]	Ni(111)[d]	Pd(111)[e]	Pt(111)[f]
ν_{CH}	3041	2930	3020	2980	3002	3100
δ_{CH}	850	930	807	790	762	850
ν_{M-C}	715	581				
ν_{M-C}	417		490		307	

a) Martin et al. (ref. 33)

b) Backx and Willis (ref. 51)

c) This study

d) Demuth and Ibach (ref. 34)

e) Gates and Kesmodel (ref. 52)

f) Baro and Ibach (ref. 53)

The formation of broad Rh-C bonds between 350-650 cm^{-1} and broad C-C vibrations between 1000-1500 cm^{-1} produced upon heating benzene or several other hydrocarbons to 800K [35] gives little insight into the formation of graphite on metal surfaces. The broadness does suggest, however, that several chemical environments exists for the carbon layer.

6.3 The Adsorption of Benzene on Potassium Dosed Rh(111)

6.3.1 Introduction

In the preceeding section, we have detailed the adsorption and decomposition of benzene on Rh(111). Benzene was found to be oriented with its ring plane parallel to the surface and π bonded. Because of this, we expect that a strong electron donor such as potassium will alter the nature of this bonding. Since the C-H out-of-plane bending mode was found to correlate with the heat of adsorption of benzene on several surfaces, we expect this mode to be sensitive to bonding changes induced by coadsorbed potassium.

Benzene adsorption has been previously studied on potassium dosed Pt(111) by Garfunkel et al. [54]. They found using TPD measurements that the presence of potassium weakened the benzene-metal bond. The benzene desorption temperature was lowered ~100K in the presence of potassium and the fraction of benzene desorbing molecularly increased (while the fraction of benzene decomposing decreased). They emphasize that although molecular desorption and decomposition are typically viewed as competing processes, only the desorption energy is affected strongly by potassium preadsorption. In a surface enhanced Raman study, Lund et al. [55] found that, for benzene adsorption on a vapor deposited sodium surface, the observed Raman lines are within 3 cm^{-1} of the gas or liquid phase benzene frequencies. This suggests that benzene adsorption on Na is almost unperturbed from its gas phase value, very similar to benzene on evaporated silver films as studied by SERS [56] and on Ag(111) as studied by HREELS [14]. However, the SERS spectra are obtained at very high benzene coverages, quoted as less than 100 monolayers [55].

6.3.2 Results and Interpretation

6.3.2a Benzene and Potassium Coadsorption on Rh(111) at 300K

Benzene adsorption on a clean and potassium dosed (θ_K = 0.10) Rh(111) surface has been studied by vibrational spectroscopy, as shown in Fig. 6.17. These spectra are recorded at 27 and 35 cm^{-1} resolution (FWHM), respectively, to examine more closely what effect potassium has on C_6H_6 bonding. We notice that the γ_{CH} vibrations at 776 and 815 cm^{-1} is unchanged from that of the clean surface. Similarly, the ν_{CH} mode at 2980 cm^{-1} does not shift upon potassium adsorption. The metal-benzene stretching vibrations at 345 and 540 cm^{-1} for the clean surface are difficult to see for the potassium dosed surface due to tailing of the strong low frequency potassium induced vibrations at 120 and 225 cm^{-1}. No CO vibration is observed at 1670 for the potassium dosed case, but the additional intensity at 1435 cm^{-1} is likely due to a strongly shifted C-O vibration. From the strong similarity in the spectra we conclude that in the presence of potassium, benzene adsorption is the same as that on the clean Rh(111) surface.

The changes seen in the γ_{CH} mode upon warming this layer to 390K is plotted in Fig. 6.18. Note that the frequencies do not change upon heating but the relative intensity of the two γ_{CH} vibrations does. Again, the presence of two γ_{CH} vibrations that vary with heating (i.e. benzene coverage) with frequencies identical to that of benzene adsorption on clean Rh(111) leads to the conclusion that the bonding, orientation, and occupation of two distinct sites is the same for both

surfaces. The only change observed in Fig. 6.18 from that of the clean surface adsorption is a difference in peak intensity ratio upon potassium adsorption. The I_{776}/I_{815} ratio is less than the comparable value for clean Rh(111). This ratio is also less at 390K. This suggests that the desorption of benzene is altered in the presence of potassium, even though the bonding is not.

In Fig. 6.19 the molecular desorption of benzene-d_6 from clean and potassium dosed (θ_K = 0.10) Rh(111) is shown. Indeed, the heat of desorption of benzene decreases with coadsorbed potassium, as indicated by the 40K shift in peak maximum. This suggests that the bonding of benzene to the Rh(111) surface is weaker with coadsorbed K.

FIGURE CAPTIONS

Fig. 6.17. Specular HREEL spectra obtained at 300K for C_6H_6 adsorption on the clean and K predosed Rh(111) surface.

Fig. 6.18. HREEL spectra obtained at 32 cm^{-1} for the γ_{CH} mode of benzene adsorbed on K dosed Rh(111) at 310K and after heating to 390K. Spectra were recorded on an expanded scale.

Fig. 6.19. TPD specta of 5.0L C_6D_6 following benzene adsorption on clean and K dosed Rh(111) at 300K.

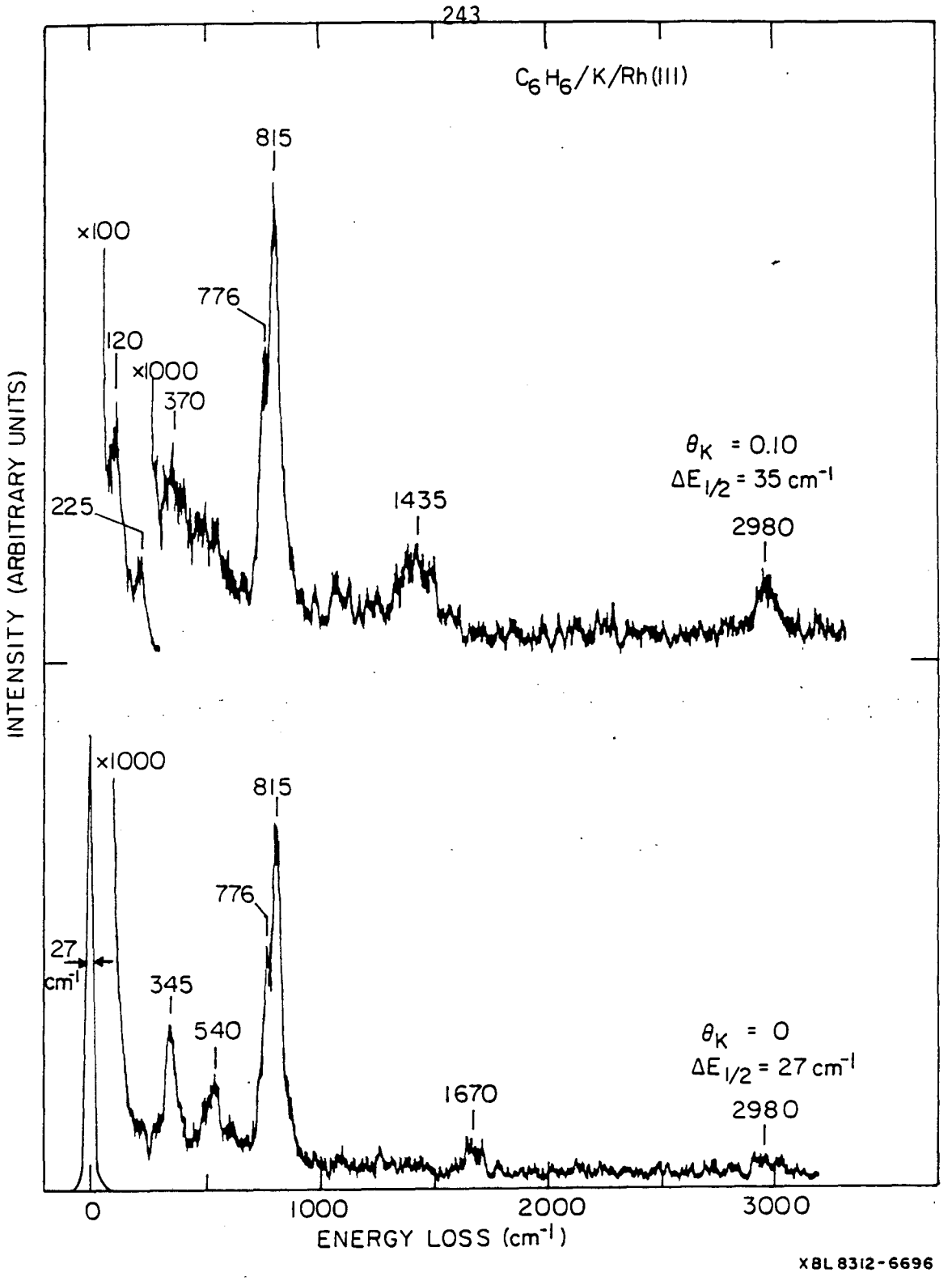
C6H6/K/Rh(111)
815
×100
776
120
×1000
370
225
1435
2980
θK = 0.10
ΔE1/2 = 35 cm-1
×1000
815
776
27
cm-1
345
540
1670
2980
θK = 0
ΔE1/2 = 27 cm-1
INTENSITY (ARBITRARY UNITS)
0
1000
2000
3000
ENERGY LOSS (cm-1)
XBL 8312-6696

Figure 6.17

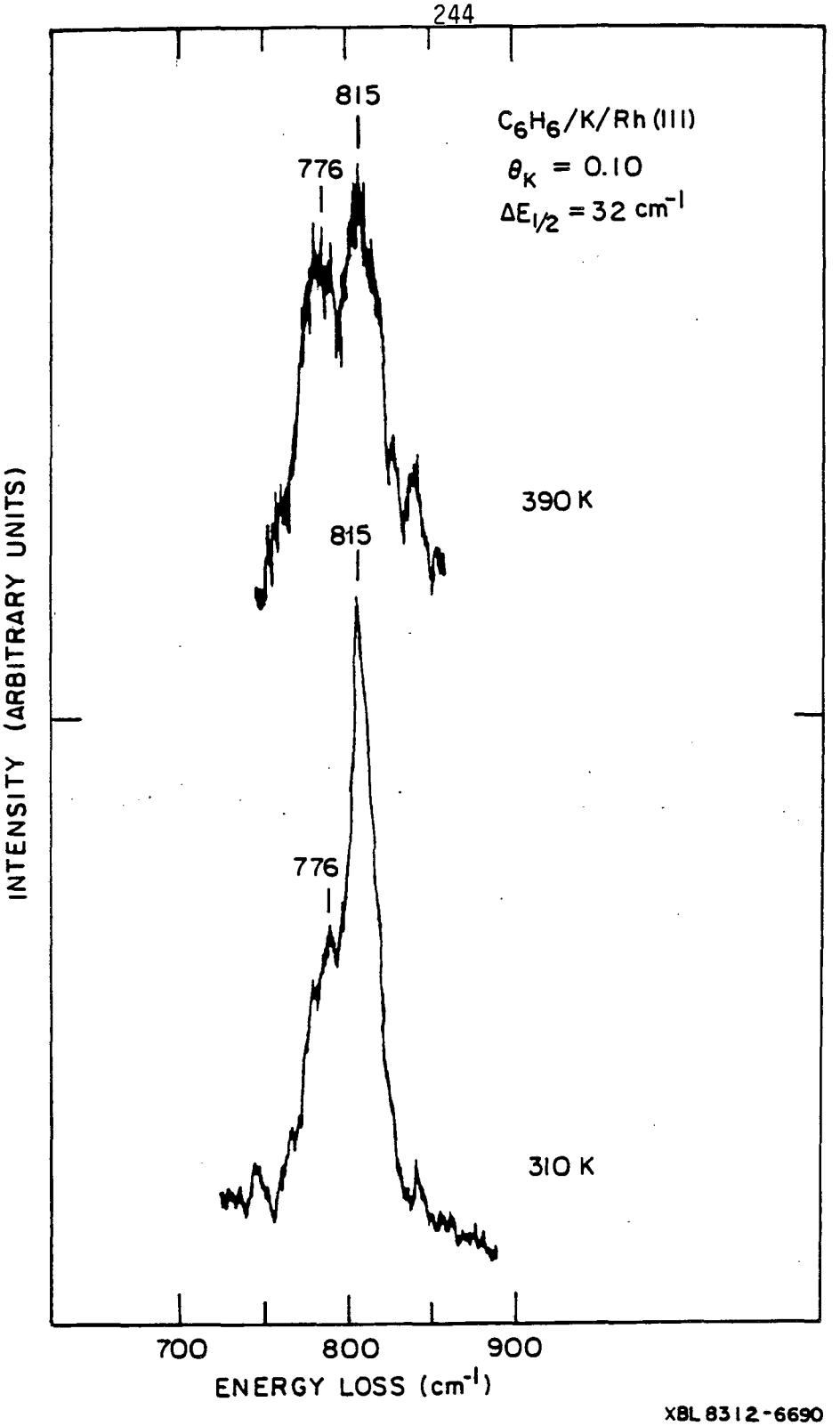
815
776
C_6H_6/K/Rh(111)
θ_K = 0.10
$\Delta E_{1/2}$ = 32 cm^{-1}
390 K
815
776
310 K
INTENSITY (ARBITRARY UNITS)
700
800
900
ENERGY LOSS (cm^{-1})
XBL 8312-6690

Figure 6.18

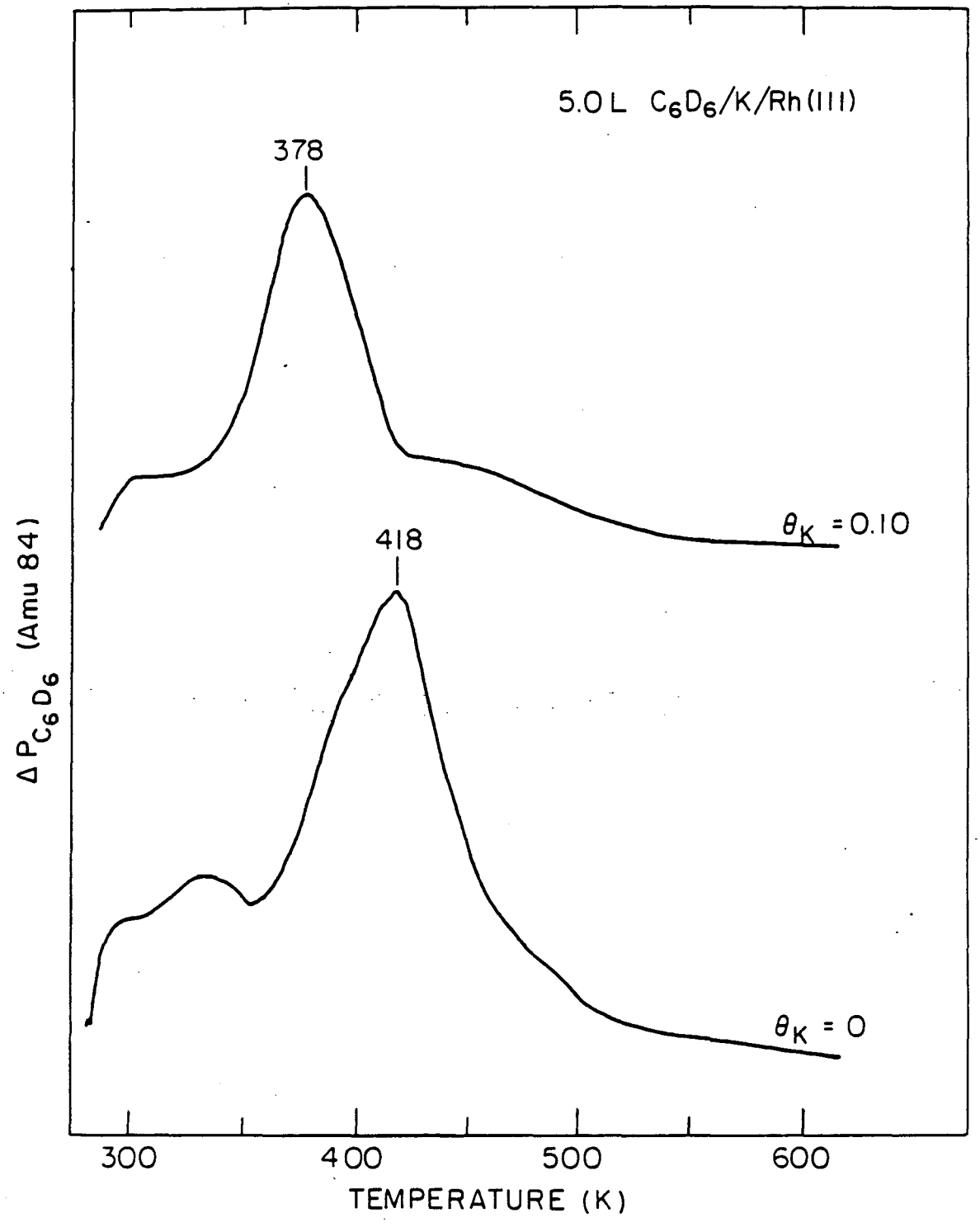
5.0 L C_6D_6/K/Rh(111)
378
418
θ_K = 0.10
θ_K = 0
$\Delta P_{C_6D_6}$ (Amu 84)
300
400
500
600
TEMPERATURE (K)
XBL 8312-6693

Figure 6.19

6.3.2b Thermal Decomposition of Benzene on Rh(111) in the Presence of Potassium

Vibrational spectra recorded as a function of annealing temperature for saturation C_6H_6 adsorption on a Rh(111) surface predosed with 0.02 monolayers of potassium is shown in Fig. 6.20. The peak positions of the benzene derived modes are very similar to the clean surface case (viz. Fig. 6.9). Also, the changes with temperature are also quite similar for the two cases, especially the changes in width of the γ_{CH} mode and the variation in the metal-benzene vibrational modes. Variations in ν_{CH} seem to be smaller for the potassium dosed surface as a function of temperature. The additional intensity at 1500-1700 cm^{-1} is likely due to CO adsorption. The additional intensity at 490 is difficult to interpret, but is too low to be oxygen adsorption. Notice that it does go away upon heating the surface to 390K.

TPD spectra for D_2 desorption after C_6D_6 adsorption on clean and K dosed Rh(111) is shown in Fig. 6.21. Note that the decomposition of benzene is drastically altered in the presence of potassium. The peak observed at 435K suggest a new pathway for benzene decomposition exists when K is adsorbed, and that this pathway leads to decomposition at an earlier temperature. Such behavior is totally unexpected in light of the changes seen in the HREEL spectra with temperature.

TPD spectra at the same potassium coverage just discussed is shown in Fig. 6.22 for D_2 desorption after benzene-d_6 adsorption, as a function of benzene exposure. The spectra indicate that decomposition becomes more complicated with coadsorbed potassium. Furthermore, the

pathway leading to decomposition at 435K is present even at very low benzene coverages.

The changes observed in the D_2 desorption spectra at low benzene-d_6 coverages are shown as a function of potassium preadsorption. Curiously, we find that the lower temperature decomposition pathway does exist for the clean surface and becomes increasingly favored at higher potassium coverages. Also notice that the desorption yield dramatically decreases by $\theta_K = 0.15$, suggesting that by this coverage benzene adsorption is significantly blocked by preadsorbed potassium. At lower potassium coverages ($\theta_K \sim 0.05$), a new state at 470K is observed. This state does not remain populated at higher coverages.

FIGURE CAPTIONS

Fig. 6.20. HREEL spectra recorded near 300K following stepwise warming of a saturation C_6H_6 overlayer in the presence of 0.02 monolayers potassium.

Fig. 6.21. TPD spectra of D_2 following adsorption of C_6D_6 on clean and K dosed Rh(111) at 300K.

Fig. 6.22. TPD spectra of D_2 following adsorption of C_6D_6 on K dosed Rh(111) at 300K as a function of benzene-d_6 exposure.

Fig. 6.23. TPD of D_2 following adsorption of 0.25L C_6D_6 on Rh(111) at 300K, as a function of K coverage.

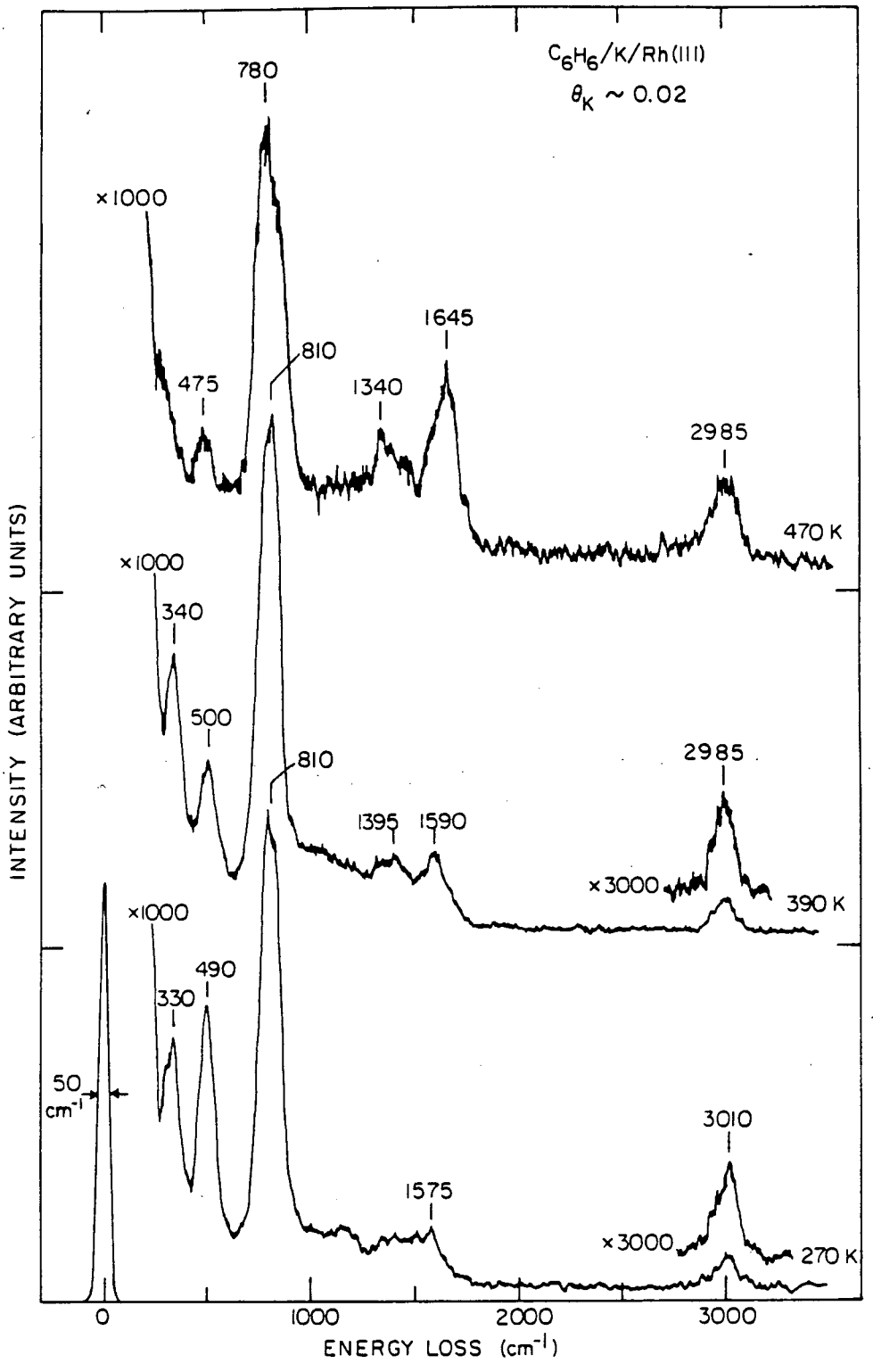
$C_6H_6/K/Rh(111)$
$\theta_K \sim 0.02$
780
×1000
475
810
1340
1645
2985
470 K
×1000
340
500
810
1395
1590
2985
×3000
390 K
×1000
330
490
50 cm⁻¹
3010
1575
×3000
270 K
INTENSITY (ARBITRARY UNITS)
0
1000
2000
3000
ENERGY LOSS (cm⁻¹)
X8L 8312-6695

Figure 6.20

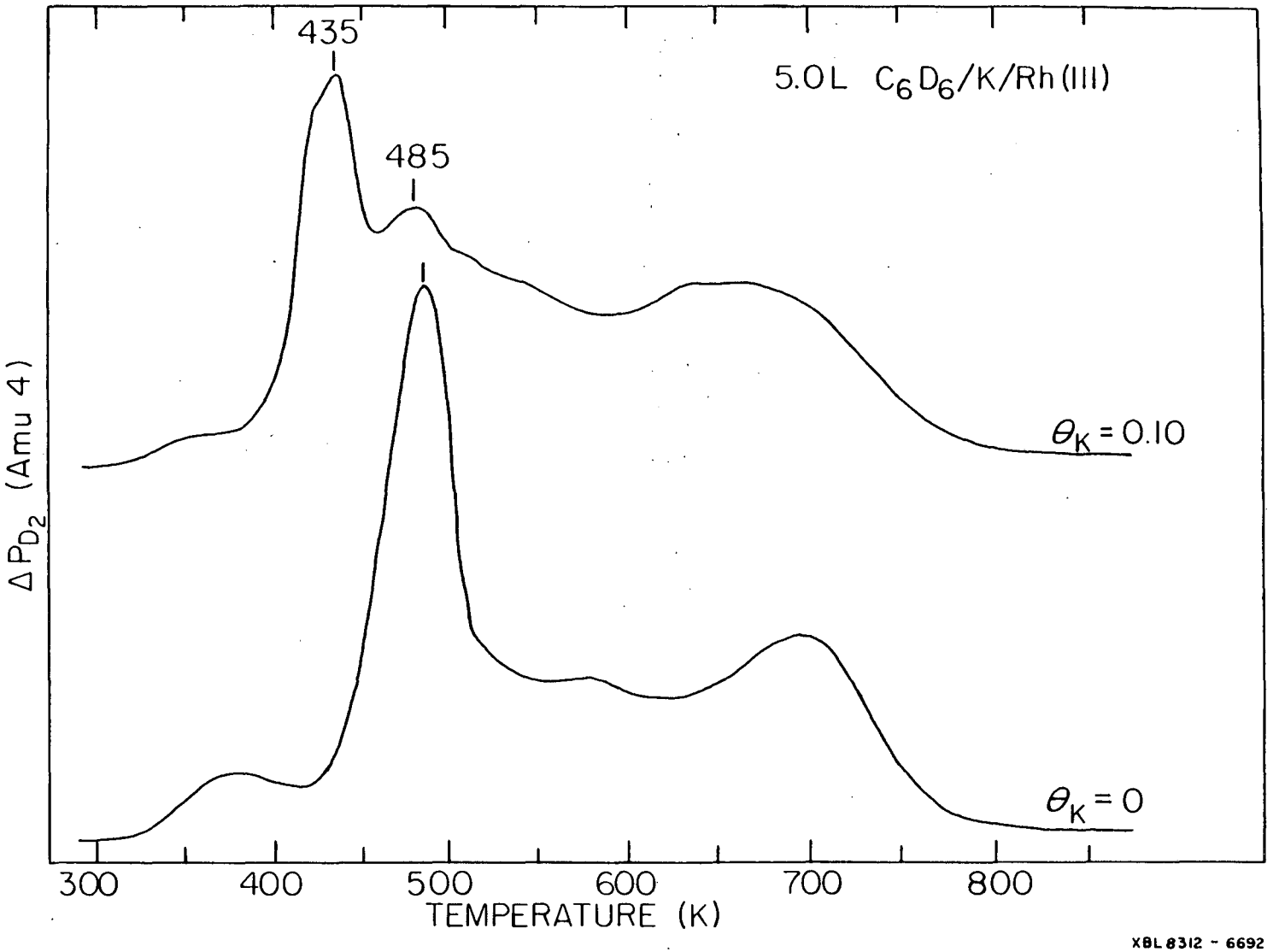
435
485
5.0L C_6D_6/K/Rh(III)
θ_K = 0.10
θ_K = 0
ΔP_{D_2} (Amu 4)
300
400
500
600
700
800
TEMPERATURE (K)
XBL 8312 - 6692

Figure 6.21

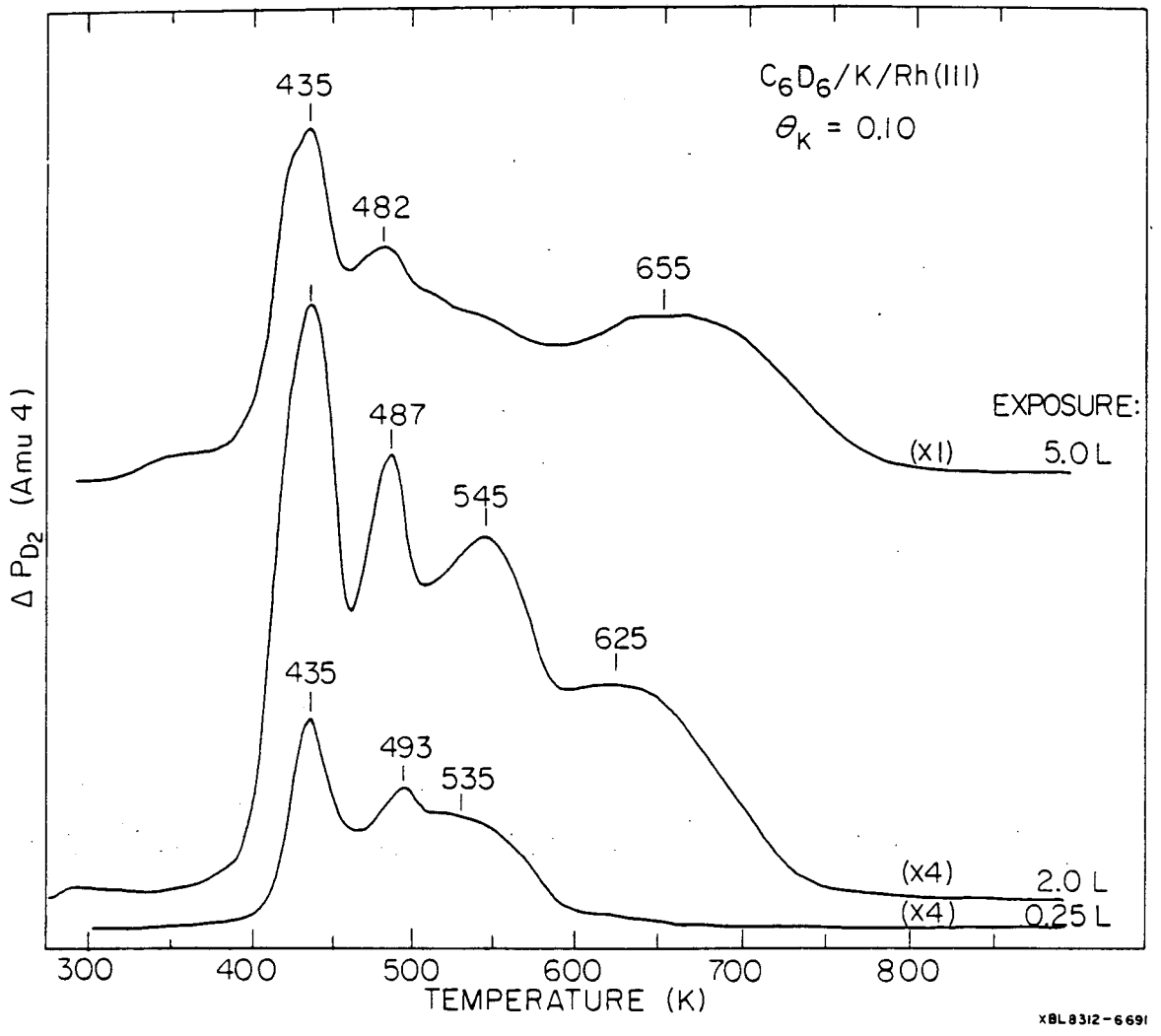
435
482
655
C_6D_6/K/Rh(111)
θ_K = 0.10
EXPOSURE:
(x1) 5.0 L
487
545
625
435
493
535
(x4) 2.0 L
(x4) 0.25 L
ΔP_{D_2} (Amu 4)
300
400
500
600
700
800
TEMPERATURE (K)
XBL8312-6691

Figure 6.22

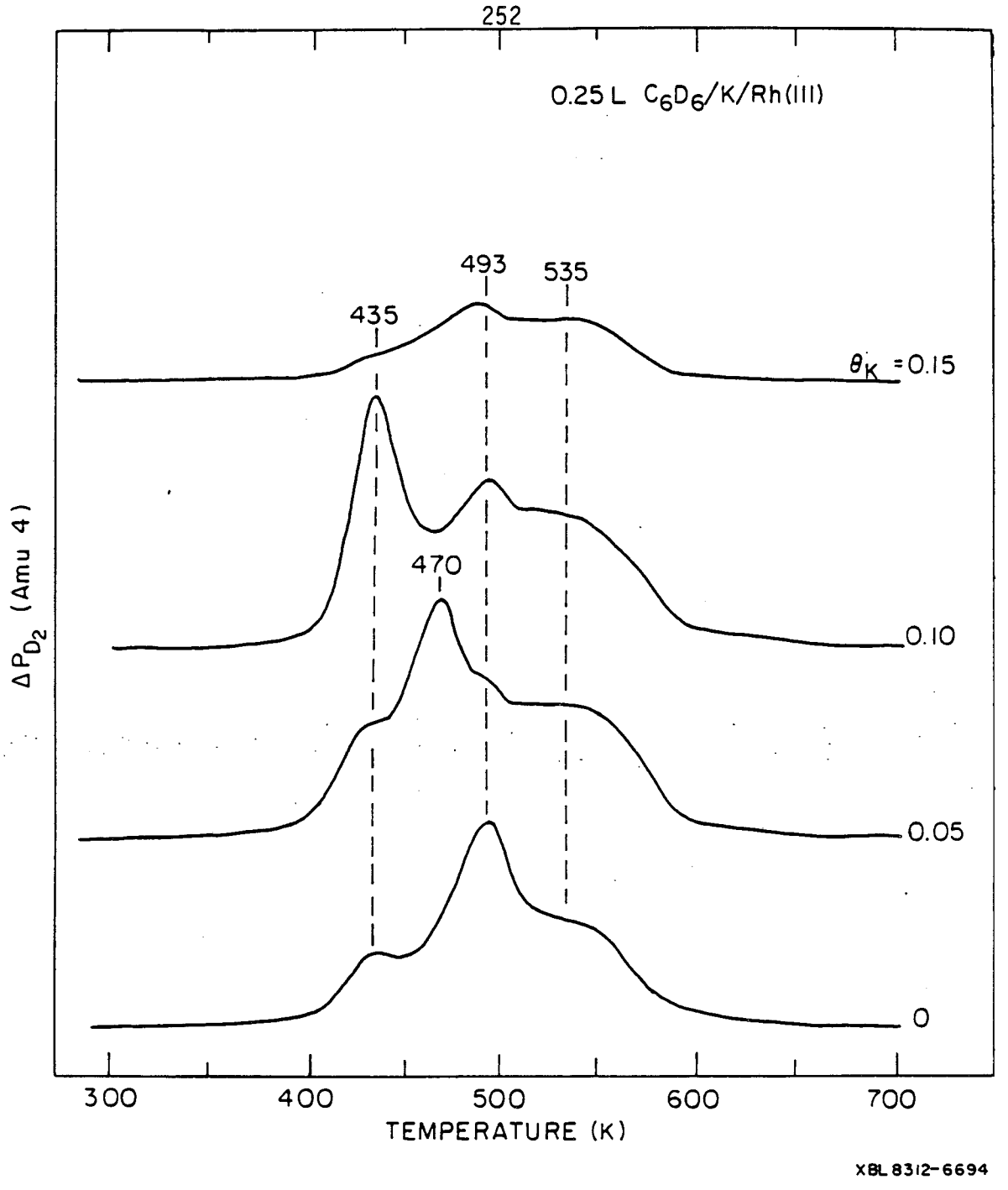
0.25 L C_6D_6/K/Rh(111)
493
535
435
θ_K = 0.15
470
0.10
0.05
0
ΔP_{D_2} (Amu 4)
300
400
500
600
700
TEMPERATURE (K)
XBL 8312-6694

Figure 6.23

6.3.3 Discussion

6.3.3a The Influence of Potassium on Benzene Adsorption

Potassium does not alter the CH out of plane bending mode frequency nor does it produce any new benzene modes compared to the clean surface. This strongly suggests that benzene is lying flat on the surface in a molecular state, it is π bonded to the surface, and it is adsorbed in two sites of $C_{3v}(\sigma_d)$ symmetry. However, the molecular TPD data suggests that benzene is less strongly bound in the presence of potassium. The changes in the ratio of the two γ_{CH} modes observed with K adsorption coupled with the desorption of benzene at significant levels by this temperature indicates that, using our previous assignment, a higher occupation of the 3-fold hollow sites exist at both coverages.

Curiously, the HREELS data suggest K has no effect on the structure and bonding of benzene while the TPD indicates that the molecule is more weakly bound. These results agree with similar changes found independently by Garfunkel et al. [54] and Lund et al. [56]. Still, the conflicting conclusions are difficult to rationalize.

6.3.3b Benzene Decompositon with Coadsorbed Potassium

Here again the two sets of data are conflicting. The decomposition certainly occurs at a lower temperature in the presence of potassium, but the vibrational spectra do not indicate such. However, the vibrational spectra presented are for a relatively small K coverage where, as seen in Fig. 6.23, the decomposition changes are less dramatic.

6.4 CONCLUSIONS

Benzene is associatively adsorbed on Rh(111) at 300K. HREEL spectra indicate that the benzene molecules lie on the surface with the ring plane parallel to the surface plane. Several ordered overlayer structures are observable by LEED near saturation coverage which have almost identical HREEL spectra as disordered overlayers. By using the surface selection rule and our assignment of the observed losses, we conclude that benzene adsorbs with $C_{3v}(\sigma_d)$ symmetry, occupying two adsorption sites. The relative population of these two sites is dependent on both temperature and coverage. Together, dynamic LEED calculations and the vibrational data indicate a dominant fraction of benzene molecules occupy hcp-type hollow sites with $C_{3v}(\sigma_d)$ symmetry. A symmetric distortion of alternating long and short C-C bonds which maintains this symmetry is suggested by the calculation [2] for the molecular geometry. Similar adsorption behavior is seen for benzene on several other transition metal surfaces, including evidence for two adsorption sites.

The frequency of the CH out-of-plane bending mode is an indirect indication of the extent of interaction between benzene and the metal surface. For the several transition metal single crystal surfaces studied so far, the strength of the metal-benzene bonding, as measured by the metal-ring vibrational frequencies or estimated from the molecular desorption temperature, is well correlated with the frequency shifts of the molecular vibrations, as well as with the work function of the surface.

Upon heating the benzene layer, two competing processes occur. At low benzene coverages irreversible benzene decomposition (to yield ultimately H_2 and a carbon-covered surface) occurs exclusively. At higher benzene coverages, molecular benzene desorption occurs in addition to decomposition. Analysis of the vibrational spectra obtained as a function of thermal decomposition indicates that C_2H and CH species are the predominate fragments formed above 410K. Both C-C and C-H bond cleavage occur at a significant level at this temperature, slightly higher than that observed on Pt(111). Some C-C bonds remained intact up to at least 800K, where spectra similar to that of graphite on Rh(111) was observed.

When potassium is preadsorbed on Rh(111), both the heat of adsorption and the temperation where maximum decomposition occurs for benzene decrease. Furthermore, the vibrational spectra indicate that the adsorption and extent of interaction of benzene with the metal surface are unchanged by preadsorbed potassium. Similar conflicting data for the benzene plus alkali adsorption system has been observed previously [54,55].

REFERENCES

1. B. E. Koel and G. A. Somorjai, J. Electron Spectrosc. Relat. Phenom. 29, 287 (1983).
2. M. A. Van Hove, R. F. Lin, and G. A. Somorjai, Phys. Rev. Lett. 51, 778 (1983).
3. D. R. Lloyd, C. M. Quinn and N. V. Richardson, Solid State Commun. 23, 141 (1977).
4. G. L. Nyberg and N. V. Richardson, Surface Sci 85, 335 (1979).
5. P. Hofmann, K Horn and A. M. Bradshaw, Surface Sci. 105, L260 (1981).
6. F. P. Netzer and J. U. Mack, J. Chem. Phys. 79, 1017 (1983).
7. C. M. Friend and E. L. Muetterties, J. Am. Chem. Soc. 103, 773 (1981).
8. M.-C. Tsai and E. L. Muetterties, J. Am. Chem. Soc. 104, 2534 (1982).
9. M.-C. Tsai and E. L. Muetterties, J. Phys. Chem. 86, 5067 (1982).
10. J. C. Bertolini and J. Rousseau, Surface Sci. 89, 467 (1979).
11. J. C. Bertolini, J. Massardier and B. Tardy, J. Chim. Phys. 78, 939 (1981).
12. J. Massardier, B. Tardy, M. Abon and J. C. Bertolini, Surface Sci. 126, 154 (1983).
13. J. C. Bertolini, G. Dalmai-Imelik and J. Rousseau, Surface Sci. 67, 478 (1977).
14. Ph. Avouris and J. E. Demuth, J. Chem. Phys. 75, 4783 (1981).
15. S. Lehwald, H. Ibach and J E. Demuth, Surface Sci. 78, 577 (1978).

16. M. Surman, S. R. Bare, P. Hofmann, and D. A. King, Surface Sci. 126, 349 (1983).

17. D. M. Haaland, Surface Sci. 102, 405 (1981).

18. D. M Haaland, Surface Sci. 111, 555 (1981).

19. H. Jobic, J. Tomkinson, J. P. Candy, P Fouilloux, and A. J. Renouprez, Surface Sci. 95, 496 (1980).

20. A. L. Cabrera, N. D. Spencer, E. Kozak, P. W. Davies, and G. A. Somorjai, Rev. Sci. Instrum. 53, 1888 (1982).

21. H. Froitzheim, H. Ibach and S. Lehwald, Rev. Sci. Instrum. 46, 1325 (1975).

22. J. E. Katz, P. W. Davies, J. E. Crowell and G. A. Somorjai, Rev. Sci. Instrum. 53, 785 (1982).

23. S. Semancik, G. L. Haller and J. T. Yates, Jr., App. Surface Sci. 10, 133 (1982).

24. R.-F. Lin, R. J. Koestner, M. A. Van Hove and G. A. Somorjai, submitted to Surface Sci..

25. H. Ibach and G. A. Somorjai, Appl. Surface Sci. 3, 293 (1979).

26. H. Ibach and D. L. Mills, Electron Energy Loss Spectroscopy and Surface Vibrations, Academic Press, New York, 1982.

27. J. A. Gates and L. L. Kesmodel, J. Chem. Phys. 76, 4281 (1982).

28. T. Shimanouchi, Tables of Molecular Vibrational Frquencies, Consolidated Volume I, NSRDS-NBS39; Vol. II, J. Chem. Ref. Data 6, 993 (1977).

29. R. D. Mair and D. F. Hornig, J. Chem. Phys. 17, 1236 (1949).

30. G. Herzberg, Molecular Spectra and Molecular Structure II, Infrared and Raman Spectra of Polyatomic Molecules, Van Nostrand, Princeton, N.J., 1945.

31. The vibration observed at 835 cm^{-1} is not due to a γ_{CH} mode due to hydrogen impurity in the deuterated benzene layer since no CH stretching vibrations were observed.

32. Due to the low intensity and broad width of the ν_{CH} vibrations at near saturation benzene coverages, the measured ν_{CH} peak center is difficult to measure accurately at these scale expansions, hence the variation in frequency. However, accurate measurements on an expanded scale place the vibration at 2988 cm^{-1}.

33. M. W. Martin, S. F. Kettle, I. A. Oxton, D. B. Powell, N. Sheppard, and P. Skinner, J. Chem. Soc. Faraday Trans. II, 77, 397 (1981).

34. J. E. Demuth and H. Ibach, Surface Sci. 78, L238 (1978).

35. An extensive study of several unsaturated hydrocarbons (ethylene, propylene, 1-butene, cis- and trans-2-butene, isobutene, and their deuterated analogues) chemisorbed on Rh(111) using principally HREELS and TPD has been performed. These species form similar fragments upon warming above 410K as found for benzene. Since these systems were not studied with coadsorbed potassium, they are not included in this thesis, but will appear elsewhere. Please see B. E. Koel, J. E. Crowell, and G. A. Somorjai, in preparation.

36. Additional evidence exists from the observation that no reversible H–D exchange occurred in this state on Ni(111) [7] and Pt(111) [8].

37. H. F. Efner, D. E. Tevault, W. B. Fox and R. R. Smardzewski, J. Organomet. Chem. 146, 45 (1978).

38. M. Brookhart and M. L. H. Green, J. Organomet. Chem. 250, 395 (1983).

39. J. E. Demuth, H. Ibach and S. Lehwald, Phys. Rev. Lett. 40, 1044 (1978).

40. E. O. Fischer and H. P. Fritz, Angew. Chem. 73, 353 (1961).

41. K. J. Klabunde and H. F. Efner, J. Fluorine Chem. 4, 114 (1974).

42. P. A. Redhead, Vacuum 12, 203 (1962).

43. N. V. Richardson, Surface Sci. 87, 622 (1979).

44. H. Ibach and S. Lehwald, J. Vac. Sci. Technol. 15, 407 (1978).

45. J. C. Bertolini, J. Massardier, and G. Dalmai-Imelik, J. Chem. Soc. Faraday Trans. I 74, 1720 (1978).

46. (a) W. T. Tysoe, G. L. Nyberg, and R. M. Lambert, J. Chem. Soc. Chem. Commun. 623 (1983).

(b) T. M. Gentle and E. L. Muetterties, J. Phys. Chem. 87, 2469 (1983).

47. J. E. Demuth, K. Christmann and P. N. Sanda, Chem. Phys. Lett. 76, 201 (1980).

48. P. C. Stair and G. A. Somorjai, J. Chem. Phys. 67, 4361 (1977).

49. S. Lehwald and H. Ibach, Surface Sci. 89, 425 (1979).

50. J. R. Creighton and J. M. White, Surface Sci. 129, 327 (1983).

51. C. Backx and R. F. Willis, Chem. Phys. Lett. 53, 471 (1978).

52. J. A. Gates and L. L. Kesmodel, Surface Sci. 124, 68 (1983).

53. A. M. Baro and H. Ibach, J. Chem. Phys. 74, 4194 (1981).

54. E. L. Garfunkel, J. J. May, J. C. Frost, M. H. Farias, and G. A. Somorjai, J. Phys. Chem. 97, 3629 (1983).

55. P. A. Lund, R. R. Smardzewski, and D. E. Tevault, Chem. Phys. Lett. 89, 508 (1982).

56. M. Moskovits and D. P. DiLella, Chem. Phys. Lett. 73, 500 (1980).

APPENDIX A

DESIGN AND CONSTRUCTION OF A HIGH STABILITY, LOW NOISE, POWER SUPPLY FOR USE WITH HIGH RESOLUTION ELECTRON ENERGY LOSS SPECTROMETERS

A.1 Introduction

This appendix describes the design and construction of a high stability, low noise, solid-state power supply for 127° Ehrhardt-type [1] high resolution electron energy loss spectrometers (HREELS). General purpose operational amplifier-based power supplies are used to provide potentials for the 22 lens elements of the spectrometer. Many of these potentials are split to provide deflecting voltages for paired lens elements of the spectrometer. The use of ultrastable, low noise difference amplifiers provide the facility to sweep all of the analyzer voltages rapidly so one may obtain repetitively scanned spectra quickly. Incorporated in this supply is a filament emission control circuit. Included along with a discussion of the design philosophy is a description of the supply electrical specifications and how they are met. Examples of spectra obtained using this supply are presented and compared with spectra obtained with the commonly used potential supply based on passive potential divider networks. Substantial improvements in both signal-to-noise ratio and time of data acquisition are observed.

A.2 Technique Description

The use of HREELS for detecting the normal vibrational modes of molecules adsorbed on single crystal surfaces under ultrahigh vacuum

conditions has increased tremendously in recent years. The technique was first implemented by Propst and Piper [2] in 1967 and has subsequently been refined mainly through the efforts of Ibach and coworkers [3]. Today there are many operational spectrometers at laboratories around the world with many more under construction. The applicability of HREELS as a surface spectroscopy capable of determining the physical and chemical properties of surfaces and adsorbates is demonstrated throughout this dissertation.

Most HREELS spectrometers, including those described in this thesis are of the 127° cylinder type, although successful systems have been built based on cylindrical mirror analyzers [4], or hemispherical analyzers [5]. A schematic of one of the HREELS apparati used in our laboratory is presented in Figure A.1. Electrons emitted from a tungsten hairpin filament are monochromatized and focussed onto the crystal specimen by means of the 127° monochromator sector. Typically, the electron impact energy is variable between 1-10 eV and the angle of incidence varies between 50-80° with respect to the surface normal. Scattered electrons, some of which have exchanged vibrational quanta with the adsorbate species, are energy analyzed (typically in the specular direction) in the second 127° analyzer sector and detected with a channeltron electron multiplier. Pulses from the channeltron are amplified, shaped and discriminated, and in this case, converted to an analogue output with a ratemeter. Spectra are scanned in a constant resolution mode by applying a linear retarding potential (V_s) to the analyzer section of the spectrometer and recorded

directly by a chart recorder driven by V_s along the Y axis. As mentioned above, potentials for the elements of the spectrometer were previously generated using a passive resistor network. Noise was reduced to what was considered an adequate level by filtering the output voltages with long time constant (up to several seconds), resistor-capacitor circuits. The scanning voltage, V_s, was generated using a motor driven potentiometer. Performance figures for both this supply and the newly designed power supply are presented in Table A.1.

A.3 Design Philosophy and Description

Table A.1

A Comparison of Measured Performance of our New HREELS Supply and an Older Potential Divider Network Type of Supply

Characteristics	New HREELS Supply	Potential Divider Network
Noise*	0.5*mV peak-to-peak	2.0 mV peak-to-peak
Ripple	less than 0.25 mV	4 to 20 mV (60 Hz) varies from lens to lens
Time constant	0.003* seconds	up to 20 seconds
Drift/hour period	0.003 mV	50 mV
Time to stabilize after start-up	100 seconds	several hours
Emission-stabilized filament supply	Less than ±0.05 mA change in 24 hours at 9 mA emission current.	This feature is not available in this supply.

* This output noise may be further reduced by limiting the speed of response. See the section on design philosophy for a discussion concerning the design of output characteristics.

Figure A.2 is a block diagram of a typical lens and delta supply. These general purpose modules are configured for a particular lens by choosing the appropriate sign of reference supply and selecting the necessary scaling resistors so as to provide the required voltage range for the lens in question.

To achieve good temperature and long term drift stability, we have used a single, temperature stable, voltage reference source. The 10 volt reference supply is a monolithic, integrated circuit device which is available with similar specifications from several manufacturers. The device we used [6] has an offset voltage temperature drift of less than 50 microvolts/°C and less than 80 microvolts/month drift. Since no voltage greater than 55 volts is required for any lens, all of the required reference voltages may be developed from a single 10 volt source by means of stable amplifiers with no more than a factor of 5.5 gain.

Two kinds of operational amplifiers are used. An extremely stable, monolithic, bipolar input, operational amplifier is used for all of the lenses but two that require a voltage greater than 18 volts with respect to the supply common. The amplifier we selected [7] has a change in offset voltage of less than 0.5 microvolts/°C and less than 2 micro volts/month offset drift. For the two lenses that require larger voltage ranges, we use a high voltage FET input, operational amplifier [8], with 25 microvolts/°C offset voltage temperature drift and less than 50 microvolts/month offset drift. The unity gain bandwidth of both amplifiers is greater than 0.6 MHz and

the full power bandwidth is greater than 30 kHz. Therefore, a 10 to 90 percent step response rise-time of less than 0.5 milliseconds for any lens supply is readily achieved along with excellent stability and very little peak-to-peak ripple and noise (see Table A.1).

A typical lens supply (Figure A.2) consists of these very stable amplifiers connected as shown to function as a difference amplifier. By means of a front panel control potentiometer, the lens voltage may be set to any value in the range allowed for that lens supply. The reference voltage supplied to the positive input of the difference amplifier will cause the output voltage of the difference amplifier to float in proportion to the reference voltage. Of course, one must initially set up the gains, offset, and common mode rejection for each lens supply. This tedious and painstaking procedure was accomplished upon the initial set up and test of the HREELS supply system and after two years of operation we have not found it necessary to calibrate or redo any of these adjustments.

The delta supply voltages for the split lens are obtained by floating two temperature stable 10 volt reference supplies upon the lens voltage. This provides a split lens voltage of up to ±10 volts. The delta supply voltage has much greater stability than that of the lens voltage it is referenced to. The raw supply voltages for the floating reference supply are provided by a commercially available DC-to-DC converter. The converter [9] used in this application is selected for the excellent shielding of the electrical noise from the internal R.F. oscillator. As shown in Figure A.2, the range of the

delta supply voltages is determined by a low impedance divider string which uses temperature stable metal film resistors and a front panel, 22 turn, cermet potentiometer.

The externally generated sweep voltage is added to each of the analyzer potentials via a buffer amplifier (Figure A.2). The magnitude of the sweep voltage for each lens may be set individually by means of a slope control. This feature is provided by changing the input gain determining resistor for each summing amplifier to allow for optimization of the energy resolution of the HREELS spectrometer throughout the spectral range.

Convenient access for adjustment and a means of measuring all lens potentials is provided on the front panel of the HREELS supply (Figure A.3). Additionally, the front panel provides a diagram of the electrical interrelation of each supply to the reference potentials and a label indicating the sign and range of each lens voltage with respect to its reference level. All test points and controls are connected by colored traces on the front panel. These red and blue traces facilitate in the set-up and operation of a HREELS experiment.

The front panel has another feature which permits the user to disconnect any lens element from its voltage supply by means of a rocker switch. These switches and the extra test points connected to the lens in question may be seen at the bottom of Figure A.3. This has proved very useful in measuring the emission current collected by any lens element. The front panel switches are used extensively in tuning the HREELS monochromator and in measuring the crystal current.

A novel feature of this HREELS supply is the emission stabilization circuit. This provides the user with the ability to set any desired emission current by means of the potentiometer on the HREELS supply front panel. A block diagram of the emission control and stability circuit is shown in Figure A.4. The center of the filament may be set to any voltage as determined by the filament level supply (one of the HREELS supplies described above). The emission current may be monitored by a voltage proportional to the emission current which is available at a front panel test point (Figure A.4). The feedback control voltage to the floating filament supply is continuously varied by the emission stabilization circuit to maintain constant emission current despite changes in filament temperature and emission properties with time (see Table A.1). Use of this circuit has resulted in accurately reproducible spectra, crystal currents, and count rates. One can set up a HREELS experiment on one day and turn off all of the supplies overnight and upon return the next day find all of the supply voltages, currents, and count rates exactly as they were after but a few minutes warm-up time.

A.4 Performance

The improvements due to the new power supply are displayed in Figure A.5. Shown here are the vibrational spectra of carbon monoxide chemisorbed on Pt(111) at 300K at a saturation coverage; spectrum A is obtained with a passive potential divider network power supply similar to that used on nearly all existing spectrometers while spectrum B is

obtained using our new high stability, low noise, power supply. Spectra were chosen to allow maximum comparison of differences due solely to the power supplies while maintaining optimal resolution and definition attainable with each power supply. Hence, the elastic beam intensity (2×10^5Hz), the FWHM of the elastically reflected beam (75 cm^{-1}), the pass energies of both the monochromator and the analyzer (0.6 eV), and the time constant of the analogue ratemeter (10 seconds) are the same for both spectra. The improved signal-to-noise ratio in spectrum B when using the new power supply is clearly evident. Note the increased resolution of all peaks in spectrum B, especially the improved definition of the peaks at 360 and 1870 cm^{-1}. Also note that the signal returns to the baseline between peaks in this spectrum. Equally important is that spectrum B was obtained 2.3 times faster than spectrum A (400 cm^{-1} in less than 26 minutes compared to over 59 minutes with use of the passive resistor network).

These improvements are directly related to the much greater stability and significantly reduced noise (see Table A.1) of our new HREELS power supply. Although the FWHM of the elastic beam for both power supplies is very similar, resolution is increased in the inelastic spectrum of the new power supply due to the ability to scan at a faster rate with higher signal-to-noise ratio and much improved stability of the supplied voltages. Just as important, yet not apparent in Figure A.5, is the ease in which the new power supply can be tuned for optimal resolution and inelastic signal intensity. The

ease of tuning, reproducibility, and stability must also be enhanced by the emission stabilization circuit added to this new power supply. These advances allow improved and increased data output in less time.

A.5 Additional Capabilities

The improvements in the signal-to-noise ratio and data acquisition time obtainable using the high stability, low noise, power supply has been demonstrated. Additionally, this supply has the necessary noise stability and response characteristics to be used in conjunction with a computer-based digital data-acquisition system; we are currently implementing this improvement. Using a computer-based system, the energy sweep input is a computer-generated stairstep ramp. At each discrete step, corresponding to a specific electron energy loss, pulses from the channeltron are counted and stored. While the data is being collected, the computer displays a real-time histogram of total number of counts [N(E)] vs. energy. The process can be terminated once sufficient S/N is achieved. The stored data may then be digitally processed to compare with previously acquired spectra, to deconvolute features, to subtract background, etc.

Furthermore, there is the possibility of replacing the channeltron with a micro-channelplate array and metal anode at the focal plane of the spectrometer. Coupled with position sensitive electronics, this arrangement would allow a broad energy range of the HREELS spectrum to be acquired simultaneously, reducing the data acquisition time to a small fraction of that required with a traditional single channel counting system.

REFERENCES

1. H. Ehrhardt, L. Langhans, F. Linder, and H. S. Taylor, Phys. Rev. 173, 222 (1968).
2. F. M. Propst and T. C. Piper, J. Vac. Sci. Technol. 4, 53 (1967).
3. See for example Chapter 6 of Electron Spectroscopy for Surface Analysis ed. H. Ibach, Springer-Verlag, Berlin, 1977.
4. S. Anderson, Solid State Commun. 20, 229 (1976).
5. C. Backx, R. F. Willis, B. Feuerbacher, and B. Fitton, Surface Sci. 68, 516 (1977).
6. Analog Devices, AD584, Pin Programmable Precision Voltage Reference.
7. Precision Monolithics, OP-07CP, Ultra-low offset voltage Op-amp.
8. Burr-Brown, 3582J, High Voltage Operational Amplifier.
9. Burr-Brown, Model 700, Isolated DC-to-DC Converter.

FIGURE CAPTIONS

Fig. A.1. Schematic diagram of a 127° HREELS spectrometer: The filament and monochromator section are rotatable so that possible angular effects can be studied. The spectrometer assembly is mounted on a 200 mm Conflat flange.

Fig. A.2. Typical lens and delta supply: The block diagram shows a typical differential amplifier circuit used to produce an ultra-stable, low noise, lens voltage. The delta voltages are developed as shown to float upon the lens voltage.

Fig. A.3. Photograph of the HREELS power supply front panel: the interrelation of each supply to the reference potentials and the signal and range of each lens voltage with respect to its reference level is diagrammed here. The bottom of the front panel contains test points to measure the emission current collected by any lens element.

Fig. A.4. Emission stabilization system: A block diagram of the emission current sensing bridge and difference amplifier circuit is shown. This circuit produces a voltage that is proportional to the emission current. This voltage is available at a front panel test point and is used by the feedback control circuit to stabilize the emission current.

Fig. A.5. Comparison of the vibrational spectra of CO chemisorbed on Pt(111) at 300K: Spectrum A is obtained with the passive potential divider network power supply, while spectrum B is obtained with our new high stability, low noise power

supply. Note the improved definition, resolution, signal-to-noise ratio, and lessened collection time of spectrum B as compared to spectrum A.

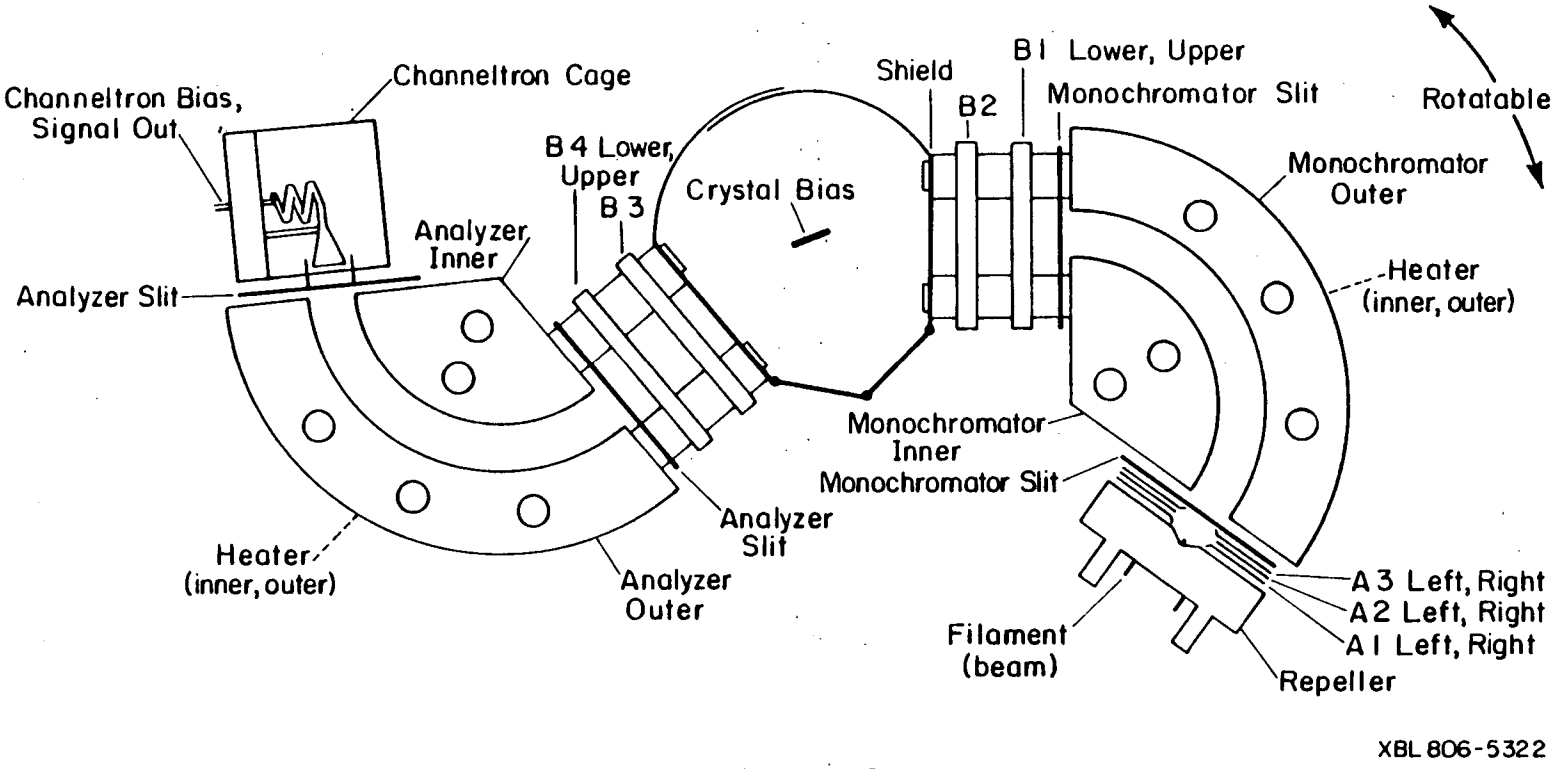
Channeltron Bias,
Signal Out
Channeltron Cage
Shield
B1 Lower, Upper
Monochromator Slit
B2
Rotatable
B4 Lower,
Upper
B3
Crystal Bias
Monochromator
Outer
Analyzer,
Inner
Heater
(inner, outer)
Analyzer Slit
Monochromator
Inner
Monochromator Slit
Analyzer
Slit
Heater
(inner, outer)
Analyzer
Outer
A3 Left, Right
A2 Left, Right
A1 Left, Right
Filament
(beam)
Repeller
XBL 806-5322

Figure A.1

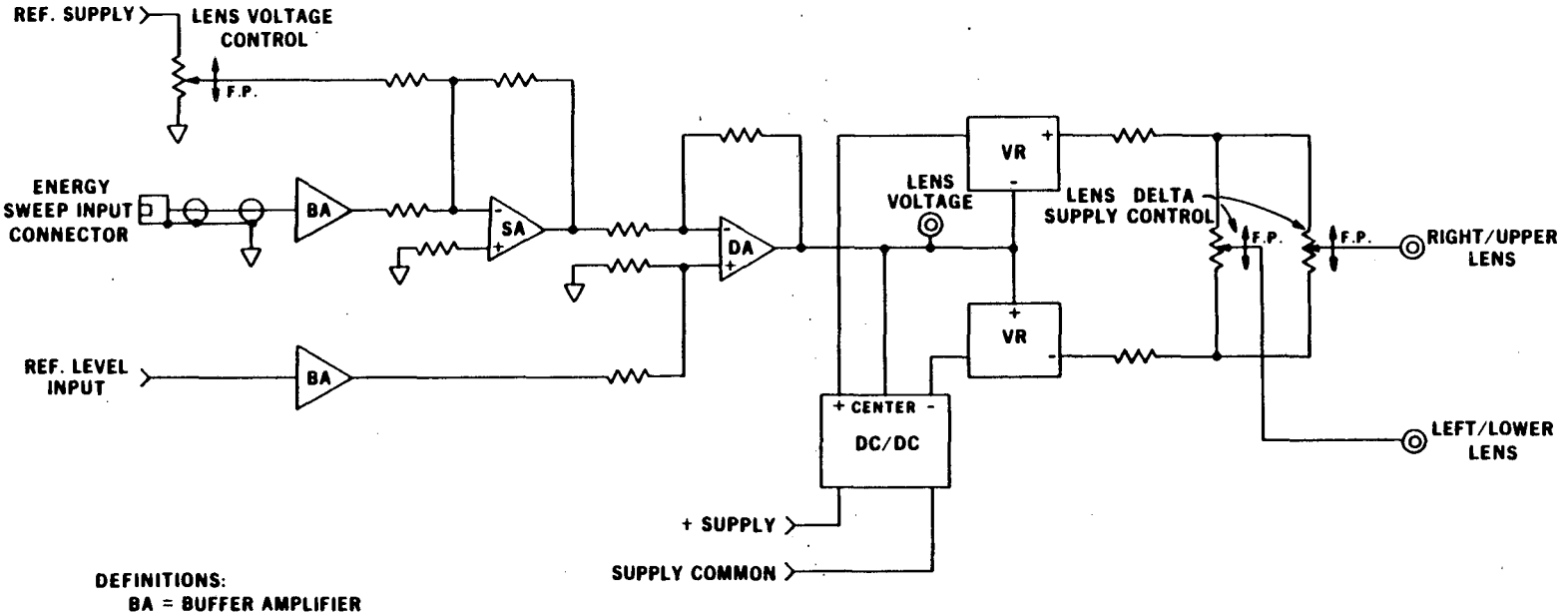

DEFINITIONS:
- BA = BUFFER AMPLIFIER
- DA = DIFFERENCE AMPLIFIER
- DC/DC = ISOLATED DC/DC CONVERTER
- F.P. = FRONT PANEL POTENTIOMETER
- SA = SUMMING AMPLIFIER
- VR = ULTRA STABLE 10 VOLT REFERENCE

TYPICAL LENS AND DELTA SUPPLY

XBL 818-11494

Figure A.2

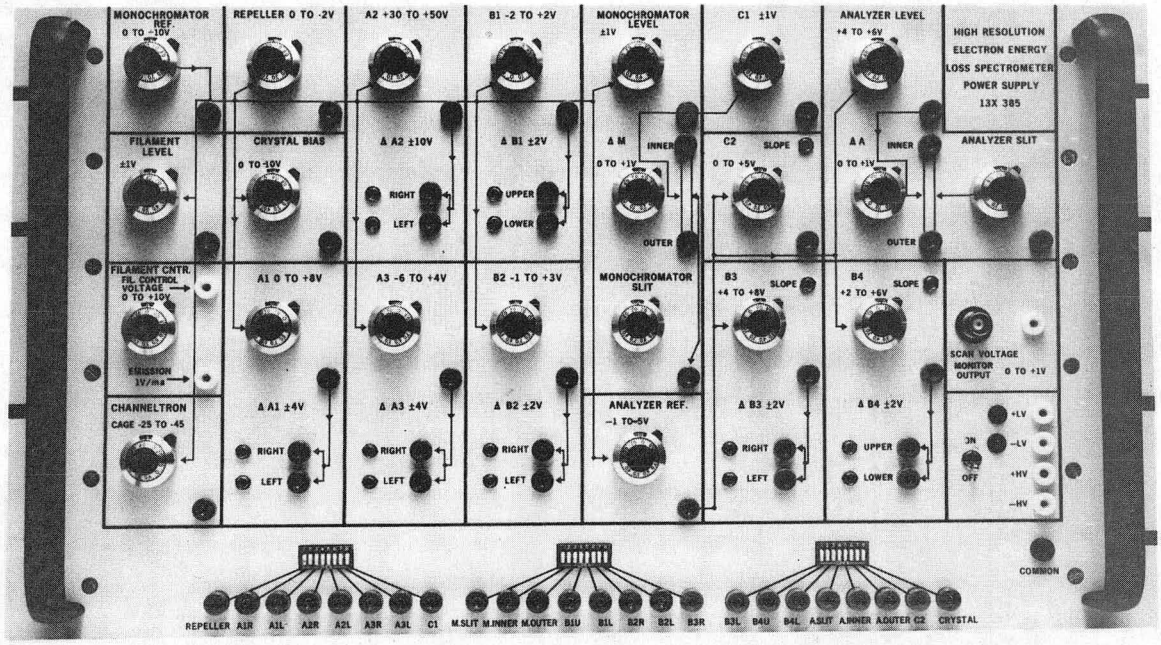

CBB 817-06812

Figure A.3

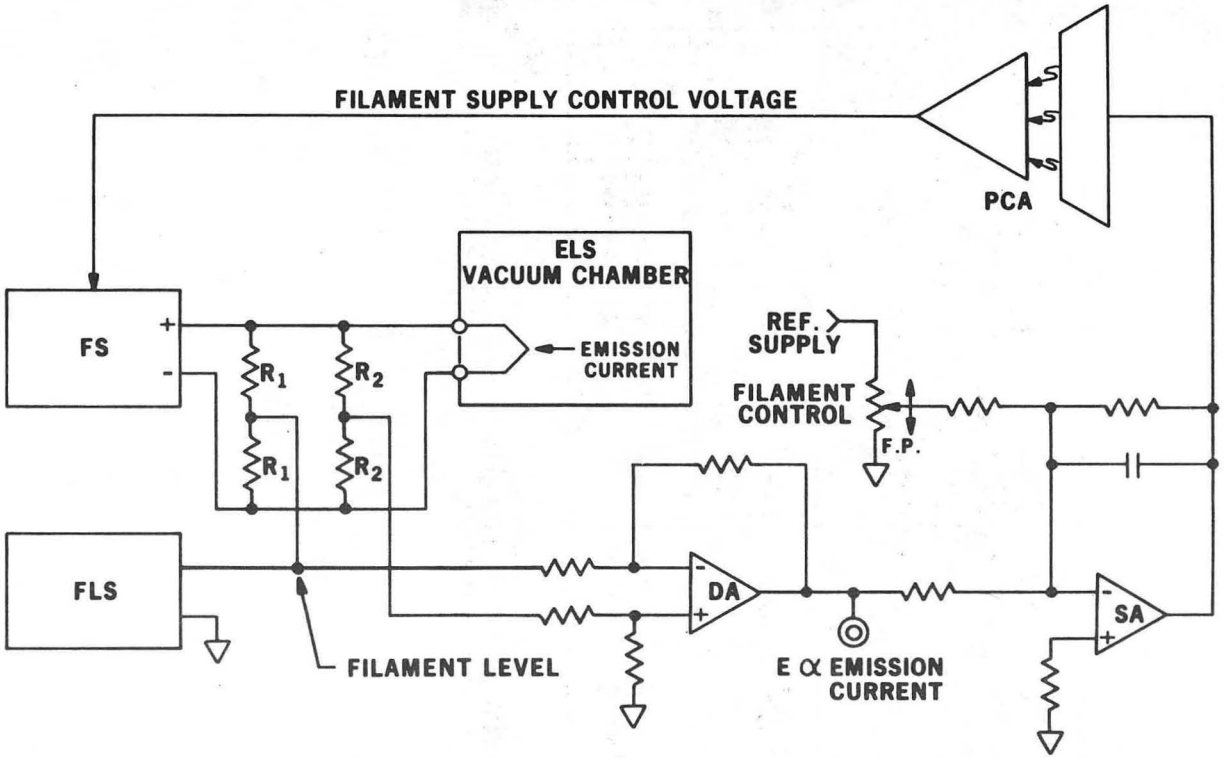

DEFINITIONS:

DA = DIFFERENCE AMPLIFIER
E = CONTROL PLUS STABILIZATION
F.P. = FRONT PANEL POTENTIOMETER
FLS = FILAMENT LEVEL SUPPLY
FS = FLOATING FILAMENT SUPPLY
PCA = PHOTO-COUPLED ISOLATION AMPLIFIER
R_1 & R_2 = EMISSION CURRENT BRIDGE RESISTORS
SA = SUMMING AMPLIFIER

EMISSION STABILIZATION SYSTEM

XBL 818-11495

Figure A.4

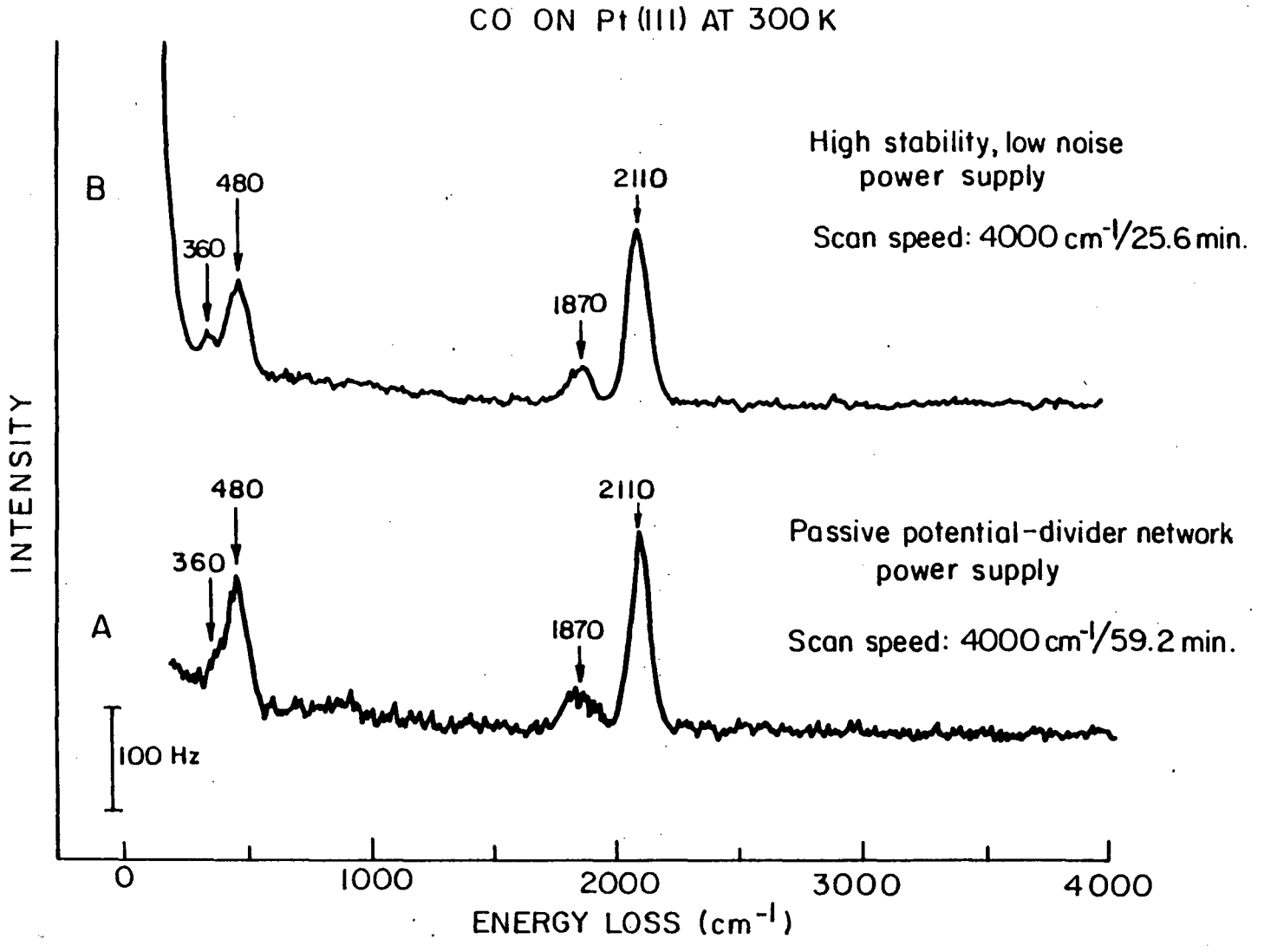

Figure A.5

XBL8111-6957

ACKNOWLEDGEMENTS

The completion of this dissertation could not have been accomplished without the help and wisdom of several others. I am especially grateful to those I have collaborated with and have learned so much from, including Eric Garfunkel, Paul Davies, Bruce Koel, Michael Van Hove, Eddy Tysoe, and Harry Tom. Their expertise and enthusiasm has brought to fruition much of the research described here.

The Somorjai group has been a valuable source of knowledge and assistance. Especially helpful in these regards has been Jack Frost, Phil Watson, Mark Davis, Roland Koestner, Mike Quinlan, Frank Ogletree, Nic Spencer, Francisco Zaera, Mario Farias, Rongfu Lin, Muhib Khan, Mathew Mate, Randy Yeates, Joe Maj, Brian Naasz and Brian Bent. I am grateful to Roger Baetzold for introducing me to surface science and the research of the Somorjai group, and to Larry Dubois and Paul Hansma for teaching me UHV and surface vibrational spectroscopy.

All of the equipment used has been skillfully hand crafted and maintained by Bob McAllister, Emergy Kozak and Kieth Franck. Joe Katz has single handedly made HREELS enjoyable to perform through his expertise in electronics design and fabrication. Gloria Pelatowski has drawn all figures with speedy craftsmanship, and Diana Morris has expertly typed this thesis.

I am endebted to my parents for their support. My accomplishments are due to their encouragement and their example. Their contribution is immersurable, and it is to them that I have dedicated this thesis.

Finally, I am most grateful to Gabor Somorjai for his enthusiasm and wisdom. His patience and understanding encourage free thinking and creative research, yet his guidance ensures accomplishment. His creativity and endless energy are an inspiration to us all. I am proud to have worked with him.

I gratefully acknowledge support from a University of California Fellowship. This work was supported by the Director, Office of Energy Research, Office of Basic Energy Sciences, Material Sciences Division of the U.S. Department of Energy under Contract No. DE-AC03-76SF00098.